GIGAWATT PICOSECOND DYE LASERS AND ULTRAFAST PROCESSES IN SEMICONDUCTOR LASERS

Thesis by

Thomas L. Koch

In Partial Fulfillment of the Requirements

for the degree of

Doctor of Philosophy

California Institute of Technology

Pasadena, California

1982

(Submitted May 24, 1982)

To

Peggy

and

Brian

- ACKNOWLEDGEMENTS -

I would like to take this opportunity to thank my advisor, Professor Amnon Yariv, for his encouragement and support throughout my graduate studies at Caltech. His valuable insights were a boon to my work, and being a member of his research group expanded my interests to many new areas of quantum electronics.

I would also like to express my gratitude to Dr. Richard H. Moyer and Dr. Pinchas Agmon, who first introduced me to the experimental aspects of picosecond laser technology. A special thanks also goes to Liew-Chuang Chiu, who collaborated in much of the work reported here. I am also indebted to many other talented and helpful colleagues. Of particular help to me was the unselfish assistance of Dr. D. P. Wilt and Christopher Harder, who both grew semiconductor lasers for this study and also provided stimulating conversation and ideas. I am also indebted to Desmond Armstrong, whose technical assistance in the experimental aspects of this thesis was invaluable. I also thank Larry Begay for his help in the construction of the experimental apparatus used in this study.

I also gratefully acknowledge the financial support of a National Science Foundation Graduate Fellowship, an Earl C. Anthony Fellowship, and several generous scholarship awards from the Los Angeles Chapter of the ARCS Foundation.

My deepest gratitude goes to my wife Peggy, whose love and support were a constant source of encouragement and inspiration.

- ABSTRACT -

This thesis is a theoretical and experimental investigation of a gigawatt picosecond dye laser oscillator-amplifier system, and the application of that system to the study of ultrafast lasing and carrier dynamics in semiconductor lasers.

Beginning with a review of traveling wave rate equations, nonlinear pulse propagation in a generalized two-level amplifying/absorbing medium is discussed. This permits a qualitative treatment of synchronously mode-locked dye lasers. The formalism is then refined to provide a quantitative analysis of picosecond dye laser amplifier chains, including amplified spontaneous emission, saturable absorbers used for amplifier stage isolation, gain saturation with "angular hole-burning" and triplet losses, and linear and nonlinear pulse shaping effects.

Experimentally, the construction and operation of a three stage Nd:YAG laser pumped picosecond dye laser amplifier chain is described. Numerical modeling is used to compare the theoretical analysis with the experimental results. In addition, a brief discussion of picosecond time domain measurement techniques is presented, focussing on nonlinear optical methods. This includes a parametric sum frequency upconversion gating technique used extensively in this work to provide linear, picosecond resolution temporal measurements of optical pulses which are synchronized to the dye laser pulses.

The output of the picosecond dye laser system is used to optically generate high carrier densities in semiconductor lasers, and the ensuing short pulse lasing dynamics are investigated and compared to the predictions of a simple rate equation analysis. Novel effects are observed in the spectrally resolved temporal measurements of the lasing output from picosecond optically pumped buried heterostructure semiconductor lasers. A model is developed which includes both broad-

band stimulated emission as well as many-valley and hot electron effects in the semiconductor, and the model is in close agreement with the observed behavior. The conclusion is drawn that the picosecond lasing dynamics of semiconductor lasers can be understood if the conventional rate equations are abandoned in favor of a more fundamental analysis which includes not just the dynamics of the optical energy exchange in the laser cavity, but the detailed picosecond dynamics of the semiconductor material as well.

- CONTENTS -

CHAPTER 1
INTRODUCTION

Throughout the last decade, picosecond pulse laser systems have proven to be very effective research tools for probing physical phenomena on ultrafast time scales which are inaccessible by other more conventional techniques. During this time there has been a continued interest in using picosecond laser pulses to study ultrafast phenomena in solids. The main thrust of the research effort of which this thesis is a part has been in this direction, in particular the study of ultrafast optical and electronic dynamics of semiconductors and semiconductor opto-electronic devices.

The impetus for these studies is the fact that a basic understanding of ultrafast optical and electronic phenomena in both bulk semiconductors and in artificial micron-sized semiconductor structures will become crucial as opto-electronic and integrated optics devices are continually pushed towards smaller sizes and faster speeds. It is also becoming increasingly apparent that a merger between picosecond laser/optical technology and more conventional semiconductor electronic technology may be fruitful, possibly extending device speeds and sizes into regimes where either technology alone begins to fail. The recent demonstration of devices and techniques ranging from picosecond opto-electronic sampling and correlators[1] to complex ultrafast analog to digital converters[2] is testimony to the promising future of these technologies. Earlier work in our research effort included studies of picosecond opto-electronic switches[3] such as the device shown in Fig. 1.1. In

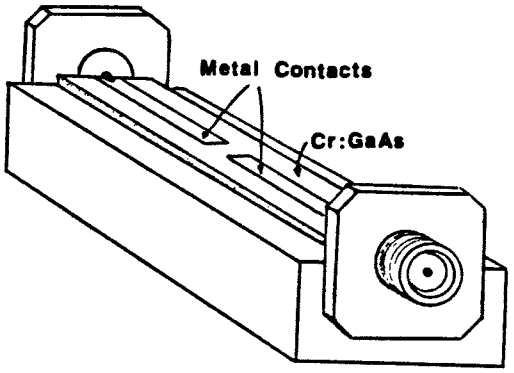

Figure 1.1 Ultrafast opto-electronic switching structure consisting of gapped microstrip line evaporated on semi-insulating GaAs.

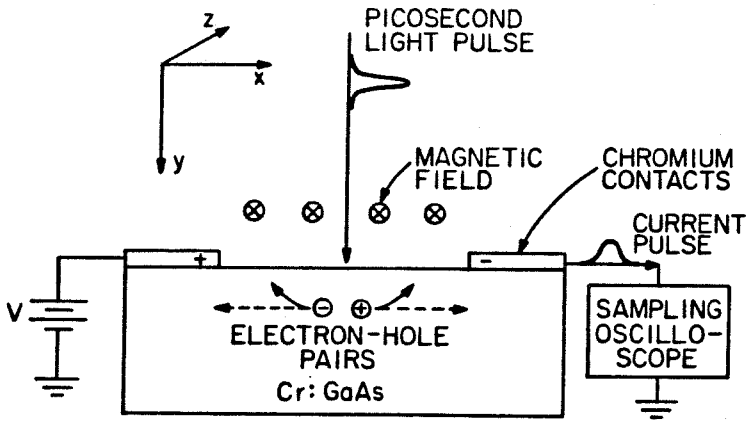

Figure 1.2 Geometry of magnetophotoconductivity experiment. $E \times B$ drift moves carriers either into the bulk or towards the surface, providing a means of discriminating between bulk and surface lifetime effects.

these devices, a transient carrier population is generated by a picosecond optical pulse in semi-insulating GaAs, with the resulting conductive surface layer completing the microstrip line to yield an ultrafast rise time current pulse. After preliminary experiments indicated that switches had very fast *decay* times as well (~ 70 psec), the study shifted towards gaining an understanding of why such fast decay should occur. Since all the photocarriers are created within a few thousand angstroms of the surface, a strong candidate was surface recombination. To confirm this, a transverse magnetic field was applied as shown in Fig. 1.2. The resulting $E \times B$ drift forces carriers towards the surface or into the bulk, depending on the sign of the field, with a concomitant increase or decrease in the speed of the switch. This was indeed the experimentally observed outcome[4]. This is cited merely as an example of the nature of our picosecond materials/device research effort. Studies of new device structures, geometries and concepts often provoke the studies of new or previously ignored physical phenomena which may arise in connection with those devices.

The particular study to be discussed in this thesis has been aimed at shedding some light on the ultrafast physics inherent in semiconductors which may ultimately limit the pulse durations and speeds of semiconductor lasers and other opto-electronic devices. In particular, picosecond optical techniques have permitted the operation and measurement of semiconductor diode lasers in high speed regimes previously inaccessible by electronic means alone. The intent here has not been to produce the shortest pulses ever observed from semiconductor lasers, but rather to investigate in a general sense carrier and lasing dynamics on time scales where the conventional rate equation analysis of transient laser response might be inapplicable. In doing so, a broader understanding of what kind of analysis *is* necessary emerges, and new phenomena which are relevant to ultrafast semiconductor laser response can also be explored.

To facilitate such studies, of necessity considerable research goes into improving the state of the art in picosecond laser systems. Probably the most well suited picosecond laser system for studying high speed phenomena in solids is the mode-locked dye laser because of its tunability, high repitition rate, and the extremely short pulses which can result from the wide bandwidth of laser dyes. The state of the art in pulse width at this writing is ~ 90 femptoseconds from colliding pulse mode-locking in a passively mode-locked ring laser configuration[5]. Additional pulse compression reduces the pulse widths further to values as low as ~ 30 femptoseconds or only ~ 14 optical cycles[6]. The earlier opto-electronic switch work mentioned above was carried out with a passively mode-locked dye oscillator. Although this provides high performance when properly maintained, for the experiments to be discussed here this was found to be too unstable and unreliable a laser system. For this reason, an actively mode-locked synchronously pumped oscillator was constructed. However, one of the principal drawbacks of mode-locked dye lasers remained which is the low pulse energy, with typical output values of $\sim 5 \times 10^{-10}$ Joules/pulse. Many of the interesting phenomena in semiconductor opto-electronic devices involve degenerate carrier populations. As an example, for short pulse, electrically pumped lasing in GaAs lasers, carrier densities of $\sim 2 \times 10^{18}$ cm^{-3} can be encountered. To generate this carrier density optically, with a typical absorption depth of ~ 0.25μm in the visible, even with perfect coupling of the optical energy into the material the experimental spot must be limited to ~ 70μm in diameter. This severely constrains the nature of the experiments which can be performed, even when the entire output is used just to excite the sample under study. Many experiments require pump-probe or similar arrangements using multiple pulse trains with precisely controlled path length delays set up on the optical table; these reduce the available energy even further.

To remove the limitations mentioned above, and to add further experimental flexibility to be detailed later, a picosecond dye laser amplifier chain was constructed which boosts the modelocked dye laser output into the gigawatt regime[7,8]. As well as providing an ample supply of photons for experiments, due to the very high peak powers an extraordinary array of nonlinear optical phenomena becomes available to vastly extend the spectral range of the laser system. Harmonic generation, frequency mixing, stimulated Raman scattering, and picosecond continuum generation together provide picosecond pulses with essentially complete coverage of the optical spectrum from the ultraviolet well into the infrared, often with efficiencies in the tens of percents.

The organization of this thesis is aimed at showing some of the common features of the physics of picosecond laser pulse interactions. Following this introduction, Chapter 2 is a review of traveling wave rate equations since these equations play a central role throughout this work. In various forms with effects added which are peculiar to each circumstance, they will be applied to (a) mode-locked dye laser oscillators, (b) signal pulse propagation in amplifier cells, (c) pump pulse propagation in laser pumped amplifiers, (d) pulse propagation in saturable absorbers, and (e) pulse evolution in semiconductor lasers.

A brief discussion of the limitations of the equations is presented along with some simple solutions and a discussion of their consequences which are relevant to the remainder of this work. Following this, Chapter 3 derives the equation which governs the evolution of a system with simultaneous signal and pump propagation together with their energy exchange. A discussion of synchronously mode-locked oscillators follows to show the versatility of the derived equation. Chapter 4 presents the full theory of picosecond dye laser amplifier chains[8], including pulse shaping with saturable absorbers, effects from angular hole burning, triplet absorption, and finite vibrational level lifetimes. For pumping of the amplifier, a

treatment of amplified spontaneous emission (ASE) is developed. This permits a reasonably accurate dynamical model of transient gain and also a discussion of amplifier efficiency and design optimization. Chapter 5 details the experimental laser apparatus including a discussion of the theory and implementation of picosecond time domain measurement techniques. Some experimental results are presented which support the amplifier chain theory of Chapter 4.

This is followed by the work on picosecond carrier and lasing dynamics in semiconductor lasers. Chapter 6 reviews the usual simple treatment of pulse evolution in gain/loss switched systems, and discusses some possible flaws from round trip modulation effects which might be expected in very short pulse operation. Experimental results from picosecond optically Q-switched semiconductor lasers[9] are presented. Chapter 7 presents the full analysis of ultrashort pulse evolution in optically pumped semiconductor lasers. This begins with a treatment of the relevant ultrafast carrier dynamics from which integro-differential "rate equations" can be derived, including a dynamical description of the hot degenerate electron and hole distributions and the broadband nature of the stimulated emission. Experimental results for the picosecond dynamics of optically pumped buried heterostructure semiconductor lasers are presented and compared with computer solutions of the rate equations[10]. The agreement indicates that the picosecond performance of semiconductor lasers can be understood if the simple rate equations are abandoned in favor of a more complete and fundamental analysis.

CHAPTER 1 REFERENCES

1. D. H. Auston, A. M. Johnson, P. R. Smith, and J. C. Bean, Appl. Phys. Lett. **37**, 371 (1980).

2. F. J. Leonberger, C. E. Woodward, and R. A. Becker, Appl. Phys. Lett. **40**, 565 (1982).

3. D. H. Auston, Appl. Phys. Lett. **26**, 101 (1975).

4. R. H. Moyer, P. Agmon, T. L. Koch, and A. Yariv, Appl. Phys. Lett. **39**, 266 (1981).

5. R. L. Fork, B. I. Greene, and C. V. Shank, Appl. Phys. Lett. **38**, 671 (1981).

6. C. V. Shank, R. L. Fork, R. Yen, and W. J. Tomlinson, Technical Digest of the Conference on Lasers and Electro-Optics, **Phoenix**, Arizona, p.32, 1982.

7. T. L. Koch, L. C. Chiu, and A. Yariv, Opt. Commun. **40**, 364 (1982).

8. T. L. Koch, L. C. Chiu, and A. Yariv, " Analysis and Performance of a Picosecond Dye Laser Amplifier Chain," to appear in J. Appl. Phys. (1982).

9. T. L. Koch, D. P. Wilt, and A. Yariv, " Q-Switching of Semiconductor Lasers with Picosecond Light Pulses " in *Picosecond Phenomena II*, Springer Series in Chemical Physics, Vol. 14, Ed. by R. M. Hochstrasser, W. Kaiser and C. V. Shank, Springer-Verlag, Berlin, Heidelberg, New York, p.34, 1980.

10. T. L. Koch, L. C. Chiu, Ch. Harder and A. Yariv, " Picosecond Carrier Dynamics and Laser Action in Optically Pumped Buried Heterostructure Semiconductor Lasers," to appear in App. Phys. Lett. (1982).

CHAPTER 2

TRAVELING WAVE RATE EQUATIONS AND SIMPLE SOLUTIONS

2.1 TW Rate Equations

Throughout this thesis, various forms of traveling wave (TW) rate equations will be used to analyze the interaction of optical pulses with a variety of amplifying and absorbing materials. In this chapter a review of the derivation of traveling wave rate equations is presented in a fairly rigorous form for a two-level system. While none of the actual microscopic systems studied in this thesis are two-level systems, the derivation serves an important pedagogical function because it demonstrates how physically intuitive appoximations can often be employed to reduce a complex set of coupled partial differential equations to a simpler and mathematically more tractable set, and it also indicates the nature of the particular approximations involved when incoherent TW rate equations are used. For a more comprehensive review of this subject, we refer the reader to the literature[1,2].

The equations to be solved here involve the interaction of an electromagnetic wave $\vec{E}(\vec{x},t)$ with a spatial distribution of two-level systems at locations $\vec{x}$ which are characterized by a density matrix $\rho(\vec{x},t)$ [3]. The first equation we wish to simplify is the wave equation with a source term

$$\nabla^2 \vec{E} - \frac{1}{c^2}\frac{\partial^2 \vec{E}}{\partial t^2} = \frac{4\pi}{c^2}\frac{\partial^2 \vec{P}}{\partial t^2} \tag{2.1}$$

We first assume one dimensional propagation so $\nabla \rightarrow \partial/\partial z$, and we consider only one vector component of Eq.2.1. The interacting systems are assumed imbedded in a medium which responds linearly to the wave E with a polarization given by the Fourier transform relation

$$\tilde{P}_{LIN}(\omega,z) = \frac{1}{4\pi}[\, n^2(\omega) - 1\,]\tilde{E}(\omega,z) \tag{2.2}$$

where $n(\omega)$ is the frequency dependent index of refraction and the total polarization is now given by

$$P = P_{LIN} + P_{NL} \tag{2.3}$$

Here P_{NL} is tentatively any polarization not included in P_{LIN}; in our case it is the polarization produced by the two-level systems. Fourier transforming Eq. 2.1 and using Eqs. 2.2-3 results in

$$\frac{\partial^2}{\partial z^2}\tilde{E}(\omega,z) + \frac{n^2(\omega)\omega^2}{c^2}\tilde{E}(\omega,z) = -\frac{4\pi\omega^2}{c^2}\tilde{P}_{NL}(\omega,z) \tag{2.4}$$

We now assume a forward traveling wave and express E(t,z) as the product of a plane wave and a "slowly varying" complex envelope

$$E(t,z) = \frac{1}{2}\mathcal{E}(t,z)e^{i(k_1 z - \omega_1 t)} + \text{C.C.} \tag{2.5}$$

where $k_1 = \frac{n(\omega_1)\omega_1}{c}$. We Taylor expand $k(\omega) = \frac{n(\omega)\omega}{c}$ in Eq. 2.4 as

$$k(\omega) = k_1 + \frac{(\omega - \omega_1)}{v_g} + \ldots \tag{2.6}$$

where $v_g \equiv \left[\, \frac{\partial k}{\partial \omega}\Big|_{\omega_1} \right]^{-1}$ is the group velocity in the host medium. Ignoring higher order terms in the expansion Eq. 2.6, the transformed wave equation Eq. 2.4 becomes upon inverse Fourier transforming

$$\frac{1}{2}e^{i(k_1 z-\omega_1 t)}\left[\frac{\partial^2\mathcal{E}}{\partial z^2}-\frac{1}{v_g^2}\frac{\partial^2\mathcal{E}}{\partial t^2}+2ik_1\left(\frac{\partial\mathcal{E}}{\partial z}+\frac{1}{v_g}\frac{\partial\mathcal{E}}{\partial t}\right)\right] + \text{C.C.} = \frac{4\pi}{c^2}\frac{\partial^2 P_{NL}}{\partial t^2} \tag{2.7}$$

where we have noted that multiplying $\tilde{\mathcal{E}}(\omega-\omega_1)$ by $(\omega-\omega_1)$ is equivalent to operating on $\mathcal{E}(t,z)$ in the time domain with $i\frac{\partial}{\partial t}$. Clearly in the absence of P_{NL} the solution of interest for a forward traveling wave is $\mathcal{E} = f(z - v_g t)$ where f is an arbitrary function. We suppose that the introduction of P_{NL} only modifies this solution by a relatively small amount such that

$$2ik_1\left(\frac{\partial\mathcal{E}}{\partial z}+\frac{1}{v_g}\frac{\partial\mathcal{E}}{\partial t}\right) >> \left(\frac{\partial}{\partial z}-\frac{1}{v_g}\frac{\partial}{\partial t}\right)\left(\frac{\partial\mathcal{E}}{\partial z}+\frac{1}{v_g}\frac{\partial\mathcal{E}}{\partial t}\right) \tag{2.8}$$

which reduces Eq. 2.7 to the simpler "wave" equation

$$ik_1 e^{i(k_1 z-\omega_1 t)}\left(\frac{\partial\mathcal{E}}{\partial z}+\frac{1}{v_g}\frac{\partial\mathcal{E}}{\partial t}\right) + \text{C.C.} = \frac{4\pi}{c^2}\frac{\partial^2\tilde{P}_{NL}}{\partial t^2} \tag{2.9}$$

For a two-level system, the polarization P_{NL} is given by

$$P_{NL} = N\langle\mu\rangle = N\,\mathrm{tr}(\rho\mu) = N\mu(\rho_{21}+\rho_{21}^*) \tag{2.10}$$

where μ is the component of the dipole moment operator for the two-level system in the direction of the electric field. The equation of motion for the density matrix is given by

$$\frac{\partial\rho(z,t)}{\partial t} = -\frac{i}{\hbar}[\,H,\rho\,] \tag{2.11}$$

where the Hamiltonian of the system is

$$H_{total} = H_o - \vec{\mu}\cdot\vec{E}(z,t) \tag{2.12}$$

and H_o is the Hamiltonian of the non-interacting two-level system. Adding the phenomenological damping terms of Bloch, Eq. 2.11 expands to

$$\frac{\partial}{\partial t}(\rho_{22} - \rho_{11}) = -\frac{2i\mu}{\hbar}E(z,t)(\rho_{21} - \rho_{21}^*) - \frac{[(\rho_{22} - \rho_{11}) - (\rho_{22} - \rho_{11})_o]}{\tau} \qquad (2.13)$$

$$\frac{\partial \rho_{21}}{\partial t} = -i\omega_0\rho_{21} - \frac{i\mu}{\hbar}(\rho_{22} - \rho_{11})E(z,t) - \frac{\rho_{21}}{T_2} \qquad (2.14)$$

where $\hbar\omega_0 = E_2 - E_1$ and the equilibrium value of the level population difference in the absence of an applied optical pulse is given by $N(\rho_{22} - \rho_{11})_o$. In introducing the damping terms we have gone to the ensemble average and used the "transverse" relaxation time T_2 and the "longitudinal" relaxation time τ. T_2 is the total decay time for the off-diagonal density matrix elements which can result from population decay, or since this is now an ensemble average, from "dephasing" effects which effectively jumble the relative phases of the individual oscillating two-level systems. This can result, for instance, from local perturbations which produce different transient adiabatic changes in the energy level separations of individual components of the ensemble average. These adiabatic changes produce no population decay, but only alter the relative phases of oscillation of the component systems. Since the total decay of the off-diagonal ensemble average is the combination of the two effects mentioned above, we have

$$\frac{1}{T_2} = \frac{1}{\tau} + \frac{1}{T'_2} \qquad (2.15)$$

where T'_2 is the time which results purely from dephasing processes.

In a manner similar to that employed with the electric field, we now implicitly define a slowly varying envelope by letting

$$\rho_{21}(z,t) = \sigma_{21}(z,t)\, e^{i(k_1 z - \omega_1 t)} \qquad (2.16)$$

and insert this into Eqs. 2.13-14 to get

$$\frac{\partial}{\partial t}(\rho_{22}-\rho_{11}) = -\frac{i\mu}{\hbar}(\mathcal{E}^*\sigma_{21} - \mathcal{E}\sigma_{21}^*) - \frac{[(\rho_{22}-\rho_{11}) - (\rho_{22}-\rho_{11})_o]}{\tau} - \left\{ \frac{i\mu}{\hbar}\mathcal{E}\sigma_{21}\, e^{-i(2k_1 z - 2\omega_1 t)} + \text{C.C.} \right\} \tag{2.17}$$

$$\frac{\partial \sigma_{21}}{\partial t} = i(\omega_1 - \omega_0)\sigma_{21} - \frac{i\mu}{2\hbar}\mathcal{E}(\rho_{22}-\rho_{11}) - \frac{\sigma_{21}}{T_2} - \left\{ \frac{i\mu}{2\hbar}\mathcal{E}^*(\rho_{22}-\rho_{11})\, e^{-i(2k_1 z - 2\omega_1 t)} \right\} \tag{2.18}$$

In these equations, we can ignore the terms in the large curly brackets which oscillate at $2\omega_1$ since these integrate to zero; i.e., we assume that σ_{21}, $(\rho_{22}-\rho_{11})$ and $\mathcal{E}$ vary slowly on the time scale of the optical period and average the equations over a few optical cycles.

Returning to Eqs. 2.10-11, we have $P_{NL} = N\mu\sigma_{21}\, e^{i(k_1 z - \omega_1 t)} + \text{C.C.}$ and therefore

$$\frac{\partial^2 P_{NL}}{\partial t^2} = -N\mu\omega_1^2\sigma_{21}\, e^{i(k_1 z - \omega_1 t)} + \ldots + \text{C.C.} \tag{2.19}$$

where we drop the higher order terms having assumed $\omega\sigma_{21} >> \frac{\partial \sigma_{21}}{\partial t}$ and $\omega^2\sigma_{21} >> \frac{\partial^2 \sigma_{21}}{\partial t^2}$. Then Eqs. 2.10-11 and Eqs. 2.17-18 are combined to give the "Bloch Equations"

$$\frac{\partial \mathcal{E}}{\partial z} + \frac{1}{v_g}\frac{\partial \mathcal{E}}{\partial t} = \frac{4\pi\omega_1}{nc}\Xi \tag{2.20}$$

$$\frac{\partial \Xi}{\partial t} + \left[i(\omega_0 - \omega_1) + \frac{1}{T_2} \right]\Xi = \frac{\mu^2}{2\hbar}\mathcal{E}\Pi \tag{2.21}$$

$$\frac{\partial \Pi}{\partial t} = -\frac{1}{\hbar}\left[\mathcal{E}^*\Xi + \mathcal{E}\Xi^* \right] - \frac{[\Pi - \Pi_0]}{\tau} \tag{2.22}$$

where $\Xi \equiv iN\mu\sigma_{21}$ and $\Pi \equiv N(\rho_{22}-\rho_{11})$.

These equations have a wide range of applicability, and can describe many features of resonant interactions, including unusual features such as self-induced

transparency[4] as well as the more ordinary features such as the transient energy transfer we are concerned with. If we suppose that the transverse relaxation time T_2 is much shorter than times of interest, Eq. 2.21 reduces to

$$\Xi = \frac{\mu^2 T_2 \mathcal{E}\Pi}{2\hbar}[\ 1 + iT_2(\omega_0 - \omega_1)\ ]^{-1} \tag{2.23}$$

This is inserted back into Eq. 2.20 and Eq. 2.22. Eq. 2.20 is then multiplied by $\mathcal{E}^*$ and the resulting equation is added to its complex conjugate. The result of these operations is, after some simplification, the pair of *incoherent T.W. rate equations*

$$\frac{\partial \varphi}{\partial t} + v_g \frac{\partial \varphi}{\partial z} = v_g \sigma(\omega_1)\, \Pi\varphi \tag{2.24}$$

$$\frac{\partial \Pi}{\partial t} = -\,2v_g \sigma(\omega_1)\, \Pi\varphi - \frac{[\ \Pi - \Pi_0\ ]}{\tau} \tag{2.25}$$

where φ is the photon density

$$\varphi = \frac{n^2 \mathcal{E}\mathcal{E}^*}{8\pi\hbar\omega_1} \tag{2.26}$$

and $\sigma(\omega_1)$ is the cross section for the transition given by

$$\sigma(\omega_1) = \frac{4\pi\mu^2 T_2 \omega_1}{n^2 \hbar v_g}[\ 1 + T_2^2(\omega_0 - \omega_1)^2\ ]^{-1} \tag{2.27}$$

The derivation of the incoherent T.W. rate equations Eqs. 2.24-25 is based on the following approximations:

a. The use of classical rather than quantum electromagnetic theory

b. The use of the phenomenological damping terms T_2 and τ.

c. The restriction to "slowly varying" envelopes, $\frac{\partial \mathcal{E}}{\partial t} << \omega\mathcal{E}$, etc.

d. The assumption of a homogeneously broadened system of identical atoms

e. T_2 << times of interest

The first approximation is excellent in most regimes of laser physics since the field amplitudes are high and quantum noise is insignificant. The second approximation is correct for the ensemble average and this is the quantity of interest here. Derivations of T_2 are difficult but can be found in the literature for some simple systems such as atomic gases, etc. The longitudinal relaxation time τ can be calculated in a more straightforward manner for an individual component of the ensemble average. The third approximation will be satisfied in all but extremely short ($\approx 10^{-14}$ sec) or extremely wide band optical pulses; these are not of principal interest in this thesis. The fourth appoximation is remedied in a particular case by easily modifiying the equations to include any inhomogeneous effects which may be present (doppler shifts from a velocity distribution in a gas, or angular hole-burning effects to be discussed in Chapter 4, for example). The last appoximation depends critically on the nature of the microscopic system under investigation. When this is not satisfied, for example with picosecond optical pulses interacting with an atomic gas, the full Bloch equations Eqs. 2.20-22 must be used. For the systems to be discussed here such as organic dyes and semiconductors, the dephasing times T'_2 are expected to be in the range of 10^{-13} to 10^{-14} seconds, in the former case from vibrational relaxation and solvent collisions and in the latter from phonon emission/absorption and electron-electron collisions.

2.2 Simple Solutions

We now discuss some simple solutions of the T.W. rate equations. First, since we anticipate frequent application to organic lasing dyes in the remainder of this work, we alter the rate equations slightly for this application. Referring to the energy level scheme shown in Fig. 2.1, we tentatively ignore any crossing to the triplet

states of the dye T and thus the dye can be considered a four level sytem. Absorption occurs from some lower vibrational-rotational level S_o in the lowest singlet electronic state to some excited level in the first excited singlet state S_1^*. This is followed by non-radiative relaxation within the upper singlet level, and emission occurs down to some excited vibrational-rotational level in the lowest singlet state S_o^*. If the nonradiative relaxation is infinitely fast, then at any time the molecule is either in the state S_o or S_1. For purposes of population "book keeping", we are therefore effectively dealing with a two-level sytem with populations which we will call N_1 and N_2 for the lower and upper levels respectively, and $N_1 + N_2 = N$, the total dye concentration. However, at any frequency the emission cross section σ^{em} and the absorption cross section σ^{abs} will not in general have the same value as they do in a real two-level system. With this in mind, we modify Eqs. 2.24-25 to read

$$\frac{\partial \varphi}{\partial t} + v_g \frac{\partial \varphi}{\partial z} = v_g(\sigma^{em} N_2 - \sigma^{abs} N_1)\varphi \tag{2.28}$$

$$\frac{\partial N_1}{\partial t} = v_g(\sigma^{em} N_2 - \sigma^{abs} N_1)\, \varphi + \frac{N_2}{\tau} \tag{2.29}$$

$$\frac{\partial N_2}{\partial t} = - \frac{\partial N_1}{\partial t} \tag{2.30}$$

For the time being we confine our attention to phenomena which occur on a time scale slow compared to the population relaxation time τ. Letting $\tau \to \infty$, Eqs. 2.28-30 become slightly modified versions of the simple two-level equations for which analytical solutions have been found[5,6] and the solution technique is summarized below. Multiplying Eq. 2.29 by σ^{abs} and Eq. 2.30 by σ^{em} and subtracting, we get

$$\frac{\partial}{\partial t}[\, \sigma^{em} N_2 - \sigma^{abs} N_1 \,] = -v_g(\sigma^{em} + \sigma^{abs})[\, \sigma^{em} N_2 - \sigma^{abs} N_1 \,]\, \varphi \tag{2.31}$$

We now change variables, introducing the local " time "

$$\xi \equiv [v_g t - z] \tag{2.32}$$

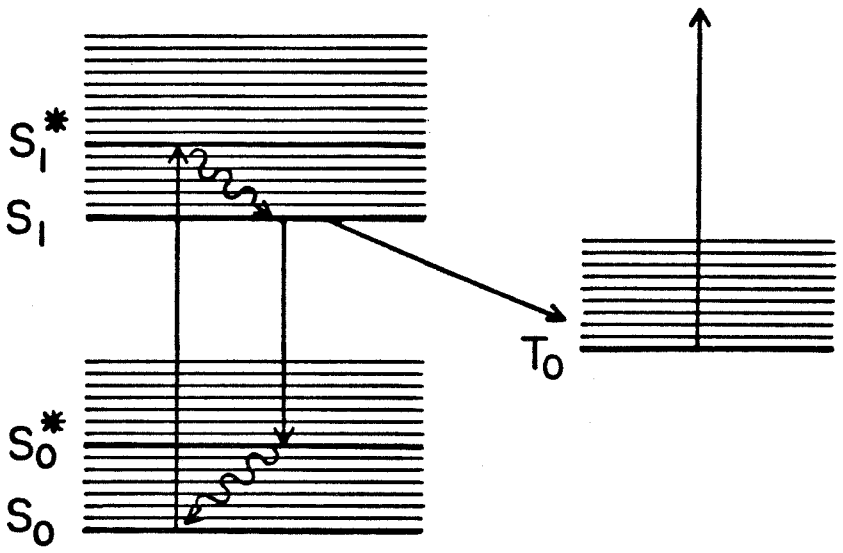

Figure 2.1 Dye molecule energy level scheme used for calculations.

while keeping the distance as a variable

$$\eta \equiv z \tag{2.33}$$

Then for an arbitrary function F

$$\frac{\partial F}{\partial z} = \frac{\partial F}{\partial \xi}\frac{\partial \xi}{\partial z} + \frac{\partial F}{\partial \eta}\frac{\partial \eta}{\partial z} = \left[\frac{\partial F}{\partial \eta} - \frac{\partial F}{\partial \xi}\right] \tag{2.34}$$

$$\frac{\partial F}{\partial t} = \frac{\partial F}{\partial \xi}\frac{\partial \xi}{\partial t} + \frac{\partial F}{\partial \eta}\frac{\partial \eta}{\partial t} = -v_g\frac{\partial F}{\partial \xi} \tag{2.35}$$

and Eq. 2.28 and Eq. 2.31 become the simple set

$$\frac{\partial \varphi}{\partial \eta} = \Delta\ \varphi \tag{2.36}$$

$$\frac{\partial \Delta}{\partial \xi} = -(\sigma^{em} + \sigma^{abs})\ \Delta\ \varphi \tag{2.37}$$

where Δ is the "inversion "variable

$$\Delta \equiv \sigma^{em}N_2 - \sigma^{abs}N_1 \tag{2.38}$$

From Eq. 2.36

$$\Delta = \frac{\partial \ln \varphi}{\partial \eta} \tag{2.39}$$

and when this is substituted in Eq. 2.37 we obtain

$$\frac{\partial}{\partial \eta}\left[\ \frac{\partial \ln \varphi}{\partial \xi} + (\sigma^{em} + \sigma^{abs})\varphi\ \right] = 0 \tag{2.40}$$

which results, after letting $\varphi \equiv \frac{1}{R}$, in

$$\frac{\partial R}{\partial \xi} + f(\xi)R = (\sigma^{em} + \sigma^{abs}) \tag{2.41}$$

where $f(\xi)$ is an arbitrary function of ξ only. The general solution of Eq. 2.41 is

$$R = e^{-\int_0^{\xi} f(x)dx}\left[c(\eta) + (\sigma^{em} + \sigma^{abs})\int_0^{\xi} e^{\int_0^{x} f(y)dy}\,dx\right] \tag{2.42}$$

where $c(\eta)$ is an arbitrary function of η only. Since $f(\xi)$ is arbitrary, we use instead

the arbitrary function

$$h(\xi) = \int_0^{\xi} (\sigma^{em} + \sigma^{abs}) e^{\int_0^x f(y)dy} dx \tag{2.43}$$

and then the general solutions to Eqs. 2.36-37 are

$$\varphi = \frac{1}{(\sigma^{em} + \sigma^{abs})} \frac{h'(\xi)}{[\, c(\eta) + h(\xi)\,]} \tag{2.44}$$

$$\Delta = - \frac{c'(\eta)}{[\, c(\eta) + h(\xi)\,]} \tag{2.45}$$

For completeness, we solve this for two types of initial/boundary conditions. The most common situation would be that depicted in Fig. 2.2 where a pulse with a known temporal waveform $\varphi_0(t)$ at $z = 0$ is incident upon a medium extending out to $z = L$ and the inversion before the pulse arrives ($t \to -\infty$) is known to be $\Delta_0(z)$. From Eq. 2.44 we thus have

$$(\sigma^{em} + \sigma^{abs})\varphi_0(x) = \frac{h'(x)}{[\, c(0) + h(x)\,]} \tag{2.46}$$

which yields the solution

$$h(x) = a\, e^{\int_{-\infty}^x \varphi_0(y)dy} - c(0) \tag{2.47}$$

where a is an arbitrary constant. As $t \to -\infty$, $\xi \to -\infty$ and $h(\xi) \to a - c(0)$. The I.C. then becomes

$$\Delta_0(x) = -\frac{c'(x)}{[\, c(x) + a + c(0)\,]} \tag{2.48}$$

which yields

$$c(x) = c(0) + b\, e^{-\int_0^x \Delta_0(y)dy} - a \tag{2.49}$$

where b is a constant, but clearly $b = a$ for consistency. The solution for arbitrary input pulse shapes and inversion profiles becomes, upon returning to the variables

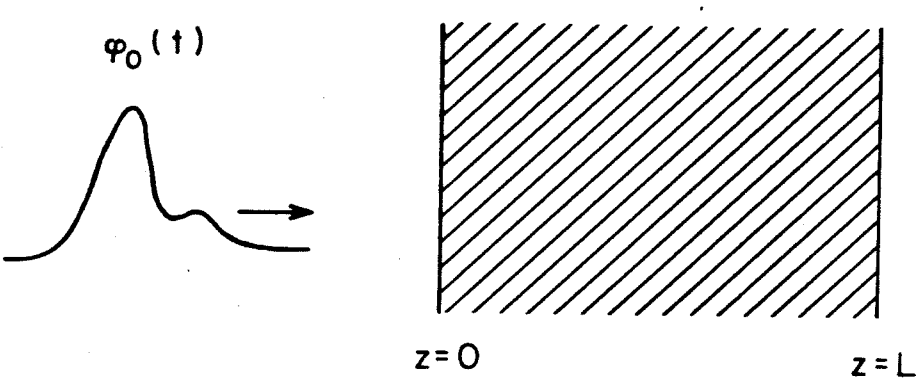

Figure 2.2 Signal waveform incident onto amplifying/absorbing medium which extends from z = 0 to z = L .

t and z,

$$\varphi(t,z) = \frac{\varphi_0(t - \frac{z}{v_g})}{1 + e^{-v_g \int_{-\infty}^{t-\frac{z}{v_g}} (\sigma^{em} + \sigma^{abs})\varphi_0(t')dt'} \left[e^{-\int_0^z \Delta_0(z')dz'} - 1 \right]} \tag{2.50}$$

$$\Delta(t,z) = \frac{\Delta_0(z)}{1 + e^{\int_0^z \Delta_0(z')dz'} \left[e^{v_g \int_{-\infty}^{t-\frac{z}{v_g}} (\sigma^{em} + \sigma^{abs})\varphi_0(t')dt'} - 1 \right]} \tag{2.51}$$

If the initial information is not given as assumed above but instead is presented as the photon density and inversion profiles within the medium at t = 0, $\tilde{\varphi}_0(z)$ and $\tilde{\Delta}_0(z)$, then using a similar but slightly lengthier procedure (see Appendix A2a) the solutions become

$$\varphi(t,z) = \frac{\tilde{\varphi}_0(z - v_g t)\, e^{\int_{z-v_g t}^{z} [(\sigma^{em} + \sigma^{abs})\tilde{\varphi}_0(x) + \tilde{\Delta}_0(x)]\, dx}}{1 + \int_{z-v_g t}^{z} (\sigma^{em} + \sigma^{abs})\tilde{\varphi}_0(x)\, e^{\int_x^z [(\sigma^{em} + \sigma^{abs})\tilde{\varphi}_0(y) + \tilde{\Delta}_0(y)]\, dy} dx} \tag{2.52}$$

$$\Delta(t,z) = \frac{\tilde{\Delta}_0(z)}{1 + \int_{z-v_g t}^{z} (\sigma^{em} + \sigma^{abs})\tilde{\varphi}_0(x)\, e^{\int_x^z [(\sigma^{em} + \sigma^{abs})\tilde{\varphi}_0(y) + \tilde{\Delta}_0(y)]\, dy} dx} \tag{2.53}$$

It is remarkable that analytic solutions can be found for the set of nonlinear coupled partial differential equations Eqs. 2.28-30 for arbitrary pulse shapes and inversion profiles. These solutions are applicable to both two-level saturable absorbers as well as two-level amplifiers. In most cases of interest, the input pulse and the $t \to -\infty$ inversion are specified, so Eqs. 2.50-51 are the relevant results.

2.3 Net Gain and Saturation

We first discuss an amplifier or absorber cell disregarding pulse shaping effects. Noting that Eq. 2.50 is a perfect differential in time, we integrate to obtain the total integrated photon flux through the output face of the cell at z = L.

$$S(z = L) \equiv S_{out} = \ln[\, 1 + G_0(e^{S_{in}} - 1)] \tag{2.54}$$

where

$$S(z) \equiv (\sigma^{em} + \sigma^{abs}) \frac{\#\ photons}{area} = v_g(\sigma^{em} + \sigma^{abs}) \int_{-\infty}^{\infty} \varphi(t,z)\, dt \tag{2.55}$$

and G_0 is the unsaturated or leading edge gain

$$G_0 = e^{\int_0^L \Delta_0(z)\, dz} = e^{\int_0^L [\, N_{20}(z)\sigma^{em} - N_{10}(z)\sigma^{abs}\,]\, dz} \tag{2.56}$$

Thus the energy gain is *independent of pulse shape* and depends only on the integrated photon flux of the input signal. When $S_{in} << 1$, we have

$$G_0(e^{S_{in}} - 1) \approx G_0 S_{in}$$

and if in addition the unsaturated gain is not too high, i.e., if $G_0 S_{in} << 1$, then we can also use $\ln(1 + x) \approx x$ to obtain

$$S_{out} = G_0 S_{in} \tag{2.57}$$

and the gain is linear, i.e., independent of the input signal.

When $\frac{G_0 E_{sig}}{A h \nu_{sig}}$ becomes comparable to $(\sigma^{em} + \sigma^{abs})^{-1}$, saturated amplification sets in. If we assume uniform inversion and consider the case where $S_{in} >> 1$, then

$$S_{out} \approx S_{in} + \ln G_0 = S_{in} + (N_{20}\sigma^{em} - N_{10}\sigma^{abs}) L \tag{2.58}$$

and the stored inversion energy is put entirely into the pulse resulting in a linear increase of photons with distance.

The entire range of saturation behavior is shown in Fig. 2.3 for a variety of unsa-

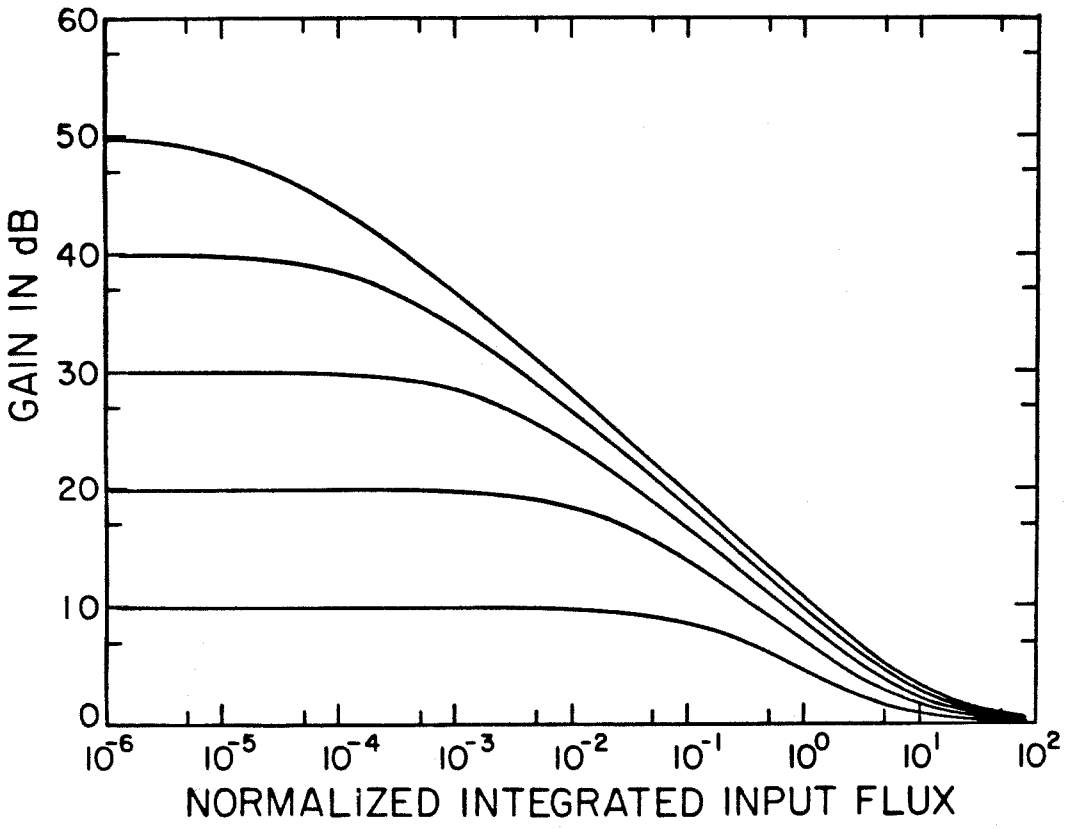

Figure 2.3 Saturation behavior for various values of small signal gain G_0. Integrated photon flux is normalized by the cross section sum as in Eq. 2.55.

turated gains G_0. The plot is the net energy gain in dB, given by $10 \log_{10}(S_{out}/S_{in})$, as a function of S_{in} for $G_0 = 10, 10^2, 10^3, 10^4,$ and 10^5. This saturation behavior is essential for understanding amplifier systems and optimizing designs and will be discussed in detail in Chapter 4.

2.4 Pulse Shape Distortion

We now consider pulse shape distortions. To facilitate the comparison of the effects on different inputs, we write φ_0 as

$$\varphi_0(t) = \frac{S_{in}}{(\sigma^{em} + \sigma^{abs})v_g T} q(t/T) \tag{2.59}$$

where $q(x)$ is normalized such that $\int_{-\infty}^{\infty} q(x)\, dx = 1$ and T is defined as the full width at half maximum of the input pulse. From Eq. 2.50, the output is given by

$$\varphi_{out}(t) = \frac{S_{in}}{(\sigma^{em} + \sigma^{abs})v_g T} \cdot \frac{q(t/T)}{1 + e^{-S_{in}Q(\frac{t}{T})}[\ \frac{1}{G_0} - 1\ ]} \tag{2.60}$$

where

$$Q(x) \equiv \int_{-\infty}^{x} q(x)\, dx \tag{2.61}$$

Figs 2.4-7 show the effects on four different pulse shapes for two different values of G_0, where the output pulse shapes $\varphi_{out}(t)$ have been normalized so their peak height is the same as the input peak height of $q(t)$. In all cases $S_{in} = 0.5$.

Fig. 2.4 shows the result for a rectangular pulse

$$q(x) = [\ H(x) - H(x - 1)\ ] \tag{2.62}$$

where $H(x)$ is the heavyside function, and

$$Q(x) = [\ xH(x) + (1 - x)H(x - 1)\ ] \tag{2.63}$$

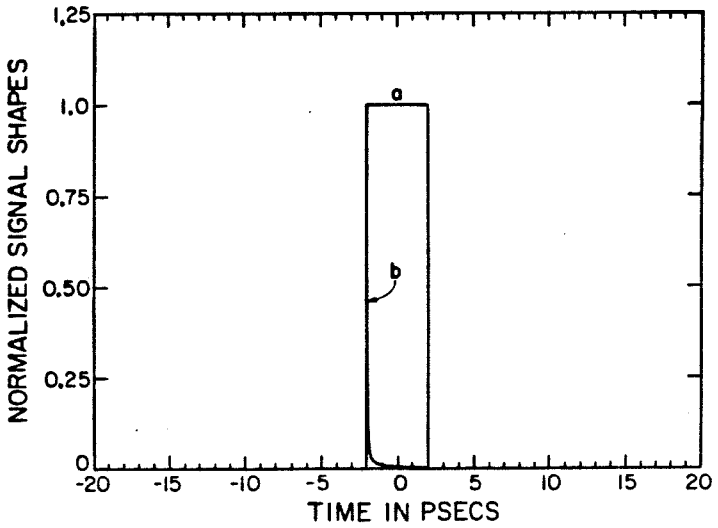

Figure 2.4 Initial pulse shape (curve **a**) and normalized ***distorted*** output pulse shape (curve **b**) for a rectangular signal pulse with total normalized photon flux $S_{in} = 0.5$ and small signal gain $G_0 = 10^3$. The distorted output pulse is the sharp spike barely discernible at the leading edge of the input pulse.

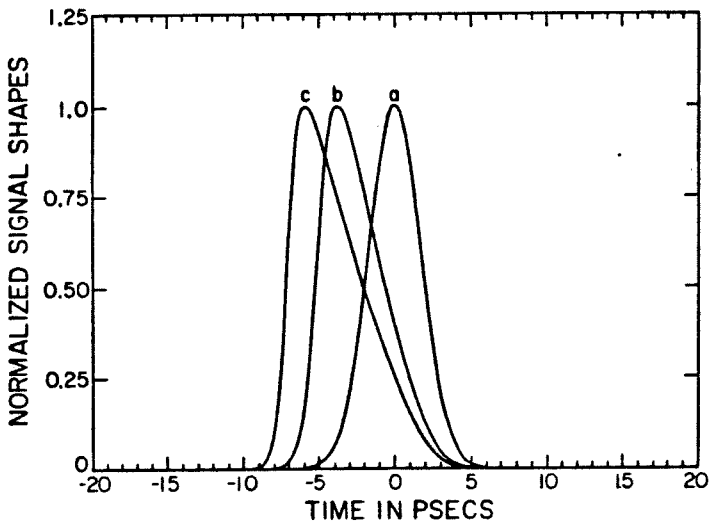

Figure 2.5 Initial pulse shape (curve **a**) and normalized ***distorted*** output pulse shapes for a Gaussian signal pulse with total normalized photon flux $S_{in} = 0.5$, and two values of small signal gain, $G_0 = 10^3$ (curve **b**) and $G_0 = 10^5$ (curve **c**).

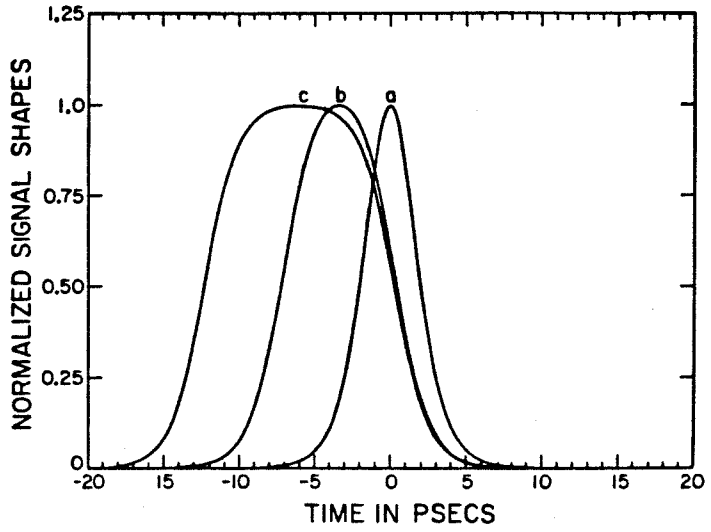

Figure 2.6 Initial pulse shape (curve **a**) and normalized ***distorted*** output pulse shapes for a sech^2 signal pulse with total normalized photon flux $S_{in} = 0.5$, and two values of small signal gain, $G_0 = 10^3$ (curve **b**) and $G_0 = 10^5$ (curve **c**).

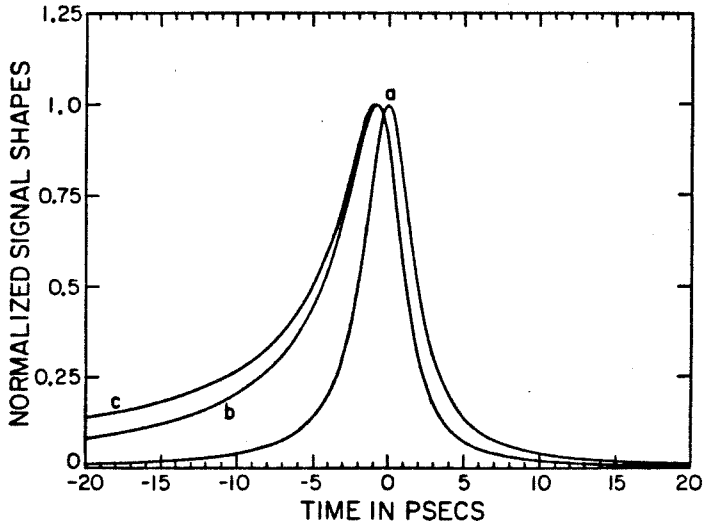

Figure 2.7 Initial pulse shape (curve **a**) and normalized ***distorted*** output pulse shapes for a Lorentzian signal pulse with total normalized photon flux $S_{in} = 0.5$, and two values of small signal gain, $G_0 = 10^3$ (curve **b**) and $G_0 = 10^5$ (curve **c**).

Due to the extreme compression evident in the figure, only one value of unsaturated gain is shown here, $G_0 = 10^3$.

Fig 2.5 shows the corresponding results for a Gaussian pulse,

$$q(x) = \left(\frac{4\ln 2}{\pi}\right)^{\frac{1}{2}} e^{-x^2 4\ln 2} \tag{2.64}$$

and

$$Q(x) = \frac{1}{2}\left[\, 1 + \mathrm{erf}(x\, 2\sqrt{\ln 2}) \,\right] \tag{2.65}$$

In this case, and for the following two pulse shapes, two values of unsaturated gain are shown, $G_0 = 10^3$ and $G_0 = 10^5$.

Fig 2.6 shows the corresponding results for a hyperbolic sech^2 pulse,

$$q(x) = \ln(\sqrt{2} + 1)\, \mathrm{sech}^2(x\, 2\ln(\sqrt{2} + 1)) \tag{2.66}$$

and

$$Q(x) = \frac{1}{2}\left[\, 1 + \tanh(x\, 2\ln(\sqrt{2} + 1) \,\right] \tag{2.67}$$

and finally Fig. 2.7 shows the results for a Lorentzian pulse,

$$q(x) = \frac{2}{\pi}\left[\, 1 + (2x)^2 \,\right]^{-1} \tag{2.68}$$

and

$$Q(x) = \frac{1}{2}\left[\, 1 + \frac{2}{\pi}\tan^{-1}(2x) \,\right] \tag{2.69}$$

There are several obvious features which emerge from these Figures. First is that extreme distortion can occur, depending upon the initial shape of the pulse. Secondly, the pulse maximum always propagates forward in time, in such a manner that the pulse *maximum* effectively moves with a velocity exceeding the velocity of light in the medium[7]. Both of these effects result simply from the selective

amplification of the leading edge compared to the depleted amplification of the trailing edge of the pulse. In the case of the sharp leading edge of the rectangular pulse, extreme pulse compression has occurred, while in Lorentzian and $sech^2$ pulses, broadening has occurred. Here the Lorentzian pulse distortion is actually more severe than that of the $sech^2$ pulse since a large fraction of the pulse energy resides in the drawn out leading edge; this will be detailed below.

To discuss the pulse shaping effects more quantitatively, we consider first weak saturation and try to determine what pulse shape is *critical*, i.e., pulses with sharper leading edges will be compressed and pulses with more gradual leading edges will be broadened. Returning again to Eq. 2.50, we re-define the time origin and write it in the form

$$\psi_{out}(t) = \frac{\psi_0(t)}{1 + e^{-F(t)}[\ \frac{1}{G_0} - 1\ ]}$$

$$= \frac{d}{dt}\ln[\ e^{F(t)} + (\frac{1}{G_0} - 1)\ ] \qquad (2.70)$$

where ψ_0 is the normalized input photon flux as a function of time, $\psi_0(t) = v_g(\sigma^{em} + \sigma^{abs})\varphi_0(t)$, and $F(t) \equiv \int_{-\infty}^{t} \psi_0(t')dt'$.

We now ask what pulse gets amplified while having its *shape* unaltered. The net energy gain in this case is still given by Eq. 2.54 where $S_{in} = F(\infty)$, and if the shape is unaltered this must also be the *amplitude* gain. The only possible distortion then is a forward shift in time by some amount δT as discussed above, and thus we require

$$G_{actual}\psi_0(t + \delta T) = \frac{d}{dt}\ln[\ e^{F(t)} + (\ \frac{1}{G_0} - 1)\ ] \qquad (2.71)$$

where G_{actual} is the energy gain

$$G_{actual} \equiv \frac{\ln[\ 1 + G_0(\ e^{F(\infty)} - 1\ )]}{F(\infty)} \tag{2.72}$$

If the saturation is *weak*, then δT is small and

$$\psi_0(t + \delta T) \approx \psi_0(t) + \delta T \frac{d\psi_0}{dt} \tag{2.73}$$

Upon integrating from $-\infty$ to t, Eq. 2.71 then becomes

$$G_{actual}F(t) + G_{actual}\delta T \frac{dF}{dt} = \ln[\ 1 + G_0(\ e^{F(t)} - 1\ )] \tag{2.74}$$

Again, when the saturation is weak, $G_0F(t) << 1$, so we can expand the RHS of Eq. 2.74 to second order in F(t) and expand the log in the definition of G_{actual} to the same order, and Eq. 2.74 then reads

$$\frac{\frac{dF}{dt}}{F[\ F(\infty) - F\ ]} \approx \frac{(G_0 - 1)}{2\delta T} \tag{2.75}$$

This has the solution

$$F(t) = F(\infty)\Big[\ 1 + e^{-\frac{F(\infty)(G_0 - 1)}{2\delta T}t}\ \Big]^{-1} \tag{2.76}$$

which yields the pulse shape

$$\psi_0(t) = \frac{F^2(\infty)(G_0 - 1)}{8\delta T}\mathrm{sech}^2\Big[\ \frac{F(\infty)(G_0 - 1)}{4\delta T}t\ \Big] \tag{2.77}$$

While this only holds for weak saturation, it indicates that saturated amplification has somewhat of a neutral effect on the shape of pulses with exponential leading edges. The dependence on δT in Eq. 2.77 also illustrates the general and important feature that pulses which advance in time by a large amount also have longer temporal pulse profiles.

To support these conclusions further, we look at Eq. 2.71 in the case of *extreme* saturation, when $G_0 \to \infty$. In this case,

$$G_{actual} \rightarrow \frac{\ln G_0}{F(\infty)} \tag{2.78}$$

and if we denote $\ln G_0$ by ζ we have then as $\zeta \rightarrow \infty$

$$\psi_0(t + \delta T) = \frac{F(\infty)\psi_0(t)}{\zeta[\, 1 + e^{-F(t)}(e^{-\zeta} - 1)\,]} \tag{2.79}$$

This is the equation which must hold if a steady state pulse ***shape*** is to result. If a steady state does *not* result as $\zeta \rightarrow \infty$, then either infinite compression results or the pulse has broadened to an infinite temporal extent. For the LHS in Eq. 2.79 to remain non-zero, clearly we require that $\delta T \rightarrow \infty$ and $t \rightarrow -\infty$ as well, which means that the leading edge determines the ultimate behavior as previously mentioned. When $t \rightarrow -\infty$, $F(t) \rightarrow 0$ and thus we can expand in the denominator $e^{-F(t)} \approx 1 - F(t)$. Then Eq. 2.79 becomes

$$\psi_0(t + \delta T) \underset{t \rightarrow -\infty}{=} \frac{F(\infty)\psi_0(t)}{\zeta[\, F + (1 - F)e^{-\zeta}\,]} \tag{2.80}$$

Clearly if $\psi_0(t)/F(t)$ remains finite as $t \rightarrow -\infty$, no matter what t we pick, the RHS will vanish as $\zeta \rightarrow \infty$. Since the RHS is the actual amplified pulse waveform, this would mean that the pulse has spread out to an infinitely wide pulse width since its amplitude is everywhere zero. Therefore, a necessary condition for the pulse to remain of finite pulse width or be compressed when the gain becomes infinite is

$$\lim_{t \rightarrow -\infty} \frac{\int_{-\infty}^{t} \psi_0(t')dt'}{\psi_0(t)} = 0 \tag{2.81}$$

This equation has also been quoted for the case of steady state pulses in a gain medium with linear losses [7].

Since a pulse with an exponential leading edge obeys

$$\lim_{t \to -\infty} \frac{\int_{-\infty}^{t} \psi_0(t')dt'}{\psi_0(t)} = T_0 \qquad (2.82)$$

where T_0 is the non-zero time constant for the leading edge, Eq. 2.81 is violated and such a pulse will eventually broaden to an infinite width. The $sech^2$ solution of Eq. 2.77 for weak saturation therefore does not rigorously hold for very strong saturation, and this is evident from Fig. 2.6 as well. However, since T_0 in Eq. 2.82 is a finite constant, pulses with exponential leading edges do represent a "borderline case" as concluded earlier. Pulses which do satisfy Eq. 2.81, such as the Gaussian or the rectangular pulse, will ultimately be *compressed* if the gain is sufficiently large.

2.4 Bleaching Waves and Pumping

We now consider briefly the inversion in an absorbing medium, using Eq. 2.51. If we assume all the atoms are initially in the ground state, then we have

$$\Delta_0(z) = -\sigma^{abs}N \qquad (2.82)$$

and if the incident wave is a step function of intensity I_0

$$\varphi_0(t) = \frac{I_0}{h\nu v_g} H(t) \qquad (2.83)$$

then the inversion becomes

$$\Delta(t,z) = \frac{-\sigma^{abs}N}{1 + e^{-\sigma^{abs}Nz}\left[e^{\frac{I_0}{h\nu}(\sigma^{em} + \sigma^{abs})(t - z/v_g)H(t - z/v_g)} - 1 \right]} \qquad (2.84)$$

If we look a few absorption depths into the material, $e^{-\sigma^{abs}Nz} << 1$ and we can ignore the -1 term in the brackets of the denominator of Eq. 2.84. Then, assuming the pulse has "arrived" at the point of observation we have

$$\Delta(t,z) = \frac{-\sigma^{abs}N}{e^{[z - v_{bleach}t]/\Lambda} + 1} \tag{2.85}$$

where

$$\Lambda = \left[\frac{I_0 (\sigma^{em} + \sigma^{abs})}{h\nu v_g} + \sigma^{abs} \right]^{-1} \tag{2.86}$$

and

$$v_{bleach} = \frac{v_g}{\left[1 + \frac{\sigma^{abs} N v_g h\nu}{(\sigma^{em} + \sigma^{abs}) I_0} \right]} \tag{2.87}$$

Eq. 2.85 demonstrates how the inversion punches into the material as a bleaching wave. This wave has the functional form of a Fermi-Dirac distribution with a "temperature" Λ controlling the sharpness of a bleaching front which propagates into the material with speed v_{bleach}. This is shown in Fig. 2.8 with a value of $\Lambda = 0.75$. This behavior is important for pumping amplifier cells and propagation through saturable absorbers. In an amplifier cell, for instance, if we want the gain to be constant over a period of time, one method of accomplishing this is to let the wave bleach all the way through the cell of length L which we see would require a pulse duration of at least $T = \frac{L}{v_{bleach}}$.

Finite inversion lifetime effects, which have been neglected in order to obtain the analytic solutions Eqs. 2.50-53, affect the dynamics considerably and will be included rigorously in Chapter 3. One obvious feature, however, is that the bleaching wave derived here cannot propagate an arbitrary depth into the medium since energy must be continually extracted from the wave to maintain the inversion at shallower depths. The *steady state* solution is obtained by returning to Eqs. 2.28-30 and letting $\frac{\partial}{\partial t} \rightarrow 0$. This yields

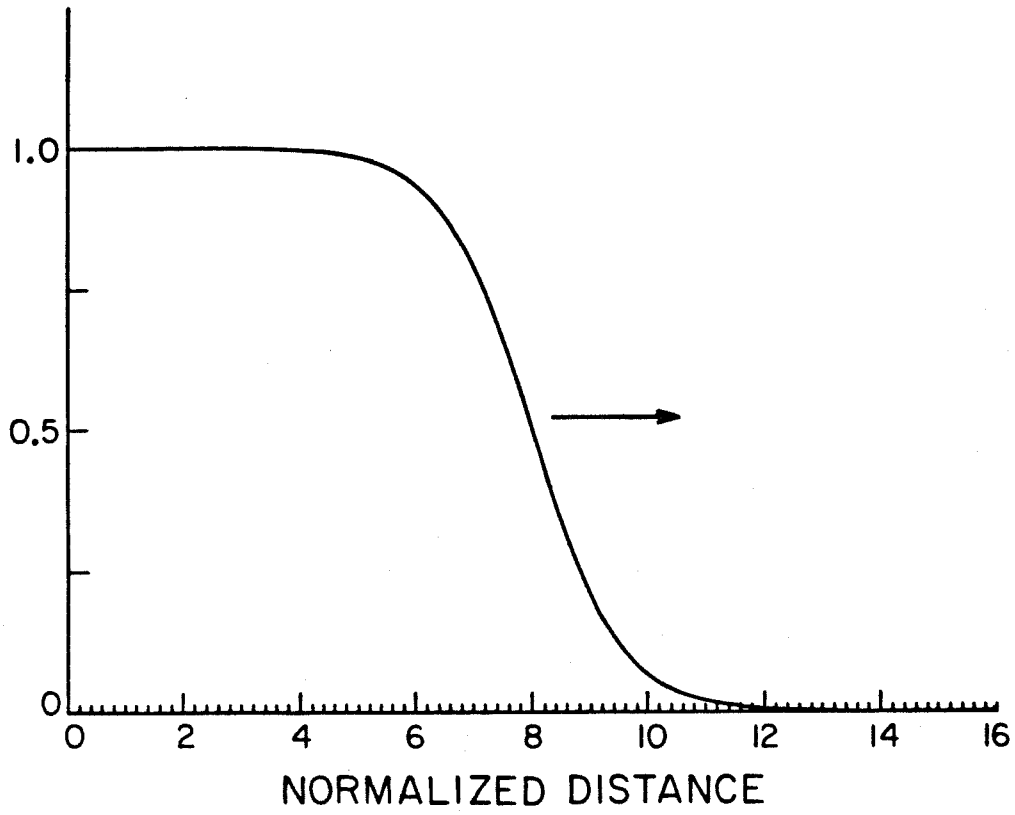

Figure 2.8 Propagating bleaching wave with $\Lambda = 0.75$. Distance is in units of $(\sigma_{abs}N)^{-1}$.

$$\frac{d\varphi}{dz} = [\ \sigma^{em}N_2 - \sigma^{abs}(N - N_2)\ ]\ \varphi \tag{2.88}$$

and

$$v_g[\ \sigma^{em}N_2 - \sigma^{abs}(N - N_2)\ ]\ \varphi = -\frac{N_2}{\tau} \tag{2.89}$$

These are combined to yield

$$\frac{dN_2}{dz} = -\frac{N_2}{\sigma^{abs}N}[\ (\sigma^{em} + \sigma^{abs})N_2 - \sigma^{abs}N\ ]^2 \tag{2.90}$$

Since $N_2(z = 0)$ is known directly from Eq. 2.89 using the input value of φ_0, solutions are easily found. They are conveniently expressed in the form

$$\sigma^{abs}Nz = \ln[\frac{W_0}{W}] + (\ W_0 - W\ ) \tag{2.91}$$

where $W_0 = v_g\varphi_0\tau(\sigma^{em} + \sigma^{abs})$ and N_2 is given by

$$N_2 = \frac{\sigma^{abs}}{(\sigma^{em} + \sigma^{abs})}N\left(\frac{W}{W + 1}\right) \tag{2.92}$$

Fig. 2.9 shows the steady state solutions Eq. 2.91 with the z axis in units of $(\sigma^{abs}N)^{-1}$, and the vertical axis showing N_2 normalized to its maximum ($\varphi_0 = \infty$) value of $\sigma^{abs}/(\sigma^{em} + \sigma^{abs})$. The five curves show the results for W_0 = 0.1, 1, 2, 5, and 10. For low intensities, the inversion decays exponentially into the medium as expected from absorption of the small signal exponentially decaying intensity. For large intensities, however, the absorption is very nonlinear and the bleaching wave propagates well into the material before it loses its "punch". In a real situation, the initial behavior for a high intensity wave ($W_0 > 1$) would be the bleaching wave result Eq. 2.85 asymptotically approaching the steady state solution Eq. 2.91 on a time scale of τ.

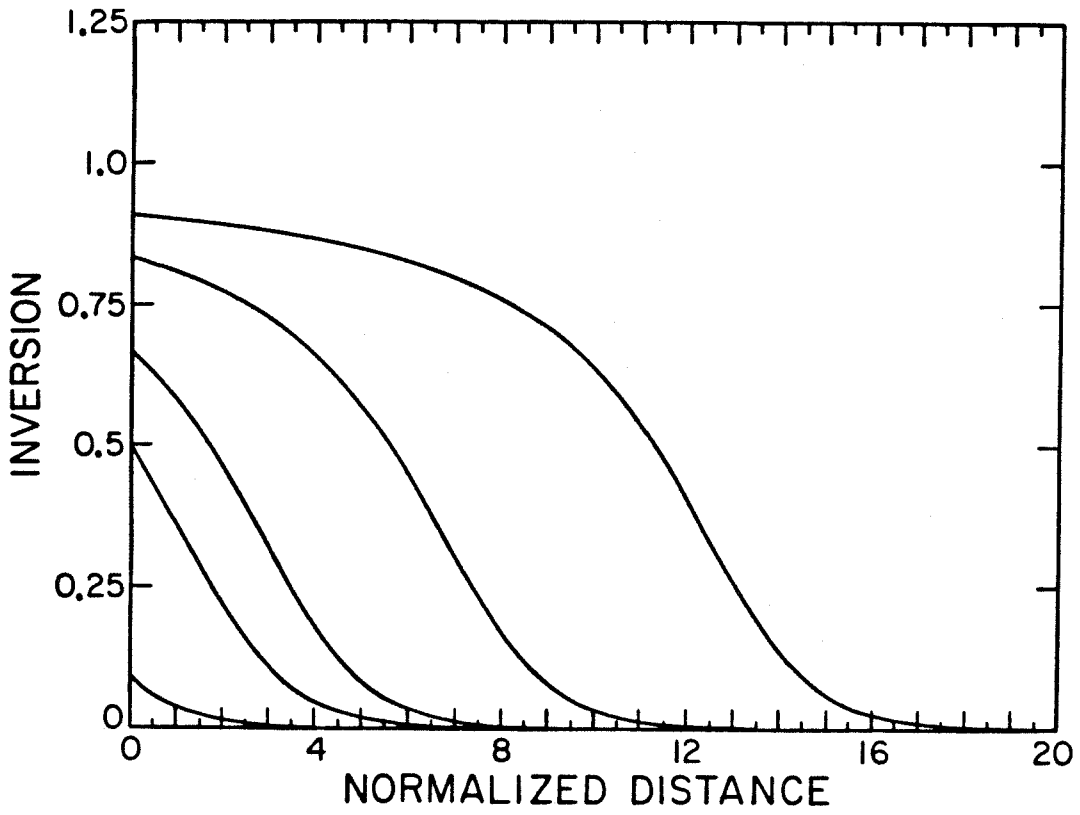

Figure 2.9 Steady state bleaching behavior with finite τ. Distance is in units of $(\sigma_{abs}N)^{-1}$ and the five curves are for $W_0 = v_g\varphi_0\tau(\sigma^{em} + \sigma^{abs}) = 0.1, 1, 2, 5$ and 10. The vertical axis is the inversion N_2 normalized to its $W_0 \rightarrow \infty$ value.

Appendix A2a

The general solution of Eqs. 2.28-30 with $\tau \to \infty$ is given in the text by Eqs. 2.44-45 which we repeat here for convenience

$$\varphi = \frac{1}{(\sigma^{em} + \sigma^{abs})} \frac{h'(\xi)}{[\, c(\eta) + h(\xi)\,]} \tag{2.44}$$

$$\Delta = -\frac{c'(\eta)}{[\, c(\eta) + h(\xi)\,]} \tag{2.45}$$

Suppose we are given the pure *initial* conditions that at t = 0 the photon density and inversion are known functions of z, $\tilde{\varphi}_0(z)$ and $\tilde{\Delta}_0(z)$ respectively. The variable η is the same as z, and at t = 0 we have $\xi = -z$ so at t = 0 $h(\xi) = h(-z)$ and $h'(\xi) = -\frac{d}{dz}h(-z)$. For convenience let $h(-z) \equiv j(z)$ which then yields

$$(\sigma^{em} + \sigma^{abs})\tilde{\varphi}_0(z) = -\frac{\frac{dj(z)}{dz}}{[\, c(z) + j(z)\,]} \tag{A2a.1}$$

$$\tilde{\Delta}_0(z) = -\frac{\frac{dc(z)}{dz}}{[\, c(z) + j(z)\,]} \tag{A2a.2}$$

Adding these yields

$$(\sigma^{em} + \sigma^{abs})\tilde{\varphi}_0(z) + \tilde{\Delta}_0(z) = -\frac{d}{dz}\ln[\, c(z) + j(z)\,] \tag{A2a.3}$$

which leads to

$$c(z) + j(z) = A\, e^{-\int_0^z [\,(\sigma^{em} + \sigma^{abs})\tilde{\varphi}_0(x) + \tilde{\Delta}_0(x)\,]\, dx} \tag{A2a.4}$$

where A is a constant. This result is re-inserted into Eqs. A2a.1-2 and these are integrated separately to yield

$$j(z) = B - A\int_0^z (\sigma^{em} + \sigma^{abs})\tilde{\varphi}_0(x)\, e^{-\int_0^x [\,(\sigma^{em} + \sigma^{abs})\tilde{\varphi}_0(y) + \tilde{\Delta}_0(y)\,]\,dy}\, dx \qquad \text{(A2a.5)}$$

$$c(z) = D - A\int_0^z \tilde{\Delta}_0(x)\, e^{-\int_0^x [\,(\sigma^{em} + \sigma^{abs})\tilde{\varphi}_0(y) + \tilde{\Delta}_0(y)\,]\,dy}\, dx \qquad \text{(A2a.6)}$$

Here B and D are new unknown constants. When these are placed back into the general solutions Eqs. 2.44-45 and the original variables t and z are re-employed, the results are

$$\varphi(t,z) = \tilde{\varphi}_0(z - v_g t)\, e^{-\int_0^{z-v_g t} [\,(\sigma^{em} + \sigma^{abs})\tilde{\varphi}_0(y) + \tilde{\Delta}_0(y)]\,dy} \qquad \text{(A2a.7)}$$

$$\times \Big[\, K - \int_0^z \tilde{\Delta}_0\, e^{-\int_0^x [\,(\sigma^{em} + \sigma^{abs})\tilde{\varphi}_0(y) + \tilde{\Delta}_0(y)]\,dy}\, dx$$

$$- \int_0^{z-v_g t} (\sigma^{em} + \sigma^{abs})\tilde{\varphi}_0(x)\, e^{-\int_0^x [\,(\sigma^{em} + \sigma^{abs})\tilde{\varphi}_0(y) + \tilde{\Delta}_0(y)]\,dy}\, dx \Big]^{-1}$$

and

$$\Delta(t,z) = \tilde{\Delta}_0(z)\, e^{-\int_0^z [\,(\sigma^{em} + \sigma^{abs})\tilde{\varphi}_0(y) + \tilde{\Delta}_0(y)]\,dy} \qquad \text{(A2a.8)}$$

$$\times \Big[\, K - \int_0^z \tilde{\Delta}_0\, e^{-\int_0^x [\,(\sigma^{em} + \sigma^{abs})\tilde{\varphi}_0(y) + \tilde{\Delta}_0(y)]\,dy}\, dx$$

$$- \int_0^{z-v_g t} (\sigma^{em} + \sigma^{abs})\tilde{\varphi}_0(x)\, e^{-\int_0^x [\,(\sigma^{em} + \sigma^{abs})\tilde{\varphi}_0(y) + \tilde{\Delta}_0(y)]\,dy}\, dx \Big]^{-1}$$

where $K = (D + B)/A$ is the only constant to be determined now. Requiring consistency at $t = 0$ is easily seen to yield $K = 1$. After a few integrations by parts and simplification, Eqs. 2.52-3 in the text result.

CHAPTER 2 REFERENCES

1. A. Icsevgi and W. E. Lamb, Jr., Phys. Rev. **185**, 517 (1969).

2. P. G. Kryukov and V. S. Letokhov, Sov. Phys. Uspekhi **12**, 641 (1970).

3. A. Yariv, *Quantum Electronics*, Second Ed., John Wiley & Sons, Inc., New York, 1975.

4. S. L. McCall and E. L. Hahn, Phys. Rev. **183**, 457 (1969).

5. R. Bellman, G. Birnbaum, and W. G. Wagner, J. Appl. Phys. **34**, 780 (1963).

6. L. M. Frantz and J. S. Nodvik, J. Appl. Phys. **34**, 2346 (1963).

7. N. G. Basov and V. S. Letokhov, Sov. Phys. Doklady **11**, 222 (1966).

CHAPTER 3
TRAVELING WAVE PUMP & SIGNAL INTERACTION EQUATION AND APPLICATIONS

3.1 TW Pump & Pulse Interaction Equation

In this brief chapter, we extend and refine some of the ideas of the previous chapter in two important ways. In many situations of interest, energy is deposited in a medium with an optical pump pulse and *simultaneously* extracted with a collinear signal pulse. The applications we have in mind here are synchronously pumped mode-locked dye laser oscillators and high power optically pumped dye laser amplifiers which follow the oscillators. The second change we implement is the inclusion of finite inversion lifetime effects by relaxing the $\tau \rightarrow \infty$ requirement. In so doing, we can no longer get analytic solutions but the ensuing equations assume a wider range of applicability. For example, in describing the behavior of a *fast* saturable absorber, the short τ is an essential part of the physics.

The geometry to be considered here is shown in Fig. 3.1. There are two waves propagating collinearly into a medium located between z = 0 and z = L. The photon densities are specified at the entrance plane z = 0 , just as in the last chapter, by $\varphi_{10}(t)$ and $\varphi_{20}(t)$. In what follows, we shall refer to the wave $\varphi_1(t,x)$ as the "pump" and the wave $\varphi_2(t,x)$ as the "signal" wave. The two waves are at two arbitrary frequencies, but we neglect any coherent interactions which could occur between the waves. Again, with the dye model of Fig. 2.1 in mind, we characterize the interaction of the two waves with the medium by assigning emission and absorption cross

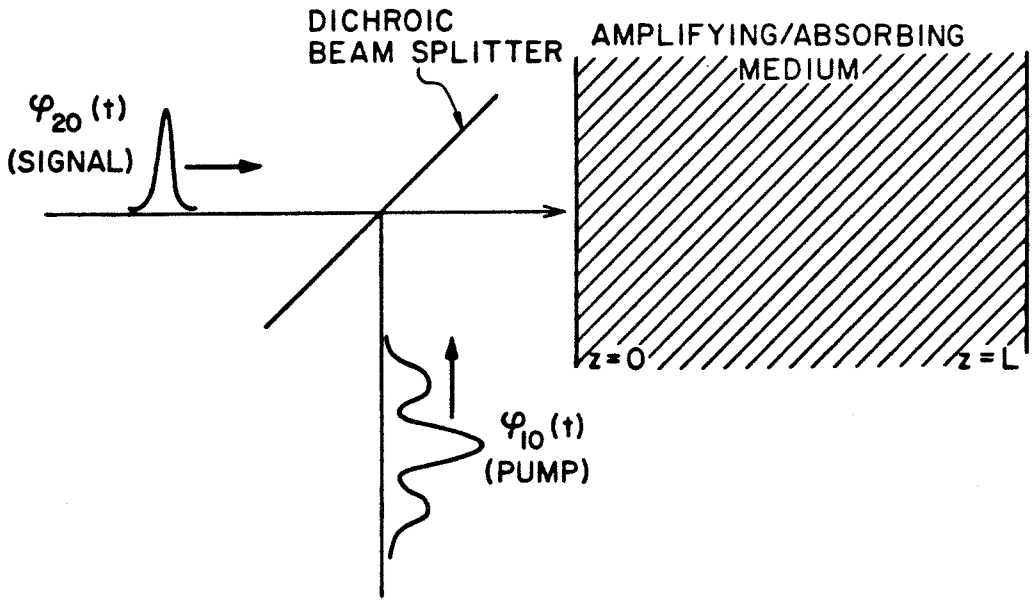

Figure 3.1 Collinear pump $\varphi_{10}(t)$ and signal $\varphi_{20}(t)$ waveforms simultaneously incident on an amplifying/absorbing medium extending from z = 0 to z = L .

sections at the pump (1) and signal (2) frequencies. These are given by σ_1^{em}, σ_1^{abs} and σ_2^{em}, σ_2^{abs} respectively. We then write the set of T.W. rate equations

$$\frac{\partial \varphi_1}{\partial t} + v_g \frac{\partial \varphi_1}{\partial z} = v_g(\sigma_1^{em} N_2 - \sigma_1^{abs} N_1)\varphi_1 \tag{3.1}$$

$$\frac{\partial \varphi_2}{\partial t} + v_g \frac{\partial \varphi_2}{\partial z} = v_g(\sigma_2^{em} N_2 - \sigma_2^{abs} N_1)\varphi_2 \tag{3.2}$$

$$\frac{\partial N_1}{\partial t} = v_g(\sigma_1^{em}\varphi_1 + \sigma_2^{em}\varphi_2)N_2 - v_g(\sigma_1^{abs}\varphi_1 + \sigma_2^{abs}\varphi_2)N_1 + \frac{N_2}{\tau} \tag{3.3}$$

$$\frac{\partial N_2}{\partial t} = -\frac{\partial N_1}{\partial t} \tag{3.4}$$

where we have invoked the same approximations as in Chapter 2 as well as the additional neglect of group velocity dispersion.

Making the change of variables

$$\xi \equiv v_g t - z \qquad \text{and} \qquad \eta \equiv z \tag{3.5}$$

and using $N_1 = N - N_2$ reduces the set Eqs. 3.1-4 to

$$\frac{\partial \ln \varphi_1}{\partial \eta} = (\sigma_1^{em} + \sigma_1^{abs})N_2 - \sigma_1^{abs} N \tag{3.6}$$

$$\frac{\partial \ln \varphi_2}{\partial \eta} = (\sigma_2^{em} + \sigma_2^{abs})N_2 - \sigma_2^{abs} N \tag{3.7}$$

$$\frac{\partial N_2}{\partial \xi} = -[(\sigma_1^{em} + \sigma_1^{abs})\varphi_1 + (\sigma_2^{em} + \sigma_2^{abs})\varphi_2]N_2 \tag{3.8}$$

$$+ (\sigma_1^{abs}\varphi_1 + \sigma_2^{abs}\varphi_2)N - \frac{N_2}{v_g \tau}$$

Combining Eqs. 3.6-7 yields the double equality

$$N_2 = \frac{1}{(\sigma_1^{em} + \sigma_1^{abs})}\left[\frac{\partial \ln \varphi_1}{\partial \eta} + \sigma_1^{abs} N\right] = \frac{1}{(\sigma_2^{em} + \sigma_2^{abs})}\left[\frac{\partial \ln \varphi_2}{\partial \eta} + \sigma_2^{abs} N\right] \tag{3.9}$$

Using this result in Eq. 3.8 yields

$$\frac{\partial^2 \ln\varphi_2}{\partial\eta\partial\xi} = -\frac{\partial}{\partial\eta}[(\sigma_2^{em} + \sigma_2^{abs})(\varphi_1 + \varphi_2) - \frac{1}{v_g\tau}\ln\varphi_2] - \frac{1}{v_g\tau}\sigma_2^{abs}N \tag{3.10}$$

Eq. (3.10) is integrated once in η to yield

$$\frac{\partial \ln\varphi_2}{\partial\xi} + (\sigma_2^{em} + \sigma_2^{abs})(\varphi_1 + \varphi_2) + \frac{1}{v_g\tau}(\ln\varphi_2 + \sigma_2^{abs}N\eta) = \Psi(\xi) \tag{3.11}$$

where $\Psi(\xi)$ is an arbitrary function of ξ only. It can be evaluated at $\eta = 0$ where $\varphi_1(\xi,\eta = 0) \equiv \varphi_{10}(\xi)$ and $\varphi_2(\xi,\eta = 0) \equiv \varphi_{20}(\xi)$ are the known input photon densities into the entrance face of the amplifier cell. This yields

$$\Psi(\xi) = \frac{\partial \ln\varphi_{20}(\xi)}{\partial\xi} + (\sigma_2^{em} + \sigma_2^{abs})[\varphi_{10}(\xi) + \varphi_{20}(\xi)] + \frac{1}{v_g\tau}\ln\varphi_{20}(\xi) \tag{3.12}$$

Returning to Eq. 3.9, we can integrate it in η to yield

$$\frac{\ln\varphi_1}{(\sigma_1^{em} + \sigma_1^{abs})} - \frac{\ln\varphi_2}{(\sigma_2^{em} + \sigma_2^{abs})} + \frac{(\sigma_2^{em}\sigma_1^{abs} - \sigma_2^{abs}\sigma_1^{em})N\eta}{(\sigma_1^{em} + \sigma_1^{abs})(\sigma_2^{em} + \sigma_2^{abs})} = \Pi(\xi) \tag{3.13}$$

where $\Pi(\xi)$ is an arbitrary function of ξ only. Again this can be evaluated at $\eta = 0$ and then Eq. 3.13 holds at all values of ξ and η to yield

$$\varphi_1 = \varphi_{10}(\xi)e^{-\kappa N\eta}\left[\frac{\varphi_2}{\varphi_{20}(\xi)}\right]^{\gamma} \tag{3.14}$$

where

$$\kappa = \frac{(\sigma_2^{em}\sigma_1^{abs} - \sigma_2^{abs}\sigma_1^{em})}{(\sigma_2^{em} + \sigma_2^{abs})} \tag{3.15}$$

and

$$\gamma = \frac{(\sigma_1^{em} + \sigma_1^{abs})}{(\sigma_2^{em} + \sigma_2^{abs})} \tag{3.16}$$

The result Eq. 3.14 is significant in itself because it uniquely relates the signal photon flux at any point in space and time to the pump photon flux at the same point.

We insert Eq. 3.14 into Eq. 3.11, using the expression Eq. 3.12 for $\Psi(\xi)$. This leads to

$$\frac{\partial}{\partial\xi}\ln\left[\frac{\varphi_2}{\varphi_{20}}\right] - \varphi_{10}(\sigma_2^{em} + \sigma_2^{abs})\left(1 - e^{-\kappa N\eta}\left[\frac{\varphi_2}{\varphi_{20}}\right]^{\gamma}\right) \tag{3.17}$$

$$+ \frac{1}{\tau v_g}\ln\left[\frac{\varphi_2}{\varphi_{20}}\right] + \frac{\sigma_2^{abs}N\eta}{\tau v_g} = 0$$

This is evaluated at $\eta = L$, noting that in this circumstance

$$\frac{\partial}{\partial\xi}\ln\left[\frac{\varphi_2(\xi, \eta = L)}{\varphi_{20}(\xi, \eta = 0)}\right] = \frac{1}{v_g}\frac{d}{dt}\ln G(t) \tag{3.18}$$

where G(t) is the appropriately *retarded* gain

$$G(t) \equiv \frac{\varphi(t' = t + \frac{L}{v_g}, z = L)}{\varphi_{20}(t)} \tag{3.19}$$

Eq. 3.17 then becomes

$$\frac{dG}{dt} = v_g(\sigma_2^{em} + \sigma_2^{abs})\, G\, [\varphi_{10}(t)(1-e^{-\kappa NL}G^{\gamma}) - \varphi_{20}(t)(G-1)] \tag{3.20}$$

$$- \frac{1}{\tau}G[\ln G + \sigma_2^{abs}NL]$$

Eq. 3.20 is the basic equation which governs the dynamics of the energy exchange between a signal and pump pulse in a generalized two-level medium with a finite lifetime τ. With no approximations we have reduced the set of coupled non-linear partial differential equations Eqs. 3.1-4 to a single *ordinary* differential equation for the retarded gain G(t). While this quantity contains no information about the local inversion, fortunately only the appropriately retarded and *integrated* effect of the gain is usually of interest. To compare with the results of the previous chapter, we note that if we let $\tau \to \infty$ and $\varphi_{10}(t) = 0$, Eq. 3.20 becomes

$$\frac{dG}{dt} = -v_g(\sigma_2^{em} + \sigma_2^{abs})\varphi_{20}(t)G(G - 1) \tag{3.21}$$

which is easily integrated to yield

$$G(t) = \left[1 + e^{-F(t)}\left(\frac{1}{G_0} - 1 \right)\right]^{-1} \tag{3.22}$$

where

$$F(t) = v_g(\sigma_2^{em} + \sigma_2^{abs}) \int_{-\infty}^{t} \varphi_{20}(t')dt' \tag{3.23}$$

and G_0 is the initial or leading edge or unsaturated gain of the amplifier cell, $G_0 = G(t \to -\infty)$. Eq. 3.22 is the time varying retarded gain defined by Eq. 3.19, and when multiplied by the signal and integrated over time yields the actual *energy* gain

$$G_{actual} = \frac{1}{S_{in}} \ln\left[1 + G_0\left(e^{S_{in}} - 1 \right)\right] \tag{3.24}$$

where $S_{in} = F(t \to \infty)$. This is exactly the same result as Eq. 2.50 and Eq. 2.54 of Chapter 2, which is expected since Eq. 3.20 is a generalization of the simpler treatment of Chapter 2.

3.2 Synchronously Mode-Locked Dye Lasers

To demonstrate the versatility of Eq. 3.20, we use it next as the basis of a brief discussion of the physics of synchronously mode-locked dye lasers. This is relevant since such a system forms the heart of the entire experimental apparatus to be described in Chapter 5. In this mode-locking scheme, one mode-locked laser is used to optically pump another laser. If the cavity lengths are almost equal, then the second laser has a strong gain modulation at its round trip frequency which, as is well known, produces mode-locking[1]. In fact, a circulating pulse can be generated in the second laser which has a much shorter duration than the pump pulse. This results from the self-depletion of the gain medium by the circulating pulse causing the laser to be over threshold only for a short "time window" which can be shorter

than the pump pulse. This behavior is depicted in Fig. 3.2 which shows the supposed relations which might exist between the pump pulse, signal pulse and gain.

A typical method of analysis of synchronously mode-locked dye lasers is summarized below.

1) An unknown functional waveform is propagated through the gain medium simultaneously with the pump pulse whose shape and amplitude are specified.

2) The wave experiences some appropriate delay and then re-enters the gain medium.

3) The wave then experiences some bandwidth limiting element which acts in a linear fashion; this represents usually some real tuning element in the cavity, or just the overall bandwidth of the gain medium.

4) The wave experiences some loss, which is a combination of the real cavity losses in addition to the output coupling.

5) The wave passes a second time through the bandwidth limiting element, and finally after an appropriate delay is ready to re-enter the gain medium to repeat the whole process.

The condition which determines the unknown pulse waveform is that the pulse reproduce exactly, after step (5), the input waveform of step (1). To make this argument quantitative, we refer to Fig. 3.3. A pump pulse with intensity $I_p(t)$ and pulse repetition period T_p enters the gain medium, which is assumed in this case to be a dye solution of thickness L. For convenience, we consider a particular pump pulse which has its peak centered at $t = 0$, thereby defining the time origin. We will call the total round trip "flight time" of the cavity $T_c \equiv 2L_c / c$, where L_c is the cavity length. However, clearly the mode-locked pulse of the synchronously pumped laser

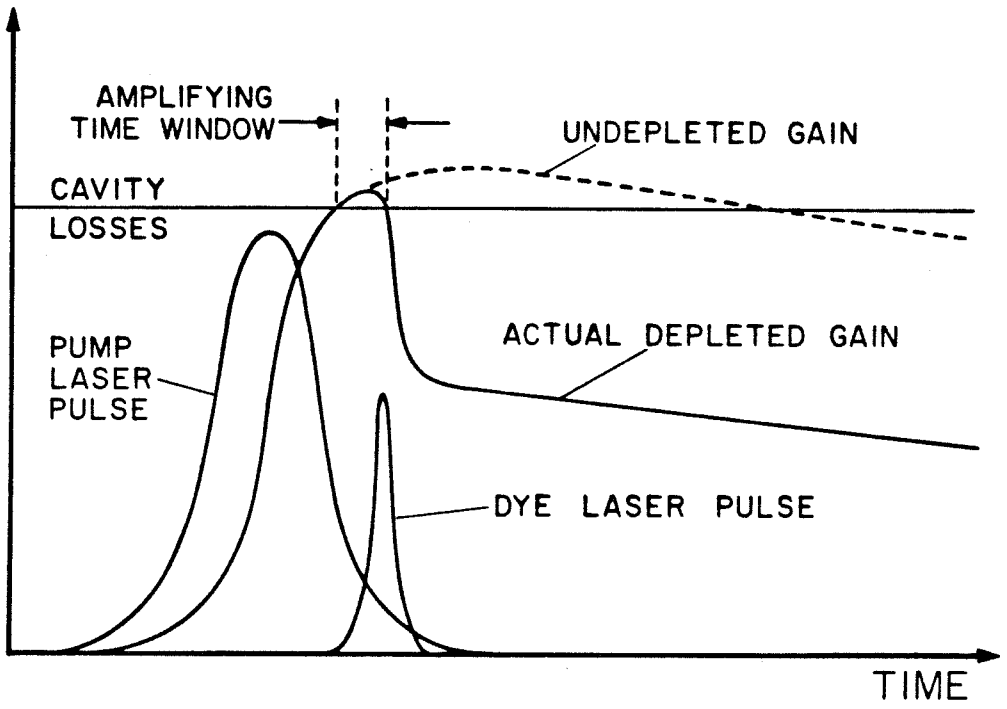

Figure 3.2 Relations which exist between pump pulse, signal pulse, gain and cavity loss in synchronously mode-locked dye laser.

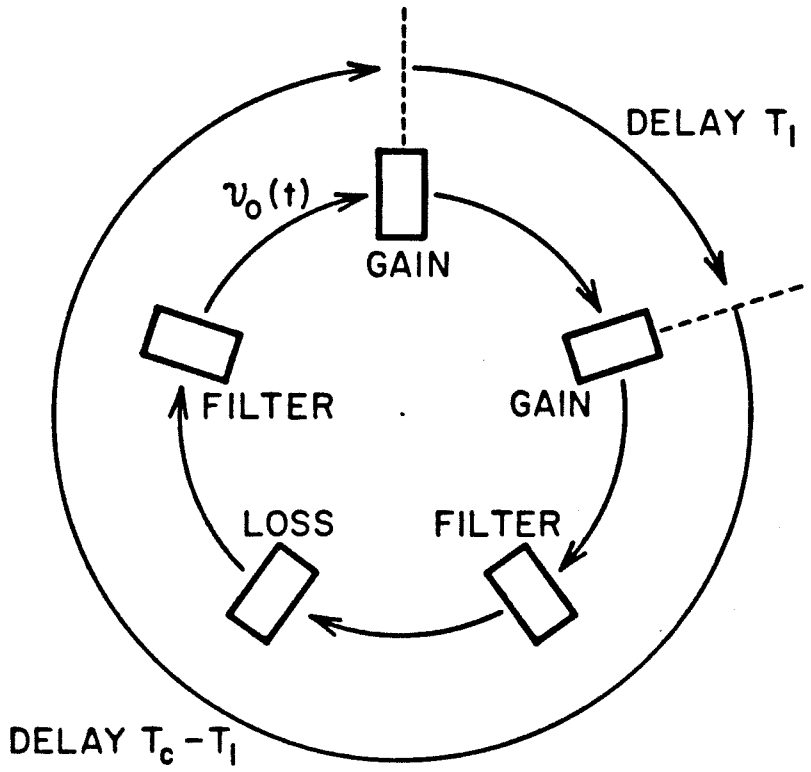

Figure 3.3 Conceptual scheme used for analysis of synchronously mode-locked dye laser.

must also have a pulse repetition period T_p rather than T_c if a steady state is to be achieved.

We let the input signal have an amplitude $\mathcal{V}_0(t)$ such that $\mathcal{V}_0^2(t) = I_0(t) = v_g h\nu\varphi_{20}(t)$ and this will be centered *near* $t = 0$. After passing through the gain medium, the amplitude becomes

$$\mathcal{V}_1(t) = \mathcal{V}_0(t)\sqrt{G_1(t)} \tag{3.25}$$

where $G_1(t)$ is obtained, using Eq. 3.20, by integration of the differential equation

$$\frac{dG_1}{dt} = (\sigma_2^{em} + \sigma_2^{abs})\, G_1 \left[\frac{I_p(t)}{h\nu_p}(1-e^{-\kappa NL}G_1\gamma) - \frac{\mathcal{V}_0^2(t)}{h\nu_{sig}}(G_1-1)\right] \tag{3.26}$$

$$- \frac{1}{\tau}G_1[\ln G_1 + \sigma_2^{abs}NL]$$

In principle, to solve Eq. 3.26 for a given $\mathcal{V}_0(t)$ some initial condition on G_1 must be applied. For convenience, we apply this boundary condition at some time $t = -a$ at which time the pump is effectively zero, and the condition is $G_1(t = -a) \equiv G_{10}$ where G_{10} is some as of yet unknown value.

Referring to Fig. 3.3, the pulse then returns to the gain medium some time T_1 later at which time we assume the pump pulse has vanished, and after propagating through has the amplitude

$$\mathcal{V}_2(t) = \mathcal{V}_0(t)\sqrt{G_2(t)G_1(t)} \tag{3.27}$$

where $G_2(t)$ is given by

$$\frac{dG_2}{dt} = -(\sigma_2^{em} + \sigma_2^{abs})\, G_2(G_2-1)\, G_1 \frac{\mathcal{V}_0^2(t)}{h\nu_{sig}} - \frac{1}{\tau}G_2[\ln G_2 + \sigma_2^{abs}Nt] \tag{3.28}$$

In this case the initial condition which must be applied is $G_2(t = -a) = G_1(t = T_1 - a)$.

To close the link on the initial conditions, we note that the gain must also repeat

itself with a period T_p, which imposes the additional condition $G_2(t = T_p - T_1 - a) = G_{10}$.

Referring again to Fig. 3.3, the remaining elements in the cavity which act on the pulse are *linear* and can thus be included in a single operator on the waveform $v_2(t)$. The effect of the losses and output coupling, which have a combined effective fractional intensity reflectivity of R, is to multiply the amplitude by $\sqrt{R}$. For the bandwidth limiting or tuning element, we assume a Lorentzian filter centered at a frequency ω_0 which we also assume is the pulse carrier frequency. In particular, we assume that the complex wave is $v(t)e^{-i\omega_0 t}$ and its Fourier transform is thus $\tilde{v}(\omega - \omega_0)$ where

$$\tilde{v}(\omega) = \frac{1}{2\pi}\int_{-\infty}^{\infty} e^{i\omega t} v(t)\, dt \tag{3.29}$$

The action of the filter is then to multiply $\tilde{v}(\omega - \omega_0)$ with the complex amplitude transmittance $[\, 1 - \frac{2i(\omega - \omega_0)}{\Delta\omega}\,]^{-1}$ where $\Delta\omega$ is the FWHM transmission width for the spectral density of the pulse. However, as is easily verified, multiplying $\tilde{v}(\omega - \omega_0)$ by $-i(\omega - \omega_0)$ in the frequency domain is equivalent to operating on $v(t)$ with $\frac{d}{dt}$ in the time domain. In the time domain the action of the filter is then formally represented by the operator $[\, 1 + \frac{2}{\Delta\omega}\frac{d}{dt}\,]^{-1}$ acting on $v(t)$. If the inherent bandwidth of the pulse is small compared with the filter bandwidth, as will usually be the case in practice, we can represent this result with a truncated series expansion of the operator, and after *two* passes through the filter combined with the losses we have the effective linear operator

$$\sqrt{R}\,[\, 1 - \frac{4}{\Delta\omega}\frac{d}{dt} + \frac{12}{(\Delta\omega)^2}\frac{d^2}{dt^2} - \ldots\,] \tag{3.30}$$

We then conclude that after step (5) , i.e., one round trip flight time T_c , the pulse has attained the form

$$v_0(t + T_c) = \sqrt{R}\,[\,1 - \frac{4}{\Delta\omega}\frac{d}{dt} + \frac{12}{(\Delta\omega)^2}\frac{d^2}{dt^2}\,]\,\sqrt{G_1(t)G_2(t)}\,v_0(t) \tag{3.31}$$

However, at steady state we require that

$$v_0(t + T_p) = v_0(t) \tag{3.32}$$

and if we define $\delta T \equiv T_c - T_p$ then Eq. 3.32 reads

$$v_0(t + T_c) = v_0(t + \delta T) \tag{3.33}$$

This is inserted as the LHS in Eq. 3.31 , and if δT is small we can expand the RHS of Eq. 3.33 in a Taylor series to obtain as the final equation for the self consistent pulse waveform $v_0(t)$

$$[\,1 - \frac{4}{\Delta\omega}\frac{d}{dt} + \frac{12}{(\Delta\omega)^2}\frac{d^2}{dt^2}\,]\,\sqrt{RG_1(t)G_2(t)}\,v_0(t) \tag{3.34}$$

$$-\,[\,1 + \delta T\frac{d}{dt} + \frac{(\delta T)^2}{2}\frac{d^2}{dt^2}\,]\,v_0(t) = 0$$

This must be solved together with Eq. 3.26 and Eq. 3.28. To apply boundary or initial conditions, we note that we have converted the discussion of the entire pulse train to the consideration of a single pulse. This is valid if we restrict the discussion to the time domain $t \in [\,-\frac{T_p}{2}\,,\,\frac{T_p}{2}\,]$ and require the pulse to satisfy

$$v_0(\,t = -\frac{T_p}{2}\,) = v_0(\,t = \frac{T_p}{2}\,) \tag{3.35}$$

and

$$\left.\frac{dv_0}{dt}\right|_{t=-\frac{T_p}{2}} = \left.\frac{dv_0}{dt}\right|_{t=+\frac{T_p}{2}} \tag{3.36}$$

The formalism developed above provides a fairly complete and rigorous descrip-

tion of the synchronously mode locked dye laser. Similar treatments appear in the literature to describe the performance of mode-locked dye lasers, both passive[2-6] and synchronously pumped[7-9], usually with a variety of approximations incorporated to replace the above equations with either a smaller number of equations, simpler equations, or both. Some models assume functional forms and then try to self-consistently fit some parameters in the functions such that they become approximate solutions of the equations for the system[10-12]. Since these are not entirely satisfactory, and a full numerical analysis is not appropriate in this thesis, we restrict our attention to general observations which can be made based upon the physics which goes into the set of equations above.

Consider first the approximate Lorentzian filter operator $[\,1 - \frac{4}{\Delta\omega}\frac{d}{dt} + \frac{12}{(\Delta\omega)^2}\frac{d^2}{dt^2}\,]$. The basic effect is that of a delay in time combined with a reduction in amplitude and some broadening which depend on the sharpness of the pulse. Physically this results from the energy in the leading edge being stored in the filter element and later being deposited back into the tail of the pulse. This will tend to discriminate against too short a pulse, and this linear action is easily understood from the Fourier transform bandwidth requirements of short pulses.

The time advance operator $[\,1 + \delta T\frac{d}{dt} + \frac{(\delta T)^2}{2}\frac{d^2}{dt^2} - \ldots\,]$ operating on a function f(t) generates a forward displacement in time by $\delta T \equiv T_c - T_p = \frac{2\delta L_c}{c} - T_p$. Lengthening the cavity *increases* the magnitude of the time delay. The effect of the linear losses are obvious, and the critical behavior is thus contained in the *nonlinear* gain operator $\sqrt{G_1(t)G_2(t)}$ which acts on the pulse waveform. The basic action of nonlinear gain has been discussed to some extent in Chapter 2 , and the elementary facts will be drawn from there.

Probably the most marked effect which is observed in synchronously mode-locked dye lasers is the strong cavity length dependence of the output pulse width. We re-write Eq. 3.34 as

$$\left[1 - \frac{4}{\Delta\omega}\frac{d}{dt} + \frac{12}{(\Delta\omega)^2}\frac{d^2}{dt^2} \right] \sqrt{RG_1(t)G_2(t)}\, v_0(t) \qquad (3.37)$$

$$= \left[1 + \delta T \frac{d}{dt} + \frac{(\delta T)^2}{2}\frac{d^2}{dt^2} \right] v_0(t)$$

to stress that any lengthening of the cavity which increases δT must be *more than* compensated for by the pulse advancing nature of the nonlinear amplification as described in Chapter 2. It must be more than compensated because the Lorentzian filter, as discussed above, tends to be a pulse delaying element. However, the basic effect of the filter is to discriminate against short pulses and the essential effect to be considered here is the interplay between cavity length adjustments and the demands placed on the nonlinear gain.

For a given pump pulse amplitude and output coupling, three quantities can vary to maintain a steady state signal pulse *amplitude*. These are: (1) The relative arrival time of the signal and pump pulses at the gain medium, since this determines the leading edge or unsaturated gain; (2) The signal amplitude since the *actual* gain saturates and (3) The pulse duration, since the filter attenuates short pulses. In turn, as described in Chapter 2, only two things strongly affect the amount of *pulse advancing* in nonlinear amplification: (1) The steepness of the leading edge and, perhaps more importantly, (2) the level of saturation of the amplification. From this, we see that time delays, or cavity length changes, are inexorably linked both to pulse amplitudes as well as pulse shape and width characteristics.

Clearly mode-locking can only result for a limited range of δL_c since the other effects are only capable of generating a limited amount of pulse advances/delays.

The amount they can generate depends primarily on the cavity bandwidth and the pump energy and pulse width. For simple trends, however, consider the extremes of the operating range of allowable values of δL_c . When δL_c is very small, there must be as little advance as possible. This will occur when the gain is unsaturated and when the pulse has a sharp temporal profile. This was illustrated in the small signal $sech^2$ solution Eq. 2.77 where a viable solution for $\delta T \rightarrow 0$ must have a small F_0 and G_0 . Thus, to have the least gain saturation the signal amplitude will be small and the initial gain will be small. Both of these occur if the signal pulse arrives *early* relative to the pump pulse. Referring back to the discussion of Fig. 3.2, this also means the gain "window" will be short, which is consistent with the sharp profile for no advancing. Therefore the short cavity extreme of the operating range is expected to produce short pulses but low energies. In practice, however, low gain and pulse energy often leads to unstable and unreliable performance. Another problem is that the early arrival and negligible depletion from the signal pulse permits the gain to grow as the remainder of the pump pulse arrives. The cavity is then able to support a longer satellite pulse following the first pulse, and the occurrence of such satellites is well documented[12].

At the opposite end of the operating range δL_c is *long*, which means than the nonlinear gain must generate as much advancing as possible. This will occur when the gain is very saturated and the pulse has a broadened temporal profile. To get saturated gain, the signal pulse should have a large amplitude and arrive *late* relative to the pump pulse when the unsaturated gain has grown to a large value. Referring to Fig. 3.2, this means the gain window is longer, which is consistent with the generation of the broader pulses more susceptible to advance. Thus the longer end of the operating range is expected to produce longer but more energetic pulses. All these general arguments are supported by the simple numerical results of Scavannec[13].

Between the extreme operating regimes, of course, we expect signal pulse behavior intermediate to the extreme behaviors. Since short pulses with reasonable stability and energy are usually the ideal product of the mode-locked dye laser oscillator, the optimal position will be as close to the short cavity extreme as energy and stability considerations permit. The qualitative dependence on other parameters is fairly straightforward. Larger bandwidths permit the generation of shorter pulses since the low energy, low gain short pulses see less attenuation. Shorter pump pulses scale the overall "gain window" arguments down and this reduces the oscillator pulse width, but the reduction is sublinear since the rapid gain modulation responsible for the mode-locking is to a large extent produced by the signal pulse itself. Increasing the cavity output coupling is conducive to operating in a higher gain mode which means less saturation and thus helps provide a more stable regime for short pulse operation. As mentioned earlier, various mathematical approximations have been made in the literature to predict specific power law type scaling with these parameters, but such approximations are questionable as is evidenced by the different results obtained by different authors. We shall remain content with the qualitative understanding based on the TW rate equations described above.

3.3 Dynamical Bleaching Behavior With Finite τ

Chapter 2 included a treatment of bleaching waves in a two-level medium, and steady state solutions with a finite inversion lifetime were presented. Using Eq. 3.20 we now present a brief discussion of the *dynamical* effects of a finite τ on bleaching waves. This is relevant for both pump bleach-through in optically pumped amplifier cells and signal bleach-through in saturable absorbers, and these phenomena both play a role in dye laser amplifier chains to be discussed in Chapter 4.

As mentioned earlier, in most situations the evolution of the net integrated and retarded gain/attenuation is the physical quantity of interest. The equation which governs the gain/attenuation of a signal $\varphi_{20}(t)$ while a pump wave $\varphi_{10}(t)$ is bleaching through a cell of length L is given by letting $\varphi_{20}(t) = 0$ in Eq. 3.20 to yield

$$\frac{dG}{dt} = v_g(\sigma_2^{em} + \sigma_2^{abs})\, G\, \varphi_{10}(t)(1-e^{-\kappa NL}G^{\gamma}) \qquad (3.38)$$

$$- \frac{1}{\tau}G[\ln G + \sigma_2^{abs}NL]$$

where γ and κ have the same meanings as before. For signal propagation through a saturable absorber, the "pump" and "signal" and are actually the same which means $\kappa = 0$ and $\gamma = 1$.

To illustrate the effects of finite τ on the bleaching of a pump wave through an amplifier cell, we consider the gain evolution resulting from rectangular pump pulses of different intensities. For simplicity of discussion here we set $\sigma_1^{em} = \sigma_2^{abs} = 0$. Fig. 3.4 and Fig. 3.5 show the gains resulting from pump pulses one lifetime τ wide, centered at t = 0 , in a cell which would have a gain of 10^4 if completely inverted. In both cases the four curves shown are the gains which result from pump photon densities of 10, 15, 20, and 30 times the saturation photon density φ_{2_s} at the *signal* wavelength, which in this case is $\varphi_{2_s} = [v_g\tau\sigma_2^{em}]^{-1}$. However, Fig. 3.4 shows the case where $\sigma_1^{abs} = \sigma_2^{em}$, while Fig. 3.5 shows the case where the absorption cross section at the pump wavelength has been reduced to a *third* of this value, $\sigma_1^{abs} = \frac{1}{3}\sigma_2^{em}$. Therefore, while the *actual* pump intensity and maximum possible gains are identical in Fig. 3.4 and Fig. 3.5, in the former the four curves correspond to φ_{10} = 10, 15, 20, and 30 times φ_{1_s} , while in the latter the four curves correspond to φ_{10} = 3.3, 5, 6.7, and 10 times φ_{1_s} where $\varphi_{1_s} = [v_g\tau\sigma_1^{abs}]^{-1}$.

Since steady state obtains on a time scale of τ , the relative amount of "punch-

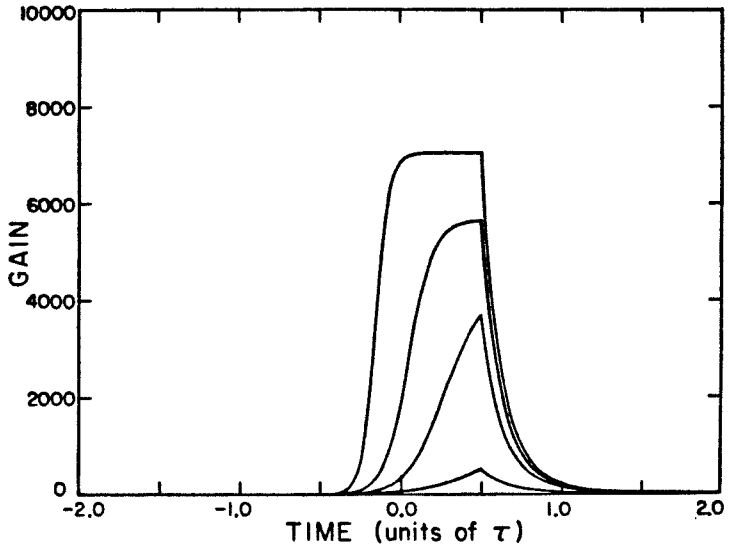

Figure 3.4 Gain clipping from pump longitudinally bleaching through an amplifier cell with finite τ. Pump is a rectangular pulse of duration τ, and the four curves are for pump intensities of 10, 15, 20, and 30 times the saturation intensity. Maximum gain with complete inversion here would be 10^4 .

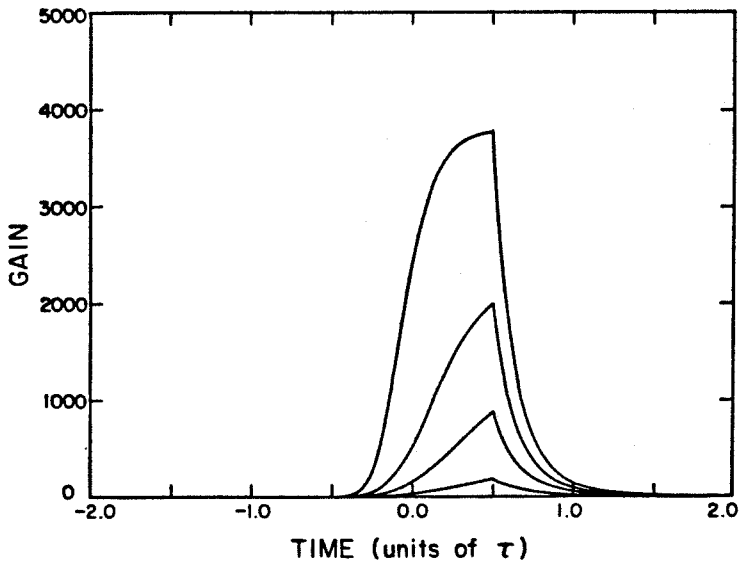

Figure 3.5 Same as above except absorption cross section at the *pump* wavelength is reduced to one third of its value above. Maximum possible gain is then still 10^4 , but now increased saturation intensity makes the pump intensities in the four curves only 3.3, 5, 6.7 and 10 time the saturation intensity.

through" should be characterized, according to the simple results of Chapter 2, by a parameter $\Theta \equiv v_{bleach}\tau/L$ where L is the cell length and v_{bleach} is defined by Eq. 2.87. Assuming $v_g\tau >> L$, we obtain the same values $\Theta \approx 1.1, 1.6, 2.2$, and 3.3 respectively for the four curves in order of increasing intensity in both Fig. 3.4 and Fig. 3.5. Fig. 3.4 is seen to conform roughly to the expected amount of punch-through while Fig. 3.5 does not. This is due to the increased saturation photon density φ_{1_s} in the latter case, and we thus conclude that the simple bleaching wave behavior is significantly modified by the finite τ unless $\varphi_{10} >> \varphi_{1_s}$. We also require $\Theta \gtrsim 1$ if the bleaching wave is to propagate through the cell before a steady state is established.

Fig. 3.6 shows the computed results of a $sech^2$ intensity profile pulse propagating through a saturable absorber. In this case we have $\kappa = 0$ and $\gamma = 1$, and we let $\sigma_2^{em} = \sigma_1^{em} = 0$ while $\sigma_2^{abs} = \sigma_1^{abs}$, since there is now only one wave $\varphi_{10}(t)$. The dashed curve is the input pulse, where again the FWHM is chosen to be one lifetime τ wide. The two solid curves are the output pulse and the transmission from the Chapter 2 analytic results, while the dotted curves are the finite lifetime output pulse and transmission calculated numerically from Eq. 3.38. The values used here were $G_0 = 1x10^{-2}$ and $F(t = \infty) = 15$ where G_0 is actually an initial *attenuation* in this case and F(t) is defined by Eq. 3.23.

Since the peak photon density $\varphi_{2_{max}}$ here is ~ 13 times the saturation photon density φ_{2_s}, the simple Chapter 2 results should be roughly applicable. Indeed, it can be seen in Fig. 3.6 that bleach-through occurs at approximately the same point in both the infinite and the finite τ calculations. The principal difference is that in the latter the peak transmission is considerably lower. This occurs since the peak transmission cannot exceed the value G_{max} where

$$G_{max} \lesssim G_0^{\left(\frac{1}{1+\frac{\varphi_{10}}{\varphi_{1s}}}\right)} \tag{3.39}$$

which is the approximate steady state solution of Eq. 3.38 under high saturation conditions. Another obvious feature in Fig. 3.6 is the return of the transmission to its initial value with a time scale of τ in the low intensity tail of the pulse. This is the basis of the gating ability of a saturable absorber and is exploited in the experimental amplifier system to be detailed in Chapter 5.

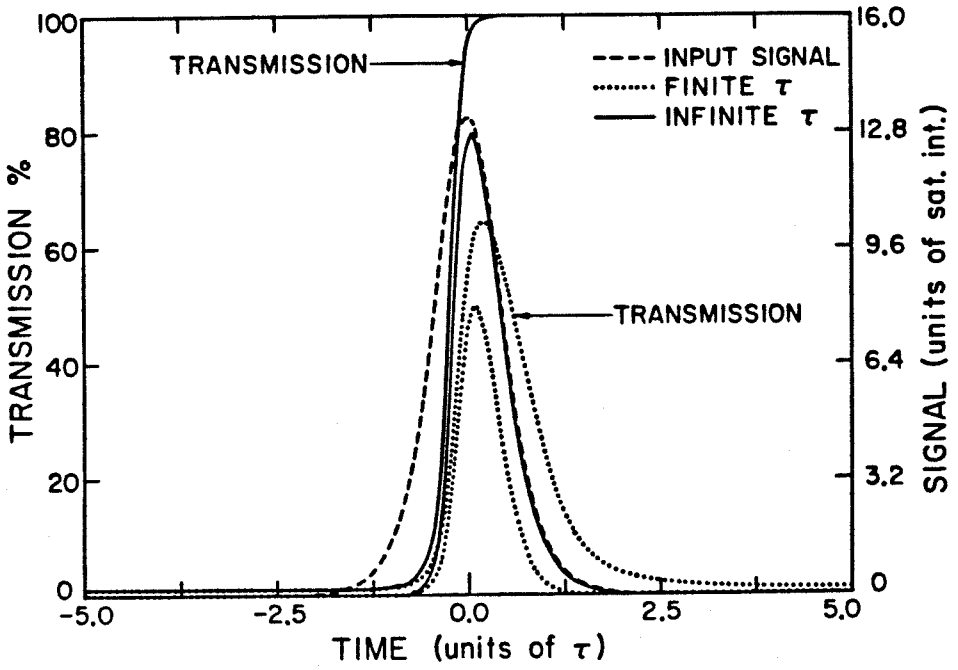

Figure 3.6 Saturable absorber transmission and output pulse for a sech^2 input pulse and initial transmission of 1%. Integrated and normalized photon flux F has a value 15 here. The two sets of curves here are the Chapter 2 analytic results for $\tau \to \infty$ and the finite τ results. For the latter, the pulse has a duration of τ.

CHAPTER 3 REFERENCES

1. A. Yariv, J. Appl. Phys. **36**, 338 (1965).

2. G. H. C. New, Opt. Commun. **6**, 188 (1972).

3. G. H. C. New, IEEE J. Quantum Electron. **QE-10**, 115 (1974).

4. H. A. Haus, IEEE J. Quantum Electron. **QE-11**, 736 (1975).

5. H. A. Haus, J. Appl. Phys. **46**, 3049 (1975).

6. H. A. Haus, IEEE J. Quantum Electron. **QE-12**, 169 (1976).

7. H. A. Haus, IEEE J. Quantum Electron. **QE-11**, 323 (1975).

8. N. J. Frigo, T. Daly, and H. Mahr, IEEE J. Quantum Electron. **QE-13**, 101 (1975).

9. J. Herrmann and U. Motschmann, Appl. Phys. **B 27**, 27 (1982).

10. C. P. Ausschnitt and R. K. Jain, Appl. Phys. Lett. **32**, 727 (1978).

11. D. M. Kim, J. Kuhl, R. Lambrich, and D. von der Linde, Opt. Commun. **27**, 123 (1978).

12. C. P. Ausschnitt, R. K. Jain, and J. P. Heritage, IEEE J. Quantum Electron. **QE-15**, 912 (1979).

13. A. Scavennec, Opt. Commun. **17**, 14 (1976).

CHAPTER 4

MODELING OF GIGAWATT PICOSECOND DYE LASER AMPLIFIER CHAINS

One of the more exciting developments in picosecond dye lasers in recent years has been the incorporation of Nd:YAG pumped dye laser amplifier chains to boost the energy of CW mode-locked dye lasers[1-5]. These systems successfully couple the many advantages of CW mode-locked dye lasers with the higher energies available from solid state lasers to create a very versatile experimental apparatus. However, there have been few publications which present any experimental results or analyze picosecond dye amplifier chains quantitatively[6-9]. In this chapter we present in detail the theory of picosecond dye laser amplifier chains[10]. This includes extensions of the mathematics of the previous chapters by adding effects peculiar to high gain amplifier cells and picosecond time scale pulse amplification. We first present a treatment of amplified spontaneous emission (ASE) which permits an analysis of practical amplifiers and optimization of pumping efficiencies. This is followed by a discussion of pulse shaping effects with saturable absorbers included, together with potential pulse shaping effects which could arise from both linear dispersive effects and finite vibrational level lifetimes in organic lasing dyes. Triplet losses are then included in the model, together with a theory of dynamic "anglular hole-burning" to give a quantitative picture of the gain saturation and net energy amplification which result in high gain dye laser amplifier chains.

4.1 Amplified Spontaneous Emission

In chapter 3, gain evolution in the combined presence of signal and pump waves was discussed including the effects of finite inversion lifetimes τ. In many circumstances that treatment is accurate. If, however, the gain of an amplifier cell becomes high enough, the spontaneous emission itself becomes amplified to a point where it causes *stimulated* emission at a rate which can exceed $1/\tau$. In this case, ASE leads to an *effective* lifetime which is shorter than τ and under some circumstances this can dominate the amplifier performance[11,8]. Whether this happens or not depends upon the gain, but also in a detailed way on the geometry of the amplifier cell. This is the problem we address next.

Well developed theories of steady state ASE effects requiring extensive numerical analysis have appeared in the literature[11]. To facilitate a less accurate but tractable dynamical treatment of ASE effects we adopt a simple approximation based on Fig. 4.1. If the gain constant is given by γ and is constant throughout an arbitrary convex volume V, it is a straightforward excercise to calculate the total number of photons per unit time leaving the volume V. This rate will yield the average *effective* lifetime τ_{eff} since if a photon experiences gain this means that it has stimulated the emission of other photons, causing the net inversion to drop with each such emission; this is exactly the effect we wish to calculate. The gain of a photon emitted at $\vec{x}'$ and propagating to $\vec{x}$ is $e^{\gamma|\vec{x}-\vec{x}'|}$, but only a fraction $(\vec{x}-\vec{x}')\cdot d\vec{A}/4\pi|\vec{x}-\vec{x}'|^3$ are emitted in this direction. The effective average lifetime including induced emissions from ASE is obtained by averaging over all possible points of emission within the volume V. The result is thus

$$\frac{1}{\tau_{eff}} = \frac{1}{\tau}\frac{1}{4\pi V}\int_V d^3x' \int_A \frac{e^{\gamma|\vec{x}-\vec{x}'|}(\vec{x}-\vec{x}')\cdot d\vec{A}}{|\vec{x}-\vec{x}'|^3} \qquad (4.1)$$

This is easily put in a form which separates out the contribution from ASE. If we let $\psi = e^{\gamma|\vec{x}-\vec{x}'|}$ and $\varphi = -\frac{1}{|\vec{x}-\vec{x}'|}$, then Eq. 4.1 becomes

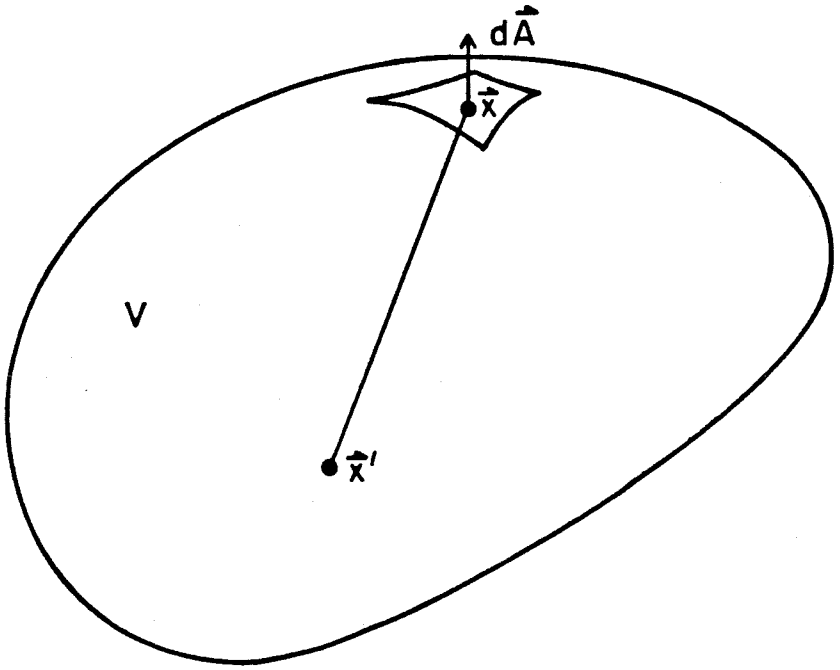

Figure 4.1 Arbitrary convex volume used in ASE depletion model.

$$\frac{1}{\tau_{eff}} = \frac{1}{\tau}\frac{1}{4\pi V}\int_V d^3x' \int_A \psi \vec{\nabla} \varphi \cdot d\vec{A} \tag{4.2}$$

Employing Green's identity

$$\int_V \psi \nabla^2 \varphi \, d^3x + \int_V \vec{\nabla} \psi \cdot \vec{\nabla} \varphi \, d^3x = \int_A \psi \vec{\nabla} \varphi \cdot d\vec{A} \tag{4.3}$$

and noting that $\nabla^2 \varphi = 4\pi\delta(\vec{x} - \vec{x}')$, we obtain after some manipulation

$$\frac{1}{\tau_{eff}} = \frac{1}{\tau} + \frac{\gamma}{\tau}\int_0^\infty e^{\gamma l} S(l) dl \tag{4.4}$$

where $S(l)$ is the "length distribution function" of the shape V given by

$$S(l) = \frac{1}{4\pi l^2 V}\int_V d^3x \int_V d^3x' \, \delta(l - |\vec{x} - \vec{x}'|) \tag{4.5}$$

To visualize what this length distribution function represents, we proceed as follows. At a given point within the volume V we construct an imaginary sphere of radius l around that point. We then calculate what fraction of the *surface area* of that sphere lies *within the volume* V. We calculate this fraction at every point within the volume and average the results over the entire volume. The resulting number is, for each value of l , just $S(l)$, the length distribution function. Thus the length distribution function gives a quantitative measure, for the geometry under consideration, of how likely a given path length l is for random directions of emission before leaving the volume.

The second term on the RHS in Eq. 4.4 accounts for the induced emission from ASE, and the geometrical dependence of the "amplifier cell" is now all contained in $S(l)$. As an example, for a sphere of diameter D it is shown in Appendix A4a that

$$S(l) = 1 - \frac{3}{2}\left[\frac{l}{D}\right] + \frac{1}{2}\left[\frac{l}{D}\right]^3 \tag{4.6}$$

and for an infinitely long cylinder of diameter D, a tedious calculation outlined in Appendix A4a yields

$$S(\ell) = \begin{cases} 1 + \frac{4}{3\pi}\left[\frac{\ell}{D}\right]F\left(\frac{\ell}{D}\right) & \text{if } \ell < D \\ 1 + \frac{4}{3\pi}F\left(\frac{D}{\ell}\right) & \text{if } \ell > D \end{cases} \tag{4.7}$$

where

$$F(x) = \frac{[\mathbf{K}(x) - \mathbf{E}(x)]}{x^2} - [\mathbf{K}(x) + \mathbf{E}(x)] \tag{4.8}$$

where **K** and **E** are the usual abreviations for the elliptic integrals. For the finite cylinder of length L which is of interest to us here, as long as $\frac{L}{D} >> 1$, it is an excellent approximation to let

$$S(\ell) = S_\infty(\ell) \cdot \left(1 - \frac{\ell}{L}\right) \tag{4.9}$$

This follows from the discussion of the meaning of $S(\ell)$ and is detailed in Appendix A4a. The integral in Eq. 4.4 can then be performed asymptotically, yielding a preliminary asymptotic result for the effective lifetime

$$\frac{1}{\tau_{eff}} \approx \frac{1}{\tau}\left[1 + \frac{2}{3}\gamma L\left(\frac{D}{L}\right) + \frac{1}{8}\frac{e^{\gamma L}}{\gamma L}\left(\frac{D}{L}\right)^2\left(1 + \frac{4}{\gamma L} + \frac{18}{(\gamma L)^2} + \ldots\ldots\right)\right. \tag{4.10}$$

which holds for $\frac{D}{L} << 1$ and $\gamma L >> 1$. In deriving Eq. 4.4, we have ignored the frequency dependence of γ. If we ignore ground state population, the emission lineshape will be given by $\gamma(\nu)$ when appropriately normalized, and in Eq. 4.4 we should replace every appearance of $\frac{1}{\tau}(\ldots.)$ with

$$\frac{1}{\tau}\frac{\int_{-\infty}^{\infty} d\nu\gamma(\nu)\,(\ldots.)}{\int_{-\infty}^{\infty} d\nu\gamma(\nu)} \tag{4.11}$$

The only term this has a significant effect on is the one containing $e^{\gamma L}$. If we assume that the emission line shape is Gaussian, we have

$$\gamma(\nu) = \gamma_{max}\, e^{-a\nu^2} \tag{4.12}$$

and the operation indicated in Eq. 4.11 becomes

$$\frac{1}{\tau}\frac{\int_{-\infty}^{\infty} d\nu\, e^{-a\nu^2}\left(e^{\gamma_{max}Le^{-a\nu^2}}\right)}{\int_{-\infty}^{\infty} d\nu\, e^{-a\nu^2}} \tag{4.13}$$

and if $\gamma_{max}L >> 1$, we expand the exponential in the exponent and Eq. 4.13 becomes

$$\frac{e^{\gamma_{max}L}}{\tau}\frac{\int_{-\infty}^{\infty} d\nu\, e^{-a\gamma_{max}L\nu^2}}{\int_{-\infty}^{\infty} d\nu\, e^{-a\nu^2}} = \frac{e^{\gamma_{max}L}}{\tau\sqrt{\gamma_{max}L}} \tag{4.14}$$

and thus asymptotically for $\gamma L >> 1$ this term is reduced by an additional factor of $(\gamma_{max}L)^{-\frac{1}{2}}$. The analagous reduction factor for a Lorentzian gain lineshape is $(\pi\gamma_{max}L)^{-\frac{1}{2}}$, and for arbitrary lineshape $g(\nu)$ normalized such that $g(\nu_{max}) = 1$, we obtain the reduction factor

$$f = \frac{1}{A}\sqrt{\frac{\pi}{B\gamma_{max}L}} \tag{4.15}$$

where

$$A \equiv \int_{-\infty}^{\infty} g(\nu)d\nu \quad \text{and} \quad B \equiv -\frac{1}{2}\frac{d^2g}{d\nu^2}\bigg|_{\nu_{max}} \tag{4.16}$$

We then let $\gamma_{max}L \equiv \ln G$ to obtain

$$\frac{1}{\tau_{eff}} \approx \frac{1}{\tau}\left[1 + \frac{2}{3}\left(\frac{D}{L}\right)\ln G + \frac{1}{8}\frac{D^2}{L^2}G(\ln G)^{-\frac{3}{2}}\left(1 + \frac{4}{\ln G} + \frac{18}{(\ln G)^2} + \ldots\ldots\right)\right] \tag{4.17}$$

The G which should be inserted above is the actual small signal gain (including the gain saturating effect of the ASE) which would be experienced by a signal propagating the length of the amplifier cell at the peak gain wavelength. We note that this

expression is similar to the results of others who were interested in upper limits on amplifier gain[12]. The most severe approximation involved in the derivation was that the gain was assumed to be uniformly saturated in space by the ASE. For a given ASE depleted G, we expect Eq. 4.17 to slightly underestimate the effective rate $\frac{1}{\tau_{eff}}$ because in the real case the inversion will be localized along the length of the cell in a manner dependent upon the pumping process. This means that, compared to the uniform case, at some points in the cell a larger solid angle of emission will experience a large gain, while at other points a smaller solid angle sees the large gain. For a given inversion nonuniformity, the trade-off in solid angle is linear but the gain trade-off is exponential, so for the same integrated gain inversion nonuniformities should increase the total ASE slightly over the uniform case. As an example, however, in one dimensional calculations which employ an average solid angle of emission, the result for τ_{eff} is independent of the spatial gain distribution. We stress that the model above does include the ASE depletion by replacing a complicated calculation with an $\vec{x}$ dependent depleted $\gamma(\vec{x})$ with a constant depleted γ such that $\gamma \equiv \frac{1}{L}\int_0^L \gamma(\vec{x})dz$.

To include the effect of ASE in a dynamical calculation, or for a discussion of steady state results, we insert the τ_{eff} from Eq. 4.17 in place of τ in the T.W. signal and pump equation Eq. 3.20 from Chapter 3. Apart from the approximations mentioned above, this introduces the additional approximation that the effects of ASE are not included with the proper *retardation*. For most purposes we do not expect this to be a serious flaw. Retardation effects only occur over the time scale of the propagation length of the amplifier cell, and in most cases this is smaller than the time scale of significant inversion change during the *pumping* process. During the short picosecond *signal* propagation we can neglect any *changes* in the effects of ASE and treat it as an "initial value" problem for the amplification process.

4.2 Efficiency Optimization

From the gain saturation results of Chapter 2 it is apparent that amplification is most efficient if the signal is as intense as possible so that most of the amplification takes place in the saturated regime. One might conclude from this that the most efficient amplifier would be one where the pump energy is distributed along as thin a region as possible. Amplified spontaneous emission alters this conclusion, and this is the subject of this section. To discuss the efficiency of an amplifier cell, we employ a number of reasonable approximations to facilitate mathematical results. In the situations of interest to us here, the pumping process will be on a nanosecond time scale while the signal pulse has picosecond time scale durations. The peak signal intensity is thus often orders of magnitude larger than the pump pulse. Even if this is not true, there is often negligible inversion change from the *pumping* during the picosecond pulse duration. This means that in Eq. 3.20, during the time when the signal $\varphi_{20}(t)$ is non-zero, we can effectively ignore the pump $\varphi_{10}(t)$. Also, as suggested above, we can usually ignore any spontaneous emission during the signal pulse duration. This permits the *decomposition* of Eq. 3.20 into *two* equations; one governs the signal pulse propagation and the other the pumping process until the arrival time of the signal at the entrance face of the amplifier cell. For the former, the results of Chapter 2 become applicable, in particular Eq. 2.54. For the latter, we use Eq. 3.20 with τ replaced by τ_{eff} as explained above, and let $\varphi_{20}(t) = 0$. Noting that we are now integrating for the *leading edge* signal gain $G_o(t)$, we have

$$\frac{dG_o}{dt} = v_g(\sigma_2^{em} + \sigma_2^{abs})\, G_o\, \varphi_{10}(t)(1-e^{-\kappa NL}G_o^{\gamma}) \qquad (4.18)$$

$$- \frac{1}{\tau_{eff}} G_o[\ln G_o + \sigma_2^{abs} NL]$$

We now restrict our attention to steady state solutions of Eq. 4.18 since we are only

interested in trends. The factor $(1-e^{-\kappa NL}G_o^{\gamma})$ in Eq. 4.18 represents the fraction of pump power absorbed. This follows directly from Eq. 3.14 evaluated at $\eta = L$ and the definition of the retarded gain Eq. 3.19. As will be discussed later, it is usually desirable to "bleach through" the cell. In this steady state approximation, we therefore assume that as we vary all quantities below, we always adjust the dye concentration N so that a sizable fraction, but not all, of the pump power is absorbed, i.e., $(1-e^{-\kappa NL}G_o^{\gamma}) = \text{const.} \equiv f$. For the approximate treatment here, we ignore the second term on the RHS of Eq. 4.17 in the expression for τ_{eff} since if ASE is an important effect we have usually reached a point where

$$\frac{2}{3}\left(\frac{D}{L}\right)\ln G << \frac{1}{8}\frac{D^2}{L^2}G(\ln G)^{-\frac{3}{2}} \tag{4.19}$$

We then obtain

$$G_o \approx C_1 \exp\left[\frac{C_2}{A\left[1 + \frac{AG_o}{2\pi L^2}(\ln G_o)^{-\frac{3}{2}}\left(1 + \frac{4}{\ln G_o} + \frac{18}{(\ln G_o)^2} + ...\right)\right]}\right] \tag{4.20}$$

and we have from Eq. 3.24 for the signal amplification

$$G_{actual} = \frac{A}{C_3}\ln\left(1 + G_o\left(e^{\frac{C_3}{A}} - 1\right)\right) \tag{4.21}$$

where C_1 is a constant depending only on f and cross sections, and C_2 and C_3 are constants proportional to pump power and signal energies, respectively.

$$\begin{aligned} C_1 &= (1-f)^{[\sigma_2^{abs}/\sigma_1^{abs}]} \\ C_2 &= \frac{P_{pump}\tau(\sigma_2^{em}\sigma_1^{abs} - \sigma_2^{abs}\sigma_1^{em})\,f}{h\nu_{pump}\sigma_1^{abs}} \\ C_3 &= \frac{E_{sig}(\sigma_2^{em} + \sigma_2^{abs})}{h\nu_{sig}} \end{aligned} \tag{4.22}$$

A is the cross-sectional area of the active region of the cell, and we assume here a perfect match between signal and pump beam diameters. P_{pump} is the incident

pump power on the amplifier entrance face.

Fig. 4.2 shows the small signal gain in dB and the actual gain on a linear scale obtained from Eqs. 4.20-22 as a function of the active diameter in the medium for various values of pump powers, all with a fixed signal energy of 1.5×10^{-6} joules and a 10 cm cell. The values of the pump were 2, 4, 6, 8 and 10 mJ in a 15 nsec pulse, and the cross secton values were $\sigma_2^{em} = 3.92\text{x}10^{-16}$ cm^2, $\sigma_2^{abs} = 5.4\text{x}10^{-17}$ cm^2, $\sigma_1^{em} = 0$, and $\sigma_2^{abs} = 1.19\text{x}10^{-16}$ cm^2. The value of f assumed was f = 0.7, and in addition there was a linear loss factor of 0.7 applied to the signal before and after the cell to simulate the effects of the dichroics used in the actual amplifier system. These are typical values for the second stage of our experimental system to be discussed in detail in Chapter 5. While the small signal gain always increases as $D \to 0$, for the actual gain there is always an optimal diameter for each pump and signal level. This results from a competition between energy storage and energy extraction and can be explained qualitatively as follows. The most efficient extraction of a fixed amount of energy occurs when the diameter is as small as possible; the signal reaches the saturation intensity very quickly and extracts most of the stored energy. However, to distribute the same total energy $E_{sto} \cong N_2ALh\nu_{sig}$ in such a thin cell requires that the small signal gain, which is roughly proportional to $e^{N_2\sigma^{em}L}$ increase as $G_o \sim \exp(\frac{E_{sto}\sigma^{em}}{h\nu_{sig}A})$ as A becomes smaller. For any finite length, Eq. 4.20 will not let G_o increase this rapidly because of ASE. As soon as $G_o(\ln G_o)^{-\frac{3}{2}} \sim \frac{2\pi L^2}{A}$, further reduction in A does not increase G_o as quickly as $\exp(\frac{E_{sto}\sigma^{em}}{h\nu_{sig}A})$ and the stored energy available for saturated pulse extraction begins to decline. The best design therefore represents a balance between the best diameter for energy storage and the small diameters needed for efficient energy extraction, and the most efficient cell will be one where ASE is just beginning to play a large role. We can also

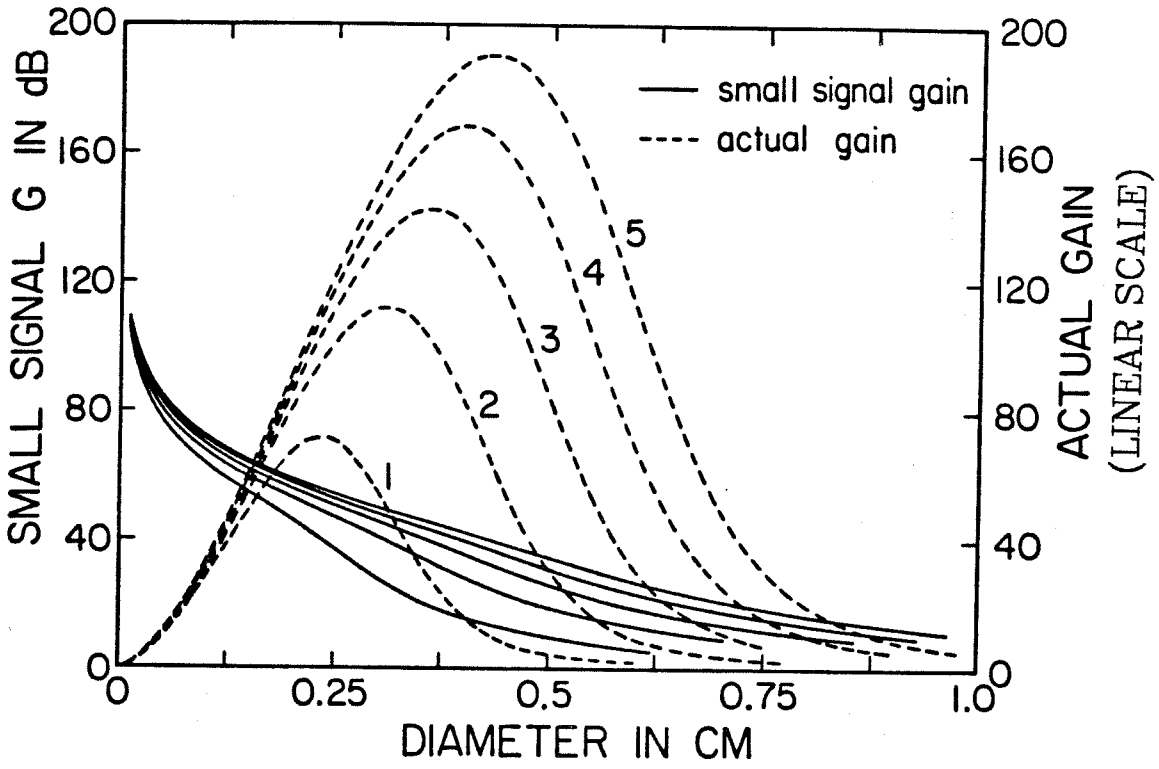

Figure 4.2 Calculated small signal and actual gain at 595 nm as a function of active diameter for input signal energy of 1.5×10^{-6} joule and cell length of 10 cm. Curves 1-5 represent results for pump energies of 2, 4, 6, 8, 10 mj respectively, in a 15 nsec pulse.

infer from this argument that the existence of an optimal diameter actually results from practical considerations on cell length since the gain was "clipped" when it approached the value $\frac{2\pi L^2}{A}$. If the amplifier were optimized in the manner to be discussed below, the area cannot increase arbitrarily or the signal saturation is reduced and the energy is not well extracted. Then the only way to increase the gain at which the "clipping" occurs is to increase the length L. However, since the stored energy only increases *logarithmically* with the gain, we expect the optimized amplified signal pulse energy to only increase logarithmically with cell length as well. Thus any sizable improvement to change the optimal cell diameter would require absurdly long cells, and in practice a long but physically reasonable cell is fixed and other parameters are varied to optimize the amplifier performance.

To both *store* and *extract* the largest energies possible, we set the cell diameter at the optimal value as we vary all quantities. In principle, we solve Eq. 4.20 for $G_o(A)$, insert this in Eq. 4.21 and maximize G_{actual} with respect to A for each pump power and then see how this varies with pump power for various values of input signal energy. This is shown in Fig. 4.3, all for L = 10 cm and signal energies ranging from 10^{-9} to 10^{-4} joule. The pump power is given by distributing the pump energy over a 15 nsec pulse, and other parameters are the same as in Fig. 4.2. If the system input is a very low level signal, it is obvious that single cell amplification to a large signal is exceptionally inefficient. This is why a multiple cell arrangement with ASE isolation is needed if reasonable efficiency is to be expected. The majority of the pump energy can then be allocated to the last stage where the storage and extraction problems have a more harmonious solution. In getting to the final stage, we can "hop" from one curve to another in Fig 4.3 using different amplifier stages rather than trying to move along a single curve. In principle a continuum of stages with ASE isolation would be best, but in practice little is lost if the early

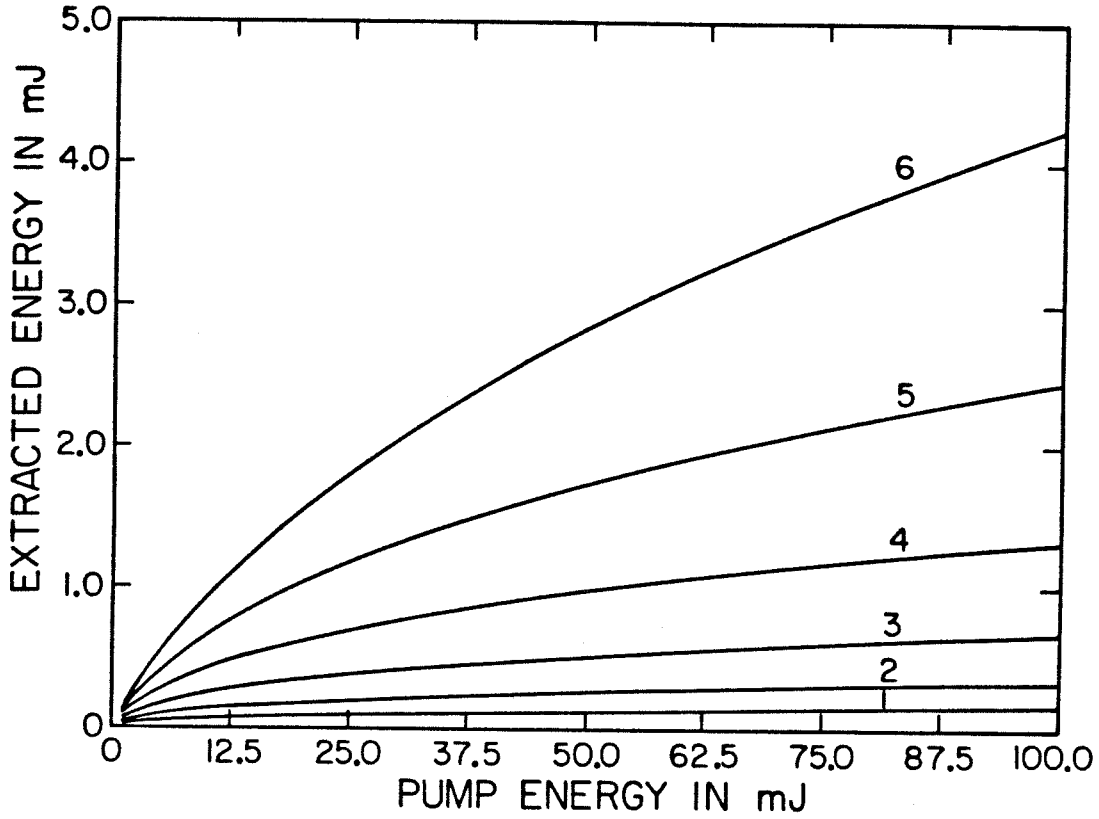

Figure 4.3 Optimized extracted energy vs. pump pulse energy at 595 nm using approximate steady state analysis. Curves 1-6 are for signal energies of 10^{-9}, 10^{-8}, 10^{-7}, 10^{-6}, 10^{-5}, and 10^{-4} Joules respectively.

amplification is done in one or a few stages since little pump energy need be devoted for this purpose anyway.

Also shown in Fig. 4.4 is the case where larger pump powers (up to 500 mJ in a 15 nsec pulse) are made available for a fixed input signal energy of 10^{-4} J. The various curves represent the optimized energy extraction as described above for different *cell lengths* rather than different signal energies. The lengths were increased geometrically for the seven curves with values of 10, 20, 40, 80, 160, 320, and 640 cm. Since the incremental improvement in the extracted signal energy is approximately a constant amount for each *doubling* of the cell length, this bears out the approximate logarithmic dependence of optimized amplified pulse energy on cell length as predicted above.

4.3 Pulse Shaping Effects

In Chapters 2 and 3 some general pulse shaping effects were discussed which occur upon passage through a nonlinear gain medium or a saturable absorber. In this section we discuss a number of effects which may modify those conclusions in the context of a high gain picosecond dye laser amplifier chain. However, we first apply the basic results of the earlier chapters to a specific physical layout similar to the exact experimental conditions to be detailed in Chapter 5.

Section 4.2 showed clearly the need for a multistage arrangement with ASE isolation. In particular, we consider here a three amplifier stage system with a saturable absorber betweeen each of the stages as shown in Fig. 4.5. The purpose of the saturable absorbers is two-fold. They attenuate the ASE flux thereby permitting efficient high gain operation without excessive superluminescent depletion of the gain. Also, by selectively passing the signal with a *truncated leading edge*, possible pulse compression can occur in the manner described in Chapter 2.

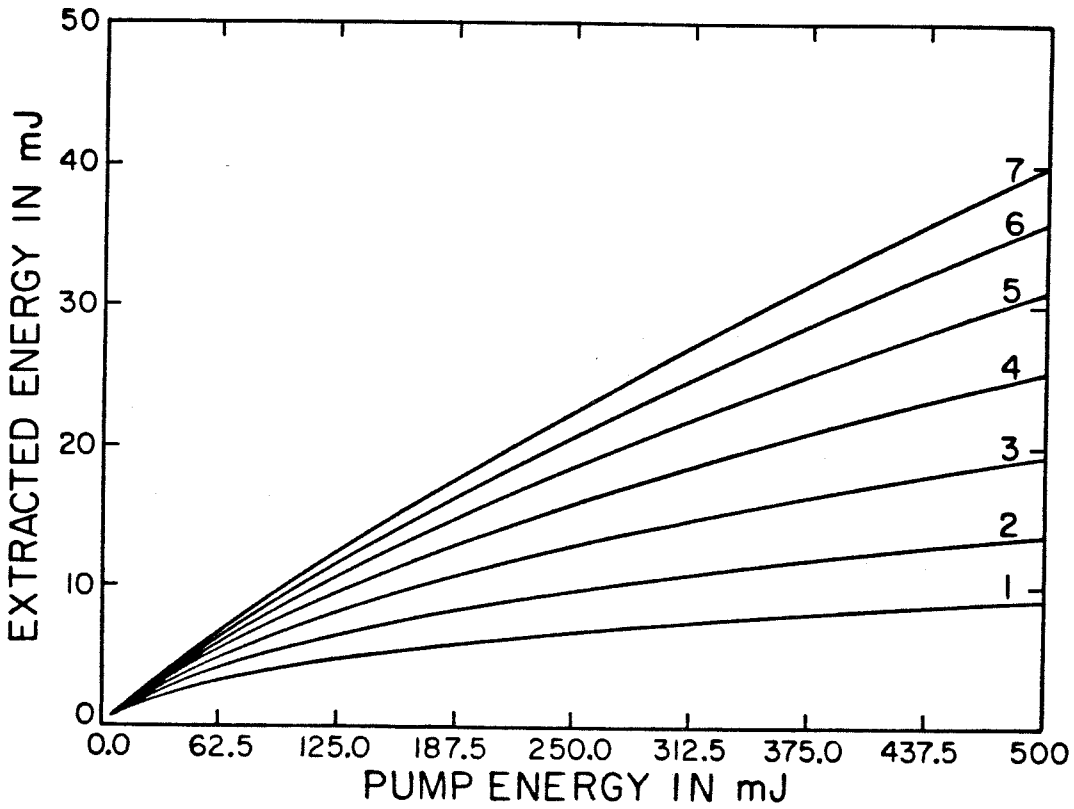

Figure 4.4 Optimized extracted energy vs. pump pulse energy at 595 nm using approximate steady state analysis. Curves 1-7 are all for a signal energy of 10^{-4} Joule, but for different cell *lengths* of 10, 20, 40, 80, 160, 320, and 640 centimeters. Approximate logarithmic dependence on cell length is evident.

There are a number of demands placed on the saturable absorber for effective performance. To establish a good truncated leading edge near the existing pulse maximum we require that the bleaching process consume a small but significant fraction δ of the pulse energy.

$$ANL \sim \delta \frac{E_{sig}}{h\nu_{sig}} \quad \text{or} \quad A \sim \frac{\delta}{(\sigma^{abs}NL)} \frac{E_{sig}}{h\nu_{sig}} \sigma^{abs} \tag{4.23}$$

where A is the signal beam cross sectional area at the saturable absorber, L is the path length in the absorber, and N is the molecular concentration of the saturable absorber molecules which have cross section σ^{abs} and we assume here $\sigma^{em} = 0$ for convenience.

Also, as discussed at the end of Chapter 3, to have a "hard" and complete punch-through we require that the pulse of duration T have an intensity which greatly exceeds the saturation intensity of the absorber whose relaxation time is τ_r

$$\frac{E_{sig}}{AT} >> \frac{h\nu_{sig}}{\sigma^{abs}\tau_r} \tag{4.24}$$

which, when combined with Eq. 4.23 translates to the condition

$$\sigma_{abs}NL >> \delta \frac{T}{\tau_r} \tag{4.25}$$

To prevent ASE transmission, especially following the signal pulse bleaching, we require a *fast* saturable absorber, preferably with $\tau_r \sim T$. For high gain cells ($\gtrsim 10^5$) we also require the attenuation preferably to be $\lesssim 10^{-5}$ which means $\sigma^{abs}NL \gtrsim 12$. With these conditions, Eq. 4.25 is always satisfied for any reasonable value of δ. The primary requirement then becomes Eq. 4.23 which means that the signal must be *focussed down* onto the saturable absorber.

We have been assuming that a pulse with its leading edge "truncated" by a saturable absorber has a sharp enough leading edge such that compression occurs upon saturated amplification. Consider a pulse with an exponential leading edge incident

upon a saturable absorber which is followed by a high gain amplifier cell. Since the small signal transmission of the absorber transmits a small but still exponential leading edge, then if the amplifier cell had an extremely large gain, we could expect pulse broadening since the condition Eq. 2.81 would not be satisfied. However, for reasonable and finite gain such that the amplified pulse maximum occurs near the point where the saturable absorber transmission bleaches through, we expect pulse compression if the saturable absorber punch-through is "hard" enough. The exact meaning of "hard" depends in detail on the gain level, input signal shapes and saturable absorber attenuation and can be verified numerically.

A numerical calculation was performed for the hypothetical three stage amplifer system shown in Fig. 4.5. The method of calculation is as follows. For the amplifier cells, the "long" radiative lifetime of the gain medium is ignored on the picosecond timescale of the signal pulse duration which means that Eq. 3.21 is used. For the saturable absorbers, Eq. 3.20 with $\varphi_{10}(t) = 0$ is used

$$\frac{dG}{dt} = v_g(\sigma_2^{em} + \sigma_2^{abs})\varphi_{20}(t)G(G-1) - \frac{1}{\tau_r}G[\,\ln G + \sigma_2^{abs}NL\,] \qquad (4.26)$$

For convenience, we assume that in the gain medium $\sigma_2^{em} \equiv \sigma = 4\text{x}10^{-16}\text{cm}^2$ and $\sigma_2^{abs} = 0$, while in the saturable absorber $\sigma_2^{abs} \equiv \sigma = 4\text{x}10^{-16}\text{cm}^2$ and $\sigma_2^{em} = 0$; these are typical numerical values for organic dyes[13].

Eq. 3.21 with the input signal gives the instantaneous gain for the first amplifier cell. This is multiplied by the input signal and is then used as the input signal to the saturable absorber whose instantaneous "gain" evolution is described by Eq. 4.26. This result is then used as the input to the next amplifer cell, etc. We denote the first amplifier cell gain by G_1 , then the *combined* gain of the first amplifier cell and the first saturable absorber by G_2 , the *combined* gain of the first amplifier cell and saturable absorber *and* second amplifier cell as G_3 , etc. This continues so the system "gain" at any of the five points shown in Fig. 4.5 is given by the appropriately

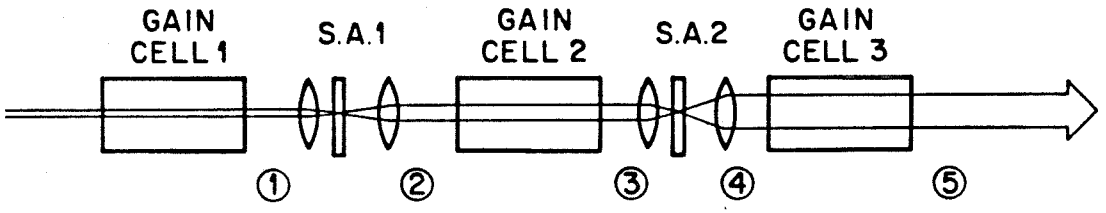

Figure 4.5 Hypothetical three stage amplifier system geometry with saturable absorber isolation between stages.

labeled gain G_i , with the final net amplification of the entire system given by $G_5(t)$. The evolution of these gains is then described by the coupled system of nonlinear equations

$$\frac{dG_1}{dt} = f_1(1, G_1) \tag{4.27}$$

$$\frac{dG_2}{dt} = \frac{G_2}{G_1}\frac{dG_1}{dt} + G_1 f_2\left(G_1 , \frac{G_2}{G_1}\right) \tag{4.28}$$

$$\frac{dG_3}{dt} = \frac{G_3}{G_2}\frac{dG_2}{dt} + G_2 f_1\left(G_2 , \frac{G_3}{G_2}\right) \tag{4.29}$$

$$\frac{dG_4}{dt} = \frac{G_4}{G_3}\frac{dG_3}{dt} + G_3 f_2\left(G_3 , \frac{G_4}{G_3}\right) \tag{4.30}$$

$$\frac{dG_5}{dt} = \frac{G_5}{G_4}\frac{dG_4}{dt} + G_4 f_1\left(G_4 , \frac{G_5}{G_4}\right) \tag{4.31}$$

where

$$f_1(x, y) = v_g \sigma \varphi_{20}(t) xy(y - 1) \tag{4.32}$$

and

$$f_2(x, y) = v_g \sigma \varphi_{20}(t) xy(y - 1) - \frac{1}{\tau_r} y[\, \ln y + \sigma NL \,] \tag{4.33}$$

In this calculation the input pulse is taken to have a sech^2 intensity profile with FWHM pulse width of T.

$$v_g \sigma \varphi_{20}(t) = \frac{E_{sig} \sigma \ln(\sqrt{2} + 1)}{h\nu_{sig} T} \mathrm{sech}^2\left(\frac{t 2\ln(\sqrt{2} + 1)}{T}\right) \tag{4.34}$$

The parameters used were T = 3 psec, $E_{sig} = 1 \times 10^{-9}$J, and $\tau_r = 5$ psec. The beam diameters at the first, second and third amplifier cells were 1.5 mm, 2.5 mm and 5.0 mm respectively, while the beam diameters at the first and second saturable absorber were 100 μm and 500 μm respectively. The initial gains of all three amplifier cells were taken to be 10^4 while the initial saturable absorber attenua-

tions were both taken at 10^{-8} so the initial conditions applied to Eqs. 4.27-31 become

$$G_1(t \to -\infty) = 10^4 \qquad G_2(t \to -\infty) = 10^{-4}$$
$$G_3(t \to -\infty) = 1 \qquad G_4(t \to -\infty) = 10^{-8} \qquad (4.35)$$
$$G_5(t \to -\infty) = 10^{-4}$$

We can analytically compute the actual gain of the first amplifier cell using Eq. 3.24 to be 7.62×10^3 so some saturation has occurred even at this stage with the nanojoule input signal. We then compute the value of δ using Eq. 4.23 to be $\delta = 0.16$, so the first sixth of the pulse would be consumed in inverting the first saturable absorber if τ_r were infinite. Assuming the remaining $(1 - \delta)$ gets through, we again apply Eq. 3.24 and thus estimate the actual gain of the second amplifier cell to be ~ 47. Then at the second saturable absorber, we estimate $\delta \approx 0.10$ by using Eq. 4.23 again. If we suppose the remaining 90% propagates to the third amplifier cell (although the finite τ_r makes these estimates only approximate) we apply Eq. 3.24 to estimate the third stage gain at 6.5. Thus the second and especially the third stage are extremely saturated. The final output energy is then estimated to be 1.77 mJ, and since a significant fraction of the pulse has been sharply truncated after the first and second amplifier cells, we expect a significant pulse compression to occur.

From the numerical integration of Eqs. 4.27-31 the pulse energies at the points 1 - 5 in Fig. 4.5 were 7.62×10^{-6}J, 5.07×10^{-5}J, 2.92×10^{-4}J, 2.42×10^{-4}J and 1.70×10^{-3}J respectively, which is quite close to the estimated values. The gains of the first, second and third amplifier cells are then 7.62×10^3, 57.6 and 7.0 which shows the expected extreme saturation from the initial gains of 10^4 in each cell.

Perhaps the most outstanding feature of the numerical integration is the extreme pulse compression which occurs, demonstrating that in principle the

saturable absorbers produce sufficiently "sharp" leading edges at this gain level. Fig. 4.6 shows the pulse profiles at the input and a points 1, 3 and 5 in Fig. 4.5. The final pulse FWHM is $T_{final} \lesssim 0.2$ psec with a shape resembling a one-sided exponential pulse. Fig. 4.7 shows the *autocorrelations* of the intensity profiles at the same points, defined as

$$G^{(2)}(\tau) \equiv \frac{\int_{-\infty}^{\infty} I(t)I(t+\tau)dt}{\int_{-\infty}^{\infty} I^2(t)dt} \tag{4.36}$$

This is shown because it is the experimentally measured quantity as will be explained in Chapter 5.

In this section we have just assumed values for the initial gains (initial in the leading edge traveling wave sense) and the calculation of the expected gain levels is deferred until section 4.5. However, we can conclude that on the basis of the T.W. rate equations for a simple "quasi two-level" gain medium and saturable absorbers, a significant pulse compression and extreme shape distortions should occur.

We now consider what effects might modify this conclusion. We must examine effects which were not included in the T.W. rate equation derivation in Chapter 2 or the approximations which were made at that point. One candidate for pulse *broadening* mechanisms is the dispersive properties of the dye solvent.

To discuss linear dispersive effects, we use standard linear propagation theory[14], in which case the dispersion of the material is characterized by the frequency dependent wave vector $k(\omega) \equiv \frac{n(\omega)\omega}{c}$ where $n(\omega)$ is the index of refraction of the material. We could analyze this problem in the time domain as was done at the beginning of Chapter 2, but it is easier to stay in the frequency domain in this case. Given a forward propagating wave

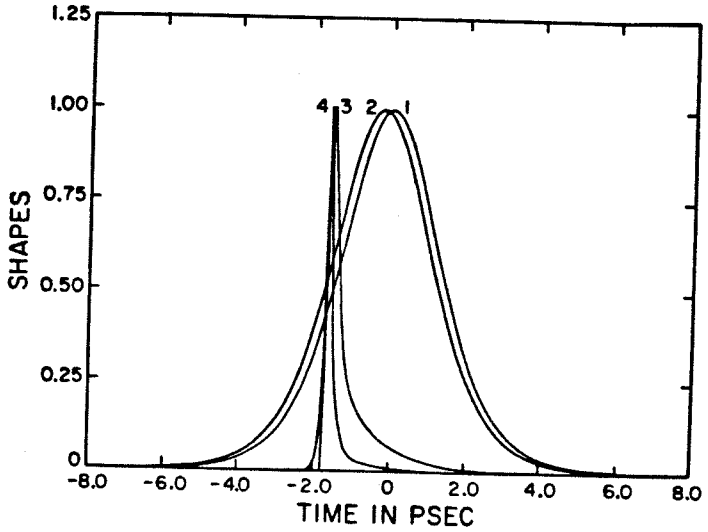

Figure 4.6 Calculated pulse shape upon propagation through hypothetical amplifier chain. Curves 1-4 represent the input and after each of the three successive stages. Energies and parameters used in calculation are given in text.

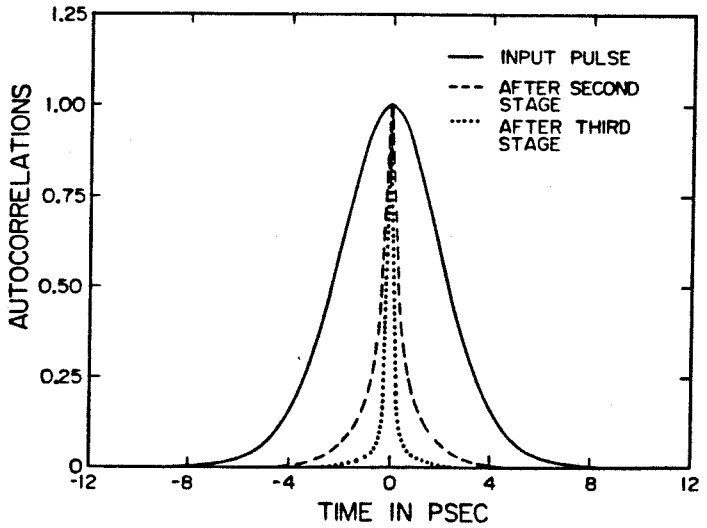

Figure 4.7 Calculated autocorrelations at different points through hypothetical amplifier chain. chain. Curves 1-3 are the input and after the second and third stages, respectively. For parameters used in calculation, see text.

$$E(z, t) = \frac{1}{2}\mathcal{E}(z, t)\, e^{i(k_1 z - \omega_1 t)} \tag{4.37}$$

where $k_1 \equiv k(\omega_1)$, the envelope $\mathcal{E}(z, t)$ at z is related to the envelope $\mathcal{E}(z = 0, t) \equiv \mathcal{E}_0(t)$ at $z = 0$ by

$$\mathcal{E}(z, t) = e^{-i(k_1 z - \omega_1 t)} \frac{1}{2\pi} \int_{-\infty}^{\infty} e^{i(k(\omega) z - \omega t)} \tilde{\mathcal{E}}_0(\omega - \omega_1)\, d\omega \tag{4.38}$$

where

$$\tilde{\mathcal{E}}_0(\Omega) \equiv \int_{-\infty}^{\infty} e^{i\Omega t'} \mathcal{E}_0(t')\, dt' \tag{4.39}$$

It is convenient to lump the pulse broadening characteristics into one parameter for the material as a first approximation. To this end, we extend the series expansion Eq. 2.6 one level higher to obtain

$$k(\omega) = k(\omega_1 + \Omega) = k_1 + \frac{\Omega}{v_g} + \frac{a\Omega^2}{v_g^2} + \cdots \tag{4.40}$$

where $v_g \equiv \left[\left. \frac{\partial k}{\partial \omega} \right|_{\omega_1} \right]^{-1}$ as before, and $a \equiv \frac{1}{2} v_g^2 \left. \frac{\partial^2 k}{\partial \omega^2} \right|_{\omega_1}$ is a parameter which characterizes the group velocity dispersion for the material, and $\Omega \equiv (\omega - \omega_1)$. We assume that $\mathcal{E}_0(t)$ is slowly varying enough in t that we can terminate the series Eq. 4.40 at second order in Ω; this series is inserted in Eq. 4.38, along with the integral expression for $\tilde{\mathcal{E}}_0(\Omega)$ given by Eq. 4.39 to obtain

$$\mathcal{E}(z, t) = \int_{-\infty}^{\infty} dt' \mathcal{E}_0(t') \left[\frac{1}{2\pi} \int_{-\infty}^{\infty} d\Omega\; e^{i\Omega\left(\frac{z}{v_g} - t + t'\right) + i\frac{\Omega^2}{v_g^2} a z} \right] \tag{4.41}$$

and completing the integral in the large brackets provides the desired "linear shift invariant filter" relation between $\mathcal{E}_0(t)$ and $\mathcal{E}(z, t)$

$$\mathcal{E}(z, t) = \int_{-\infty}^{\infty} dt' \mathcal{E}_0(t')\, h_z(t - t') \tag{4.42}$$

where

$$h_z(\xi) \equiv \frac{v_g\, e^{i\frac{\pi}{4}}}{\sqrt{4\pi a z}}\, e^{-i\frac{v_g^2(\xi - \frac{z}{v_g})^2}{4az}} \tag{4.43}$$

As a typical example[15], suppose the input electric field envelope is Gaussian such that the pulse *intensity* has a FWHM of T.

$$\mathcal{E}_0(t) = \mathcal{E}_0\, e^{-\frac{2\ln 2\, t^2}{T^2}} \tag{4.44}$$

Upon executing the integral in Eq. 4.42 we obtain

$$\mathcal{E}(z, t) = \mathcal{E}_0\Big(1 - \frac{8iaz\ln 2}{v_g^2 T^2}\Big)^{-\frac{1}{2}} \exp\Big[-\frac{2\ln 2(t - \frac{z}{v_g})^2}{T^2\big(1 - \frac{8iaz\ln 2}{v_g^2 T^2}\big)}\Big] \tag{4.45}$$

in which case the intensity becomes

$$I(z, t) \propto |\mathcal{E}(z, t)|^2 = \mathcal{E}_0^2 \frac{T}{\tilde{T}(z)}\, e^{-\frac{4\ln 2(t - \frac{z}{v_g})^2}{\tilde{T}^2(z)}} \tag{4.46}$$

where $\tilde{T}(z)$ is the new z dependent increasing pulse width,

$$\tilde{T}(z) = T\Big[1 + \Big(\frac{8az\ln 2}{v_g^2 T^2}\Big)^2\Big]^{\frac{1}{2}} \tag{4.47}$$

We then see that a typical distance over which the pulse width doubles in duration is given by the result

$$L_{\text{double}} = \frac{\sqrt{3}(v_g T)^2}{8a\ln 2} \tag{4.48}$$

In ethyl alcohol, for example, from standard index of refraction vs. wavelength data[16] we can calculate at 6000 Å

$$a \approx 1.0\text{x}10^{-7}\text{cm} \quad \text{and} \quad v_g = 2.20\text{x}10^{10}\text{cm/sec} \tag{4.49}$$

For a 1 psec pulse we then obtain from Eq. 4.45 the result $L_{double} = 1514$ cm . For a 0.2 psec pulse, however, $L_{double} = 61$ cm , and so at extremely short pulse durations some solvent dispersive effects become significant. Also, for many other solvents the parameter a is larger than the ethanol value[16].

We also have contributions to pulse broadening from the dye molecules themselves. These can be categorized into two effects. The first results from "dispersive" effects which occur from non-zero values of T_2 . Since the interaction with the dye molecules is so nonlinear, however, linear dispersive concepts are not really applicable. As stated in Chapter 2, the full Bloch equations must be used if T_2 becomes comparable to the times of interest. However, crudely speaking, nonzero T_2 results in intertial or "ringing" effects in the molecular polarization with a time scale of T_2 , and we can then expect that pulses should not achieve durations any shorter than T_2 . If we do apply the linear dispersive concepts, we can estimate that a typical contribution from the gain medium itself might be

$$\left.\frac{\partial^2 k}{\partial \omega^2}\right|_{\omega_1} \lesssim \frac{T_2^2 \ln G}{4L} \tag{4.50}$$

where G is the gain of a cell of length L. Applying the previous results yields

$$L_{double} \gtrsim \frac{\sqrt{3}}{\ln 2}\left(\frac{L}{\ln G}\right)\left(\frac{T}{T_2}\right)^2 \tag{4.51}$$

For a typical high gain 10 cm cell, $G \sim 10^4$ and for $T_2 = 10^{-13}$ sec which is a reasonable upper limit for organic dyes, we conclude that a 1 psec pulse would require *270 cm* of gain medium to double. However, for a pulse duration of 0.2 psec, we expect doubling to occur in $\sim$ 11 cm . Again, the value of T_2 for organic dyes is not well known, but clearly group velocity dispersion could play a significant pulse broadening role from both solvent dispersion and dye molecule resonant dispersion.

The second effect mentioned for broadening from the dye molecules themselves occurs from finite vibrational relaxation rates, which is an *energy* relaxation rather than the *phase* relaxation which is given by T_2. Referring to Fig. 2.1, in converting the dye molecule to a "quasi two-level" system, we assumed that the vibrational relaxation from S_1^* to S_1 and from S_0^* to S_0 was infinitely fast. Consider pump absorption from S_0 to S_1^* at some frequency with a cross section σ. If the density of states at these two levels were roughly equal, then the stimulated emission from S_1^* to S_0 would be governed by the same cross section and would occur at the transition rate given by

$$\frac{1}{T_{trans}} \sim \frac{\sigma I_{pump}}{h\nu_{pump}} \tag{4.52}$$

Typical pump intensities are $\lesssim$ 50 megawatts/cm^2 on our experiments, and for a typical cross section up to 4×10^{-16} cm^2 we obtain from Eq. 4.52 $T_{trans} \gtrsim$ 18.7 psec. Since the vibrational relaxation rates are sub-picosecond, in this case the infinite vibrational relaxation rate appears justified.

However, for the *signal* pulse amplification, the intensities become much higher. The analagous effect here is that, following stimulated emission from S_1 to S_0^*, reabsorption to the S_1 level can occur with the rate given by Eq. 4.52. Assuming a signal energy of 1 mJ in a 5 mm diameter cell, we obtain $T_{trans} \sim T_{pulse}/6$ in this case, where T_{pulse} is the signal pulse width. For sub-picosecond pulses, the transition time easily gets down to the 10^{-13} sec regime, at which point the infinite relaxation rate assumption clearly becomes invalid. We then expect deviations from the simple results predicted by Eqs. 4.27-31 when extreme saturation occurs with a sharp leading edge as shown in Fig. 4.6 at the last stage.

To assess the importance of finite vibrational relaxation rates, we first assume negligible population of the S_1^* state at the arrival time of the signal pulse; we have seen that this is a valid approximation. Then the three levels under consideration

for the signal propagation are S_0 , S_0^* , and S_1 . Rather than considering the complicated nature of the continuum of levels, we adopt a three discrete level model shown in Fig. 4.8. At the signal frequency there is no absorption from S_0 to S_1 , and in this model the finite ensemble average absorption cross section of the dye molecules at the signal frequency results from a thermal population of S_0^* level. Since we are considering only signal propagation, we drop the subscripts 1, 2 on the cross sections and photon densities. The cross section for emission from S_1 to S_0^* is σ_{em} and we denote the absorption cross section from S_0^* to S_1 by the quantity σ_{abs}^* . If the density of states at S_1 and S_0^* were equal we would have $\sigma_{em} = \sigma_{abs}^*$. We refer to the populations of S_0 , S_0^* , and S_1 as N_1 , N_1^* and N_2 respectively for consistency with previous results, and here $N_1 + N_1^* + N_2 = N$, where N is the constant total dye concentration. As stated above, we assume that in equilibrium the population N_1^* is a fraction f of the combined ensemble average N_1 and N_1^* populations. Then the usual quoted ensemble average for absorption at the signal frequency would be given by $\sigma_{abs} = f\sigma_{abs}^*$.

On the picosecond signal time scale we ignore the spontaneous relaxation from S_1 to S_0^*. We assume that vibrational relaxation from S_0^* to S_0 occurs with a time constant given by τ_R which allows us to write the T.W. rate equations

$$\frac{\partial \varphi}{\partial t} + v_g \frac{\partial \varphi}{\partial z} = v_g(\sigma_{em}N_2 - \sigma_{abs}^*N_1^*)\,\varphi \tag{4.53}$$

$$\frac{\partial N_2}{\partial t} = -\,v_g(\sigma_{em}N_2 - \sigma_{abs}^*N_1^*)\,\varphi \tag{4.54}$$

$$\frac{\partial N_1^*}{\partial t} = v_g(\sigma_{em}N_2 - \sigma_{abs}^*N_1^*)\,\varphi - \frac{1}{\tau_R}[\,N_1^* - (N - N_2)f\,] \tag{4.55}$$

In a manner similar to the earlier derivations in Chapters 2 and 3, it is shown in Appendix A4b that these equations can be combined and reduced again to a single *ordinary* differential equation, but second order in this case.

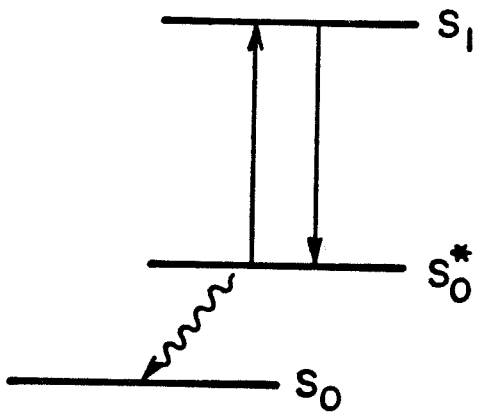

Figure 4.8 Simplified three level model for finite vibrational lifetime τ_R discussion.

$$\frac{d}{dt}\left[\frac{d\ln G}{dt} + (\sigma_{em} + \sigma^{*}_{abs})\varphi_0(t)(G-1) \right]$$

$$+ \frac{1}{\tau_R}\left[\frac{d\ln G}{dt} + (\sigma_{em} + f\sigma^{*}_{abs})\varphi_0(t)(G-1) \right] = 0 \qquad (4.56)$$

Here G(t) is the appropriately retarded gain as given by Eq. 3.19. From Eq. 4.56 we see that if $\tau_R \to \infty$, we again have the same equation Eq. 3.21 for the quasi two-level system, but now the levels are S_0^* and S_1. If $\tau \to 0$ on the other hand, we have a two-level system equation with $\sigma_{em} + f\sigma^{*}_{abs} = \sigma_{em} + \sigma_{abs}$ which was the original assumption in Chapter 2.

We then repeat the entire amplifier chain calculation using Eq. 4.56 for the gain cells rather than Eq. 3.21.The parameters used were the same as used in the previous integration of Eq. 4.27-31 and for simplicity we assume that $f = 0$ and $\sigma^{*}_{abs} = \sigma_{em} = 4\text{x}10^{-16}\text{cm}^2$. The value of τ_R was chosen to be 0.25 psec. From this calculation, the pulse energies at the points 1 - 5 in Fig. 4.5 had the values $7.48\text{x}10^{-6}$J, $4.23\text{x}10^{-6}$J, $2.75\text{x}10^{-4}$J, $2.23\text{x}10^{-4}$J, and $1.55\text{x}10^{-3}$J respectively. The energies are thus only slightly lower than the $\tau_R \to 0$ calculation. The important effect can be seen on the pulse shapes. Fig. 4.9 shows the normalized pulse shapes at the input and at points 1, 3, and 5 in Fig 4.5, while Fig. 4.10 shows the intensity autocorrelations. These should be compared with Figs. 4.6-7 for $\tau_R \to 0$. The final output pulse shows an easily discernible increase in the relative amount of energy located in the "base" of the pulse. This is also apparent from the broadened nature of the autocorrelation even for τ as small as 0.25 psec.

This effect is easily understood on a qualitative basis. When the intense leading edge of the pulse is incident on the gain medium, the re-absorption time from Eq. 4.52 is very short. The behavior then is essentially that of a two-level system between the S_0^* and the S_1 levels with equal cross sections for emission and absorption. In this case, complete saturation occurs when $N_1^* = N_2$, and only *half* the

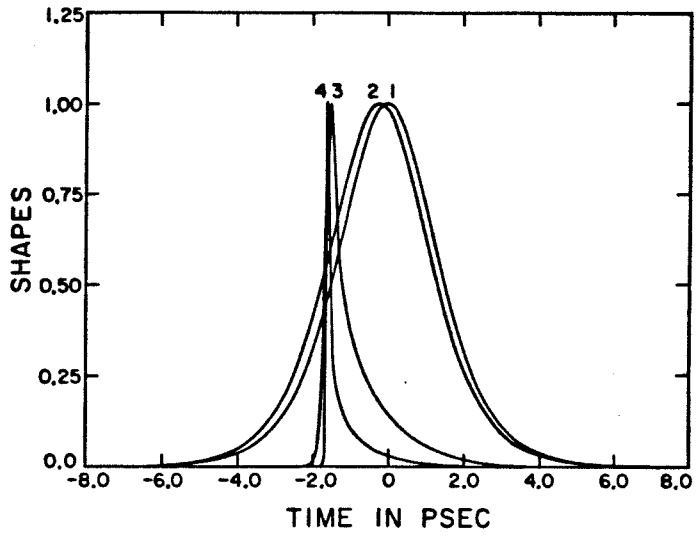

Figure 4.9 Calculated pulse shape upon propagation through hypothetical amplifier chain with finite vibrational lifetime of τ_R = 0.25 psec. Curves 1-4 represent the input and after each of the three successive stages. Energies and parameters used in calculation are given in text.

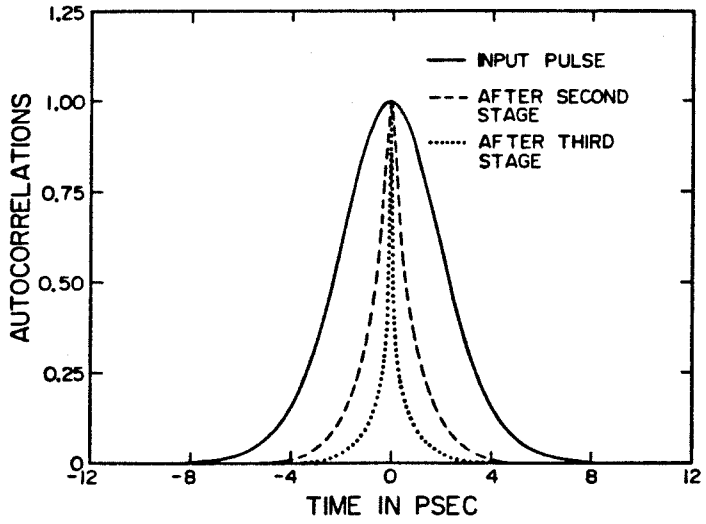

Figure 4.10 Calculated autocorrelations at different points through hypothetical amplifier chain with finite vibrational lifetime of τ_R = 0.25 psec. chain. Curves 1-3 are the input and after the second and third stages, respectively. For parameters used in calculation, see text.

available inversion energy can be removed. The other half can only be extracted after the S_0^* population has decayed to S_0 with a time constant τ_R. This "bottle-neck" effect thus will eventually result in pulses with ~ half of the pulse energy located in a base a few τ_R in duration. The extremely sharp initial spike results from the extra large effective cross section sum between S_0^* and S_1 which makes the initial saturation more rapid than the $\tau_R \to 0$ case.

As mentioned earlier, dispersive solvent effects and finite T_2 effects will tend to wash out the sharp spikes predicted from the T.W. rate equations. We thus finally expect pulses which may attain overall widths $\gtrsim \tau_R$ with spikes on the order of T_2 under extreme saturation conditions in organic dyes.

4.4 Angular Hole Burning and Quantitative Energy Gain

In this section we include some effects which modify the nature of gain saturation through the amplifier chain, and aid in getting a quantitative understanding of the final pulse energies which can be generated[9]. Eq. 3.24 is the usual result quoted for short pulse saturation behavior, but it assumes an ensemble of dye molecules all with the same cross sections $\sigma_{em,\,abs}$. If we assume the dye molecule has a well defined axis for its dipole transition moment[17] and a linearly polarized incident beam, we would actually have for a given molecule

$$\sigma_{em,\,abs} \to \sigma_{em,\,abs}(x) = 3\bar{\sigma}_{em,\,abs}\, x^2 \tag{4.57}$$

where $x = \cos\vartheta$ and ϑ is the angle between the dipole axis of the molecule and the signal polarization. Here $\bar{\sigma}_{em,\,abs}$ are the usual quoted angularly averaged values of the cross sections. We must then also take into account the angular distribution of excited dye molecules, $N_{1,2} \to N_{1,2}(x)$, while the overall dye concentration N maintains an isotropic angular distribution. If we consider only the short time scale behavior, we ignore pumping and look only at the signal propagation, replacing Eqs.

2.28-30 with

$$\frac{\partial \varphi}{\partial t} + v_g \frac{\partial \varphi}{\partial z} = \frac{3 v_g}{2} \int_{-1}^{1} [\, \bar{\sigma}_{em} N_2(x) - \bar{\sigma}_{abs} N_1(x) \,] \, x^2 dx \; \varphi \tag{4.58}$$

$$\frac{\partial N_1(x)}{\partial t} = 3 v_g [\, \bar{\sigma}_{em} N_2(x) - \bar{\sigma}_{abs} N_1(x) \,] \, x^2 \, \varphi \tag{4.59}$$

$$\frac{\partial N_2(x)}{\partial t} = - \frac{\partial N_1(x)}{\partial t} \tag{4.60}$$

Making the usual change of variables to local " time ", $\xi \equiv v_g t - z$ we have

$$\frac{\partial \varphi}{\partial z} = \frac{3}{2} \int_{-1}^{1} \Delta \; x^2 dx \; \varphi \tag{4.61}$$

$$\frac{\partial \Delta}{\partial \xi} = - 3 [\, \bar{\sigma}_{em} + \bar{\sigma}_{abs} \,] x^2 \, \Delta \, \varphi \tag{4.62}$$

where $\Delta = [\, \bar{\sigma}_{em} N_2(x) - \bar{\sigma}_{abs} N_1(x) \,]$.

Here we note two circumstances where we can make a very simple approximation. If Δ were initially isotropic in x and the signal were to deplete the inversion only slightly, Δ would remain roughly isotropic in x. Alternatively, if the absorption or stimulated emission occurs on a time scale slow compared to orientational relaxation times (as might occur in pumping processes) then Δ would also remain isotropic. In either case we approximate Δ with a quantity $\tilde{\Delta}$ which is independent of x to obtain

$$\frac{\partial \varphi}{\partial z} = \tilde{\Delta} \, \varphi \tag{4.63}$$

$$\frac{\partial \tilde{\Delta}}{\partial \xi} = - \frac{9}{5} [\, \bar{\sigma}_{em} + \bar{\sigma}_{abs} \,] \, \tilde{\Delta} \, \varphi \tag{4.64}$$

These are identical to the ordinary rate equations, except we would change the results derived from Eq. 3.20 by simply letting

$$[\, \sigma_{em} + \sigma_{abs} \,] \rightarrow \frac{9}{5} [\, \bar{\sigma}_{em} + \bar{\sigma}_{abs} \,] \tag{4.65}$$

We refer to this approximation to the effects of angular hole burning as the

"modified" theory. This approximation says that the gain is depleted (or excited, if we had been discussing a pumping process) as if the molecules had cross sections $\frac{9}{5}$ as large as the ensemble average, and the effect occurs because the molecules which are oriented to make the largest contribution to the gain are the first ones to be depleted (or excited).

Returning to the exact treatment, it is shown in Appendix A4c that the set of equations Eqs. 4.61-2 integrates out to yield the result for the net energy gain

$$\frac{S}{\ln G_o} \int_1^{G_{actual}} \frac{d\xi}{\left[1 - \left(\frac{\pi}{12S\xi}\right)^{\frac{1}{2}} \mathrm{erf}(\sqrt{3S\xi})\right]} = 1 \qquad (4.66)$$

where $S = \frac{E_{sig}(\bar{\sigma}_{em} + \bar{\sigma}_{abs})}{h\nu_{sig}A}$ just as before. Eq. 4.66 is analagous to the simpler Eq. 3.24 but includes angular hole burning.

Fig. 4.11 compares the results of Eq. 3.24, Eq. 3.24 with the $\frac{9}{5}$ modification and Eq. 4.66 for a hypothetical amplifier cell with an initial gain $G_o = 10^5$ and a typical cross section value of $(\bar{\sigma}_{em} + \bar{\sigma}_{abs}) = 4\times10^{-16}\mathrm{cm}^2$. The deviation from the simple theory can be as much as ~ 2.5 dB, and even the simple $\frac{9}{5}$ modified result is a sizeable improvement, especially in the mildly saturated regime as expected. Fig. 4.12 shows the analagous result for a saturable absorber with an initial attenuation of 10^{-6}.

For quantitative comparison with the experimental results of Chapter 5 we also include triplet losses, for simplicity assuming the initial inversion and triplet populations are approximately uniform in z. As shown in Appendix A4c, Eq. 4.66 then is modified to

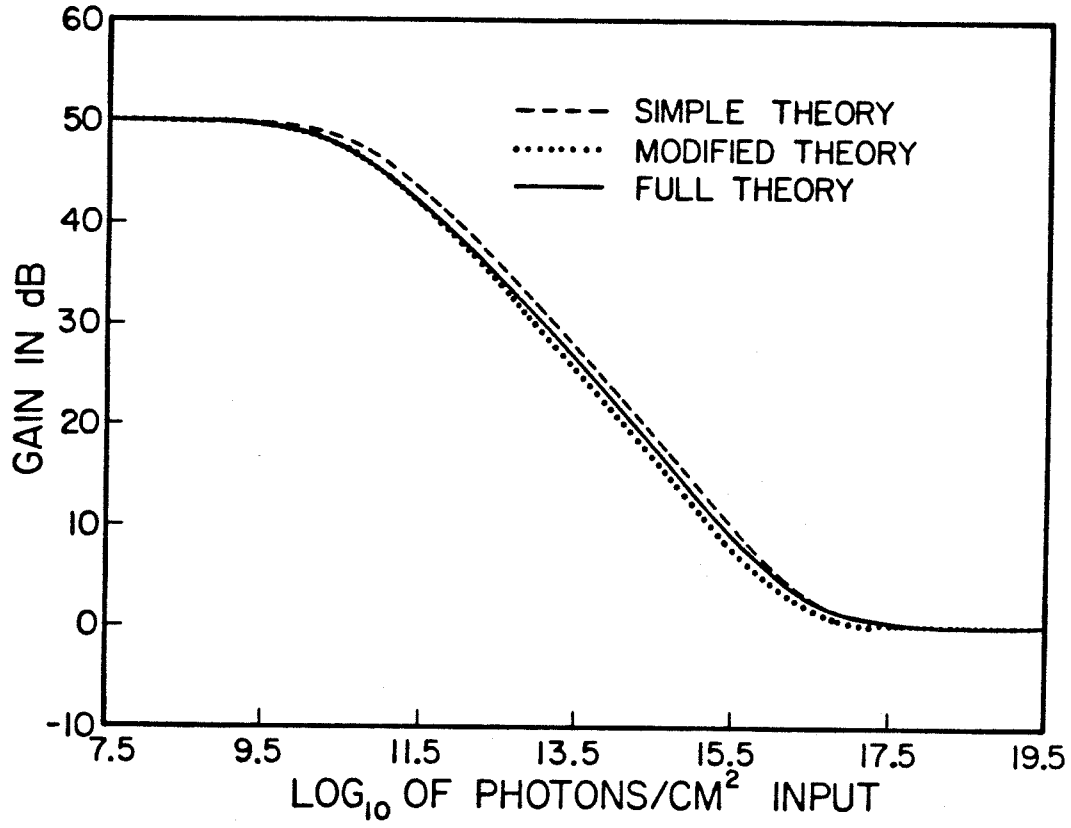

Figure 4.11 Saturation behavior for a hypothetical amplifier stage with $G_o = 10^5$ and $(\bar{\sigma}_{em} + \bar{\sigma}_{abs}) = 4 \times 10^{-16}$. The dashed curve represents Eq. 3.24, the dotted curve is Eq. 3.24 with the $\frac{9}{5}$ modification, and the solid curve is the exact result, Eq. 4.66.

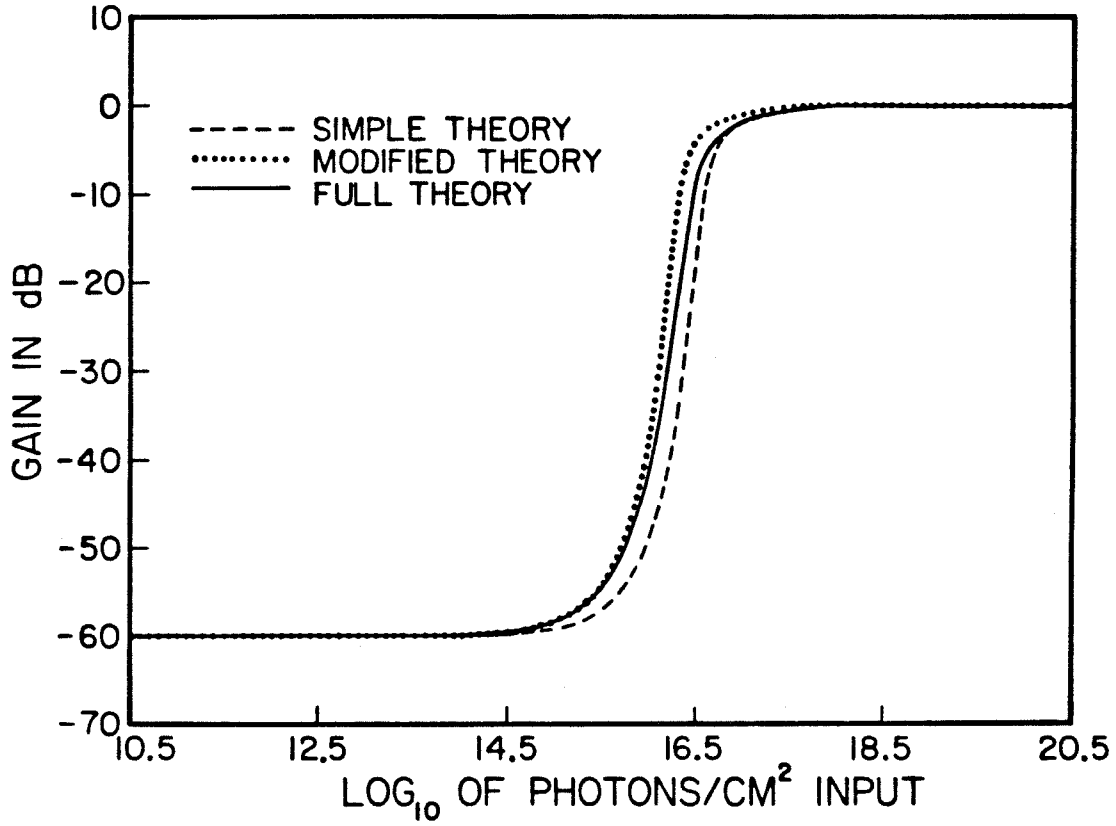

Figure 4.12 Saturation behavior for a hypothetical saturable absorber with $G_o = 10^{-6}$ and $(\bar{\sigma}_{em} + \bar{\sigma}_{abs}) = 4 \times 10^{-16}$. The dashed curve represents Eq. 3.24, the dotted curve is Eq. 3.24 with the $\frac{9}{5}$ modification, and the solid curve is the exact result, Eq. 4.66.

$$\frac{S}{\ln G_o}\int_1^{G_{actual}} \frac{d\xi}{\left[1-(1-\alpha)\frac{\beta}{\alpha}-(1-\beta)\left(\frac{\pi}{12S\xi}\right)^{\frac{1}{2}}\mathrm{erf}(\sqrt{3S\xi})+\frac{\beta}{\alpha}\left(\frac{\pi}{12S\xi\alpha}\right)^{\frac{1}{2}}\mathrm{erf}(\sqrt{3S\xi\alpha})\right]} = 1 \qquad (4.67)$$

Here $\beta \equiv -\frac{\ln R_0}{\ln G_0}$ where R_0 is the initial or leading edge loss factor due to triplet absorption, and $\alpha \equiv \frac{\overline{\sigma}_{trip\ abs}}{(\overline{\sigma}_{em}+\overline{\sigma}_{abs})}$.

4.5 Dynamical Gain Calculations with Triplet Losses

To analyze the pumping process, we note that Eq. 4.18 now has the depleting effect of amplified spontaneous emission (ASE) included, but leaves out the effects of angular hole burning and triplet state population build-up. For the pumping process, it is adequate to use the 9/5 "modified" result as mentioned in the last section. The inclusion of the triplet state population build-up can also be included in a straightforward manner, and this is outlined in Appendix A4d. The principal effect of the triplet state population is to increase the losses for the signal pulse propagation. Referring to Fig. 2.1, we see that the triplet state population begins to accumulate by inter-system crossing as soon as the upper singlet state first becomes populated. This results in an increase in the losses at later times resulting from absorption by the triplet state population to upper triplet levels. The result from Appendix A4d is the replacement of the single differential equation Eq. 4.18 with the pair of equations

$$\frac{dG_o}{dt} = \frac{9}{5}\nu_g(\sigma_2^{sm} + \sigma_2^{sbs})\, G_o\, \varphi_{10}(t)\Big[1 - e^{-\sigma NL} G_o^{\gamma} R^{-\left[\gamma + \frac{\varepsilon}{\sigma_{trip\ abs}}\right]}\Big] \qquad (4.69)$$

$$- \Big[\frac{1}{\tau_{eff}} + \frac{1}{\tau_{trip}} \frac{(\sigma_{trip\ abs} + \sigma_2^{sm})}{(\sigma_2^{sm} + \sigma_2^{sbs})}\Big] G_o\Big(\ln G_o + \sigma_2^{sbs} NL + \frac{(\sigma_2^{sbs} - \sigma_{trip\ abs})}{\sigma_{trip\ abs}} \ln R \Big)$$

$$\frac{dR}{dt} = -\frac{R}{\tau_{trip}(\sigma_2^{sm} + \sigma_2^{sbs})}[\sigma_{trip\ abs} \ln G_0 + (\sigma_2^{sbs} - \sigma_{trip\ abs}) \ln R + \sigma_{trip\ abs}\sigma_2^{sbs} NL\,] \qquad (4.70)$$

where R is the reduction factor of the gain due to absorption from the triplet state, and τ_{trip} is the triplet crossing time, and $\sigma^{trip\ abs}$ is the absorption cross section from the triplet state T_0. We have already modified the exact result by letting $\tau \rightarrow \tau_{eff}$ where τ_{eff} given by Eq. 4.17 approximates the effects of ASE depletion. We use the set of equations Eqs. 4.69-70 as the full description of the longitudinal pumping process.

A number of points have already been addressed to some extent in earlier chapters. To reduce the sensitivity of the gain on the relative timing of the pump and signal pulses, it is desirable to achieve a steady state, which inherently requires energy dissipation after a certain point in time. There are two important features which accomplish this and effectively put a "ceiling" on the gain. One is the strong dependence of τ_{eff} on gain and the second is the fact that once the pump has longitudinally bleached all the way through the dye cell, no further gain can result. Both of these effects make a "steady state" obtain rapidly and make pulse timing less critical.

The results of numerical calculations employing Eqs. 4.69-70 are shown in Figures 4.13 and 4.14. The curves show the input pump pulse, the transmitted pump pulse at the end of a hypothetical amplifier cell, the triplet state gain reduction factor R described above, and the small signal gain of the cell (which includes the reduction factor R). The parameters used in these calculations are as follows: The pump pulse was taken to be Gaussian with a FWHM of 5 nsec, which was also the value taken for lifetime of the dye τ. The emission cross section at the signal

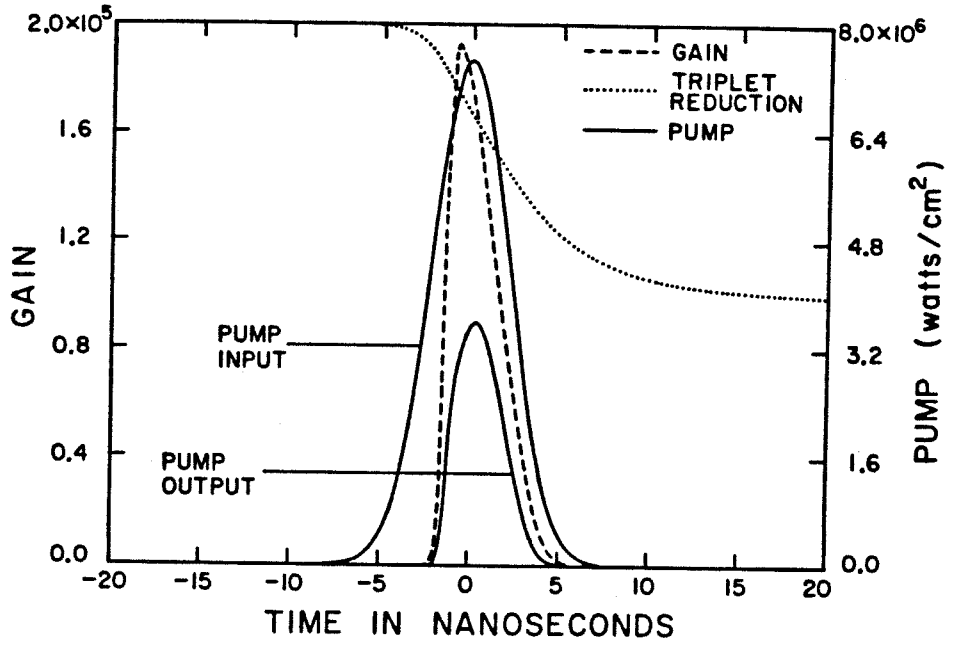

Figure 4.13 Full dynamic gain calculation including ASE depletion and triplet losses for a Gaussian pump pulse. Gain is the actual gain including the triplet loss reduction factor. Curves here are for a 4 mm diameter active region in a 10 cm long cell; for values of other parameters see text.

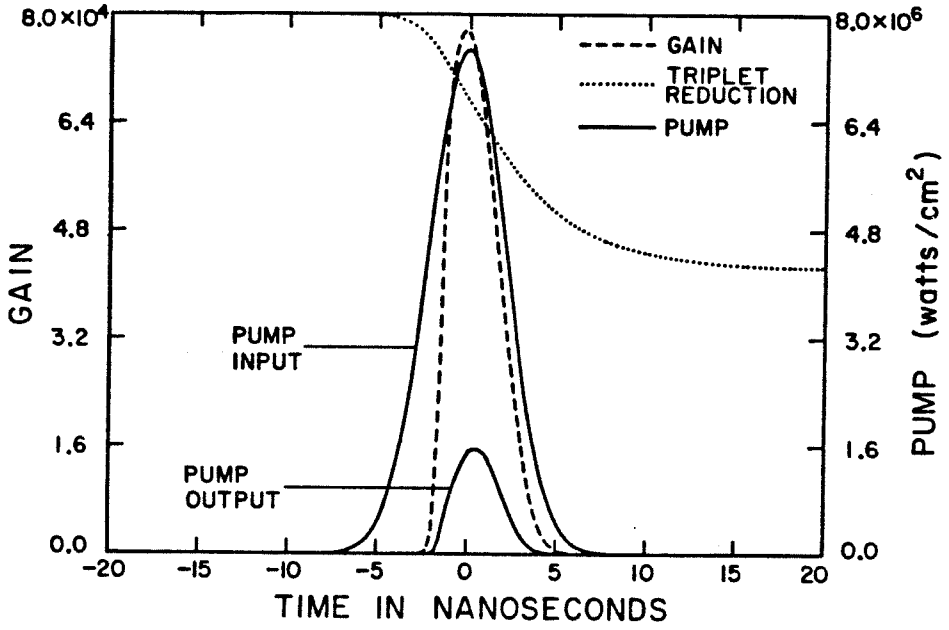

Figure 4.14 Full dynamic gain calculation, with all parameters identical to those in Fig. 4.13 except active cell diameter has been increased to 8 mm, thereby affecting the ASE depletion.

frequency was $\sigma_2^{em} = 3.5x10^{-16}cm^2$, while at the pump frequency $\sigma_1^{em} = 0$. The absorption cross sections were $\sigma_2^{abs} = 5.0x10^{-17}cm^2$ and $\sigma_1^{abs} = 3.5x10^{-16}cm^2$. The cell length was taken as 10 cm while the dye concentration was set at $4.5x10^{15}cm^{-3}$. The triplet absorption cross section was assigned the value $\sigma_{trip\ abs} = 7.5x10^{-17}cm^2$, and the triplet crossing time was taken to be 40 nsec. In both figures 4.13 and 4.14, the same pump energy per unit area was incident on the cell entrance face, and had the value 39.8 mJ/cm^2. However, Fig. 4.13 shows the case where the cell diameter is 4 mm with a pump energy is 5 mJ, while Fig 4.14 shows the case where the cell diameter is 8 mm with a pump energy of 20 mJ.

The effect of the triplet losses is easily seen in both figures. In Fig. 4.13, for example, even after the pump has bleached through fairly well, the gain peaks early and then drops down. This is due to both the increasing triplet absorption and to the smaller supply of dye molecules which are available for the upper S_1 state. The gain then does not have as long a steady region as might have been hoped from the earlier discussion of Figs. 3.4-5. Without any ASE depletion, both Figures would produce identical gains, etc. As is apparent, however, the large diameter cell has significantly less gain and less transmitted pump because of the shorter gain dependent effective lifetime from ASE depletion. In Fig. 4.13, ASE has only a small effect due to the smaller diameter. In Fig. 4.14, on the other hand, ASE has a noticable effect as mentioned above. Not only is the *magnitude* of the gain affected, but the gain has a slightly wider temporal profile due to the limiting nature of τ_{eff}. This was expected and is desirable for timing purposes, but it also implies that energy is wasted in the form of ASE noise.

Appendix A4a

We wish to calculate

$$S(l) = \frac{1}{4\pi l^2 V}\int_V d^3x \int_V d^3x'\, \delta(l - |\vec{x} - \vec{x}'|) \qquad \text{(A4a.1)}$$

for various volumes V. For the $\vec{x}'$ integral, we convert to a local spherical coordinate system with its origin at $\vec{x}$. Then $S(l)$ is given by

$$S(l) = \frac{1}{V}\int_V d^3x \quad \frac{1}{4\pi} \int_{\varphi'_{min}(\vec{x},l)}^{\varphi'_{max}(\vec{x},l)} d\varphi' \int_{\cos\vartheta'_{min}(\vec{x},l)}^{\cos\vartheta'_{max}(\vec{x},l)} d(\cos\vartheta') \qquad \text{(A4a.2)}$$

where we have emphasized that the limits of integration on the angles are in general restricted in a manner which depends on $\vec{x}$ and l. The only values allowed in the range of integration are now those which could be subtended from $\vec{x}$ with a rod of length l while still remaining entirely within the volume V. The interpretation given in the text is then clear; $S(l)$ represents, on the average, the *fraction* of surface area of a sphere of radius l, randomly located in the volume V, which lies *within* the volume V.

For an actual calculation, we will refer to Eq. A4a.2 and to carry out the $\vec{x}$ integral over the volume V where we consider the *fraction* (which is the ramaining two integrals) as some function of l and $\vec{x}$. For a sphere of radius R, we first assume $l < R$. In executing the $\vec{x}$ integral, if $r < (R - l)$, all solid angles are accessible so the contribution from this part of the volume is

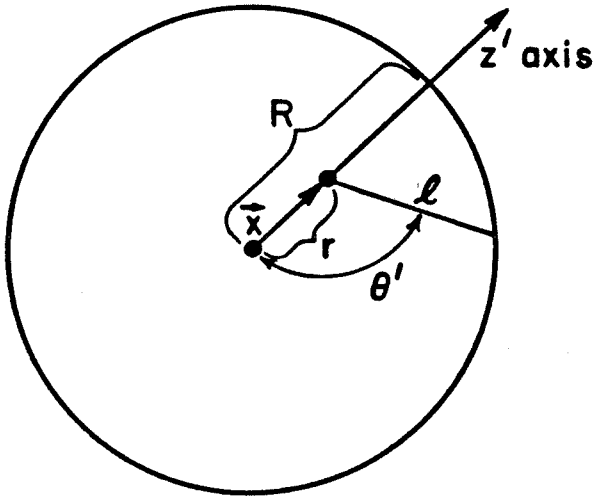

Figure A4a.1 Geometry for calculation of length distribution function in spherical geometry.

$$\frac{\frac{4}{3}\pi(R-\ell)^3}{\frac{4}{3}\pi R^3} \tag{A4a.3}$$

When $r \geq (R-\ell)$, the available solid angle in Eq. A4a.2 becomes restricted. Referring to Fig. A4a.1, we define the local z' axis to be in the direction of the radius vector r of the unprimed coordinate system. We then have

$$\cos\vartheta' = -\frac{R^2 - r^2 - \ell^2}{2r\ell} \tag{A4a.4}$$

and for φ' the full 2π is accessible. The contribution from this part of the volume is then

$$\frac{2\pi}{\frac{4}{3}\pi R^3} \int_{(R-\ell)}^{R} r^2\, dr \int_{\frac{-(R^2-r^2-\ell^2)}{2r\ell}}^{1} d(\cos\vartheta') \tag{A4a.5}$$

When this integral is carried out and added to Eq. A4a.3 the result is

$$S(\ell) = 1 - \frac{3}{2}\left(\frac{\ell}{D}\right) + \frac{1}{2}\left(\frac{\ell}{D}\right)^3 \tag{A4a.6}$$

where D = 2R as quoted in the text. In a similar fashion one shows that this holds also for $R < \ell \leq D$.

The infinite cylinder is much more complicated. Referring to Fig. A4a.2, for every point $\vec{x}$ within the cylinder we again construct the local spherical coordinate system with its z' axis along the radius vector to the wall of the cylinder. In computing the accessible solid angles now we have lost the φ' symmetry. For each φ' we now have $\cos\vartheta'$ contained by an *ellipse*, rather than a circle, with minor axis 2R and major axis $\frac{2R}{\cos\varphi'}$. First assume $\ell < R$. Since the cylinder is infinite, in computing the $\vec{x}$ integral we just look at a unit length Δz. As before, if $\rho < (R-\ell)$, all solid angles are accessible and the contribution from this part is, following Eq. A4a.2

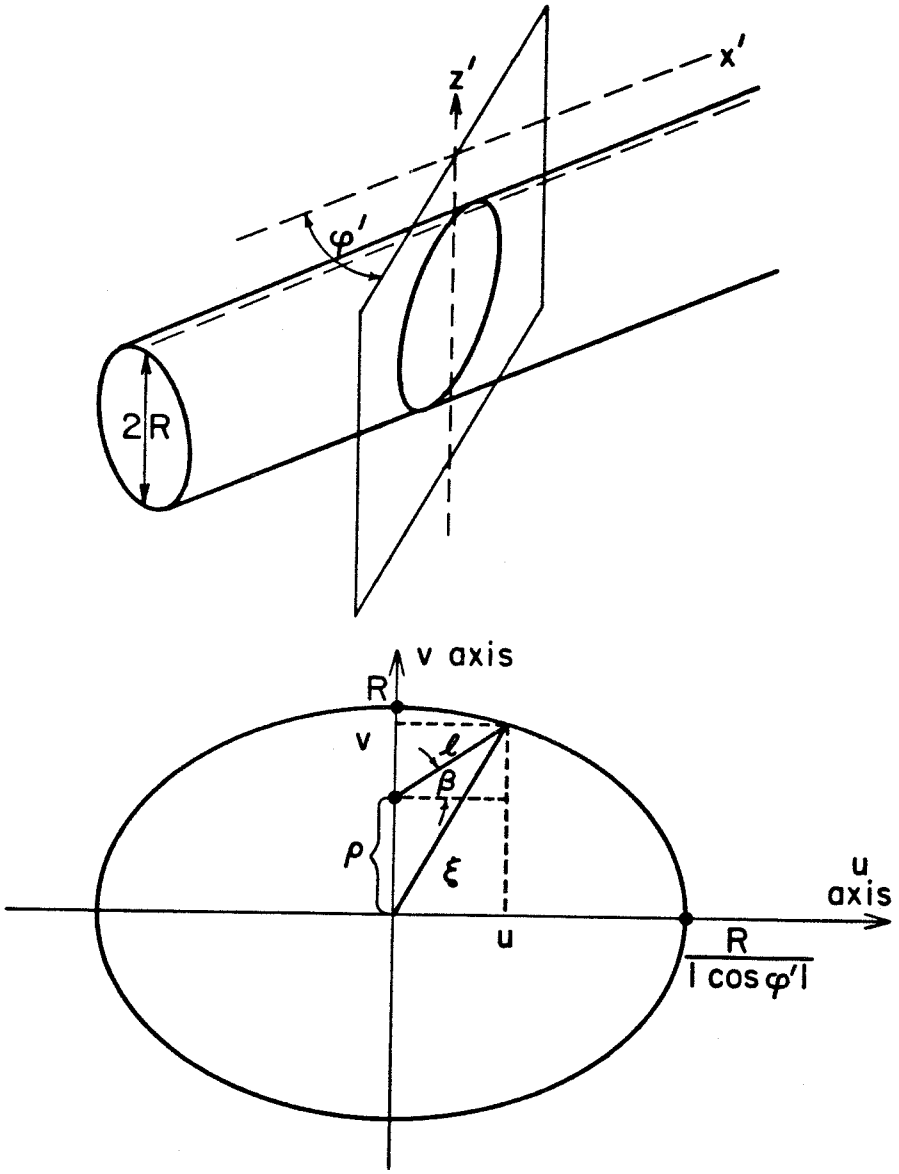

Figure A4a.2 Geometry for calculation of length distribution function in cylindrical geometry.

$$\frac{\pi(R-l)^2\Delta z}{\pi R^2\Delta z} \tag{A4a.7}$$

When $\rho \geq (R-l)$, the accessible solid angle becomes restricted; referring to Fig. A4a.4, we have

$$\frac{u^2}{(\frac{R}{\cos\varphi'})^2} + \frac{v^2}{R^2} = 1 \tag{A4a.8}$$

$$u^2 + v^2 = \xi^2 \tag{A4a.9}$$

$$u = l\cos\beta \tag{A4a.10}$$

$$\xi^2 = l^2 + \rho^2 + 2l\rho\sin\beta \tag{A4a.11}$$

From this we obtain

$$\cos\vartheta'_{\rho,\varphi'} = \cos(\frac{\pi}{2} + \beta) = -\sin\beta \tag{A4a.12}$$

$$= \frac{\rho}{l\sin^2\varphi'}\Big[\, 1 - (\cos^2\varphi' + \frac{R^2}{\rho^2}\sin^2\varphi' - \frac{l^2}{\rho^2}\sin^2\varphi'\cos^2\varphi')^{\frac{1}{2}}\,\Big]$$

The contribution from this portion of the volume then becomes

$$\frac{1}{\pi R^2\Delta z}\frac{\Delta z}{2}\int_0^{2\pi} d\varphi' \int_{(R-l)}^{R} \rho d\rho\Big[\, 1 - \cos\vartheta'_{\rho,\varphi'}\,\Big] \tag{A4a.13}$$

While individual components of this integral diverge, the integrand as a whole is well behaved. In a rather tedious manner, each component is executed in a limiting sense, and cancellation of the divergent terms then yields a finite result. When this is added to the contribution Eq. A4a.7, the result is

$$S(l) = 1 + \frac{4}{3\pi}\Big[\frac{l}{D}\Big]F(\frac{l}{D}) \qquad \text{if } l < D \tag{A4a.14}$$

where

$$F(x) = \frac{[K(x) - E(x)]}{x^2} - [K(x) + E(x)] \tag{A4a.15}$$

where **K** and **E** are the usual abreviations for the elliptic integrals[18]. When $l > R$, the execution of the integrals becomes more tedious still, but in a similar fashion the result Eq. 4.7 in the text is obtained.

To obtain the finite cylinder result exactly is prohibitively difficult. However, with the interpretation Eq. A4a.1 of $S(l)$ the modification of Eq. 4.7 is obvious. Consider the infinite cylinder. If $l > D$ then the portion of the surface area of the sphere of radius l within the cylinder comes from just two "caps" on the sphere. Each of these two (in general non-circular) caps makes an equal contribution for each $\vec{x}$ within the cylinder. Now consider the finite cylinder. As $\vec{x}$ approaches within a distance l of one end, one of the caps is omitted and only half as large a contribution results. Since this happens at both ends, the overall reduction of the infinite cylinder result is by a factor $(1 - \frac{l}{L})$. The error here is due to the neglect of the detailed behavior for small l near the "corners" of the cylinder, but as long as the cylinder is still reasonably long, i.e., $L >> D$, then the contribution from these portions is negligibly small anyway.

Appendix A4b

Starting with Eqs. 4.53-5, we make the usual change of variables to $\xi \equiv v_g t - z$ and $\eta \equiv z$ to get

$$\frac{\partial \varphi}{\partial \eta} = v_g[\, \sigma_{em} N_2 - \sigma^*_{abs} N_1^* \,]\, \varphi \tag{A4b.1}$$

$$\frac{\partial N_2}{\partial \xi} = -\, v_g[\, \sigma_{em} N_2 - \sigma^*_{abs} N_1^* \,]\, \varphi \tag{A4b.2}$$

$$\frac{\partial N_1^*}{\partial \xi} = v_g[\, \sigma_{em} N_2 - \sigma^*_{abs} N_1^* \,]\, \varphi - \frac{1}{\tau_R}[\, N_1^* - (N - N_2) f \,] \tag{A4b.3}$$

and we have used $N_1 = N - N_2 - N_1^*$. Letting $[\, \sigma_{em} N_2 - \sigma^*_{abs} N_1^* \,] \equiv \Delta$, we have $N_1^* = \sigma_{em} N_2 - \Delta$. Eq. A4b.3 combined with Eq. A4b.2 can then be simplified to

$$\frac{\partial \Delta}{\partial \xi} = -\, v_g(\sigma_{em} + \sigma^*_{abs})\, \Delta\, \varphi - \frac{\Delta}{\tau_R} + \frac{1}{\tau_R}(\sigma_{em} + \sigma^*_{abs}) N_2 - \frac{1}{\tau_R} f \sigma^*_{abs} N \tag{A4b.4}$$

Using Eq. A4b.1 we substitue $\partial\varphi/\partial\eta$ for $v_g \Delta\varphi$ in Eq. A4b.4 and then differentiate the resulting equation in ξ. Then by using Eq. A4b.2 again and Eq. A4b.1 in the form $\Delta = \frac{1}{v_g} \frac{\partial \ln \varphi}{\partial \eta}$ we obtain

$$\frac{\partial}{\partial \eta} \left\{ \frac{\partial^2 \ln \varphi}{\partial \xi^2} + (\sigma_{em} + \sigma^*_{abs}) \frac{\partial \varphi}{\partial \xi} \right.$$

$$\left. + \frac{1}{v_g \tau_R}\left[\frac{\partial \ln \varphi}{\partial \xi} + (\sigma_{em} + f \sigma^*_{abs}) \varphi \right] \right\} = 0 \tag{A4b.5}$$

This requires that the expression in brackets be some function $\Pi(\xi)$ of ξ only. This function can be evaluated at $\eta = 0$ where the input photon density and its temporal derivatives are known quantities;

$$\Pi(\xi) = \frac{\partial^2 \ln\varphi_0}{\partial\xi^2} + (\sigma_{em} + \sigma^*_{abs})\frac{\partial\varphi_0}{\partial\xi}$$

$$+ \frac{1}{v_g\tau_R}\left[\frac{\partial \ln\varphi_0}{\partial\xi} + (\sigma_{em} + f\sigma^*_{abs})\varphi_0\right] \qquad \text{(A4b.6)}$$

WE insert this value of $\Pi(\xi)$ as the 'integration constant" on the RHS of the integrated Eq. A4b.5, and then evaluate the resulting equation at $\eta = L$ where L is the length of the amplifier cell. Re-defining the time origin then results in the equation given in the text

$$\frac{d}{dt}\left[\frac{d\ln G}{dt} + (\sigma_{em} + \sigma^*_{abs})\varphi_0(t)(G-1)\right]$$

$$+ \frac{1}{\tau_R}\left[\frac{d\ln G}{dt} + (\sigma_{em} + f\sigma^*_{abs})\varphi_0(t)(G-1)\right] = 0 \qquad \text{(A4b.7)}$$

and G(t) is the retarded gain given by

$$G(t) \equiv \frac{\varphi(t' = t + \frac{L}{v_g},\ z = L)}{\varphi_{20}(t)} \qquad \text{(A4b.8)}$$

Appendix A4c

Eq. 4.62 in the text is integrated in ξ from $-\infty$ to ξ to yield

$$\Delta = \Delta_o(x,z)\exp[\,-3x^2(\overline{\sigma}_{em} + \overline{\sigma}_{abs})\int_{-\infty}^{\xi} \varphi\, d\xi] \qquad \text{(A4c.1)}$$

where $\Delta_o(x,z)$ is the initial ($\xi \to -\infty$) value of $\Delta(x,z)$. Placing this into Eq. 4.61 and integrating once more from $-\infty$ to ξ yields

$$\frac{\partial F(z,\xi)}{\partial z} = \frac{1}{2}\int_{-1}^{1} \Delta_o(x,z)[\,1 - e^{-3F(z,\xi)x^2}]dx \qquad \text{(A4c.2)}$$

where $F(z,\xi)$ is the appropriately retarded integrated photon flux past the point z in the cell

$$F(z,\xi) = (\overline{\sigma}_{em} + \overline{\sigma}_{abs})\int_{-\infty}^{\xi} \varphi(z,\xi)d\xi \qquad \text{(A4c.3)}$$

We now assume that the initial distribution $\Delta_o(x,z)$ is angularly isotropic and then Eq. A4c.2 is readily integrated in x and z to yield

$$\int_{F(z=0,\,\xi)}^{F(z=L,\,\xi)} \frac{dF}{[\,1 - (\frac{\pi}{12F})^{\frac{1}{2}}\mathrm{erf}(\sqrt{3F})]} = \int_0^L \Delta_o(z)\, dz = \ln G_o \qquad \text{(A4c.4)}$$

and for the net energy gain, we let $\xi \to \infty$ and perform a simple change of variables in the integral to get the desired result, Eq. 4.66 in the text:

$$\frac{S}{\ln G_o}\int_1^{G_{actual}} \frac{d\xi}{[\,1 - (\frac{\pi}{12S\xi})^{\frac{1}{2}}\mathrm{erf}(\sqrt{3S\xi})]} = 1 \qquad \text{(A4c.5)}$$

where $S = \dfrac{E_{sig}(\overline{\sigma}_{em} + \overline{\sigma}_{abs})}{h\nu_{sig}A}$. This equation also holds for a saturable absorber which can be modeled by the level scheme in Fig. 2.1 ignoring the triplet state. In this

case, G_0 and G_{actual} will be the leading edge or small signal *attenuation* and the actual *attenuation*, respectivley.

To approximate the effects of triplet state losses, we assume that in Fig. 2.1, the upper lasing level S_1^* can decay over to the triplet state T_0 with a decay lifetime τ_{trip} and that once there it can absorb from T_0 with a cross section $\overline{\sigma}_{trip\ abs}x^2$ where $x = \cos\vartheta$ as before. We assume also that after an absorption event from T_0 there is no subsequent decay or emission from the upper triplet state manifold on the short signal time scale. Eqs. 4.61-2 in the text then become modified to

$$\frac{\partial\varphi}{\partial z} = \frac{3}{2}\int_{-1}^{1}\Delta\ x^2dx\ \varphi - \frac{3}{2}\int_{-1}^{1}\Delta_T\ x^2dx\ \varphi \qquad \text{(A4c.6)}$$

$$\frac{\partial\Delta}{\partial\xi} = -3[\ \overline{\sigma}_{em} + \overline{\sigma}_{abs}\ ]x^2\ \Delta\ \varphi \qquad \text{(A4c.7)}$$

$$\frac{\partial\Delta_T}{\partial\xi} = -3\overline{\sigma}_{trip\ abs}\ x^2\ \Delta_T\ \varphi \qquad \text{(A4c.8)}$$

where $\Delta_T = N_{trip}\overline{\sigma}_{trip\ abs}$ and Δ is the same as given in the text.

Just as before, Eqs. A4c.7-8 are integrated in ξ and then inserted into Eq. A4c.6 which can then also be integrated in ξ to yield

$$\frac{\partial F(z,\xi)}{\partial z} = \frac{1}{2}\int_{-1}^{1}\Delta_o(x,z)[\ 1 - e^{-3F(z,\xi)x^2}]dx$$

$$- \frac{1}{2}\int_{-1}^{1}\Delta_{To}(x,z)[\ 1 - e^{-3\alpha F(z,\xi)x^2}]dx \qquad \text{(A4c.9)}$$

where $\alpha \equiv \dfrac{\overline{\sigma}_{trip\ abs}}{(\overline{\sigma}_{em} + \overline{\sigma}_{abs})}$ and $F(z,\xi)$ has the same meaning as before. Again we use the fact that Δ_o and Δ_{To} are isotropic in x and for simplicity we assume that they are also approximately uniform in z. In this case we have $\Delta_{To}(x,z) \rightarrow -\dfrac{\ln R_0}{L}$ where R_0 is the initial small signal attenuation factor from the triplet absorption. The initial inversion then becomes $\Delta_o(x,z) \rightarrow \dfrac{\ln G_0}{L} - \dfrac{\ln R_0}{L}$ where G_0 is the net small signal

initial gain. Eq. 4.67 in the text then follows upon integrating Eq. A4c.9 over the cell length and letting $\xi \rightarrow \infty$.

Appendix A4d

Since we are just considering the pumping process and we assume that at the pump frequency the triplet state absorption is negligible, if we denote the triplet state population by N_T , Eqs. 3.1-3 in the text become modified to

$$\frac{\partial \varphi_1}{\partial t} + v_g \frac{\partial \varphi_1}{\partial z} = v_g(\sigma_1^{em} N_2 - \sigma_1^{abs} N_1)\varphi_1 \qquad \text{(A4d.1)}$$

$$\frac{\partial N_1}{\partial t} = \frac{9}{5} v_g(\sigma_1^{em} N_2 - \sigma_1^{abs} N_1)\varphi_1 + \frac{N_2}{\tau} \qquad \text{(A4d.2)}$$

$$\frac{\partial N_2}{\partial t} = -\frac{\partial N_1}{\partial t} - \frac{N_2}{\tau_{trip}} \qquad \text{(A4d.3)}$$

$$\frac{\partial N_T}{\partial t} = \frac{N_2}{\tau_{trip}} \qquad \text{(A4d.4)}$$

where now $N_1 + N_2 + N_T = N$ where N is the total dye concentration. We have already included the 9/5 modification for angular hole burning on a time scale slow compared to orientational relaxation times.

Just as in Appendix A4c we make the same change of variables and let $\Delta \equiv [\sigma_1^{em} N_2 + \sigma_1^{abs} N_1]$. Then we obtain

$$\frac{\partial \ln \varphi_1}{\partial \eta} = \Delta \qquad \text{(A4d.5)}$$

$$\frac{\partial \Delta}{\partial \xi} = -\frac{9}{5}(\sigma_1^{em} + \sigma_1^{abs})\Delta\, \varphi_1 \qquad \text{(A4d.6)}$$

$$- \left[\frac{1}{\tau} + \frac{\sigma_1^{em}}{(\sigma_1^{em} + \sigma_1^{abs})\tau_{trip}} \right] (\Delta + \sigma_1^{abs}[N - N_T])$$

$$\frac{\partial N_T}{\partial \xi} = \frac{1}{(\sigma_1^{em} + \sigma_1^{abs})\tau_{trip}}(\Delta + \sigma_1^{abs}[N - N_T]) \qquad \text{(A4d.7)}$$

We will just outline the procedure from here. Again, we insert Eq. A4d.5 into Eq. A4d.6 and Eq. A4d.7 and integrate from 0 to L in η. Eq. A4d.6 becomes

$$\frac{\partial}{\partial \xi}\ln\left[\frac{\varphi_1(\eta = L)}{\varphi_{10}}\right] = -\frac{9}{5}(\sigma_1^{em} + \sigma_1^{abs})\varphi_{10}\left[\frac{\varphi_1}{\varphi_{10}} - 1\right]$$

$$-\left[\frac{1}{\tau} + \frac{\sigma_1^{em}}{(\sigma_1^{em} + \sigma_1^{abs})\tau_{trip}}\right]\left\{\ln\left(\frac{\varphi_1}{\varphi_{10}}\right) + \sigma_1^{abs}NL - \sigma_1^{abs}\int_0^L N_T\, d\eta\right\} \qquad \text{(A4d.8)}$$

while Eq. Ad4.7 becomes

$$\frac{\partial}{\partial \xi}\int_0^L N_T\, d\eta = \frac{1}{(\sigma_1^{em} + \sigma_1^{abs})\tau_{trip}}\left\{\ln\left(\frac{\varphi_1}{\varphi_{10}}\right) + \sigma_1^{abs}NL - \sigma_1^{abs}\int_0^L N_T\, d\eta\right\} \qquad \text{(A4d.9)}$$

Noting that $\varphi_1 = \varphi_{10}e^{\int_0^L \Delta\, d\eta}$ and that $N_1 + N_2 + N_T = N$ allows us to solve for both $\int_0^L N_1\, d\eta$ and $\int_0^L N_2\, d\eta$ in terms of the other dependent variables as follows:

$$\int_0^L N_1\, d\eta = -\frac{1}{(\sigma_1^{em} + \sigma_1^{abs})}\left\{\ln\left(\frac{\varphi_1(\eta = L)}{\varphi_{10}}\right) + \sigma_1^{em}NL - \sigma_1^{em}\int_0^L N_T\, d\eta\right\} \qquad \text{(A4d.10)}$$

$$\int_0^L N_2\, d\eta = -\frac{1}{(\sigma_1^{em} + \sigma_1^{abs})}\left\{\ln\left(\frac{\varphi_1(\eta = L)}{\varphi_{10}}\right) + \sigma_1^{abs}NL - \sigma_1^{abs}\int_0^L N_T\, d\eta\right\} \qquad \text{(A4d.11)}$$

The net small signal gain for the *input signal*, including triplet losses, is given by

$$G_0 = e^{\int_0^L (\sigma_2^{em}N_2 - \sigma_2^{abs}N_1 - \sigma_{trip\ abs}N_T)\, d\eta} \qquad \text{(A4d.12)}$$

where, as before, G_0 is evaluated at the arrival time of the signal pulse and

$$G_0 \equiv \frac{\varphi_2(\xi,\eta = L)}{\varphi_{20}(\xi,\eta = 0)} \tag{A4d.13}$$

It follows from Eqs. A4d.10-12 that we can obtain an expression for $\varphi_1(\eta = L) / \varphi_{10}$ in terms of $G_0(\xi)$ and $\int_0^L N_T \, d\eta$ only, which are now considered the dependent variables. This is

$$\frac{\varphi_1(\eta = L)}{\varphi_{10}} = G^{\gamma} \, e^{-\kappa NL} \, R^{\left[\gamma + \frac{\kappa}{\sigma_{trip\ abs}}\right]} \tag{A4d.14}$$

where we have let

$$R(\xi) \equiv e^{-\sigma_{trip\ abs} \int_0^L N_T \, d\eta} \tag{A4d.15}$$

which is the small signal attenuation factor of the signal pulse from triplet losses. Eqs. A4d.8-9 can then be re-written using the results Eqs. A4d.14-15 and after some algebra and the change from τ to τ_{eff} for approximate ASE inclusion, the results become the pair of equations Eqs. 4.69-70 in the text.

CHAPTER 4 REFERENCES

1. E. P. Ippen and C. V. Shank in *Picosecond Phenomena*, Springer Series in Chemical Physics, Vol. 4, Ed. by C. V. Shank, E. P. Ippen, and S. L. Shapiro, Springer-Verlag, Berlin, Heidelberg, New York, p.103, 1978.

2. J. L. Martin, R. Astier, A. Antonetti, C. A. Minard, and A. Orszag, C. R. Acad. Sc. Paris, **t.289**, 45 (1979).

3. S. R. Rotman, C. B. Roxlo, D. Bebelaar, T. K. Yee and M. M. Salour in *Picosecond Phenomena II*, Springer Series in Chemical Physics, Vol. 14, Ed. by R. M. Hochstrasser, W. Kaiser and C. V. Shank, Springer-Verlag, Berlin, Heidelberg, New York, p.50, 1980.

4. M. Matsuoka, H. Nakatsuka and M. Fujita in *Picosecond Phenomena II*, Springer Series in Chemical Physics, Vol. 14, Ed. by R. M. Hochstrasser, W. Kaiser and C. V. Shank, Springer-Verlag, Berlin, Heidelberg, New York, p.357, 1980.

5. P. G. Kryukov, Yu. A. Matveets, and V. A. Semchishen, Sov. J. Quantum Electon. **10**, 1418 (1980).

6. E. P. Ippen, C. V. Shank, J. M. Wiesenfeld and A. Migus, Phil. Trans. R. Soc. Lond. **A298**, 225 (1980).

7. A. Migus, J. L. Martin, R. Astier and A. Orszag in *Picosecond Phenomena II*, Springer Series in Chemical Physics, Vol. 14, Ed. by R. M. Hochstrasser, W. Kaiser and C. V. Shank, Springer-Verlag, Berlin, Heidelberg, New York, p.59, 1980.

8. A. Migus, C. V. Shank, E. P. Ippen, and R. L. Fork, IEEE J. Quantum Electron. **QE-18**, 101 (1982).

9. T. L. Koch, L. C. Chiu, and A. Yariv, Opt. Commun. **40**, 364 (1982).

10. T. L. Koch, L. C. Chiu, and A. Yariv, "Analysis and Performance of a Picosecond Dye Laser Amplifier Chain," to appear in J. Appl. Phys. (1982).

11. U. Ganiel, A. Hardy, G. N. Neumann, and D. Treves, IEEE J. Quantum Electron. **QE-11**, 881 (1975).

12. M. H. Gassman and H. Weber, Opto-Electron. **3**, 177 (1971).

13. See for example: *Dye Lasers*, Ed. by F. P. Schafer, Topics in Applied Physics, Vol. 1, Second Edition, Springer-Verlag, Berlin, Heidelberg, New York, 1977.

14. L. Brillouin, *Wave Propagation and Group Velocity*, Academic Press, New York, 1960.

15. A. Yariv, *Introduction to Optical Electronics*, Second Edition, Holt, Rinehart and Winston, New York, 1976.

16. *International Critical Tables of Numerical Data, Physics, Chemistry and Technology*, Vol. 7, Ed. by E. W. Washburn, McGraw-Hill Book Co., New York, 1930.

17. D. W. Phillion, D. J. Kuizenga, and A. E. Siegman, J. Chem. Phys. **61**, 3828 (1974).

18. I. S. Gradshteyn and I. M. Ryzhik, *Table of Integrals, Series, and Products*, Ed. by A. Jeffrey, Academic Press, New York, 1980.

CHAPTER 5

EXPERIMENTAL APPARATUS &

MEASUREMENT TECHNIQUES AND RESULTS

In this chapter we present the experimental aspects of the gigawatt picosecond dye laser oscillator- amplifier system. This consists of a description of the physical apparatus, the experimental performance of that apparatus, and a comparison with the theoretical modeling of Chapter 4. We begin with a brief discussion of the measurement techniques used in this work to study picosecond phenomena in the time domain.

5.1 Picosecond Time Domain Measurement Techniques

Many of the measurements described in this thesis consist of determining some temporal characteristics of an optical signal with a picosecond time scale intensity envelope. There are a number of methods for accomplishing this, and the particular one employed depends largely on the actual temporal resolution required.

For rough monitoring purposes, or for quantitative measurements of signals with durations $\gtrsim$ 75 psec, commercially available photodetector-oscilloscope combinations are appropriate. In particular, photoconductive detectors, Schottky barrier, avalanche, and PIN photodiodes can be constructed and packaged to have "fast" response times and can be used in conjunction with a 25 psec risetime sampling

oscilloscope (Tektronix 7904 with 7S-11, 7T-11 sampling unit and S-6 sampling head) to provide a "real time" monitor of optical pulses. The measurements here are not actually "real time" since the process is a sampling scheme. This is one of the drawbacks, since fairly high repetition rates are needed, ruling out the application to single shot laser pulse experiments.

Apart from the sampling scope resolution, the basic limitations on photodiode response are RC time constants associated with inherent capacitances as well as the transit time delays which charge carriers experience during transport across the voltage drop region of the device. Photoconductive detectors have the same RC problems. In addition, high speed photoconductive detectors (similar in design to the opto-electronic "switch" shown in Fig. 1.1) rely on short carrier lifetimes to make the net optically generated carrier population in the material follow the optical signal as instantaneously as possible. Response times as short as 10 psec have been observed in amorphous silicon[1]. However, the short response times lead to low sensitivity in keeping with the familiar gain bandwidth problems.

PIN diodes usually have longer response times due to the long drift times across the intrinsic region, but were used extensively for crude monitoring purposes where it was not essential to resolve picosecond pulses. Avalanche photodiodes operate at higher voltages, and with narrow depletion regions can be made fairly fast. Commercially available inexpensive silicon APD's have risetimes as low as 100 psec, and were also used extensively for more critical monitoring purposes where full resolution was not required. Schottky photodiodes are potentially the fastest when constructed with small active areas and narrow depletion regions in high mobility materials (GaAs, etc.)[2].

In all photodetector applications, careful packaging is essential for two reasons. Any impedance discontinuities cause reflections which can give spurious signal

shapes and modulate the frequency response. Also, parasitic capacitances, inductances and resistance can dominate the performance of the device. Fig. 5.1 shows the mount and bias scheme used for the APD. The intent is to have a 50 Ω transmission line right up to the diode itself, and to provide a large capacative charge reservoir so as not to limit the amplitude reponse on short impulses. Fig. 5.2 shows the output of the Telefunken BPW-28 APD which was mounted in this package monitoring a mode-locked argon ion laser in conjunction with the sampling oscilloscope mentioned above. The bottom shows the pulse train, while the top shows a single pulse on a faster timescale. The ~ 200 psec wide pulse is still detector limited by the ~ 100 psec risetime diode, but this arrangement is suitable for rough monitoring of the argon ion mode-locking, to be discussed in more detail in the next section. Fig. 5.3 shows the same pulse observed with a Spectra-Physics 403B Shottky barrier diode. The risetime of the diode was measured with the mode-locked dye laser output to be ~ 45 psec, so here the argon mode-locked pulse is fairly well resolved and gives a very good indication of mode-locking quality.

When laser pulses approach a time scale of ~ 50 psec and less, the presently available conventional electronic means for temporal measurements become inadequate. Streak cameras have been designed with picosecond resolution but suffer from high cost and require film developing and densitometer tracing before the results are known. Presently available commercial "real time" streak cameras for high repition rate systems have resolutions of several picoseconds which is inadequate for many applications.

The technique used for high resolution measurements in this thesis is auto- and cross-correlation measurements via nonlinear optical mixing. This encompasses both the well known SHG autocorrelation technique[3] shown in Fig. 5.4, as well as the cross-correlation parametric sum frequency technique[4] to be employed for the results of Chapters 6 and 7. In the SHG method, a pulse at frequency ω is split,

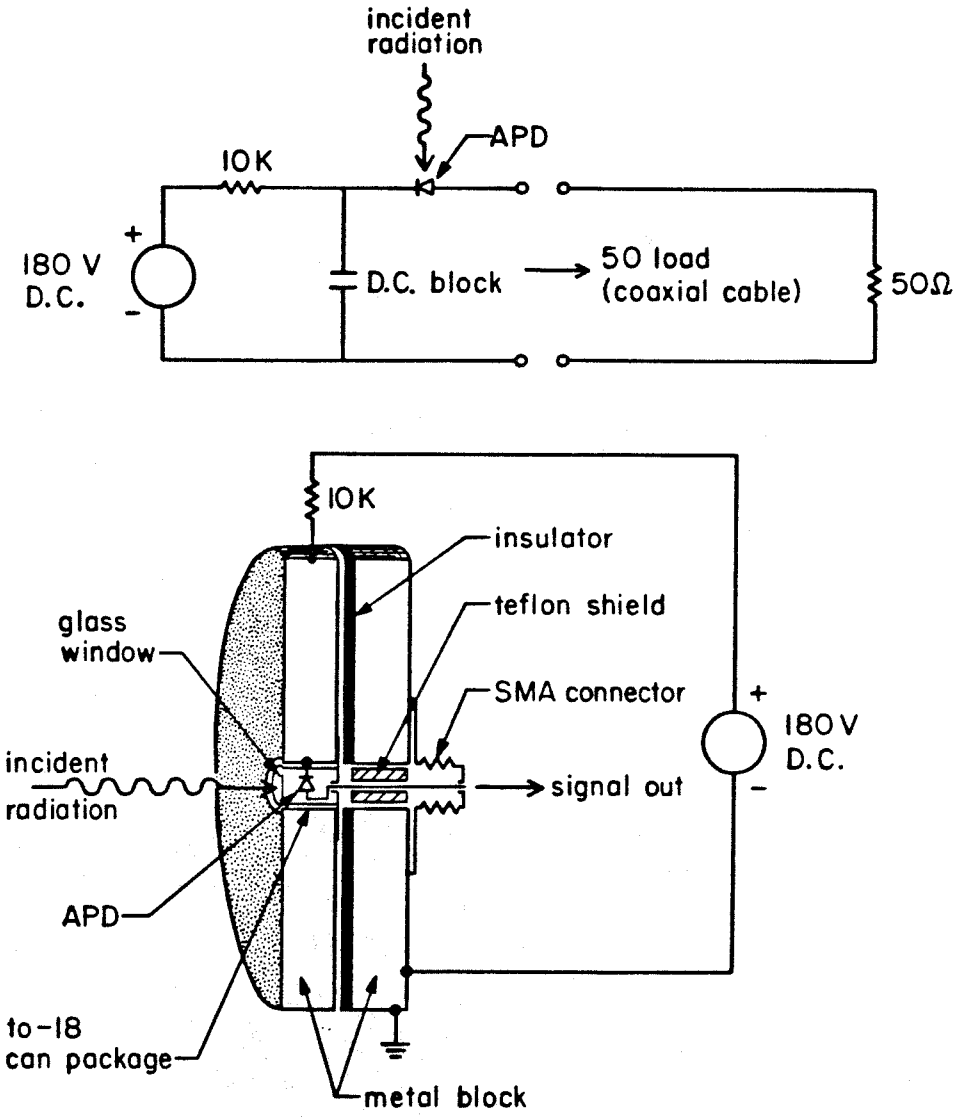

Figure 5.1 Packaging and bias scheme for APD and PIN photodiode used for ultrafast optical pulse monitoring.

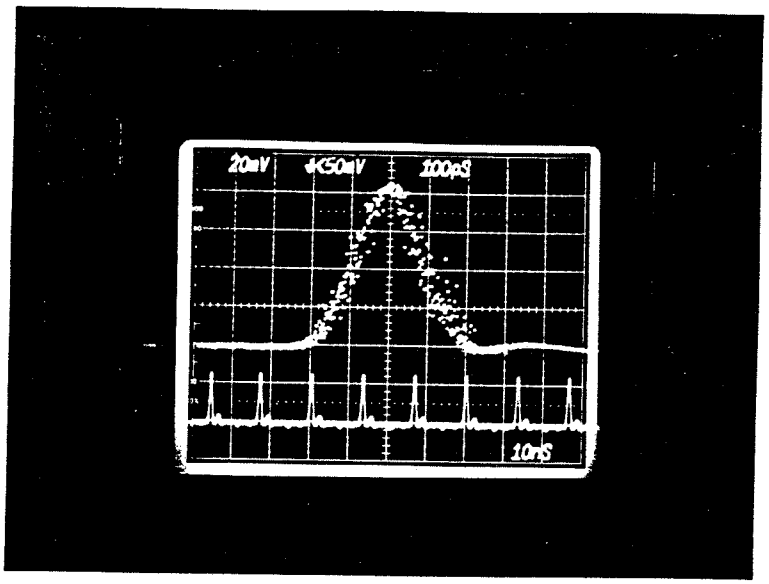

Figure 5.2 Unresolved but useful monitor of mode-locked argon laser pulses using a Telefunken BPW-28 avalanche photodiode. Upper trace: 100 psec/div. Lower trace: 10 nsec/div.

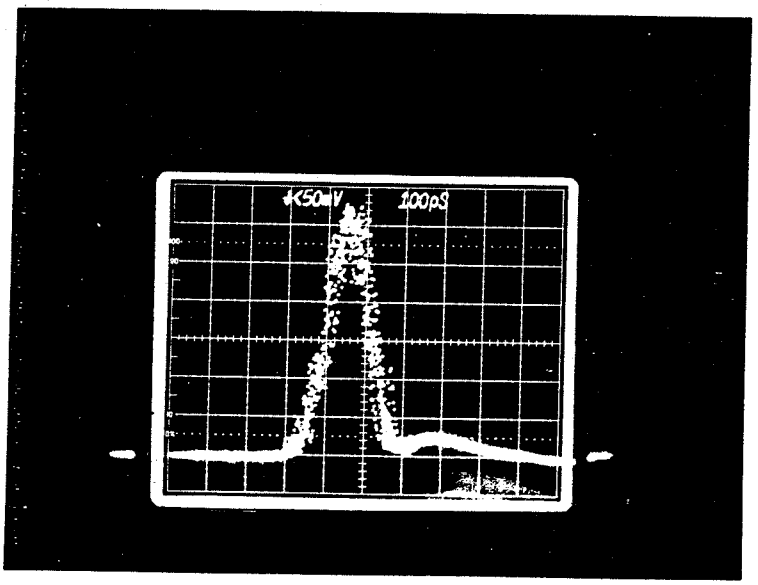

Figure 5.3 Resolved mode-locked argon laser pulses using a Spectra-Physics Model 403B Shottky barrier photodiode. Scale is 100 psec/div.

with one half being delayed with respect to the other by an amount τ just by a path length difference. The pulses are then recombined in a nonlinear crystal which generates a polarization

$$P_{2\omega}(t, z) \propto e^{i(2\omega t - 2k_\omega z)}\left[\mathcal{E}^2(t, z) + \mathcal{E}^2(t-\tau, z)e^{-2i\omega\tau}\right. \tag{5.1}$$

$$\left. + 2\mathcal{E}(t, z)\mathcal{E}(t-\tau, z)e^{-i\omega\tau}\right] + \text{C.C.}$$

where $k_\omega = n(\omega)\omega/c$ and $\mathcal{E}(t, z)$ is the envelope waveform of the pulse in the same sense as in Section 2.1. Assuming one dimensional spatial variation in the z direction only, the wave equation in a material with index $n(\omega)$ and the polarization source above yields for the envelope of the 2ω wave at $z = L$ the value[5]

$$\mathcal{E}_{2\omega}(t) \propto L\frac{\sin[\frac{\Delta kL}{2}]}{[\frac{\Delta kL}{2}]}\left[\mathcal{E}^2(t) + \mathcal{E}^2(t-\tau)e^{-2i\omega\tau}\right. \tag{5.2}$$

$$\left. + 2\mathcal{E}(t)\mathcal{E}(t-\tau)e^{-i\omega\tau}\right]$$

where $\Delta k = k_{2\omega} - 2k_\omega = 2\frac{\omega}{c}[n(2\omega) - n(\omega)]$ and we have ignored pump depletion. Due to material dispersion, in general the *phase matching* condition $\Delta k = 0$ is not satisfied and signal strength then suffers following Eq. 5.2. When the condition $\Delta k = 0$ is violated, the oscillating polarization at 2ω is not properly phased *spatially* to radiate a forward propagating wave. This phase matching problem can be circumvented by exploiting the well known birefringent properties of uniaxial nonlinear crystals such as KDP or $LiIO_3$ which were both employed in this work. For any direction of propagation in such a crystal, an arbitrarily polarized wave can be decomposed into an *ordinary* polarization component which propagates with an index of refraction n_o and another *extraordinary* polarization component orthogonal to the ordinary component which propagates with an index $n_e(\vartheta)$ which depends on the angle of propagation ϑ with respect to the *optic axis* in the crystal. Here[5]

$$n_e^{(\omega)}(\vartheta) = \left[\frac{\sin^2(\vartheta)}{[n_e^{(\omega)}]^2} + \frac{\cos^2(\vartheta)}{[n_o^{(\omega)}]^2} \right]^{-\frac{1}{2}} \tag{5.3}$$

The indices $n_o^{(\omega)}$ and $n_e^{(\omega)}$ are given typically by dispersion formulas of the form

$$n_j^2(\lambda) = A_j + \frac{B_j}{\lambda^2 - C_j} + \frac{\lambda^2 D_j}{\lambda^2 - E_j} \tag{5.4}$$

where $j = o, e$ and A_j through E_j are material constants. The relevant values for KDP and $LiIO_3$ are as follows:

KDP:[6] (5.5)

$A_o = 2.260476$ $B_o = 1.011279 \times 10^{-2}$ $C_o = 1.2942384 \times 10^{-2}$ $D_o = 12.997972$ $E_o = 400$

$A_e = 2.133831$ $B_e = 8.653247 \times 10^{-3}$ $C_e = 1.2293261 \times 10^{-2}$ $D_e = 3.2279352$ $E_e = 400$

$LiIO_3$:[7] (5.6)

$A_o = 3.407$ $B_o = 0.05059$ $C_o = 0.03049$ $D_o = 0$ $E_o = 0$

$A_e = 2.923$ $B_e = 0.03423$ $C_e = 0.02015$ $D_e = 0$ $E_e = 0$

and the λ to be used in Eq. 5.4 is in μm . These formulas will be essential in interpreting the results of the measurements in Chapter 7.

We now assume that the fundamental waves are ordinary and the SHG is extraordinary (Type I phase matching), and the crystal is cut with its optic axis at the phase matching angle ϑ_m so $\Delta k = 0$. In the general case of parametric sum frequency generation using waves at ω_1 and ω_2 , a polarization is generated at the sum freqency $\omega_1 + \omega_2 \equiv \omega_{12}$. In this case, the phase matching condition becomes $\omega_1 n_o^{\omega_1} + \omega_2 n_o^{\omega_2} = \omega_{12} n_e^{\omega_{12}}(\vartheta)$ and the phase matching angle ϑ_m can be shown through Eq. 5.3 to be

$$\vartheta_m = \sin^{-1} \left[\frac{\left[\frac{\omega_1}{\omega_{12}} n_o^{(\omega_1)} + \frac{\omega_2}{\omega_{12}} n_o^{(\omega_2)} \right]^{-2} - [n_o^{(\omega_{12})}]^{-2}}{[n_e^{(\omega_{12})}]^{-2} - [n_o^{(\omega_{12})}]^{-2}} \right]^{\frac{1}{2}} \tag{5.7}$$

In the case of SHG, the resulting intensity at 2ω becomes

$$I_{2\omega}(t) \propto |\mathcal{E}^2(t)|^2 + |\mathcal{E}^2(t-\tau)|^2 + 4|\mathcal{E}(t)\mathcal{E}(t-\tau)|^2 \tag{5.8}$$

$$+ \left\{\mathcal{E}(t)^2\mathcal{E}^{*2}(t-\tau)e^{2i\omega\tau} + 2\mathcal{E}(t)\mathcal{E}^{*}(t-\tau)[|\mathcal{E}(t)|^2 + |\mathcal{E}(t-\tau)|^2]\, e^{i\omega\tau} + \text{C.C.}\right\}$$

Here the terms which involve the product of $\mathcal{E}(t)$ and $\mathcal{E}(t-\tau)$ provide the basis for the measurement technique; when the intensity at 2ω is integrated in time we conclude that the energy $E_{2\omega}$ at 2ω obeys

$$E_{2\omega}(\tau) \propto 1 + 2G^{(2)}_{\omega,\omega}(\tau) + r(\tau) \tag{5.9}$$

where in general we define

$$G^{(2)}_{\omega_1,\omega_2}(\tau) \equiv \frac{\int_{-\infty}^{\infty} I_{\omega_1}(t) I_{\omega_2}(t-\tau)\,dt}{\left[\int_{-\infty}^{\infty} I^2_{\omega_1}(t)\,dt \int_{-\infty}^{\infty} I^2_{\omega_2}(t)\,dt\right]^{\frac{1}{2}}} \tag{5.10}$$

and $r(\tau)$ is a term which oscillates rapidly in τ and can be ignored experimentally; we consider it no further. If we *cross correlate* two pulses at different frequencies ω_1 and ω_2, the integrated energy at the sum freqency $\omega_1 + \omega_2 \equiv \omega_{12}$ becomes

$$E_{\omega_{12}}(\tau) \propto G^{(2)}_{\omega_1,\omega_2}(\tau) \tag{5.11}$$

Clearly the information about the temporal pulse characteristics is contained in the $G^{(2)}$ term in both the autocorrelation and the cross correlation. The width of $G^{(2)}$ conveys a rough indication of the pulse width but in a general case there is no unique way to extract the pulse shapes from the correlation alone. Only if functional forms have been assumed for the pulses can the pulse widths can be determined by the correlation width. However, the width of an autocorrelation trace is almost always between one and two times the width of the pulse intensity envelope

itself, so in practice it is often sufficient to demand only that the autocorrelation width be less that the experimentally acceptable temporal resolution.

It has often been stated in the literature that the resolution of the autocorrelation pulse width measuring method is limited by crystal thickness. This appears to follow since the inherent large bandwidth of short pulses makes perfect phase matching for all frequency components of the pulse impossible. Many authors quote a limit on crystal thickness which follows from earlier work[8,9] which derives conditions under which the SHG pulse is not broadened significantly in time compared to the fundamental. However, since the integrated *energy* of the sum frequency or SHG is the measured quantity, this condition is not particularly relevant. In a manner similar to the work of Glenn [RR], it is a straightforward exercise to extend the theory to yield the quantity which replaces $G^{(2)}_{\omega_1,\omega_2}(\tau)$ when the finite bandwidth of the pulses is included. It is

$$\tilde{G}^{(2)}_{\omega_1,\omega_2}(\tau) = \left[N_{\omega_1}N_{\omega_2}\right]^{\frac{1}{2}} \int_0^1 dr \int_0^1 ds \int_{-\infty}^{\infty} dt\ \mathcal{E}_{\omega_1}(t - \alpha Lr + \gamma L)\ \mathcal{E}_{\omega_2}(t - \beta Lr - \gamma L - \tau) \quad (5.12)$$

$$\times\quad \mathcal{E}^{*}_{\omega_1}(t - \alpha Ls + \gamma L)\ \mathcal{E}^{*}_{\omega_2}(t - \beta Ls - \gamma L - \tau)$$

where

$$N_\omega \equiv \left[\int_{-\infty}^{\infty} dt \int_0^1 dr \int_0^1 ds\, |\mathcal{E}_\omega(t - \alpha Lr)|^2 \mathcal{E}_\omega(t - \alpha Ls)|^2 \right]^{-1} \quad (5.13)$$

and

$$\alpha \equiv v_g(\omega_{12})^{-1} - v_g(\omega_1)^{-1} \qquad \beta \equiv v_g(\omega_{12})^{-1} - v_g(\omega_2)^{-1} \qquad \gamma = \frac{\beta - \alpha}{2} \quad (5.14)$$

where $v_g^{-1} = \frac{\partial k}{\partial \omega}$ and L is the crystal length. Consider the case of SHG where $\gamma = 0$. For rectangular pulses of width T_{pulse}, if $|\tau| > T_{pulse}$ we have $\tilde{G}^{(2)}_{\omega_1,\omega_2}(\tau) = 0$ just as in the case of no group velocity differences. While the integrals in r and s do tend to *smear* the result, we conclude that the autocorrelation is not significantly

broadened. However, since information is lost on any fine autocorrelation features which may be present, it is best to keep the crystal length L such that $\alpha L,\ \beta L \lesssim T_{pulse}$. In addition, if this condition is severely violated, the signal *amplitude* is reduced, possibly to a point where noise becomes a problem. One factor which clearly can contribute to a real loss of resolution in the correlation method is group velocity dispersion within the fundamental pulse itself; here the pulse actually does broaden within the nonlinear medium and the measured result is that of the broadened pulse. This type of broadening was discussed in Chapter 4 , and clearly for no significant loss of resolution, the crystal length must satisfy $L << L_{double}$ where L_{double} is given by Eq. 4.48.

Another phenomenon which occurs in the SHG measurement is due to the fact that there can be noise-like stochastic variations in the phase and amplitude of the carrier wave for which $\mathcal{E}_\omega(t)$ is the envelope. In this case, we assume that $\mathcal{E}_\omega(t)$ is the modulation envelope on random field e(t) which is a stationary Gaussian random signal characterized by

$$< e(t)e^*(t-\tau) > \equiv \Gamma(\tau) \tag{5.15}$$

where < > denotes an ensemble average. It can then be shown[10] that the measured autocorrelation will be changed in general to

$$\tilde{G}^{(2)}_{\omega,\omega}(\tau) = \frac{1}{2}\left(1 + \frac{|\Gamma(\tau)|^2}{|\Gamma(0)|^2}\right) G^{(2)}_{\omega,\omega}(\tau) \tag{5.16}$$

which produces the well known noise or coherence spikes with the width of the function $|\Gamma(\tau)|^2$ superposed on the "deterministic" envelope autocorrelation $G^{(2)}_{\omega,\omega}(\tau)$. For noise free pulses, $\Gamma(\tau) = \Gamma(0)$ for all τ and the old result obtains, but in the general case with noise present, the actual pulse width autocorrelation width of interest is just that due to $G^{(2)}_{\omega,\omega}(\tau)$.

Another experimentally measurable quantity which characterizes the temporal characteristics of optical pulses is the optical power spectrum of the pulses. From the "uncertainty principle", we know

$$T_{FWHM}\Delta\nu_{FWHM} \gtrsim K \tag{5.17}$$

where T_{FWHM} is the pulse *intensity* FWHM and $\Delta\nu_{FWHM}$ is the FWHM of the power spectrum. The constant K depends on the functional form of the deterministic envelope for which T_{FWHM} is a parameter. As an example, for a Gaussian, $sech^2$ and one-sided exponential pulse shapes, K = 0.441, 0.315, and 0.11 respectively[3]. As mentioned earlier, for each shape there is also a relation between the autocorrelation width τ_{FWHM} and the intensity envelope pulse width T_{FWHM}. In the cases above, this is τ_{FWHM}/T_{FWHM} = 1.414, 1.55, and 2 for the Gaussian, $sech^2$ and one-sided exponential pulse shapes respectively.

The SHG measurement scheme used experimentally is shown in Fig. 5.4. The linear translation stage was driven by a stepping motor and driver with a step size of 0.125 mil/ step. Since each length step is traversed twice for the net path length, the step size in time delay becomes $2.12\text{x}10^{-14}$ sec/ step. The beam splitter is a cube metal dielectric type and a 50 mm lens is used to focus onto the 1 mm thick KDP crystal which was obtained from Cleveland Crystals[11]. The crystal is cut with its optic axis at 60° 28' to the surface normal which corresponds from Eq. 5.6 to frequency doubling 6000Å at normal incidence. For application at other wavelengths near 6000Å, the crystal is mounted in a gimbal mount with micrometer adjustments for angle tuning. The second harmonic signal is detected with an RCA 1P28 photomultiplier tube and is typically run at ~ 500 volts. A pair of Schott UG-11 filters block out the fundamental beam as well as the flourescent room lighting to facilitate easy routine measurements.

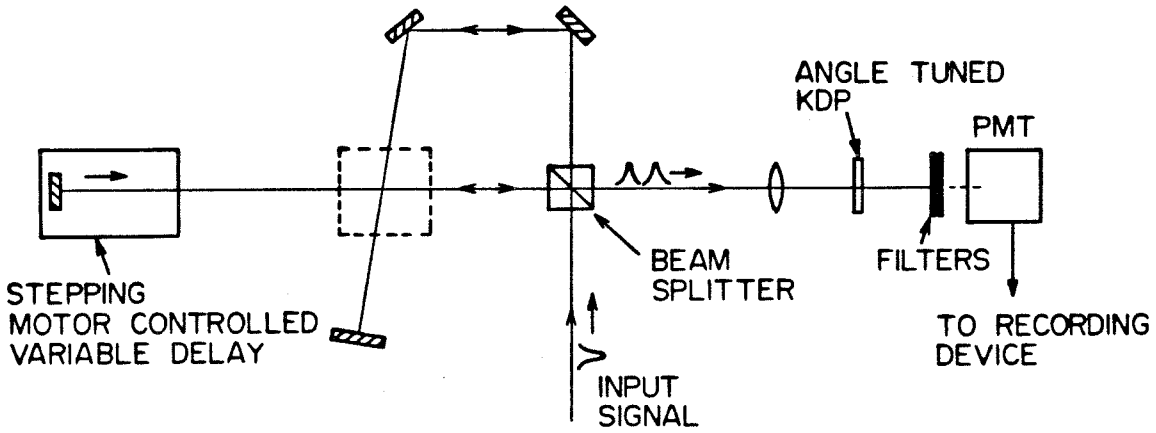

Figure 5.4 Second harmonic generation autocorrelation measurement apparatus. For discussion of box outlined in dotted lines, see text and Fig. 5.7.

For high resolution recording, the output of the PMT is filtered to pick out the DC level of the SHG signal which is fed into a Nicolet 1174 signal averager. This is a digital recording device with 4096 sequentially addressable channels. For this application the channel address is advanced with each step of the stepping motor (or some multiple of steps), and at each step the DC voltage proportional to the average second harmonic optical power is recorded in a channel. This can be repeated many times for averaging purposes if desired. The 4096 channel output can then be displayed on a CRT for a direct display of $G^{(2)}_{\omega,\omega}(\tau)$. This is a convenient recording scheme since pulse parameters such as the SHG autocorrelation width are available in digital form right at the time of execution.

Autocorrelations of the mode-locked dye laser pulses obtained by this method are shown in Figures 5.5 and 5.6; the full scale in both cases is 43.4 psec. Fig. 5.5 corresponds to a better adjustment of the oscillator, with a autocorrelation width of ~ 1.8 psec, indicating a sech^2 pulse width of ~ 1.2 psec. Fig. 5.6 shows typical results if the cavity length is too long for clean mode-locking; the noise spike of Eq. 5.16 is clearly visible. The relevant autocorrelation width here is that of the *base* pedestal, and is 8.6 psec FWHM, for a sech^2 pulse width of 5.5 psec. The pulse broadening effect of lengthening the cavity discussed in Chapter 3 is therefore easily observed experimentally. Length changes as small as 10 μm have an easily noticeable effect on the mode-locking near the short cavity, short pulse operation range of the oscillator.

The step scanning process described above is fairly slow, requiring at least tens of seconds to complete the scan of a useful observation range $\sim$ 40 psec. All adjustments made to the laser are essentially "blind" unless a more "real time" method is devised for observing $G^{(2)}_{\omega,\omega}(\tau)$. For this purpose, a rotating prism autocorrelation device was constructed similar in principle to a commercially available Spectra-Physics Model 409 Scanning Autocorrelator. The set up shown in Fig. 5.4 is

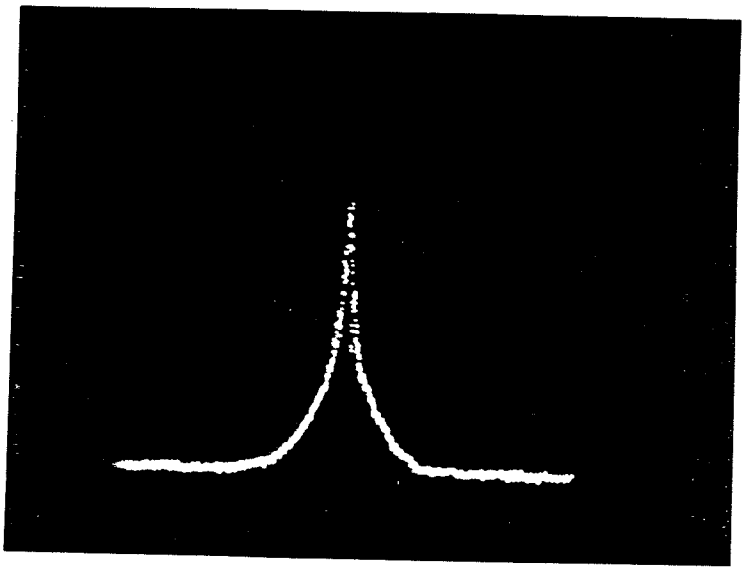

Figure 5.5 Slow scan, high resolution autocorrelation of mode-locked dye laser oscillator viewed on Nicolet 1174 signal averager when cavity length and output coupling are near optimal. Full screen is 43.4 psec, with the autocorrelation trace FWHM of ~ 1.8 psec. This indicates a $sech^2$ pulsewidth of ~ 1.2 psec.

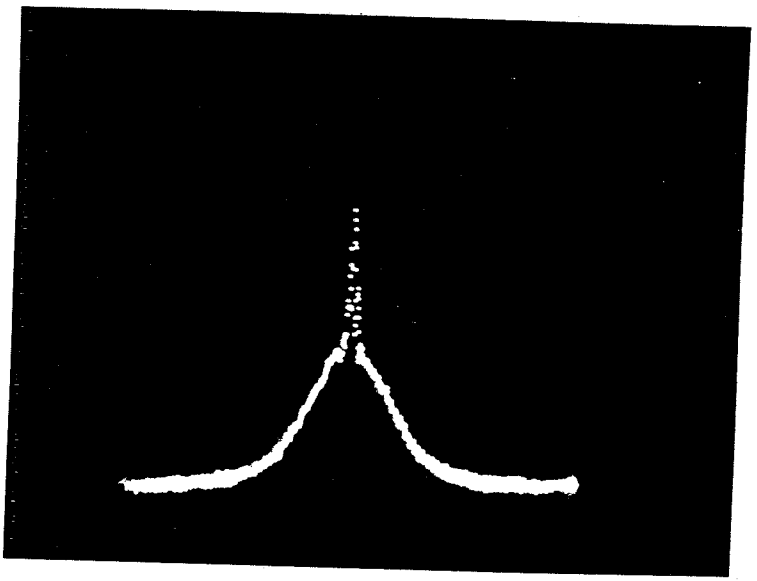

Figure 5.6 Slow scan, high resolution autocorrelation of mode-locked dye laser oscillator viewed on Nicolet 1174 signal averager when cavity length is adjusted too long. Full screen is 43.4 psec, and classic "noise spike" structure indicates incomplete mode-locking. FWHM of autocorrelation *pedestal* is ~ 8.6 psec for a $sech^2$ pulsewidth of ~ 5.5 psec.

converted by adding a rotating prism near the intersection point of the two beams within the dotted square; the precise location is not important. Fig. 5.7 shows a blow-up of the rotating prism assembly. Regardless of the angular position of this thick flat of glass, the two beams, having been displaced from their original path, return from the flat mirrors and exactly retrace their path into the original beam path. If this glass block is held stationary, the original slow scan stepping motor method is still operable. If the prism is rotated, the optical path length $\int n(s)ds$ of both beams depends on the angular position of the block. With increasing angle the beams are displaced to the side *and* they also experience a larger path in the higher index glass with $n \sim 1.5$. From a reference angular position at which the normal to the glass surface bisects the angle between the two beams, any rotation *increases* the optical path length for one beam, while it *decreases* the optical path length for the other. Referring to Fig. 5.7, the time shift τ resulting from the path difference can easily be shown to be given by (up to a constant)

$$\tau = \frac{2d}{c}\left\{ 2\sin(\frac{\varphi}{2})\sin\delta + \left(n^2 - \sin^2(\frac{\varphi}{2} + \delta)\right)^{\frac{1}{2}} - \left(n^2 - \sin^2(\frac{\varphi}{2} - \delta)\right)^{\frac{1}{2}}\right\} \qquad (5.18)$$

where d is the thickness of the glass slab of index n, φ is the fixed angle between the two beams, and δ is the angular deviation of the slab from the position where the normal to the glass bisects the angle between the two beams. For small δ a Taylor expansion of Eq. 5.18 yields

$$\tau \approx \frac{4d}{c}\sin(\frac{\varphi}{2})\left[\, 1 - \frac{\cos(\frac{\varphi}{2})}{\sqrt{n^2 - \sin^2(\frac{\varphi}{2})}}\right]\delta + \vartheta(\delta^3) \qquad (5.19)$$

The experimental system used a glass slab with a thickness d = 2.54 cm and index 1.52. The angle φ was fixed at $\approx 83°$. This corresponds to a time delay, from Eq. 5.19, of 1.77 psec/ degree of rotation. This was set on a heavy (several pounds) steel flywheel which was driven by a hysteresis synchronous motor through a

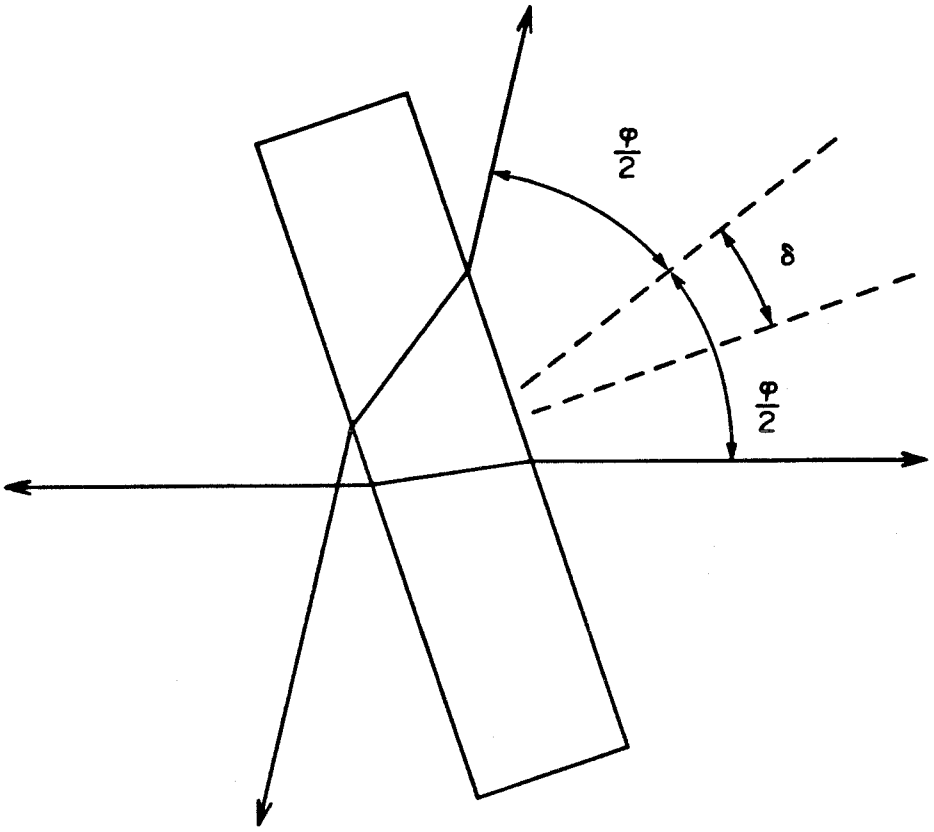

Figure 5.7 Geometry for rotating prism real time autocorrelation device.

toothed belt system at 600 RPM. A slit on a rim at the edge of the flywheel passed a slit-collimated beam from an LED through another slit onto a phototransistor to provide a trigger pulse. The slits are narrow enough to provide a 60 μsec risetime, and the rotation during this total risetime corresponds to 0.38 psec in relative autocorrelation delay. The triggering accuracy can thus be kept below $\lesssim$ 0.04 psec in delay. The trigger system is itself mounted on a rotatable arm to provide adjustable triggering position. With the trigger set typically $\approx$ 20° before the autocorrelation center, for an accuracy of 0.1 psec, the flywheel speed accuracy must be maintained to $\lesssim$ 0.3 % which is easily achieved. The trigger pulse then triggers an oscilloscope which free-runs as the flywheel turns, thereby converting the horizontal time axis of the scope to angular position or autocorrelation delay τ. The verticle axis of the scope monitors the DC component of the SHG intensity as before to provide a "real time" autocorrelation on the CRT of the scope. The actual repitition rate of the scan is 10 Hz.

There are two sources of nonlinearity in this measurement. One is the actual nonlinearity of the τ vs. δ relation given by Eq. 5.18, but if the total time window in τ is restricted to $\sim$ 40 psec, the deviations from the linear relation Eq. 5.19 are less than 5%. Another source of nonlinearity is in amplitude due to the angular variation in Fresnel reflections from the glass slab; since the SHG depends on the square of intensity, this has a sizable effect. Throughout the same 40 psec window, a simple calculation reveals that this produces $\lesssim$ 5.4% amplitude nonlinearity on the autocorrelation when horizontal polarization is used. If larger time windows are needed with the same level of linearity, a thicker prism is required.

Fig. 5.8 shows the laser output with fairly good length adjustment, where the noise (exaggerated by the SHG) is due to amplitude flucuations in the dye oscillator. With sufficient care in adjusting the argon ion laser mode-locking, this noise can be substantially reduced, but as indicated in Chapter 3, the short pulse end of

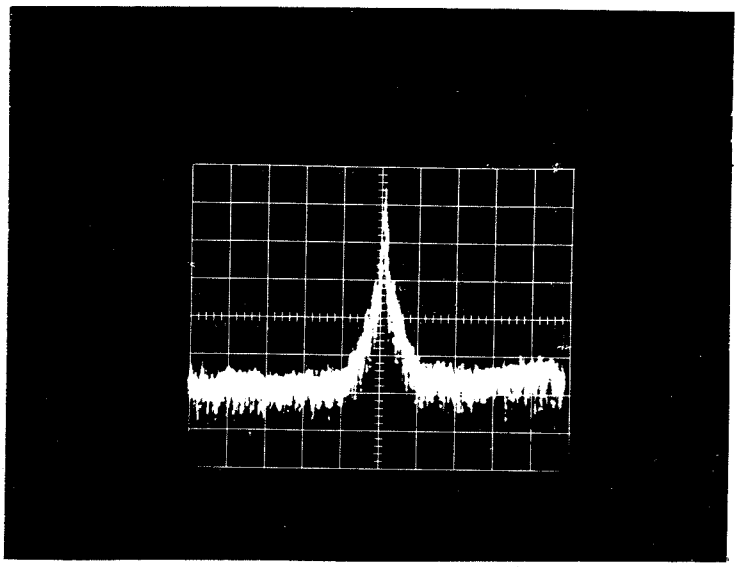

Figure 5.8 Real time rotating prism autocorrelation trace with near optimal cavity length and output coupling. Noise is due to amplitude fluctuations which are enhanced in the second harmonic. Time scale is 6 psec/div, with the ~2.4 psec FWHM autocorrelation indicating a sech^2 pulsewidth of ~ 1.5 psec.

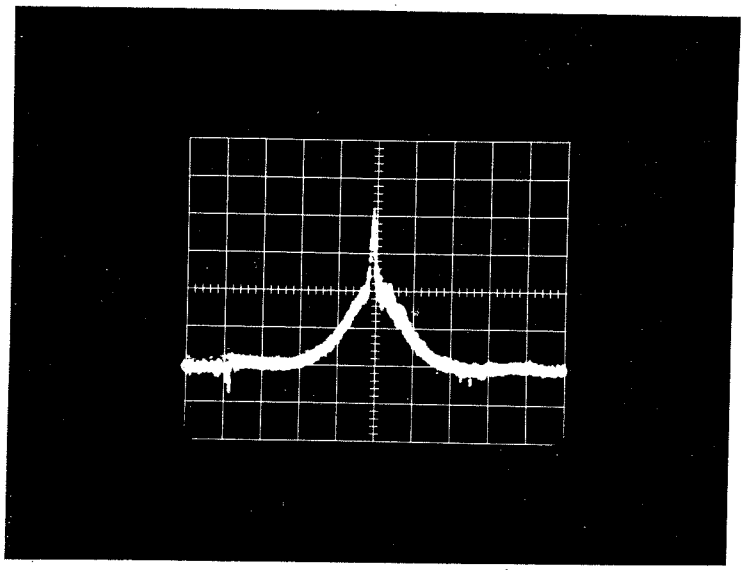

Figure 5.9 Real time rotating prism autocorrelation trace with cavity length adjusted too long. Operation is more stable, but noise is also filtered out using an RC filter. Time scale is 6 psec/div, and the FWHM of the autocorrelation *pedestal* is ~ 9.6 psec, indicating a sech^2 pulsewidth of ~ 6.2 psec.

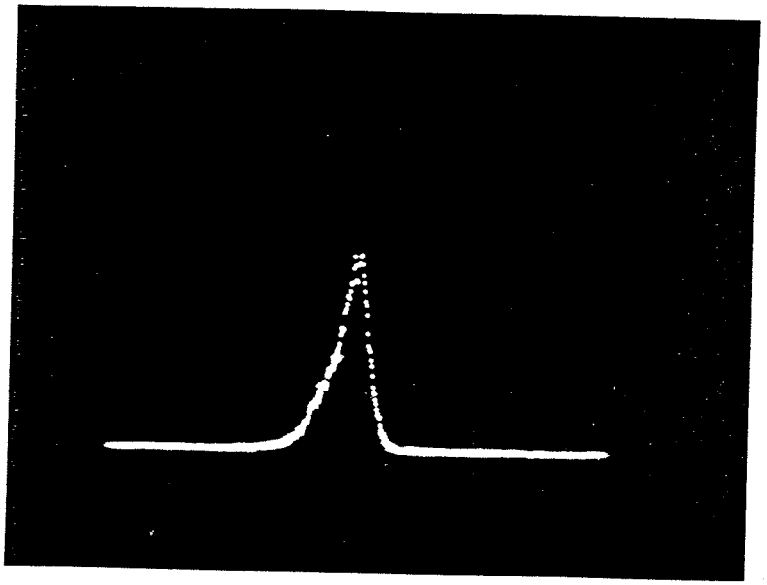

Figure 5.10a Optical power spectrum of mode-locked dye laser oscillator using a grating spectrometer and an optical multichannel analyzer. FWHM of spectrum is ~6.5 Å at a center wavelength of 5914 Å which is sufficient to generate bandwidth limited $sech^2$ pulses of 0.57 psec duration.

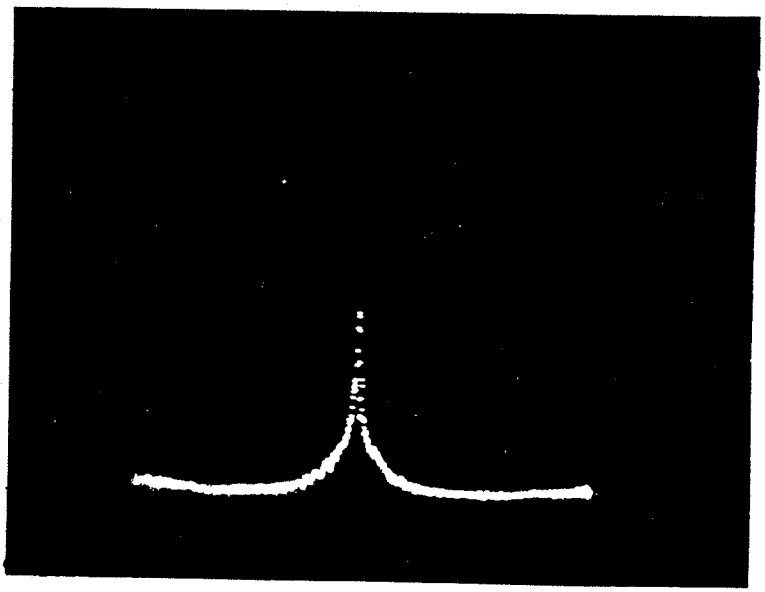

Figure 5.10b Autocorrelation associated with power spectrum above using the slow scan Nicolet signal averaging method. Full screen width is 43.4 psec and the autocrrelation FWHM is 0.76 psec, although there is some indication of possible noise structure. The $sech^2$ pulsewidth would be ~0.5 psec.

operation is always less stable. The 2.4 psec FWHM of the autocorrelation trace indicates a $sech^2$ pulse width of ~ 1.5 psec. Fig. 5.9 shows the real time display when the dye laser cavity is adjusted too long; a noise spike is clearly visible as in Fig. 5.6. The time scale here is 6 psec/ div, and the "base" width of 9.6 psec indicates a $sech^2$ pulse width of 6.2 psec. The trace here has been filtered with an RC filter to reduce noise from high speed laser amplitude fiucuations.

The "real time" aspect of the autocorrelation device described above is essential for the dye laser oscillator adjustments. Simultaneous monitoring of the optical power spectrum is accomplished by feeding stray reflections through an optical fiber into the entrance slit of a GCA McPherson 2051 grating spectrometer whose output slit has been replaced with a Princeton Applied Research 1205A vidicon-optical multichannel analyzer with 512 optical elements and recording channels. The resolution of this instrument is 0.186 Å / channel, for a total range of ~ 95 Å . A spectrum of the mode-locked dye laser pulses is shown in Fig. 5.10a as viewed on the CRT output of the optical multichannel analyzer. The FWHM of the power spectrum is 5.55×10^{11} Hz at a center wavelength of 5914 Å . The associated autocorrelation, taken by the slow stepping motor scan with the Nicolet signal averager, is shown in Fig. 5.10b. The FWHM is 0.763 psec, but the shape of the trace indicates some possible noise structure. Ignoring this, and assuming a $sech^2$ pulse shape, the resulting time-bandwidth product would be $\Delta\nu_{FWHM}\Delta T_{FWHM} = 0.273$, which is less than the bandwidth limited value of 0.315, indicating that nearly transform limited pulses with durations of ~ 0.5 psec have been generated.

5.2 The Synchronously Pumped Dye Laser Oscillator

Fig. 5.11 shows the layout of the mode-locked dye laser. A Coherent CR12 argon ion laser with a Coherent 467-SE mode-locker is the pump source[12], providing ~ 1

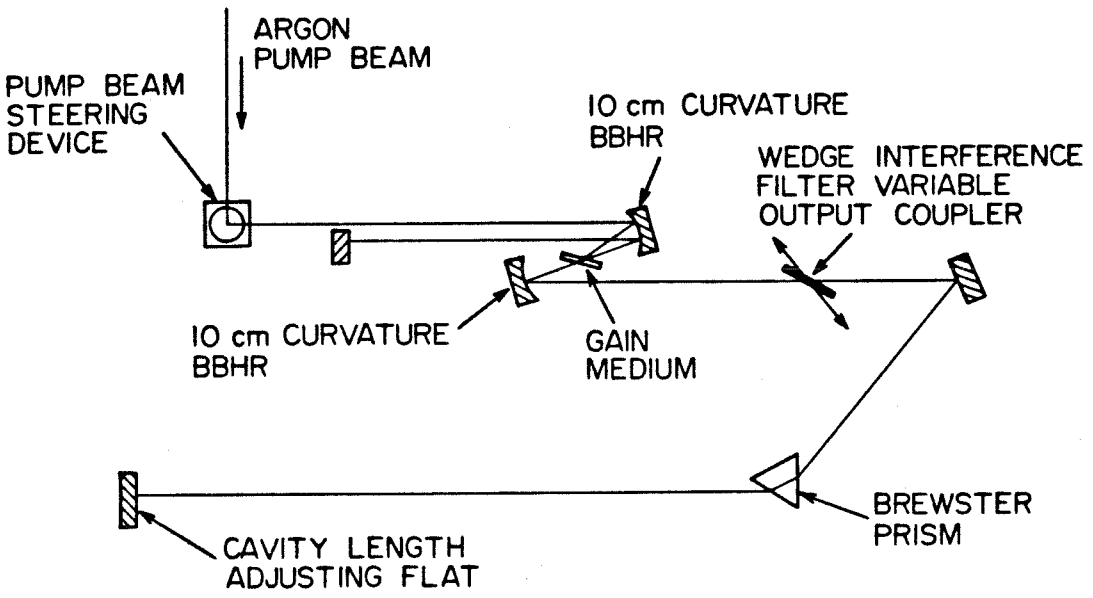

Figure 5.11 Synchronously mode-locked dye laser configuration.

Watt average power in ~ 100 psec wide pulses at 5145 Å . A fairly well resolved typical output pulse is shown in Fig. 5.3. The 75.7 MHz repetition rate is determined by the 396 cm cavity which has a 13.2 nsec round trip time. The pump pulse energy is then roughly in the 10 nJ range with a typical operating current of ~ 40 amps and a 30% output coupler. The argon laser is actively mode-locked by generating a standing acoustic wave in a quartz wavelength selecting Brewster prism. This acousto-optically diffracts energy from the resulting index grating at twice the RF frequency applied to the acoustic transducer on the prism. In practice, a very stable ($\lesssim$ 10 Hz jitter) driver is applied to the prism whose impedance is monitored to select an acoustic resonant frequency. This establishes a good index grating since a large amplitude acoustic standing wave is generated. The argon laser cavity length is then fine tuned with a micrometer adjustment until the round trip frequency matches twice that of the RF drive. As stated earlier, the mode-locking quality is monitored both during adjustments and routinely during normal operations with the APD as shown in Fig. 5.2.

The pump beam enters an eye protecting dust hood made from green-absorbing acrylic which encloses the entire oscillator system. The vertically polarized output at 5145 Å is rotated to horizontal with the beem steering device and incident upon a 10 cm radius of curvature broad band high reflecting mirror. This focusses the pump pulse into the gain medium where it is almost completely absorbed in a ~ 30 μm diameter spot. The gain medium of the dye oscillator is a flowing ethylene glycol jet of ~ 100 μm thickness. The ethylene glycol contains Rhodamine 6G chloride (or R590 chloride, depending on the distributor) in a several millimolar concentration. This flows at ~ 10 m/ sec to help eliminate both thermal problems as well as physically removing dye molecules before the ensemble average triplet state population becomes too large from triplet crossing as shown in Fig. 2.1. The stainless steel nozzle[12] is mounted on an x-y-z stage with the additional capability

of providing angular adjustments to achieve Brewster angle transmission for the signal and pump beams.

The cavity for the dye laser is essentially a 4 mirror cavity, but uses an additional folding flat for practical space considerations. Referring to Fig. 5.11, starting from a Gaussian beam waist at the flat near the beam steering device, the intracavity signal propagates parallel to the pump so it is focussed by the 10 cm mirror to the same spot as the pump in the gain jet. Another 10 cm mirror re-collimates the beam which then propagates eventually to another waist at the end flat and then retraces this path. All mirrors are mounted on micrometer adjustable mounts, with the second 10 cm mirror and the end flat mirror mounted on micrometer driven translation stages as well. This is obviously essential for the 10 cm mirror to provide focussing adjustments, but is also essential on the end to match cavity lengths with the argon ion laser as discussed in Chapter 3. An NRC DM-13 differential micrometer with 0.1 μm resolution provides this length adjustment[13]. The additional bend in the beam path shown in Fig. 5.11 is due to a Brewster prism which by itself would provide tuning and the bandwidth control discussed in Chapter 3; only a select bandwidth is refracted properly to maintain alignment into the highest net gain cavity mode.

The laser has been operated with good results using just the prism for tuning, where the output coupling is achieved using various transmitting mirrors (up to 40%) as the end flat. However, the gain at each wavelength varies and hence the optimal output coupling for good mode-locking is different for each frequency of operation. To achieve some means of establishing a ***variable*** output coupling, a Brewster angle Spectra-Physics wedge interference filter[14] is used in the cavity in *addition* to the tuning prism, and no transmitting mirrors were used anywhere in the cavity. The principle of operation here is that the bandwidth of the interference filter is considerably wider than the effective bandwidth of the prism, so the

prism determines to a large extent at what wavelength lasing occurs. The losses of the interference filter, however, are actually reflections or useful output coupling, so when it is tuned off the lasing wavelength, an increasing and variable amount of output coupling can be achieved in the form of beams reflected in each direction from the filter face. To make this argument quantitative, and to point out the possible drawbacks, we assume two Gaussian filters for the prism and the wedge with transmissions given respectively by

$$P(\lambda) = e^{-\frac{(\lambda-\lambda_p)^2}{\alpha^2}} \qquad W(\lambda) = e^{-\frac{(\lambda-\lambda_w)^2}{\beta^2}} \tag{5.20}$$

Here α and β determine the width of the prism and wedge filters respectively. On a round trip, the net product transmission then becomes

$$P^2(\lambda)W^2(\lambda) = e^{-\frac{2(\Delta\lambda)^2}{(\alpha^2+\beta^2)}} e^{-2\left(\frac{\alpha^2+\beta^2}{\alpha^2\beta^2}\right)(\lambda-\lambda')^2} \tag{5.21}$$

where $\Delta\lambda \equiv \lambda_w - \lambda_p$ and $\lambda' \equiv \dfrac{\beta^2\lambda_p + \alpha^2\lambda_w}{\alpha^2+\beta^2}$.

Assuming that the gain is relatively flat spectrally, the oscillation will then be at λ' where the *total* losses are

$$1 - e^{-2\frac{(\Delta\lambda)^2}{(\alpha^2+\beta^2)}} \tag{5.22}$$

However, the only *useful* output coupling losses are the two beams reflected from the wedge filter whose combined relative intensity is given by

$$\left(1 - W(\lambda')\right)\left(1 + P^2(\lambda')W(\lambda')\right) \tag{5.23}$$

or, letting

$$\delta \equiv \frac{\Delta\lambda}{\sqrt{\alpha^2+\beta^2}} \quad \text{and} \quad f \equiv \frac{\alpha^2}{\alpha^2+\beta^2} \tag{5.24}$$

the total losses become $1 - e^{-2\delta^2}$, and defining $R(\delta, f) \equiv$ useful power expended/

total power expended, we obtain

$$R(\delta, f) = 1 - \frac{\sinh(f\delta^2)}{\sinh(\delta^2)} \tag{5.25}$$

If $f << 1$, almost all losses are in the form of useful output coupling ($R \approx 1$) and the amount of output coupling is controlled just by varying δ. For example, if $\alpha \sim \frac{1}{4}\beta$ already $f = 0.059$ which means that even for losses as high as 50%, in excess of 94% of these losses are in the form of useful output coupling. This corresponds to a practical situation, since the filter bandwidth is $\sim$ 400Å [15] and the prism has an effective bandwidth in the neighborhood of 100Å [16].

One of the drawbacks of this method is that when very little output coupling is desired (for operation at the extreme red or yellow ends of the lasing range), the interference filter must be tuned near its transmission maximum. Since the beam spot is fairly sizable ($\gtrsim$ 1 mm) at the filter, significant transmission changes occur across the spatial profile of the beam and the output beam can then acquire an undesirable spatial modulation with a "bar" in the middle. For most purposes, operation was limited to the higher gain regions of operation and the variable output scheme discussed above was both effective and desirable. Two output beams are then generated; one was fed into the rotating "real time" autocorrelator, while the other coming directly from the gain jet is the beam used for experiments or fed into the amplifier chain. This is because it is larger by a factor $[\, P^2(\lambda' W(\lambda')\,]^{-1} = e^{(1+f)\delta^2}$.

Typical operation of the synchronously pumped dye laser oscillator described above yields pulses in the range of 1 → 3 psec, with operation at the low end of this range and below being hindered by small signal strength and noise problems as discussed in Chapter 3. Longer pulses are achieved by lengthening the cavity, although due to the excess bandwidth of the cavity, long pulse width operation was almost

always accompanied by "noise", as shown in Figures 5.6 and 5.8, in the form of random amplitude or phase fluctuations on the carrier wave. For transform limited long pulse operation, a suitable method is to insert narrower bandwidth birefringent filters in the cavity[15]. The tuning range of the dye laser with R6G is from ~ 5700 Å to ≳ 6500 Å , but very good mode-locking (i.e., noise-free operation) becomes more difficult at the extremes of this range due to the low gain. Typical output energies are ~ $5 - 10 \times 10^{-10}$ joules with the 13.2 nsec pulse repitition period of the argon ion laser.

5.3 The Gigawatt Picosecond Dye Laser Amplifier Chain

5.3a Pump Source

As detailed in the modeling of Chapter 4, due to ASE depletion a pump source should ideally provide its energy in a time comparable to the fluorescence lifetimes of the lasing dyes which comprise the gain medium of the amplifier. The short energetic pulses from a frequency doubled, Q-switched Nd:YAG laser provide an almost ideal pump source for dye laser amplifiers in the 6000 Å region of the spectrum. The Nd:YAG model we employed, chosen for its excellent temporal triggering stability and good spatial beam profile, provided ~ 200 mj at 1.06 μm in a ~ 15 nsec pulse at a 10 hz repetition rate. While there was a pronounced mode-beating structure on the pulse, it was very reproducible from pulse to pulse; this is attributed to good resonator design and the simmering of the flashlamps which gives good reproduction of the gain at the time of Q-switch triggering for each pulse. The output is polarization coupled with a polarizing beam splitter - quarter wave plate combination. The Q-switch is a KD*P Pockels cell. The SHG is performed externally along with the optics for dividing the output to the various amplifier cells.

The 532 nm pulses are generated externally in a KDP crystal using the Type II

process which combines ordinary and extraordinary fundamental pulses to generate an extraordinary freqency doubled pulse. A half wave plate rotates the vertically polarized 1.06 μm fundamental to a 45° angle so it has equal ordinary and extraordinary components in a crystal with its ordinary polarization axis in the vertical direction so the second harmonic can be generated with horizontal polarization. In this case the phase matching condition becomes

$$\Delta k = \frac{\omega}{c}[\, 2n_e^{2\omega}(\vartheta) - n_e^{\omega}(\vartheta) - n_o^{\omega}\,] = 0 \tag{5.26}$$

When this condition is satisfied, a standard calculation gives the power conversion efficiency in a crystal of length L for plane waves taking into account the depletion of the pump waves[5]. This can be recast in a convenient form

$$\frac{P^{2\omega}(z = L)}{P^{\omega}(z = L)} = \tanh^2\left[\, \alpha\sqrt{P_o^{\omega}}\,\frac{L}{D}\right] \tag{5.27}$$

where D is the beam diameter and α is (in MKS units)

$$\alpha = \sqrt{\frac{2}{\pi}}\,\frac{4\pi c}{\lambda n^{\frac{3}{2}}}\left(\frac{\mu_o}{\varepsilon_o}\right)^{\frac{3}{4}}\left[\, \frac{1}{2}(d_{14} + d_{36})\sin 2\vartheta_m\,\right] \tag{5.28}$$

where d_{14} and d_{36} are components of the nonlinear susceptibility tensor. To increase the efficiency of the doubling process, the ~ 8 mm output beam of the Nd:YAG oscillator is reduced in diameter to ~ 5.3 mm before passing through the KDP crystal. This is chosen since it is also the diameter of the 532 beam needed for the last amplifier stage and still keeps the intensities safely below the optical damage thresholds in KDP. For KDP, assuming the Kleinman condition holds[5] and $d_{14} = d_{36} = 4.2\text{x}10^{-24}$ in MKS units[17], the calculated conversion efficiency for plane waves in a 5 cm long crystal is ~ 79% for a 13 megawatt 1.06 μm fundamental in a 5.3 mm beam. This is well into the saturating regime which occurs from the $\tanh^2$ conversion behavior.

One source of errors here results from the finite spatial extent of the beam and the deviation from a true Gaussian beam profile due to the unstable resonator of the Nd:YAG oscillator. This means that a spread in k vectors is present and perfect phase matching cannot occur simultaneously for all components. Another effect from the finite spatial extent of the beams is the so called "double refraction" effect. Assuming the crystal is cut so that $\Delta k = 0$ at normal incidence, Snell's law dictates that the *phase velocity* vectors of the ordinary and extraordinary fundamentals as well as the extraordinary second harmonic all be collinear and normal to the surface. However, the *group velocity* vectors are not in general parallel. It is a straightforward excercise to show that the fundamental veers off from the surface normal by an angle

$$\varphi = \tan^{-1}\left[\frac{1}{2}\left(\frac{1}{(n_o^{\omega})^2} - \frac{1}{(n_e^{\omega})^2}\right)\sin(2\vartheta_m)(n_e^{\omega}(\vartheta_m))^2\right] \tag{5.29}$$

while the extraordinary second harmonic veers off by an angle

$$\rho = \tan^{-1}\left[\frac{1}{2}\left(\frac{1}{(n_o^{2\omega})^2} - \frac{1}{(n_e^{2\omega})^2}\right)\sin(2\vartheta_m)(n_e^{2\omega}(\vartheta_m))^2\right] \tag{5.30}$$

For a 1.06 μm fundamental in KDP, use of Eqs. 5.29-30 yields $\varphi = -1.15°$ and $\rho = -1.40°$ so we have the behavior shown in Fig. 12. For circular beams, the energy overlap is then confined to an elliptically shaped region. Due to this imperfect registration through the crystal, the efficiency suffers and the second harmonic output beam acquires an ellipical shape also. Other factors such as local index fluctuations in an imperfect crystal also reduce the conversion efficiency. In practice, the power conversion efficiency is ~ 35-40% so the output pulse at 532 nm has an energy of ~ 80 mJ. The conversion in the SHG process is a sensitive function of angle, dropping as $\text{sinc}^2(\frac{\Delta kL}{2})$ for imperfect phase matching just as in Eq. 5.2. For an angular deviation $\Delta\vartheta$ such that $\frac{d(\Delta kL)}{d\vartheta}\Delta\vartheta \sim 2\pi$, all conversion is lost. An ele-

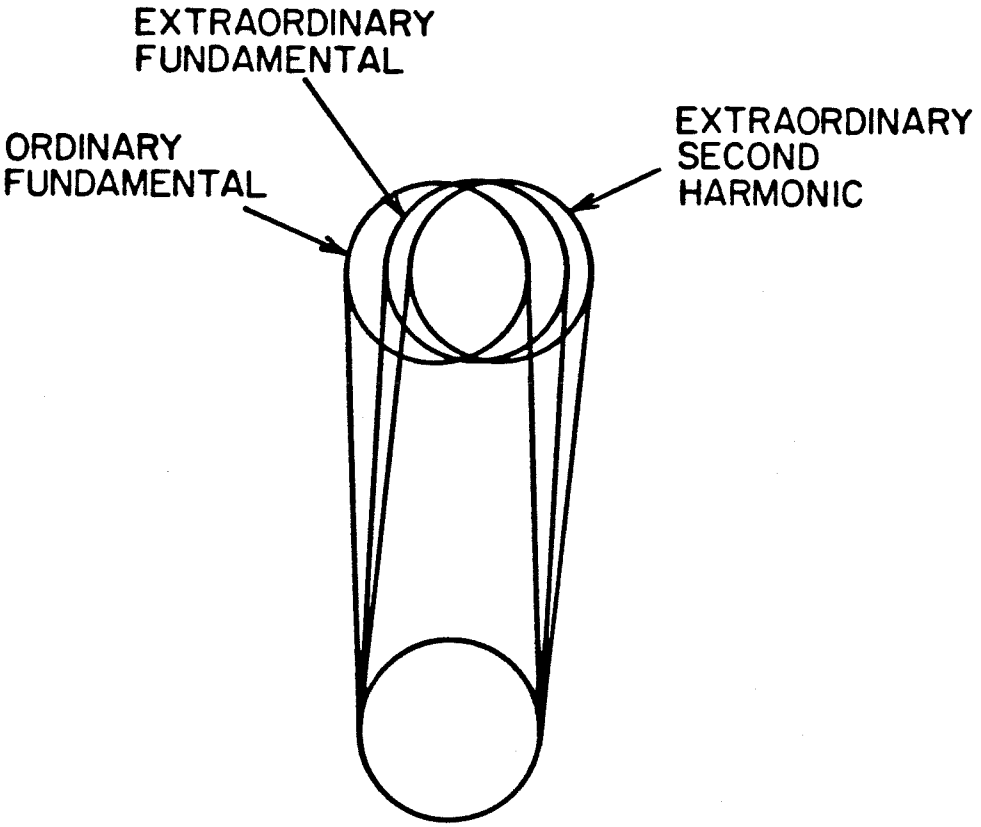

Figure 5.12 Overlap of ordinary and extraordinary fundamental and extraordinary second harmonic for Type II frequency doubling of 1.06 μm in KDP.

mentary calculation for a 5 cm crystal of KDP using Type II phase matching yields $\Delta\vartheta \sim$ 0.5 mrad. For this reason, the KDP is mounted in a quality gimbal mount for fine adjustments in the angle tuning. In practice, this adjustment is done routinely with every use since the oscillator is often re-adjusted; in addition, slow thermal drifts also cause ϑ_m to vary slightly.

As mentioned earlier, mode-beating effects in the Nd:YAG oscillator modulate the intensity envelope of the output. For modeling purposes, the second harmonic pump power was characterized by the normalized functional form

$$P(t) = \sqrt{\frac{4\ln 2}{\pi}}\frac{E}{T_{FWHM}}\left[1 + \delta\cos\varphi e^{-\frac{\pi^2 T_{FWHM}^2}{T_{osc}^2 4\ln 2}}\right]^{-1}\left\{1 + \delta\cos\left(\frac{2\pi t}{T_{osc}} + \varphi\right)\right\} e^{-\frac{t^2 4\ln 2}{T_{FWHM}^2}} \quad (5.31)$$

Here δ controls the modulation depth from the mode-beating and this was set to $\delta = 0.9$ since experimentally the modulation was nearly complete. The oscillation period was fixed by the Nd:YAG oscillator cavity length and was 7.5 nsec. The phase φ was an experimentally adjustable quantity. The "nodes" in Eq. 5.31 are fixed in time relative to the pockels cell Q-switch activation as expected, but the relative amount of energy in the various "beats" depends on the gain at the time of Q-switching since this controls the pulse evolution time. Thus φ is easily varied by small adjustments of the flashlamps with only small concomitant changes in the Nd:YAG pulse *energy*. The over-all pulse width T_{FWHM} depends upon the gain level and on the amount of output coupling. This behavior will be discussed in some detail in Chapter 6 in the context of semiconductor laser pulses. Experimentally, we typically ran the laser with $T_{FWHM} \approx$ 12 nsec. The overall reproducibility of the waveform Eq. 5.31 is fairly good, with peak to peak amplitude flucuations typically $\lesssim \pm 8\%$, while the subnanosecond fluctuation in the temporal position of the nodal points relative to the Q-switch trigger signal was almost negligible.

The excellent triggering stability is invaluable when the 10 Hz 532 nm doubled

Nd:YAG pulses are synchronized with the mode-locked argon ion laser and dye laser. This was accomplished by constructing a synchronous counting circuit[18] which counts down the 37.85 MHz sine wave from the synch output of ultra-stable oscillator of the mode-locker driver for the argon ion laser. At a fixed point in the counting sequence, one pulse generator is triggered for firing the flashlamp of the Nd:YAG oscillator. This pulse generator has a variable delay control to vary the flashlamp firing time over a time scale of ~ 50 μsec. At a later fixed count, (corresponding to ~750 μsec later) a second pulse generator is triggered for the Q-switch. This has only a fine variable delay control with a window of ~ 20 nsec. Since the Q-switched Nd:YAG pulse follows the Q-switch trigger by ~ 100 nsec with very little jitter, this control is used to determine the relative timing of the pump pulse and signal pulse arrival times at the entrance face of the amplifier cells. In addition to these two pulses, there is a pulse generator which puts out a trigger pulse a few hundred nanoseconds before the Q-switch trigger for driving associated equipment such as current pulsers, acousto-optic cavity dumpers, etc. Each of the above mentioned trigger pulses also has a synch output associated with it.

5.3b Physical Layout

The amplifier system is shown in Fig. 5.13. All components are mounted the same floating NRC optical table[13] as the dye oscillator with either magnetic bases or bolts. The amplifier is also enclosed in the same eye protecting dust hood as the oscillator, except the doubling optics are enclosed in an opaque housing to keep all the 1.06 μm high power invisible radiation contained. As already stated, the ~ 8 mm diameter 1.06 μm output beam is rotated by a an anti-reflection coated half wave plate HWP to 45° polarization and then telescoped by T1 to ~ 5.5 mm diameter to insure good doubling efficiency in the 5 cm type II KDP crystal which follows and attain the diameter appropriate for the third amplifier stage. The telescopes are

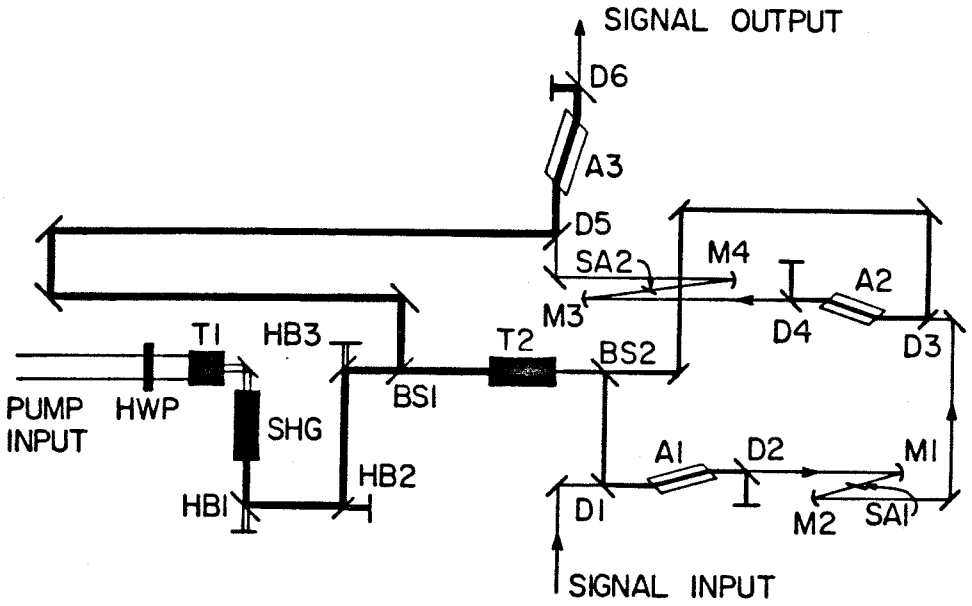

Figure 5.13 Physical layout of the three stage gigawatt picosecond dye laser amplifier chain.

Galilean, using "best form" anti-reflection coated positive and negative lenses[19] to reduce spherical aberration. The KDP crystal is contained in an index matching liquid filled cell with anti-reflection coated windows. Dielectric coated harmonic beamsplitters[20] HB1-3 remove ~ 99.8% of the fundamental and beamsplitter BS1 sends 80% of the energy down a delay line to the third stage A3, while the remaining 20% is telescoped by T2 to ~ 2.5 mm diameter and split approximately in half by BS2 and sent to the first and second stages A1 and A2, again with appropriate delays. The path lengths are adjusted on the table to insure that the relative arrival time of the signal and pump beams are the same at all three stages within ~ 100 psec. All three stages of the system are longitudinally pumped. This follows the analysis of Chapter 4, and as we will explain later, we believe this provides higher gains, better beam homogeneity, and easier alignment than transverse pumping. The 532 nm pump is reflected into and out of the beam path using dichroic mirrors D1-6 which pass most of the signal while reflecting $\gtrsim$ 99% of the pump at 532 nm.

The three flowing dye cells are identical 1.8 cm bore clear tubes shown in Fig. 5.14 with nickel-plated brass end caps to hold the fused quartz Brewster windows. This permits the use of high quality windows and also allows easy and economical replacement of damaged windows. The top exit hole was necessary to allow the escape of bubbles which may enter the circulation system when the pumps are first turned on. The cells are mounted on rotatable x-y-z stages to allow accurate positioning and rotation to the Brewster angle. The system design allows the same (~ 10^{-5} M Rhodamine 640 in methanol) solution of dye to flow in all three cells with one low capacity gear pump[21]. Good filtration for the flow system was necessary to insure the removal of all air bubbles from the optical path; in addition to the filtration, a pinhole with a bleed valve which returned to the main reservoir was used to allow any air to escape from the system. Saturable absorbers SA1-2 are identical ethylene glycol jets formed from stainless steel nozzles mounted in the

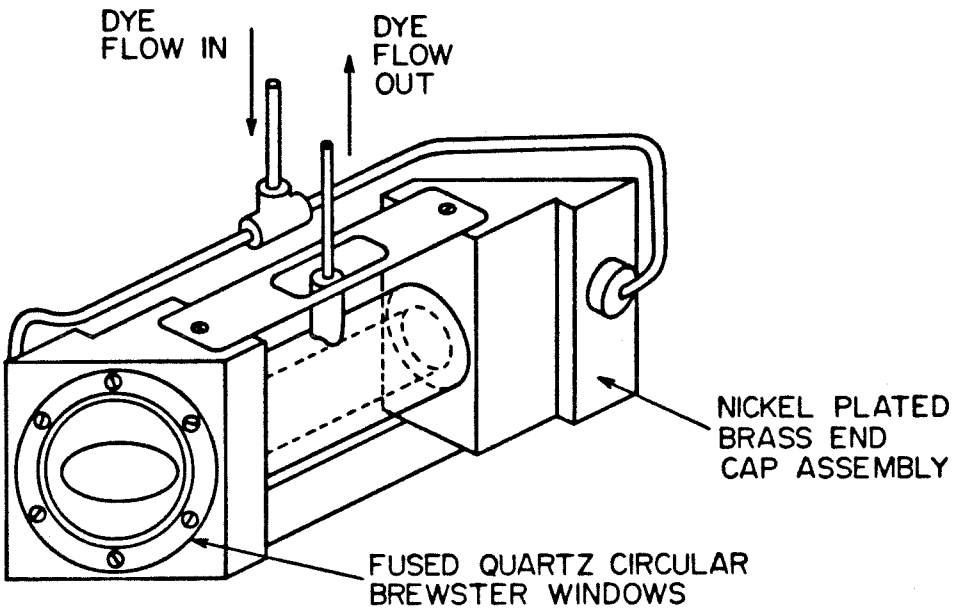

Figure 5.14 Flowing Brewster window dye cell used for all three amplifier stages.

same arrangement as the dye oscillator gain jet described in Section 5.1 for accurate positioning and rotation. The ethylene glycol jets have a high concentration of malachite green having a small signal transmission of $\lesssim 10^{-7}$ at 630 nm. In the manner described in Chapter 4, this provides good control of the leading edge to prevent pulse broadening [8] but still passes ~ 75% of the pulse energy. Without the saturable absorbers flowing, the amplifier chain emits a low divergence superradiant pulse of several millijoules with no input. Mirrors M1 and M2 are 5 cm radius of curvature while M3 and M4 are 20 cm and 50 cm respectively to expand the beam to the appropriate diameter for the last stage. Reflecting optics and Brewster angles at all interfaces are used to eliminate any reflections which would limit the gain in a given stage.

From a practical point of view, the system is designed with simplicity of operation in mind. To simplify the alignment process, no spatial filters have been employed in the design. The high small signal gains ($\gtrsim 10^5$ in a single stage) allow saturable absorber isolation instead, even after the first stage. The transient character of the gain, combined with the threshold effect of the saturable absorber-amplifier combination make it unnecessary to select out a single dye oscillator pulse for amplification; a timing adjustment of the Nd:YAG oscillator Q-switch is sufficient to effectively isolate a single pulse. Since the CW dye oscillator beam and the first stage pump are collinear and have comparable average powers, the first stage alignment is routinely performed visually in seconds. Following SA1, the amplified dye pulse is easily seen even at its low repitition rate, and alignment of the remaining cells proceeds in a similar fashion. This procedure can be repeated quickly any time the pump or signal lasers are adjusted.

Only one circulation system and dye solution is used for all three stages. This is possible with the proper choice of pump beam cross-sectional areas and energies in the various stages, and results in fewer parts and solutions to maintain with

negligible sacrifice of amplification efficiency. Several solvents as well as dyes were tried. Dye selection is discussed in the next section, while methanol or ethanol were found to be the most suitable solvents. Water-Ammonyx LO[22] solutions work equally well as far as amplification is concerned, but seemed to make the optics more susceptible to damage at the solution interface and also left deposits after extensive use.

5.3c Dye Selection

In choosing a lasing dye for the oscillator and amplifier, detailed knowledge of the cross section variations with wavelength is required. Figures 5.15-19 show the emission lineshape and absorption cross sections for five dyes[23] which are of potential interest in the oscillator-amplifier combination. These are Rhodamine 6G chloride (also called R590 chloride, depending upon the manufacturer), Rhodamine B (R610 chloride), Kiton Red (KR620), Rhodamine 101 (R640 perchlorate), and DCM. All are for methanol solutions except DCM which is in the solvent DMSO. The absorption cross sections units are given on the graphs, while the emission cross sections are deduced from the flourescence lineshapes as discussed in the text.

It is well known that in high power pulsed operation, a given lasing dye will almost always have its peak lasing wavelength blue-shifted from its CW lasing value. This results from the much larger ground state population in the CW case and the overlap of the emission and absorption cross sections; at the peak emission cross section, the absorption cross section still has a significant value except in dyes with an extraordinary Stokes shift. Since our dye oscillator uses Rhodamine 6G, its CW lasing range is centered at about 6000 Å. Rhodamine 101 has its peak emission cross section in just this range with a methanol solvent, and is thus an appropriate choice for the high power pulsed amplifier cells. It is known to have an excellent quantum efficiency and has been used in our system for many months wihout

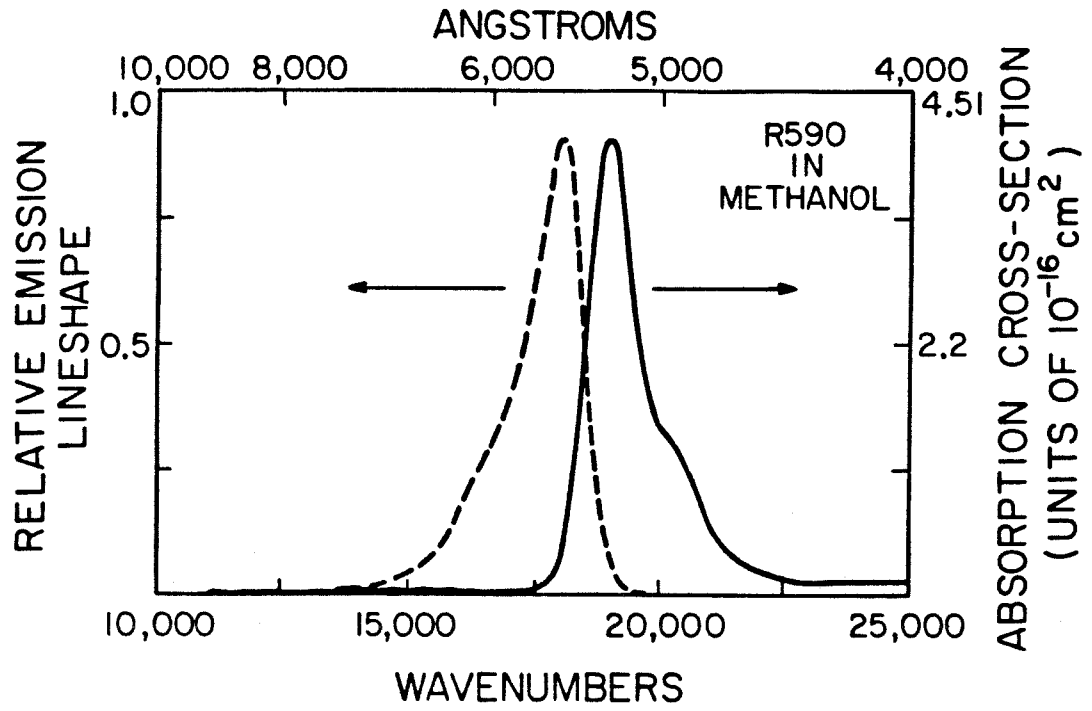

Figure 5.15 Absorption cross section and relative emission lineshape $F(\tilde{\nu})$ for R590 in methanol. For emission cross section see text.

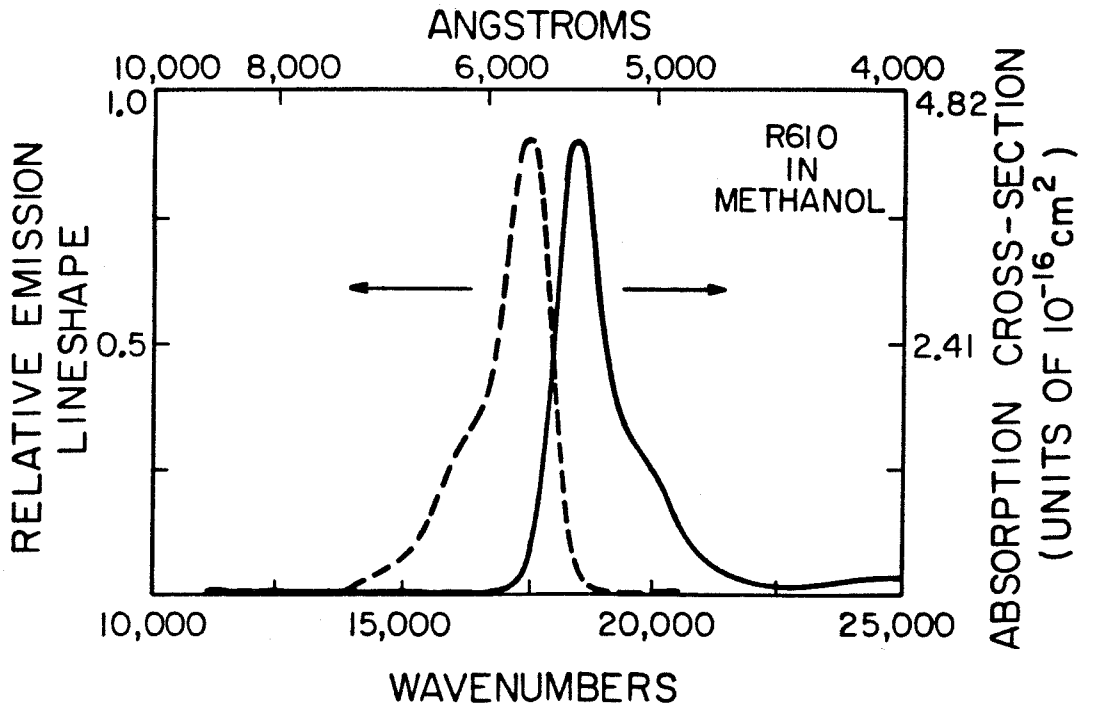

Figure 5.16 Absorption cross section and relative emission lineshape $F(\tilde{\nu})$ for R610 in methanol. For emission cross section see text.

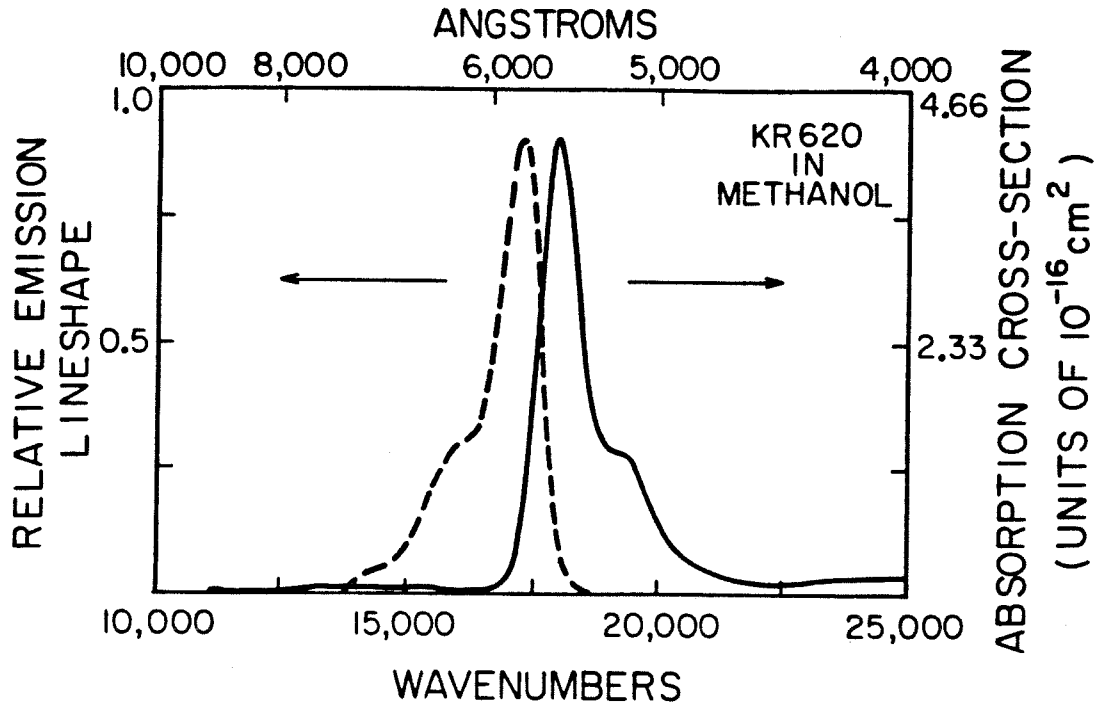

Figure 5.17 Absorption cross section and relative emission lineshape $F(\tilde{\nu})$ for Kiton Red 620 in methanol. For emission cross section see text.

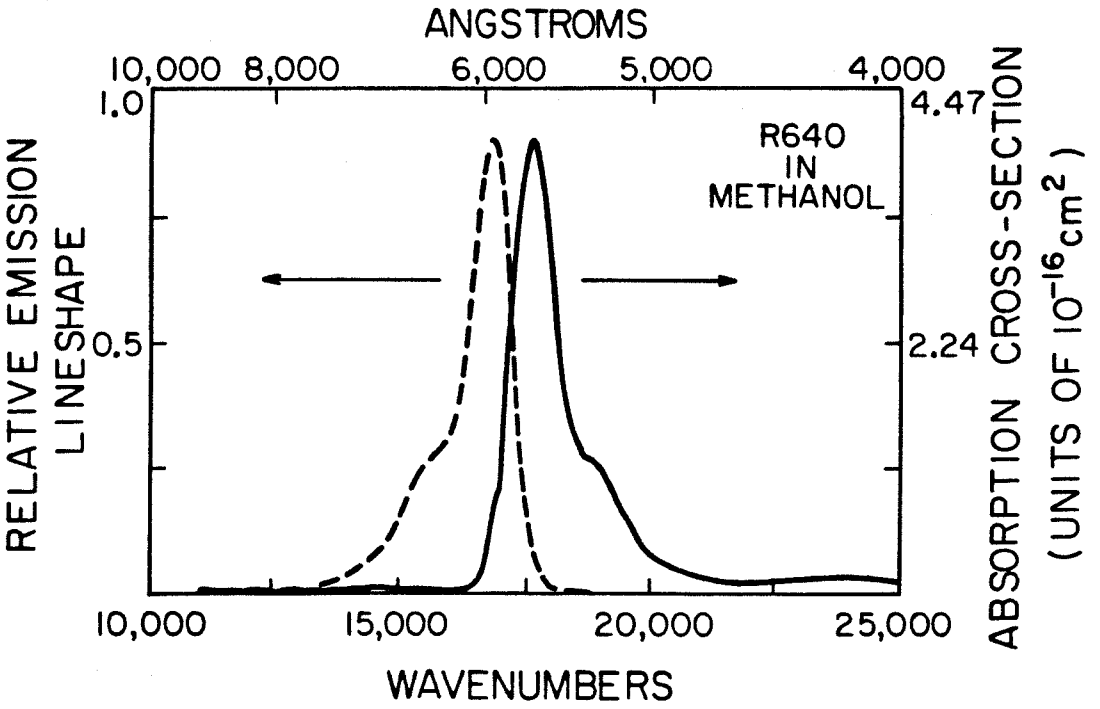

Figure 5.18 Absorption cross section and relative emission lineshape $F(\tilde{\nu})$ for R640 in methanol. For emission cross section see text.

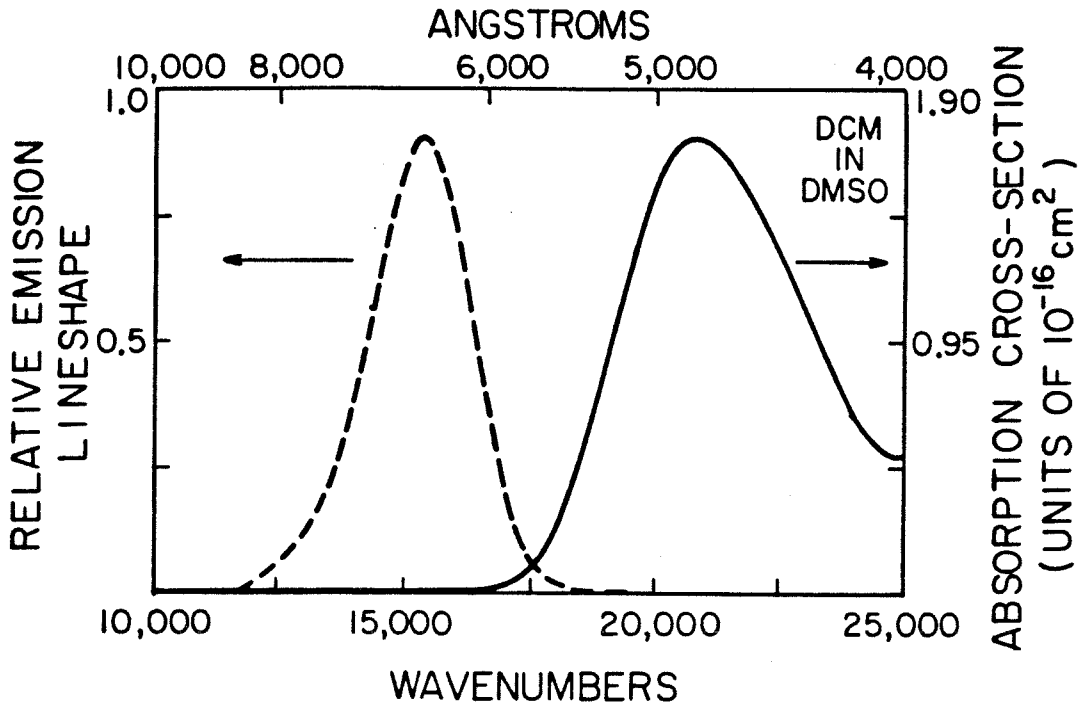

Figure 5.19 Absorption cross section and relative emission lineshape $F(\bar{\nu})$ for DCM in DMSO. For emission cross section see text.

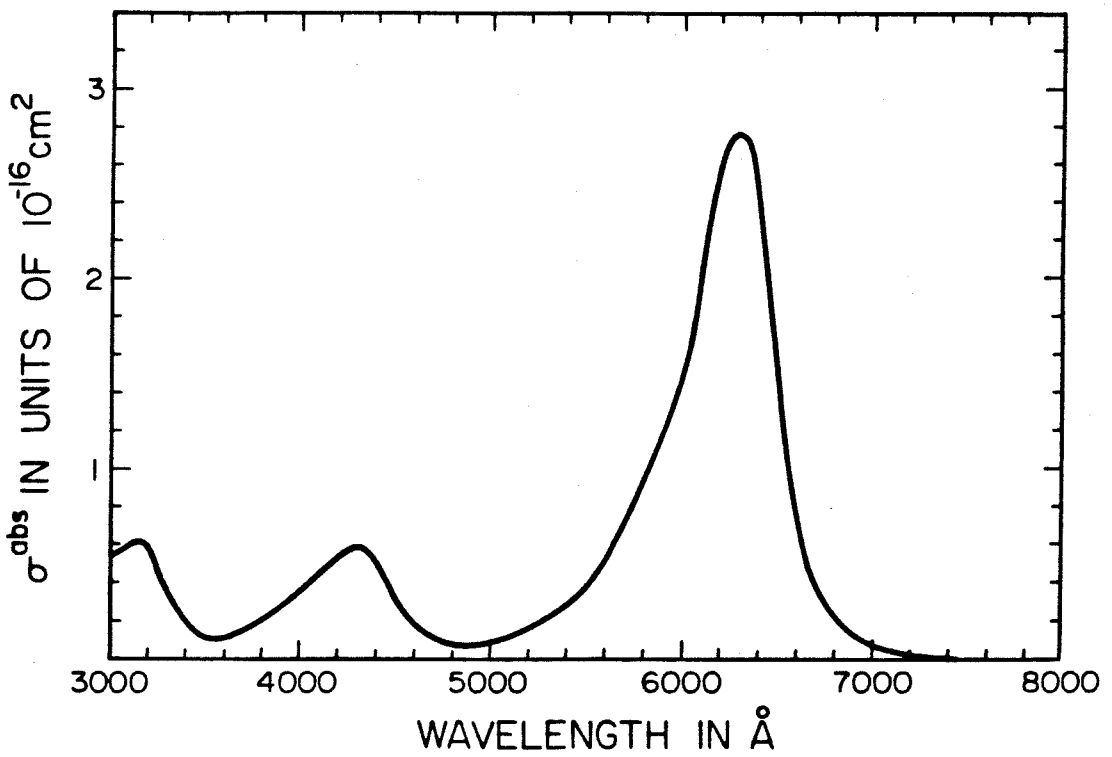

Figure 5.20 Absorption cross section for Malachite Green in Ethylene Glycol.

replacement, which attests to its good chemical stability. Other workable dyes are Kiton Red or Rhodamine B which are slightly yellower, and for operation in the green or red extremes of the oscillator lasing range, Rhodamine 6G or DCM, respectively, have been successfully employed. The matching of the desired amplifier spectral range with the peak emission cross section is essential due to ASE depletion. The gain dependent lifetime τ_{eff} discussed in Chapter 4 depends on the *peak* gain G_0 which occurs near the peak emission cross section under Q-switched pumping. If this gain is geometry-limited by ASE, then the small signal gain at other wavelengths varies *exponentially* with cross section; i.e., the gain $G(\lambda_1)$ at one wavelength λ_1 is related to the gain $G(\lambda_2)$ at λ_2 by

$$G(\lambda_2) = G(\lambda_1)^{\left[\frac{\sigma^{em}(\lambda_2)+\sigma^{abs}(\lambda_2)}{\sigma^{em}(\lambda_1)+\sigma^{abs}(\lambda_1)}\right]} e^{-[\sigma^{abs}(\lambda_2)-(\frac{\sigma^{em}(\lambda_2)+\sigma^{abs}(\lambda_2)}{\sigma^{em}(\lambda_1)+\sigma^{abs}(\lambda_1)})\sigma^{abs}(\lambda_1)]NL} \tag{5.32}$$

Since the amplifier gain is very saturated, this is not a severe problem, but there must still be enough small signal gain for the signal to pass easily through the first saturable absorber. In practice, with Rhodamine 101 an amplifier bandwidth of 350–400 Å is observed under normal conditions. It is also necessary for the dye to have a reasonable absorption cross section at the pump frequency. This is so the pump can be efficiently absorbed, and if the "punch-through" effect discussed in earlier chapters is to operate, the pump must greatly exceed the saturation intensity at the pump frequency. Fig. 5.18 shows the absorption cross section and the flourescence line shape of Rhodamine 101 The absorption cross section is measured in a straightforward manner, but the emission cross section must be deduced from a knowledge of the measured flourescence lineshape $F(\tilde{\nu})$, the flourescence decay time τ, and the quantum yield Φ of the dye using the relation[5]

$$\sigma^{em}(\tilde{\nu}) = \frac{F(\tilde{\nu})\Phi}{8\pi c\tilde{\nu}^2 n^2 \tau} \tag{5.33}$$

where n is the index of the solvent, and $\tilde{\nu}$ is $\frac{1}{\lambda}$ and $F(\tilde{\nu})$ is normalized such that

$\int_0^\infty F(\tilde{\nu})d\tilde{\nu} = 1$. Since accurate knowledge of the flourescence decay time of Rhodamine 101 is not available, we rely instead on an alternative estimate of the emission cross section[24] which says that since transition matrix element for emission and absorption should not differ greatly, the peak emission and absorption cross section should scale proportionally to their frequencies

$$\frac{\sigma_{max}^{em}}{\nu_{max}^{em}} = \frac{\sigma_{max}^{abs}}{\nu_{max}^{abs}} \tag{5.34}$$

Since the quantum efficiency of Rhodamine 101 is known to be very high[25], we assume that a realistic value is 90%, and this in turn allows us to estimate the fluorescence decay time from Eq. 5.33. The result is 4.3 nsec, in good agreement with rough measurements[25]. These are the values which we will use in the remainder of this paper. In passing, we note that the estimated quantum efficiency was also chosen to give a reasonable value for the triplet crossing time

$$\tau_{trip} \approx \tau \frac{\Phi}{(1-\Phi)} \tag{5.35}$$

of 40 nsec which is consistent with observations to be presented in the next subsection.

In general cross sections can be inferred from Figs. 5.15-19 at all wavelengths by using Eq. 5.33 and the relative values of $F(\tilde{\nu})$ read from the graph multiplied by a different normalization constant in each case which is found by integrating the curves. These constants are 6.45×10^{-4} cm, 6.85×10^{-4} cm, 7.52×10^{-4} cm, 7.80×10^{-4} cm, and 4.20×10^{-4} cm, respectively for Figs. 5.15-19. Alternatively, if the experimental values of Φ and τ are not available, an estimate based on Eq. 5.34 and Fig. 5.15-19 suffices.

Another dye which must be chosen is the saturable absorber for stage isolation. The absorption cross section for Malachite Green is shown in Fig. 5.20. This absorbs

strongly in the peak ASE regions of most of the lasing dyes above. In addition, it has been experimentally shown to have extremely short recovery times, which is desirable for gating. In the fairly viscous solvent ethylene glycol which was used, the recovery time τ_r has the value of 5.9 psec[26], while in methanol it is as low as 2 psec. For these reasons, Malachite Green was chosen as the saturable absorber, and was used in what was or nearly was a saturated solution, with a concentration on the order of $\sim 5X10^{18}cm^{-3}$.

5.3d Amplifier Performance and Comparison to Theory

The output of the amplifier system has energy up to 0.7 mj with no pulse broadening unless the saturable absorbers are intentionally misadjusted by a large amount. Fig. 5.21 shows a typical autocorrelation of the output pulse, having a FWHM of 1.36 psec or a pulse width of 0.88 psec if we assume a $sech^2$ pulse shape. Fluctuation in the amplified pulse energy was measured at $\lesssim \pm 6\%$ P-P which was actually a little less than the frequency doubled pump laser energy fluctuation at the time of the measurement. This sub-linear relation between the pump and signal is expected since the ASE depletion makes the signal energy actually sub-linear in pump energy as shown in Fig. 4.3. The spatial profile of the pulse is very good at all points throughout the amplifier chain.

To observe the dependence of the temporal gain profile on the pump temporal profile, the on-axis ASE was monitored with a PIN photodiode. A straightforward calculation reveals that the on-axis ASE power is proportional to $G(\ln G)^{-\frac{1}{2}}$ for high gain, where we have included the spectral narrowing as in Eq. 4.15. This is thus a good monitor of the gain shape. Figs. 5.22-24 show the experimentally observed on-axis ASE together with the pump for three different settings of the adjustable pump phase φ discussed in the context of Eq. 5.31. The first case, Fig. 5.22, shows when the pump has two roughly equal lobes; that the gain is much lower on the second

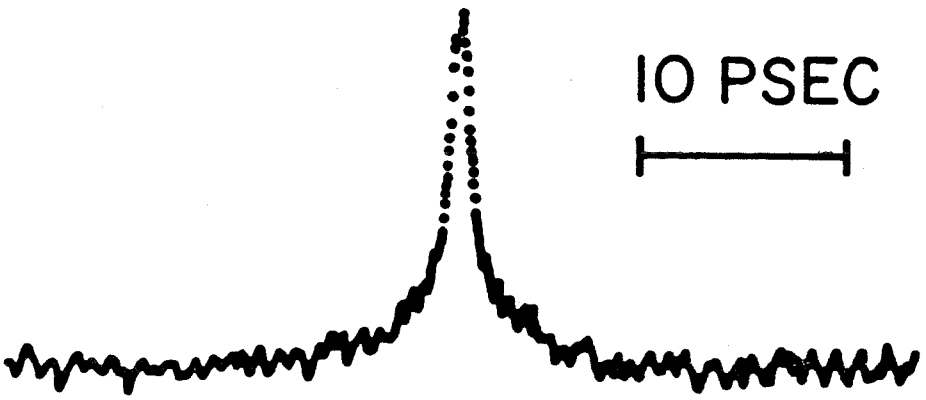

Figure 5.21 Typical autocorrelation trace of amplifier output obtained by slow scan SHG method.

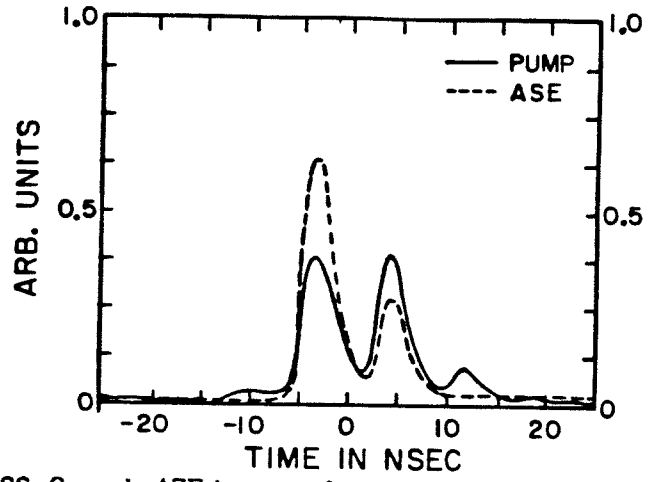

Figure 5.22 On-axis ASE temporal profile from isolated first stage amplifier cell when pump was set to have two equal lobes as shown.

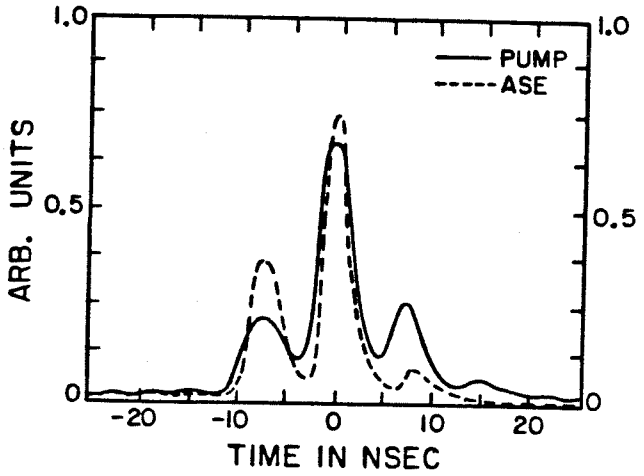

Figure 5.23 On-axis ASE temporal profile from isolated first stage amplifier cell when pump was set to have one main central lobe as shown.

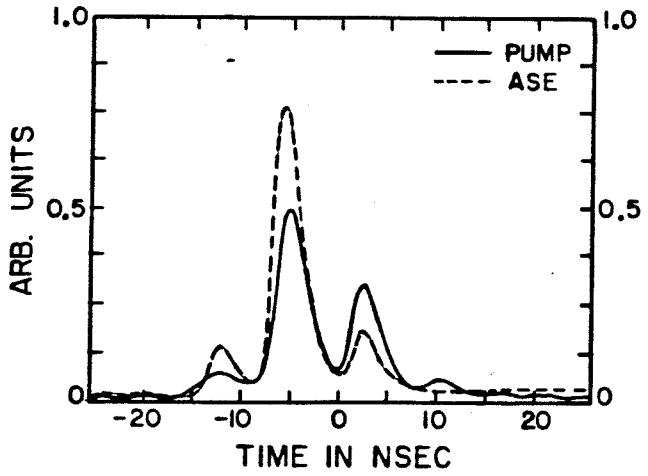

Figure 5.24 On-axis ASE temporal profile from isolated first stage when pump temporal profile was adjusted to the shape which was required to produce the desire single main gain peak.

testifies to the increasing triplet population which reduces the gain in a manner similar to the behavior depicted in Figs. 4.13-14. When φ is phased so the pump is symmetrical in shape and mostly in the central lobe as shown in Fig 5.23, the gain is still quite large in the first small pump lobe. Since one of the desired effects is a "gating" such that only one signal pulse gets amplified, it is desirable to only have one large gain lobe during which signals can gain sufficient energy to bleach through the first saturable absorber. Fig. 5.24 shows this case, which requires an unusual asymmetrical pump pulse. The peak magnitude of the gain, to be discussed more later, was slightly in excess of 50 dB.

For a comparison with the modeling of Chapter 4, we note that the gain evolution is described by Eqs. 4.69-70, with the pump functional form being given by Eq. 5.31. For the first stage of the amplifier chain, the estimated input energy is ~ 6 mJ in typical operation with a pump beam diameter of 2.5 mm. However, for the pump intensity in the dye one must account for the fact that upon entering the dye cell at the Brewster angle, the beam profile becomes elliptical. A straightforward calculation reveals that for a circular beam incident at the Brewster angle for the air/quartz interface, within the liquid the ratio of the major to the minor axis (which is the unchanged input circular diameter) becomes $(1 + n_q^2 - n_q^2/n_L^2)^{1/2}$ where n_q is the quartz index and n_L is the liquid index. This reduces the pump intensity by a full 30%. The absorption cross section at the pump frequency was determined from Fig. 5.18 to be $1.1 \times 10^{-16} cm^2$ while at the emission cross section maximum, the signal emission cross section is $3.92 \times 10^{-16} cm^2$ while the absorption cross section was $5.4 \times 10^{-17} cm^2$. The triplet absorption cross section was taken to be $7.5 \times 10^{-17} cm^2$ with a triplet crossing time of 40 nsec. The dye concentration was $5.2 \times 10^{15} cm^{-3}$. Fig. 5.25 shows the calculated gain behavior for the symmetrical pump pulse case. The agreement with the experimentally observed gain evolution is very good in both magnitude and in temporal shape. Also shown is the triplet loss

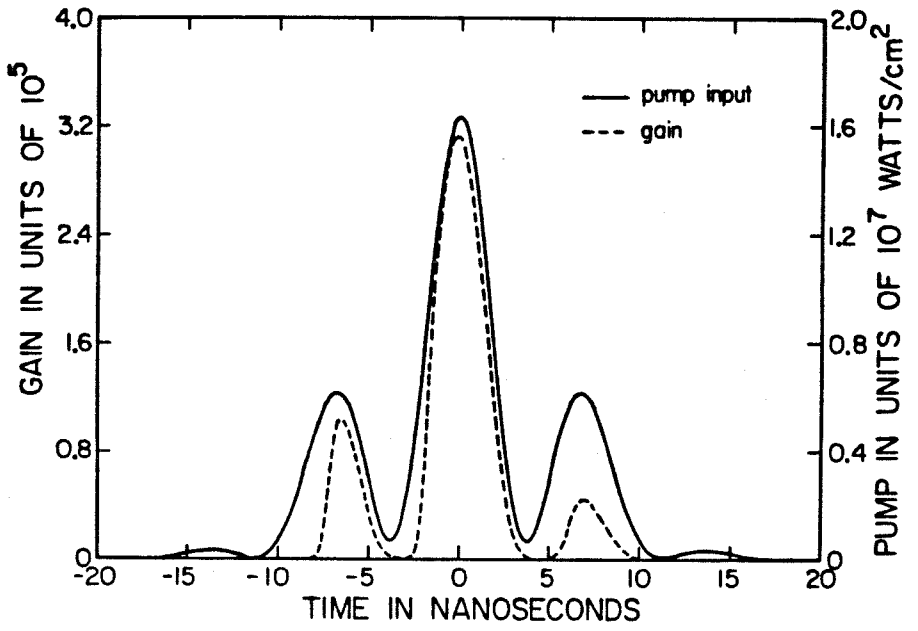

Figure 5.25 Transient gain calculation at 595 nm for first cell including ASE depletion and triplet losses. Pump is measured doubled Nd:YAG power going into first stage.

factor which is incorporated in G just as in Figs. 4.13-14. It can be seen that the triplet state parameters used fit fairly well with the observed gain reduction as shown in Fig. 5.23. Similarly good agreement is found with calculations for the larger diameter final cell, where ASE limits the gain to a slightly smaller value. All calculations ignore the Gaussian nature of the transverse signal profile assuming instead uniform circular spots. The spot diameter estimates for the pump beams were based upon calculated values from the known optics, as well as burn patterns at various points through the system. For the signal, calculated estimates from the known optics and visual estimates were both used; however, where more quantitative numbers were required, the signal beam was expanded and limited with an accurately known aperture for a fairly uniform circular spot.

Figs. 5.26-27 give a comparison of the experimental gain saturation with the simple saturation Eq. 3.24 and the full angular hole burning and triplet loss result Eq. 4.67. Fig. 5.26 shows the gain saturation results for the second amplifier cell of the chain where the dye laser oscillator has been tuned to the peak gain wavelength. Here the small signal gain G_0 of the theoretical expressions were fit to the observed small signal gains. The actual gains were higher since both the calculations and the measured values include the linear losses of the dichroics before and after each cell. The dashed curve shows the simple result Eq. 3.24, while the full curve shows Eq. 4.67. For the latter, the value of R_0 was taken to be 0.6 which was derived from a transient gain calculation just like that of Fig. 5.25; this is a reasonable value and the saturation behavior is not extremely sensitive to this parameter. As can be seen, the agreement with the more complete theory is quite good. Fig. 5.27 shows the results for the third amplifier cell at two different wavelengths. The peak gain is smaller, but again the agreement is quite good.

Output pulse widths were almost always roughly the same as the input value. One of the shorter pulse autocorrelations is shown in Fig. 5.28, with a FWHM of 1.0

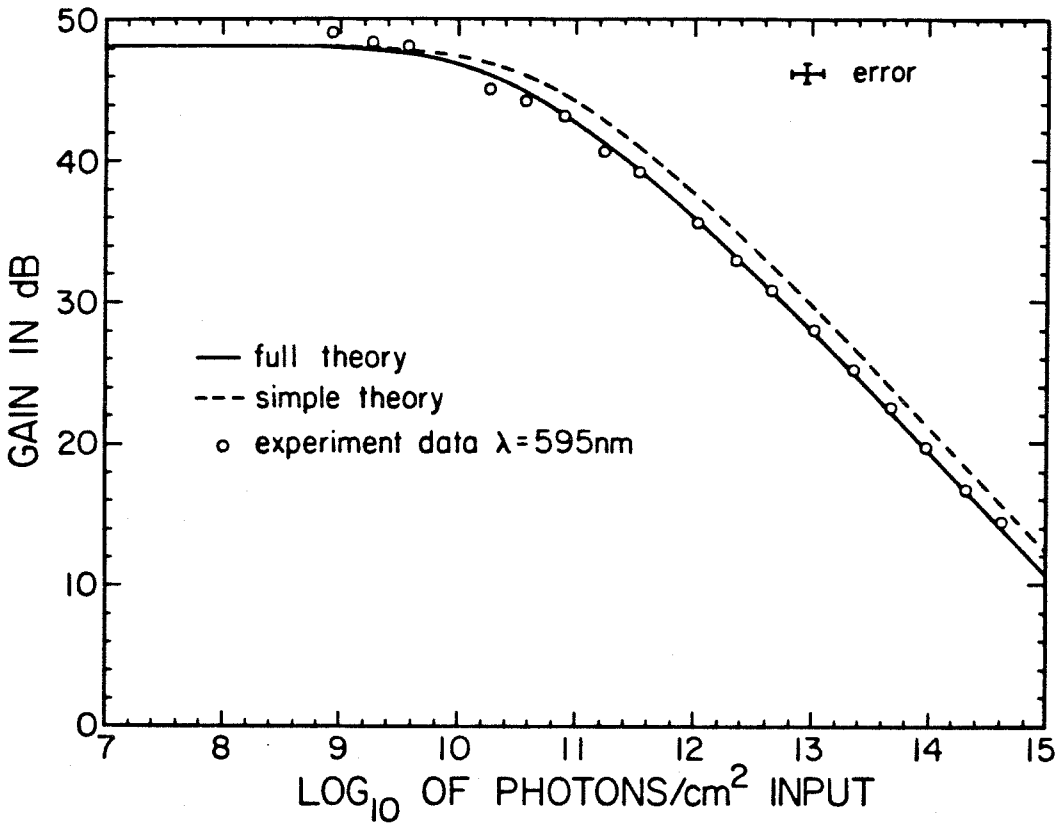

Figure 5.26 Second stage saturation behavior at 595 nm. Dashed curve represents Eq. 3.24; solid curve is Eq. 4.67. Linear losses are included in measured values, so actual gain is higher.

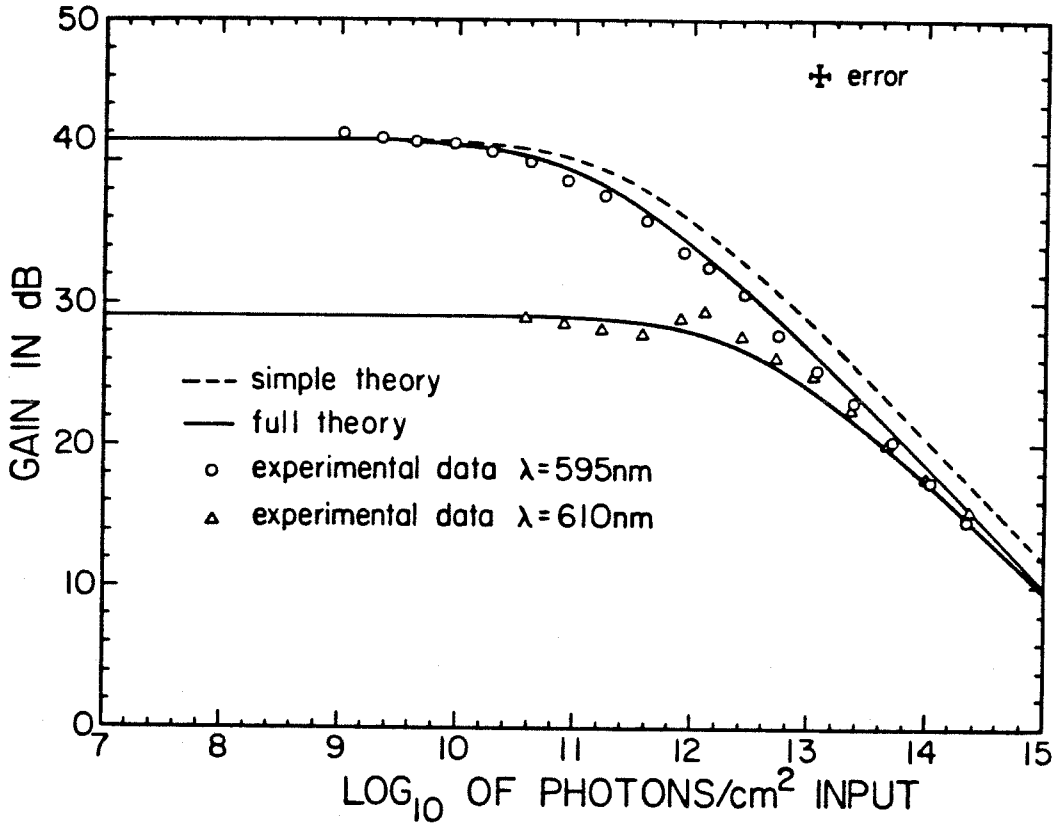

Figure 5.27 Third stage saturation behavior at 595 nm and 610 nm. Dashed curve represents Eq. 3.24; solid curve is Eq. 4.67. Linear losses are included in measured values, so actual gain is higher.

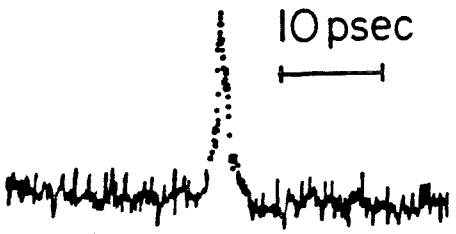

Figure 5.28 Short pulse autocorrelation from the amplifier system with only two sweeps, or very little signal averaging.

psec, indicating a pulse width of ~ 0.65 psec where no averaging has been done. A more typical result is shown in Fig.5.21. For a comparison with the pulse shaping effects discussed in Chapter 4, the set of equations Eqs. 4.27-31 were integrated with the parameter values corresponding to experimental conditions at the peak gain wavelength. This was done in two cases, one with normal amplifier adjustment, the other with first saturable absorber jet moved intentionally out of focus to hinder the pulse compression process. The results of such a calculation are shown in Figs. 5.29-32 where the input signal pulse is taken to have a 2 psec FWHM $sech^2$ intensity profile. The data used for G_o are actual typical measured values for the small signal gains or attenuations of each amplifier section. In Fig. 5.29, the curves show the input pulse shape, and the shape after the first, second, and third stages at the equivalent to points 1,3, and 5 in Fig. 4.5. The curves are normalized to have the same amplitude, but with a nJ input, the calculated pulse energies are $1.0x10^{-5}$, $4.2x10^{-5}$, and $7.1x10^{-4}$ joules respectively for the same points in the chain. These are the same orders of magnitude as the observed energies, but exact agreement with the experimental gain distribution among the three cells can not be expected since the Eqs. 4.27-31 are somewhat simplistic. In addition, the actual distrubution is extremely wavelength sensitive, although the net *combined* gain is not. Fig. 5.30 shows the computed autocorrelation curves of the input, and the second and third stage outputs. The first stage output autocorrelation is not shown since its shape varies only slightly from the input autocorrelation. These figures correspond to "normal" adjustment of the amplifier apparatus and the numerical values used in the calculation reflect this. The most obvious feature is the pulse compression at the amplifier output just as in the earlier modeling of Fig. 4.6. The extreme saturation of the second stage in this calculation has led to a tail before entering the third stage. Either a reduction in the first stage gain or a larger optical density of the saturable absorber would eliminate this effect without appreciably changing the

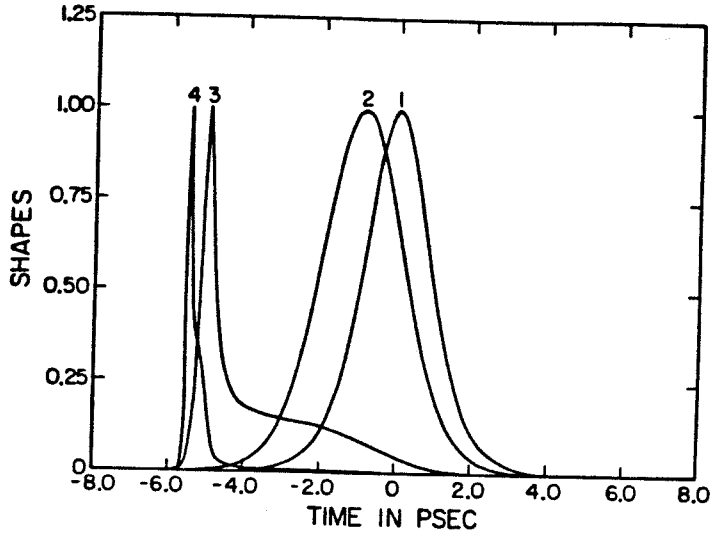

Figure 5.29 Calculated pulse shape upon propagation through amplifier chain. Curves 1-4 represent the input and after each of the three successive stages. Energies and parameters used in calculation are given in text.

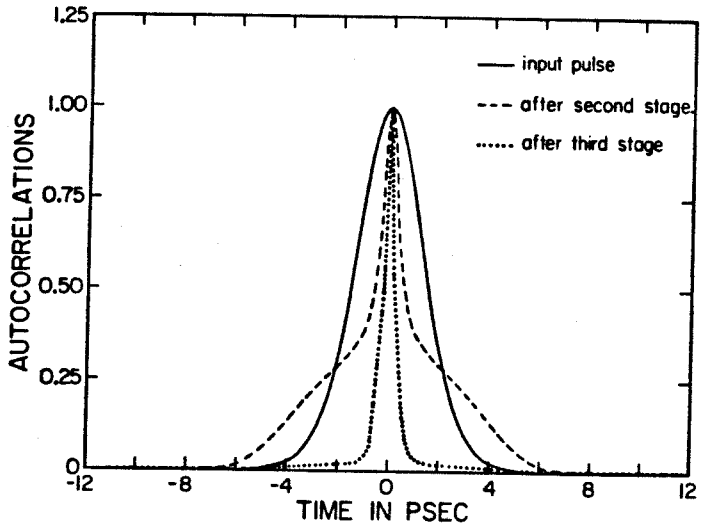

Figure 5.30 Calculated autocorrelations at different points through amplifier chain. Curves 1-3 are the input and after the second and third stages, respectively. Parameters used are given in text.

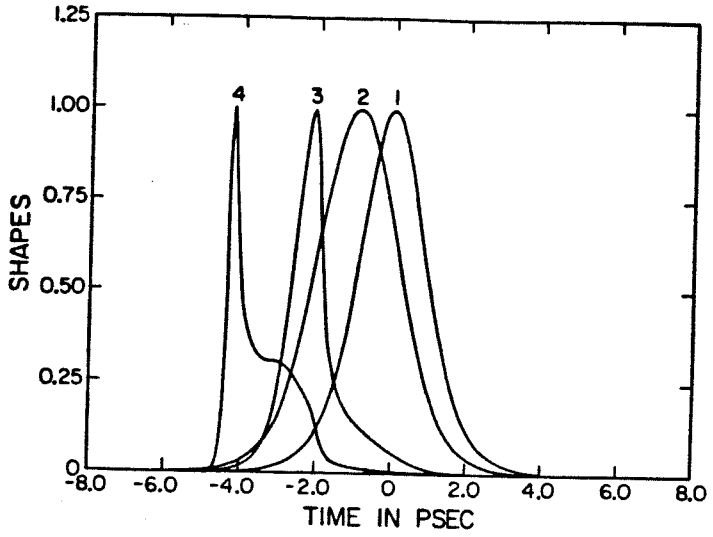

Figure 5.31 Calculated pulse shapes of misadjusted amplifier chain (see text); curves have same meaning as in Fig. 5.29.

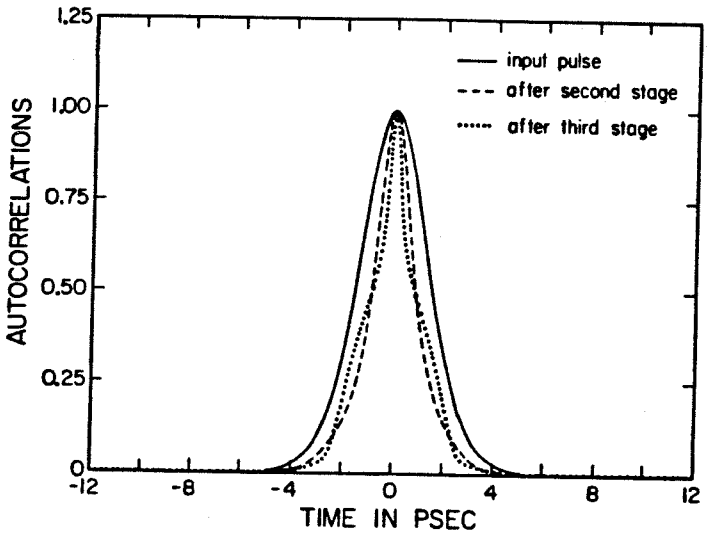

Figure 5.32 Calculated autocorrelations of misadjusted amplifier chain (see text); curves have same meaning as in Fig. 5.30.

energy. However, note that the tail has disappeared after the third stage and the compression has occurred despite the tail.

Figs. 5.31-32 show the same results with the first saturable absorber intentionally misadjusted by moving the saturable absorber jet ≈ 0.5 centimeter away from the focal point of the first set of fucussing optics. This reduces the intensity so that it does not exceed the saturation intensity of the saturable absorber dye by as large an amount and effectively softens the leading edge of the pulse going into the second stage. This hinders the compression process and after the third stage the pulse displays an undesirable lobe on the tail with no compression at all.

Experimentally, we found some of the expectations of the simple analysis above to be exaggerated. In particular, we found little pulse compression, although routine operation resulted in an output pulse which was almost always the same or only slightly shorter than the input pulse. However, when the first saturable absorber jet was intentionally misadjusted as described above, very noticeable pulse *broadening* resulted. This is shown in Fig. 5.33. The upper trace is the input to the amplifier, with the dye oscillator slightly misadjusted to get pulses which were a little broader than their minimum value, just to see if any compression would be visible. The second trace is the amplifier output with normal adjustment and is almost a perfect replica of the input pulse, an unexpected result in light of the extreme nonlinearity in the amplification process. The third trace shows the amplifier output with the first saturable absorber jet moved out of focus as explained above, and the broadening is easily seen. The lack of compression seems to indicate that there is a significant pulse broadening process which competes with the compression mechanism described above. A number of potential mechanisms for broadening were discussed in Section 4.3. One likely candidate is the finite vibrational lifetime in conjuntion with ordinary dispersion. Recent literature[27] has found for R6G in ethanol a vibrational relaxation time in the lowest singlet state a value of $\tau_R \sim 0.5$

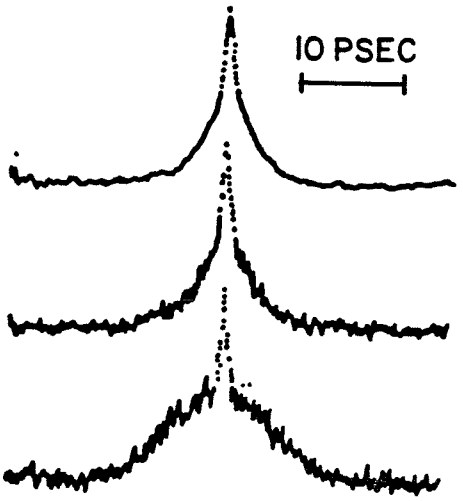

Figure 5.33 Experimental test for compression. Upper trace is input autocorrelation, with slight intentional broadening. Middle trace is amplifier chain output under normal adjustment, lower trace is with amplifier chain misadjusted as explained in text.

psec. Earlier work[28] found $\tau_R \lesssim 0.2$ psec for R640 in ethylene glycol. The vibrational relaxation times appear to be difficult to measure, but values in this time regime ($\tau_R = 0.25$ psec) were used for the numerically simulated propagation in Chapter 4, and significant pulse broadening effects were evident. As mentioned at that time, ordinary dispersion could prevent the predicted leading spike formation resulting in expected pulses of duration $\sim \tau_R$. However, neither of these effects should be sufficiently strong in this time regime to prevent a *small* amount of pulse compression from taking place even when a reasonable amount of self-phase modulation[29] is included to enhance the pulse dispersion.

CHAPTER 5 REFERENCES

1. D. H. Auston, A. M. Johnson, P. R. Smith, and J. C. Bean, Appl. Phys. Lett. **37**, 371 (1980).

2. D. M. Bloom, S. Y. Wang, and D. M. Collins, " 10 GHZ Bandwidth GaAs Photodiodes," Technical Digest, Conference on Lasers and Electro-Optics, Phoenix, Arizona, p.64, 1982.

3. See for example: E. P. Ippen and C. V. Shank, " Techniques for Measurement," in *Ultrashort Light Pulses*, Topics in Applied Physics, Vol. 18, Ed. by S. L. Shapiro, Springer-Verlag, Berlin, Heidelberg, New York, 1977.

4. H. Mahr and M. D. Hirsch, Opt. Commun. **13**, 96 (1975).

5. A. Yariv, *Quantum Electronics*, John Wiley & Sons, Inc., New York, 1975.

6. F. Zernike, Jr., J. Opt. Soc. Am. **54**, 1215 (1964).

7. S. K. Kurtz, " Nonlinear Optical Materials," in *Laser Handbook*, Vol. 1, Ed. by F. T. Arecchi and E. O. Schulz-Dubois, North-Holland Publishing Co., Amsterdam, 1972.

8. J. Comly and E. Garmire, Appl. Phys. Lett. **12**, 7 (1968).

9. W. H. Glenn, IEEE J. Quantum Electon. **QE-5**, 284 (1969).

10. H. A. Pike and M. Hercher, J. Appl. Phys. **41**, 4562 (1970).

11. Cleveland Crystals, Inc., Cleveland, Ohio.

12. Coherent Radiation, Inc., Palo Alto, California.

13. Newport Research Corp., Newport Beach, California.

14. Spectra-Physics, Inc., Mountain View, California.

15. C. P. Ausschnitt and R. K. Jain, Appl. Phys. Lett. **32**, 727 (1978).

16. F. P. Schafer, "Liquid Lasers," in *Laser Handbook*, Vol. 1, Ed. by F. T. Arecchi and E. O. Schulz-Dubois, North-Holland Publishing Co., Amsterdam, 1972.

17. S. Singh, "Nonlinear Optical Materials," in *CRC Handbook of Lasers with Selected Data on Optical Technology*, Ed. by R. J. Pressley, The Chemical Rubber Co., Cleveland, Ohio, 1971.

18. Circuit designed and constructed by D. A. Armstrong, Eng., California Institute of Technology, 1981.

19. Special Optics, Little Falls, New Jersey.

20. CVI Laser Corp., Albuquerque, New Mexico.

21. Micropump Corp., Concord, California.

22. Onyx Chemical Co., Jersey City, New Jersey.

23. S. Batchelder, Ph. D. Thesis, California Institute of Technology, 1982.

24. P. R. Hammond, IEEE J. Quantum Electron., Vol. **QE-16**, 1157 (1980).

25. T. Karstens and K. Kobs, J. Phys. Chem. **84**, 1871 (1980).

26. E. P. Ippen, C. V. Shank and A. Bergman, Chem. Phys. Lett. **38**, 611 (1976).

27. D. Reiser and A. Laubereau, Appl. Phys. **B 27**, 115 (1982).

28. J. M. Weisenfeld and E. P. Ippen, Chem. Phys. Lett. **67**, 213 (1979).

29. See for example: D. H. Auston, " Picosecond Nonlinear Optics," in *Ultrashort Light Pulses*, Ed. by S. L. Shapiro, Springer-Verlag, Berlin, Heidelburg, New York, 1977.

CHAPTER 6

CAVITY RATE EQUATIONS AND APPLICATIONS TO OPTICALLY Q-SWITCHED SEMICONDUCTOR LASERS

In this chapter we modify the TW rate equations of Chapter 2 for a simple treatment of semiconductor laser dynamics. This permits some general but approximate observations on short pulse evolution in semiconductor lasers while reserving a more sophisticated treatment of picosecond carrier dynamics in short pulse semiconductor lasers for Chapter 7. Experimentally, results from a stripe geometry picosecond optically Q-switched semiconductor laser are presented to support the gross features of the rate equation analysis in ultra-fast time regimes.

6.1 TW Rate Equations for Semiconductor Laser Cavities.

For bi-directional propagation of light in a semiconductor laser cavity, we must write a TW rate equation for both a positive traveling wave φ^+ and a negative traveling wave φ^-. In addition, a source term must be added to account for the spontaneous emission which "feeds" the two waves. To account for linear losses while propagating down the cavity, a linear distributed loss α is also added; this includes both linear absorption in the semiconductor as well as scattering losses which may result from imperfections in the dielectric waveguiding structure. With these modifications, the equations Eqs. 2.24-25 become generalized to the well known rate

equations

$$\frac{\partial \varphi^+}{\partial t} + v_g \frac{\partial \varphi^+}{\partial z} = v_g(\Gamma\gamma(n) - \alpha)\varphi^+ + \frac{\beta n}{2\tau_s} \tag{6.1}$$

$$\frac{\partial \varphi^-}{\partial t} - v_g \frac{\partial \varphi^-}{\partial z} = v_g(\Gamma\gamma(n) - \alpha)\varphi^- + \frac{\beta n}{2\tau_s} \tag{6.2}$$

$$\frac{\partial n}{\partial t} = P_n(z, t) - v_g\gamma(n)(\varphi^+ + \varphi^-) - \frac{n}{\tau_s} \tag{6.3}$$

Here n is the electron density in the conduction band, and we assume for simplicity intrinsic material so n = p ; $\gamma(n)$ is the carrier density dependent gain coefficient which is analogous to the concentration cross section product in the dye rate equations. The actual gain is $\Gamma\gamma(n)$ where Γ is a mode confinement factor. This arises since we have continued to use the photon density concept but have neglected transverse variations in the fields and carrier densities. Under the assumption that the transverse behavior is not z dependent, one way to deal with this is to specify that rate equations are for the on-axis (x = 0, y = 0) values of $\varphi^{+,-}$ and n but the $\gamma(n)$ which appears is actually $\frac{V_m}{V_c}\bar{\gamma}$ where

$$\bar{\gamma} \equiv \frac{\int\int dxdy\ \varphi\gamma(n)}{\int\int dxdy\ \varphi} \tag{6.4}$$

and

$$V_m \equiv \frac{\int\int dxdy\ \varphi}{\varphi(x = 0, y = 0)} \quad \text{and} \quad V_c \equiv \frac{\int\int dxdy\ n}{n(x = 0, y = 0)} \tag{6.5}$$

In this case, we obtain $\Gamma = \frac{V_c}{V_m}$. We note that this is not the conventional definition[1] of Γ, but it suits the present formalism.

The term $P_n(z, t)$ which appears in Eq. 6.3 is a pumping term for the carrier density which in general can be n dependent. As mentioned above, α is the distributed linear loss, while β is the fraction of spontaneous emission[2] into the lasing

mode(s). The spontaneous lifetime τ_s is in general also n dependent.

The essential ingredient of the laser cavity is the optical feedback provided by the end mirrors, and this feature is incorporated into the boundary conditions for Eqs. 6.1-3. For a laser extending from $z = -\frac{L}{2}$ to $Z = \frac{L}{2}$ these conditions are

$$\varphi^+(z = -\frac{L}{2}) = R\varphi^-(z = -\frac{L}{2}) \quad \text{and} \quad \varphi^-(z = \frac{L}{2}) = R\varphi^+(z = \frac{L}{2}) \tag{6.6}$$

Here we make no attempt to discuss the coherence properties of the pulsed semiconductor laser optical fields. However, as will be discussed later, Eqs. 6.1-3 can be used for a discussion of some aspects of multi-mode "mode-beating" phenomena which can manifest themselves as an intensity modulation at the round trip frequency of the cavity.

For a general discussion of the gross features of short pulse evolution, we temporarily abandon the full set of equations Eqs. 6.1-3 in favor of a simpler space-independent treatment. The essential approximation in this scheme is common to many treatments of laser dynamics and consists of some means of spatial averaging. The conditions under which this procedure is accurate in steady state have been dealt with in some detail and the reader is referred to the literature[3]. The basic result of spatial averaging is the replacement of the z derivatives in Eqs. 6.1-2 with an effective distributed loss. This is reasonable since under steady state the gain must equal the loss, and the boundary conditions Eqs. 6.6 demand that the intensity grow by a factor of $\frac{1}{R}$ across the length of the device. If the gain is fairly uniform, which follows when the mirror reflectivity is not too low, this will be roughly exponential growth and hence the derivatives in z can be replaced by an additional distributed loss on the RHS of Eqs. 6.1-2

$$\alpha_{\text{mirrors}} = -\frac{\ln R}{L} \tag{6.7}$$

We then obtain the equations

$$\frac{dF}{dt} = v_g(\Gamma\gamma(n) - \alpha + \frac{\ln R}{L})F + \beta\frac{n}{\tau_s} \tag{6.8}$$

$$\frac{\partial n}{\partial t} = P_n(t) - v_g\gamma(n)F - \frac{n}{\tau_s} \tag{6.9}$$

Where $F = \frac{1}{L}\int_{-\frac{L}{2}}^{\frac{L}{2}}(\varphi^+ + \varphi^-)dz$ and n and P_n are also spatially averaged. We also adopt the standard approximation of a linear gain dependence on carrier density, letting $\Gamma\gamma(n) = \kappa(n - n_0)$ where κ is the effective gain/(unit inversion).

To extract some simple analytical results, we note that the spontaneous emission source terms in Eqs. 6.8-9 merely serve to "start" the oscillation if the gain is reasonably large; very quickly the signal grows to a level where the "noise" contribution is negligible. In this regard, providing an *initial value* to the field F can substitute for the τ_s terms on the RHS of Eqs. 6.8-9, and if there is no pumping present as well, we then deal with the much simpler set

$$\frac{dF}{dt} = v_g[\ \kappa(n - n_0) - \alpha + \frac{\ln R}{L}\ ]F \tag{6.10}$$

$$\frac{dn}{dt} = -v_g[\ \kappa(n - n_0)\ ]F \tag{6.11}$$

We define

$$\tau_p \equiv [\ v_g(\alpha - \frac{\ln R}{L})\ ]^{-1} \tag{6.12}$$

where τ_p is referred to as the "photon lifetime" or the "cavity lifetime". Similarly, we let $n - n_0 \equiv N$ where N is the effective inversion level and then define

$$N_T \equiv \frac{(\alpha - \frac{\ln R}{L})}{\kappa} = \frac{1}{\tau_p v_g \kappa} \tag{6.13}$$

which is the threshold inversion level. Eqs. 6.10-11 become

$$\frac{dF}{d\tau} = \left[\frac{N}{N_T} - 1 \right] F \tag{6.14}$$

$$\frac{dN}{d\tau} = -\frac{N}{N_T} F \tag{6.15}$$

where $\tau \equiv \frac{t}{\tau_p}$ is the normalized time variable.

These equations were first developed for a description of giant pulse evolution in Q-switched lasers[4] and have been used extensively for that purpose. We now review the basic results. Dividing Eq. 6.14 by Eq. 6.15 and integrating in N yields

$$F = F_0 + (N_0 - N) - N_T \ln\left[\frac{N_0}{N}\right] \tag{6.16}$$

where F_0 and N_0 are the initial values of the average photon densities and inversion levels. For most purposes, $F_0 << N_0, N_T$ and is thus neglected. The total power emitted from the laser is simply given by

$$P(\tau) = - v_g A F(\tau) h\nu \ln R \tag{6.17}$$

where A is the cross sectional active area of the laser. From Eq. 6.16, $\left.\frac{\partial F}{\partial N}\right|_{N_T} = 0$, so the maximum in the pulse occurs when $N = N_T$ at which point the peak power is thus

$$P_{peak} = = - v_g A N_T h\nu \ln R \left[\left(\frac{N}{N_T} - 1\right) - \ln\left(\frac{N_0}{N_T}\right) \right] \tag{6.18}$$

The total energy in the pulse can be obtained by setting $F = 0$ in Eq. 6.16 to obtain the final inversion N_F when the optical energy has all decayed away. The difference between this and the initial inversion is the expended inversion; since only a frac-

tion $\ln R/(\ln R - \alpha L)$ of this is output, the pulse energy becomes

$$E_{pulse} = \frac{\ln R}{\ln R - \alpha L} h\nu AL\Delta N \tag{6.19}$$

where $\Delta N \equiv N_0 - N_F$ and is given by solving

$$\Delta N = N_0\left[\, 1 - e^{-\frac{\Delta N}{N_T}} \,\right] \tag{6.20}$$

A measure of the pulse *width* in time is obtained by dividing the energy in Eq. 6.19 by the peak power in Eq. 6.18

$$T_{pulse} \sim \frac{E_{pulse}}{P_{peak}} \tag{6.21}$$

Inserting Eq. 6.16 back into Eq. 6.15 and integrating yields the "solution" to Eqs. 6.13-14 as

$$\tau(N) = N_T \int_N^{N_0} \frac{dN'}{N'\left[\, F_0 + N_0 - N' - \ln\left(\frac{N_0}{N'}\right) \,\right]} \tag{6.22}$$

A quantity of interest is the *delay* time τ_d which is required for the optical pulse to reach its peak value where $N = N_T$. We define δ by

$$\delta \equiv \frac{N_0}{N_T} - 1 \tag{6.23}$$

and then Eq. 6.22 is manipulated to yield the delay time as

$$\tau_d = \int_0^{\left(\frac{\delta}{1+\delta}\right)} \frac{d\xi}{(1-\xi)\left[\, \frac{F_0}{N_T} + (1+\delta)\xi + \ln(1-\xi) \,\right]} \tag{6.24}$$

In general, the results from the equations above must be computed numerically which can be done with relative ease. However, in the case where the semiconductor laser is pumped only slightly over threshold before the pulse evolution begins, we can obtain the first order appoximate behavior analytically. This means $\delta << 1$

in Eq. 6.23, and from Eq. 6.18 we obtain

$$P_{peak} \approx \tfrac{1}{2}h\nu v_g A N_T(-\ln R)\,\delta^2 \;+\; \mathcal{O}(\delta^3) \tag{6.25}$$

while the energy is obtained from Eqs. 6.19-20 as

$$E_{pulse} \approx 2h\nu\left(\frac{\ln R}{\ln R - \alpha L}\right) A L N_T\,\delta \;+\; \mathcal{O}(\delta^2) \tag{6.26}$$

which yields for the pulse width in Eq. 6.21

$$T_{pulse} \approx 4\tau_p\left[\,\frac{1}{\delta} \;+\; \mathcal{O}(1)\,\right] \tag{6.27}$$

From Eq. 6.22 the delay time T_{delay} is given by

$$T_{delay} = \tau_p\tau_d \approx \frac{\tau_p}{\delta}\ln\left[\frac{2\delta^2 N_T}{3F_0}\right] \;+\; \cdots \tag{6.28}$$

To see what behavior might be expected in a GaAs laser, we assume $h\nu \sim 1.43$ eV, $R = 0.32$, $L = 250\ \mu$m, and $v_g \approx c/n$ where $n \sim 3.5$. For the values of κ and n_0 in Eq. 6.13, we use the experimentally determined values for a 0.2 μm thick GaAs active region device[5] which are $\kappa = 2.82\text{x}10^{-16}$ cm^2 and $n_0 = 0.83\text{x}10^{18}$ cm^{-3}. This value of κ already incorporates a Γ value of ~ 0.6. We furthermore assume a distributed loss of $\alpha \approx 15$ cm^{-1} which is typical for stripe geometry double heterostructure semiconductor lasers. For purposes of energy and power, we assume an active area width of 8 μm and, as mentioned above, an active area thickness of 0.2 μm.

The photon lifetime derived from Eq. 6.12 and the parameters above is $\tau_p = 1.93$ psec. This simple fact is one of the essential points of this chapter; even for typical semiconductor laser parameters, the photon lifetime is well down into the picosecond regime. This is due mostly to the low reflectivity of the cleaved "mirror" facets on the semiconductor crystal and the fairly short cavity lengths of typical devices. For other device structures, the distributed loss can be considerably higher, reducing τ_p even further. The importance of the low τ_p lies in the fact that

to a large extent this is the parameter which governs the time scale of the "giant optical pulse" evolution in a semiconductor laser.

From Eq. 6.13, the threshold inversion is determined with the above parameters to be $N_T \equiv (n_T - n_0) = 2.15 \times 10^{17}$ cm^{-3} which corresponds to a carrier density n_T of 1.05×10^{18} cm^{-3}.

Consider the case where the device is initially pumped to a level 50% in excess of N_T, or a carrier density of only 1.15×10^{18} cm^{-3}. This results in a δ value of 0.5, and from Eq. 6.26 the pulse energy is $E_{pulse} \sim 1.48 \times 10^{-11}$ Joules. From Eq. 6.25, the peak power is $P_{peak} \sim$ 0.96 Watts, and the resulting pulse width from Eq. 6.27 is $T_{pulse} \sim$ 15.4 psec. For the delay time T_{delay} we need some reasonable value for F_0. Since this enters only logarithmically, if we only want crude accuracy to a few picoseconds, we assign a typical spontaneous lifetime τ_s of $\sim$ 3 nsec, and let all the fluorescence (multiplied by some reasonable β value of $\sim 10^{-4}$) emitted within one τ_p be the starting value. We then obtain $F_0 \sim 8 \times 10^{10}$ cm^{-3}, which yields from Eq. 6.28 a delay time of $T_{delay} \approx$ 50 psec.

The purpose of the excercise above is merely to point out that with ordinary device parameters, for reasonable inversion levels, one can expect to generate "giant pulses" in semiconductor lasers with pulse widths in the several to tens of picoseconds range. Pulse energies of 10^{-11} to 10^{-10} Joules should be easily attainable, with peak powers of Watts to tens of Watts. The delay times will also typically be several to tens of picoseconds.

For more accurate modeling of expected performance we return to either the full set of equations Eqs. 6.1-3 or the spatially averaged equations Eqs. 6.8-9 and resort to numerical solutions. From the estimates above, it is apparent that for higher inversion levels predicted pulse widths in the spatially averaged model can easily get down to a several picoseconds. However, the round trip time T_{RT} for a

semiconductor laser with a typical length of ~ 250 μm is $T_{RT} = 2L/v_g = 5.8$ psec, and one may then question the validity of the spatially averaged model. This suspicion appears justified since for pulse widths on the time scale of T_{RT} and less, the optical pulse energy must be localized along the length of the cavity a some points in time.

There are two alternate ways to discuss this problem, one in the time domain and the other in the frequency domain. As pulse widths become comparable to the round trip time, $T_{pulse} \sim T_{RT}$, the laser is necessarily not running in a single longitudinal mode. This is because the mode spacing in frequency is $\Delta\nu = \frac{1}{T_{RT}}$, while from the Fourier transform considerations of Section 5.1, a pulse of duration T_{pulse} has a power spectrum width of the order of magnitude of $\Delta\nu_{FWHM} \sim \frac{1}{T_{RT}}$. The spectral energy then spreads at least over a few modes. Also, since the gain in the cavity is modulated on a timescale of T_{RT}, the spectral width of the "modes" themselves may become comparable to the inter-mode spacing. Then as pulse widths become comparable to T_{RT}, the optical power spectrum should spread at least over a few inter-mode spacings with perhaps some modulation to indicate the mode structure.

Typically in lasers with well defined modes, in multimode operation a fixed phase relation between the modes implies energy localization within the cavity at any point in time, and the "mode-beating" would produce a modulation of the output at the beat frequency which has the period T_{RT}. Physically, the optical energy in this case is in the form of a packet reflecting back and forth between the cavity mirrors. This is exactly the same behavior which in the extreme multimode case produces mode-locking as discussed at some length in Chapter 3. The analysis there made use of the TW rate equations, and thus we should expect that Eqs. 6.1-3 are adequate to describe any mode-beating modulation at T_{RT} in the semiconductor laser. This is because any feature on φ^+ propagates to $z = \frac{L}{2}$ and is there converted to a

feature on φ^- via the imposed boundary conditions Eq. 6.6, and after propagating to $z = -\frac{L}{2}$ is re-converted to a feature on φ^+ for the round trip periodicity.

However, the "mode-beating" is only incorporated in the TW equations Eqs. 6.1-3 if it is of a *deterministic* nature. To clarify this statement, consider a laser with homogeneously broadened gain which has initially several longitudinal modes over threshold with comparable gains. If the modes are noise-fed, after the amplitude grows above the noise level, the field of a given mode develops a well defined phase which in general has a random relation to the phases of the other modes. The resulting intensity from the coherent sum of the mode amplitudes displays a temporal modulation at the mode beat frequency with period T_{RT}. However, the photon density rate equations Eqs. 6.1-3 cannot describe this phenomenon since there is no allowance for the coherent addition of amplitudes. In the above process the growth from noise insures that, in the absense of any *deterministic* pulse forming mechanism, the relative mode phases should be random. Then if an *ensemble average* of pulses were measured, there should be no modulation at T_{RT}, in agreement with the incoherent TW equations.

If there is some *deterministic* feature which generates the modulation, this will be (or can be if it is external) incorporated in the TW rate equations. In the frequency domain, this would mean that there is some physical process which "locks" the relative phases of the modes just as in the application of the TW equations to mode-locking. Here the physical process was the temporal modulation of the cavity in conjunction with the nonlinear gain medium. For "giant pulse" evolution, such a physical process might be a fixed spatial distribution of optical energy and gain in the cavity at the time of "Q-switching". This is exactly the behavior depicted in the output of the Q-switched Nd:YAG output shown in Figs. 5.22-24. Here the switching of the Pockels cell at a fixed spatial point in the cavity on a time scale short com-

pared to T_{RT} specifies that the mode phases be fixed for each pulse evolution process such that initially no energy exists past the Pockels cell position. In the TW intensity picture, the Pockels cell acts as a "gate" which releases the noise to begin its cavity traversals with a temporal envelope already imprinted on in.

We conclude then that a *deterministic* round trip modulation effect would be described by the TW equations Eqs. 6.1-3. If the ensemble average of pulses were observed, as is the case in many experimental situations, only a deterministic mode-locking feature would appear anyway. If is manifestly obvious that any modulation at T_{RT} due to the processes above is *not* included in the spatially averaged equations Eqs. 6.8-9.

To investigate under what conditions any round trip modulations are expected, numerical integrations of both Eqs 6.8-9 and the full TW equations Eqs. 6.1-3 were performed. For the full TW set, the sharp temporal transients demand that the time variable be dealt with carefully. However, since the expected round trip modulation effects are not too severe, we expect only slow variations of all quantities along the *length* of the cavity at any given time. For these reasons, the TW equations Eqs. 6.1-3 were re-written by approximating the spatial variations with a discrete spatial grid as shown in Fig. 6.1, while the time variable was left as a continuous quantity. We then have a discrete set of dependent variables $\varphi_j^{+,-}(t)$ and $n_j(t)$ for $j = 1,\ldots,N$ at the locations $z_j = -\frac{L}{2} + (j-1)\Delta L$ where $\Delta L = \frac{L}{(N-1)}$. At each z_j the spatial derivatives are given approximately by the finite differences

$$\left.\frac{\partial \varphi^+}{\partial z}\right|_j = \frac{\varphi_j^+ - \varphi_{j-1}^+}{\Delta L} \tag{6.29}$$

and the boundary conditions become

$$\varphi_1^+(t) = R\varphi_1^-(t) \quad \text{and} \quad \varphi_N^-(t) = R\varphi_N^+(t) \tag{6.30}$$

In this manner the set of coupled *partial* differential equations Eqs. 6.1-3 are

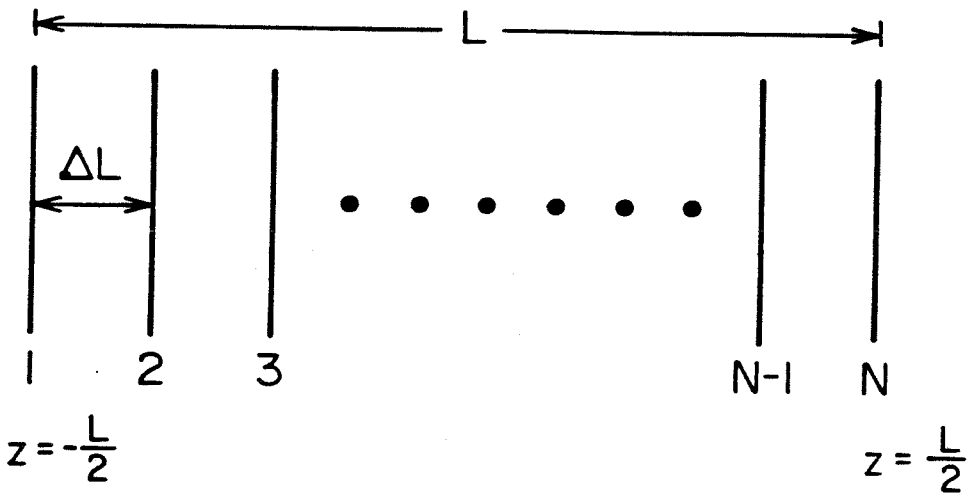

Figure 6.1 Discrete spatial grid used for full T.W. cavity rate equations.

converted approximately to a set of 3N − 2 *ordinary* differential equations; for the present application, the value N = 7 was deemed adequately accurate.

Fig. 6.2 shows the results of a computation using the spatially averaged equations Eqs. 6.8-9 with a sech^2 temporal pump profile

$$P_n(t) = \frac{n_i}{T_{FWHM}} q(t/T_{FWHM}) \tag{6.31}$$

where q(x) is given by Eq. 2.66, and T_{FWHM} = 2.0 psec. The same laser parameters are used as for the approximate discussion given earlier, except we also must include the spontaneous source term. For this we assume the radiative rate $\frac{1}{\tau_s}$ is proportional to the carrier density n and thus employ the quantity βBn^2 and Bn^2 on the RHS of Eqs. 6.8 and 6.9 respectively. The β value is taken to be 10^{-4} as before and B was taken to have the value $B = 0.9 \times 10^{-10}$ cm^3–sec^{-1} . For a comparison with the approximate estimates, the first curve is $\delta = 0.5$ corresponding to $n_i = 1.15 \times 10^{18} cm^{-3}$, where δ is defined by Eq. 6.23. The four remaining curves are for δ = 1.0, 3.0, 5.0, and 7.0 corresponding to injected carrier densities n_i of $1.90 \times 10^{18} cm^{-3}$, $1.48 \times 10^{18} cm^{-3}$, $2.34 \times 10^{18} cm^{-3}$, and $2.77 \times 10^{18} cm^{-3}$ respectively. To convert to the signal levels to Watts, multiply the vertical scale by the constant 5.26. Also shown are the pump levels. The numerical values for the $\delta = 0.5$ case were a peak power of 0.68 Watts, a FWHM pulse width of 16 psec, and a delay time of 48.5 psec. This is in excellent agreement with the simple small δ arguments. For the other extreme $\delta = 7.0$, the numerical calculation produced a peak power of 44 Watts, a FWHM pulse width of only ~ 2.6 psec, with a delay time of only 5 psec.

The exact same values were then used for the full TW equations Eqs. 6.1-3 using the solution method described above. The results were virtually identical to the uniform results above, and a figure is omitted since it would be indistinguishable to the eye from Fig. 6.2. The only sizable difference occurs at the low δ value of 0.5,

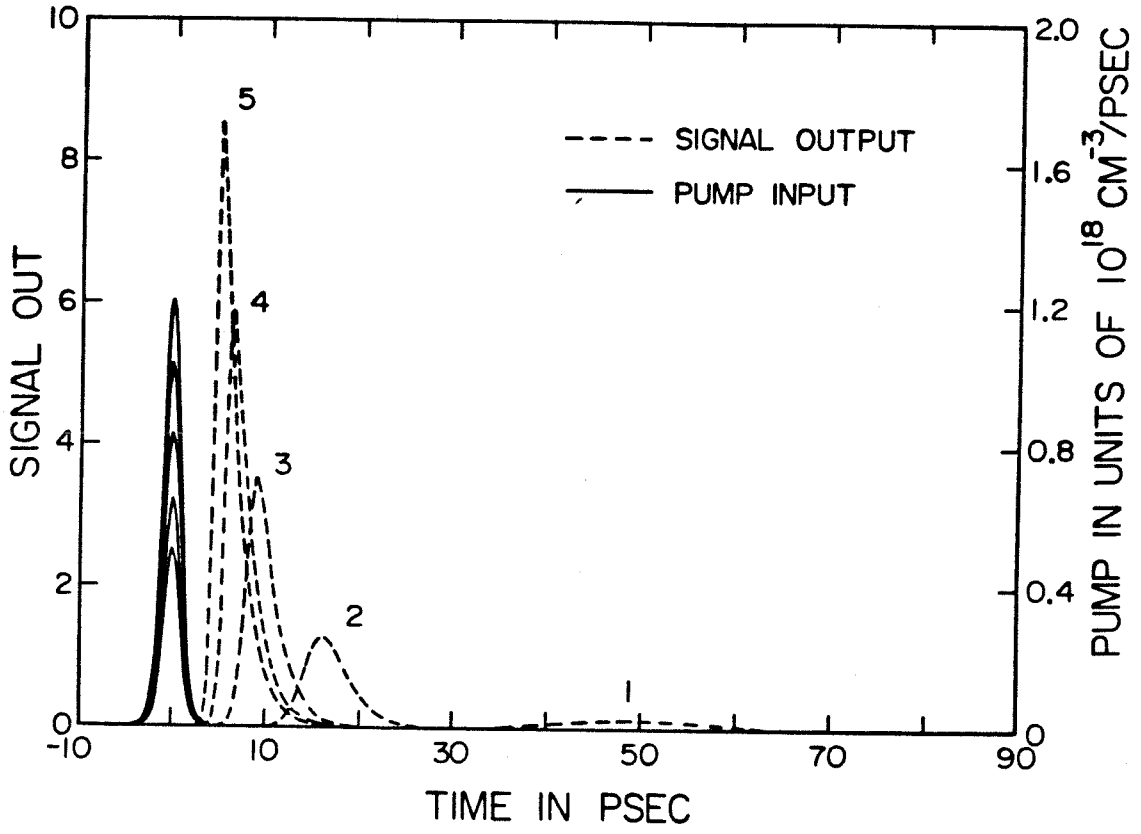

Figure 6.2 " Giant pulses " from a 250 μm long diode laser with δ = 0.5, 1.0, 3.0, 5.0, and 7.0. For other parameters see text.

where the peak power was ~ 30% higher for the more exact equations, but the delays and pulse widths were the same within a few percent. At the higher δ values, the peak power was also the same for the two solutions within a few percent.

These small differences are probably due to the approximate inclusion of the mirror losses in the spatially averaged model by using the photon lifetime concept, as well as the inherent inaccuracies in spatially averaging nonlinear products[3]. One important result is that no round trip modulations are present even when the pulse width T_{pulse} is only about one half the round trip time T_{RT}. Referring to the earlier discussion, there is no "mode-locking" feature here to introduce the modulation. It is more important to note, however, that the spatially averaged equations Eqs. 6.8-9 give accurate results even when the resulting pulse widths are less than the cavity round trip time. This is perhaps surprising since at any point in time the optical energy is necessarily localized longitudinally within the cavity when $T_{pulse} < T_{RT}$, and this appears to invalidate the spatial averaging assumptions.

To illustrate round trip modulation effects, a mode-locking feature is incorporated by pumping only ***half*** of the cavity. This should produce modulation in the same sense as the discussion earlier for the Q-switched Nd:YAG laser. Fig. 6.3 shows the computed results on an expanded time scale for the output from one end only, here the end which is pumped. The solid curves are the pumping rates, corresponding to two different integrated injection densities n_i in the pumped half of 2.77×10^{18} cm^{-3} and 1.91×10^{18} cm^{-3} which previously gave δ values of 3.0 and 7.0; δ is somewhat ill-defined in the case at hand. For each of the two pump levels, there is a pair of signal curves, one dashed and the other dotted. The dashed curve is the output when the distributed loss α has been set to zero, while the dotted curves are the outputs for the previously assume α value of 15 cm^{-1}. To convert to power in Watts, multiply the ordinate value by the constant 2.63 since this is just the power out one end. The modulation is obvious for the larger pump level, with "ringing" at

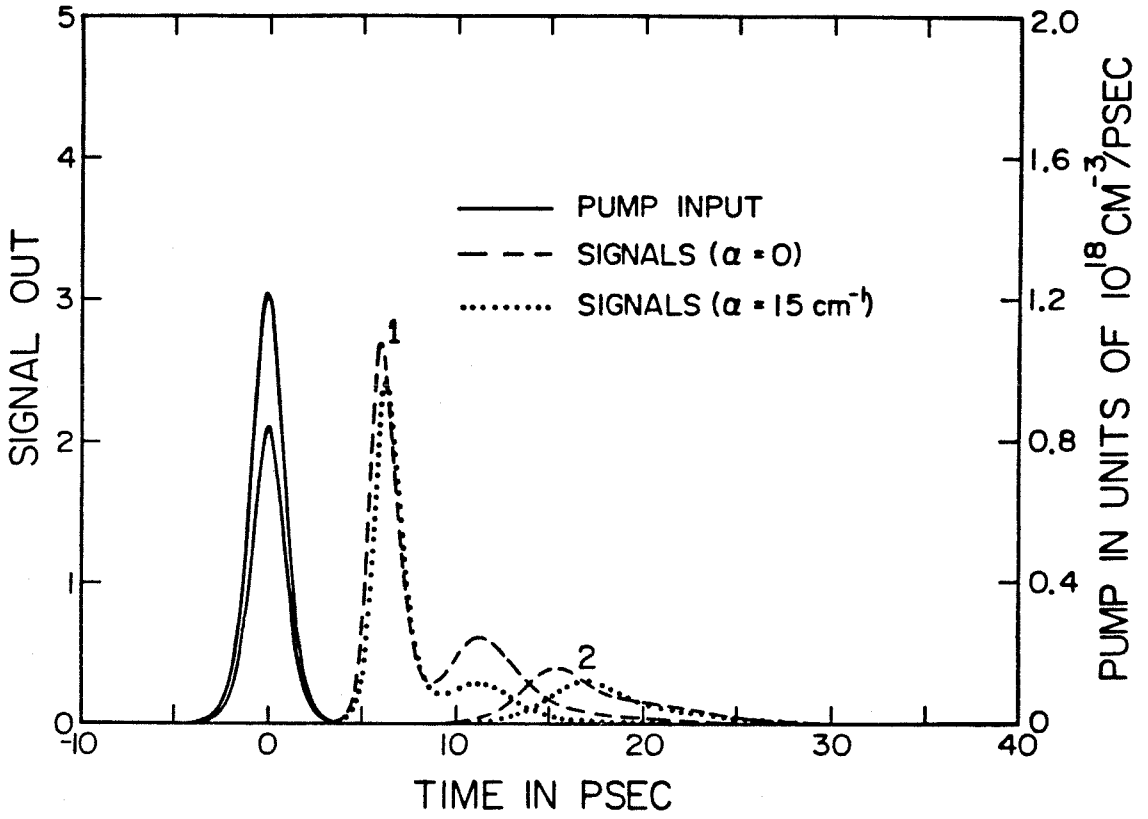

Figure 6.3 "Giant pulses" from a 250 μm long diode laser exhibiting modulation at the round trip frequency. Results for two different pump levels are shown labeled 1 and 2. Two sets of curves are shown with each of these to demonstrate the effect of a small additional distributed loss α.

the expected period T_{RT}. The spatially asymmetrical original noise distribution "rattles back and forth" in the cavity, evolving into a short packet with $T_{pulse} < T_{RT}$. The energy localization is probably aided by the unpumped end of the cavity which acts as a saturable absorber. The lower pump level shows no modulation at T_{RT}.

The dotted curves show that the addition of even the small amount of distributed loss $\alpha = 15\ cm^{-1}$ tends to suppress the ringing. This is important because the $\sim 15\ cm^{-1}$ distributed loss for a stripe geometry double heterostructure laser is among the lowest values attainable for semiconductor lasers. For other device structures, such as the buried heterostructure lasers to be considered in Chapter 7, α can be much higher, easily reaching values in excess of $30\ cm^{-1}$ from scattering losses in the thin etched transverse waveguide. In this case the round trip modulations would be suppressed even further.

The occurrence of T_{RT} modulation is thus contingent upon several factors. Clearly one is the need for a mode-locking mechanism or initial condition. In addition the gain must be at a level capable of evolving pulse widths comparable to T_{RT}. However, an additional factor is that the pulse width also be comparable to τ_p, for as τ_p is decreased by increasing α, the ringing tails on the pulses are suppressed. The fundamental conclusion here is that under most circumstances, even when $T_{pulse} < T_{RT}$, the spatially averaged rate equations Eqs. 6.8-9 give valid results.

6.2 Picosecond Optically Q-switched Semiconductor Lasers

An experimental investigation was conducted[6] to investigate some of the ultrashort pulse capabilities of semiconductor lasers discussed above. Stripe geometry double heterostructure GaAs–$Al_xGa_{1-x}As$ lasers were grown by liquid phase epitaxy with an active GaAs region thickness of 0.2 μm and a stripe width of $\sim 8\ \mu$m as shown in Fig. 6.4. The junction was formed by a Zn diffusion up to the active region.

Evaporated contacts of chrome-gold were etched off in a central region 50 μm long, while typical device lengths were 250 μm .

The essential feature of this device is that the unpumped central region offers considerable loss to the cavity, allowing the laser to be *electrically* pumped to an initial average gain $\Gamma\gamma_0$ in excess of what the threshold gain $\Gamma\gamma_T$ would be in the absence of the central region losses. A picosecond optical pulse incident on the central region creates carriers which, by virtue of band filling, reduce the losses or actually even provide additional gain. It is essential for high speed response that the carriers be produced directly in the active region to avoid diffusion times, etc. To achieve this result, the aluminum content of the upper $Al_xGa_{1-x}As$ cladding layer should be such that the direct band gap is larger than the pump photon energy. For the 2.03 eV photons used, to be described below, this corresponded to $x \gtrsim 0.5$ [7].

The initial Q-switching experiments were conducted before the completion of the gigawatt picosecond system described in Chapter 5. The picosecond optical pump source used initially was a *passively* mode-locked, cavity dumped, CW dye laser employing DODCI as the saturable absorber and R6G as the gain medium using a seven mirror folded cavity[8]. One disadvantage of this system is its lack of tunability; operation is restricted to a range within a hundred angstroms of ~6100 angstroms due to the limited effective range of the saturable absorber. Another major drawback was the low pulse energies which severely limits the experimental techniques which can be employed. The pulse width of the dye laser was typically $\lesssim$ 2 psec as determined by the KDP SHG autocorrelation measurement techniques discussed in Chapter 5. The semiconductor lasers were placed at the edge of a gold plated contact platform which was mounted on a micrometer driven x-y-z stage, with the top contacts made through a pair of standard semiconductor device probes. The platform was placed in front of a 60X microscope objective to

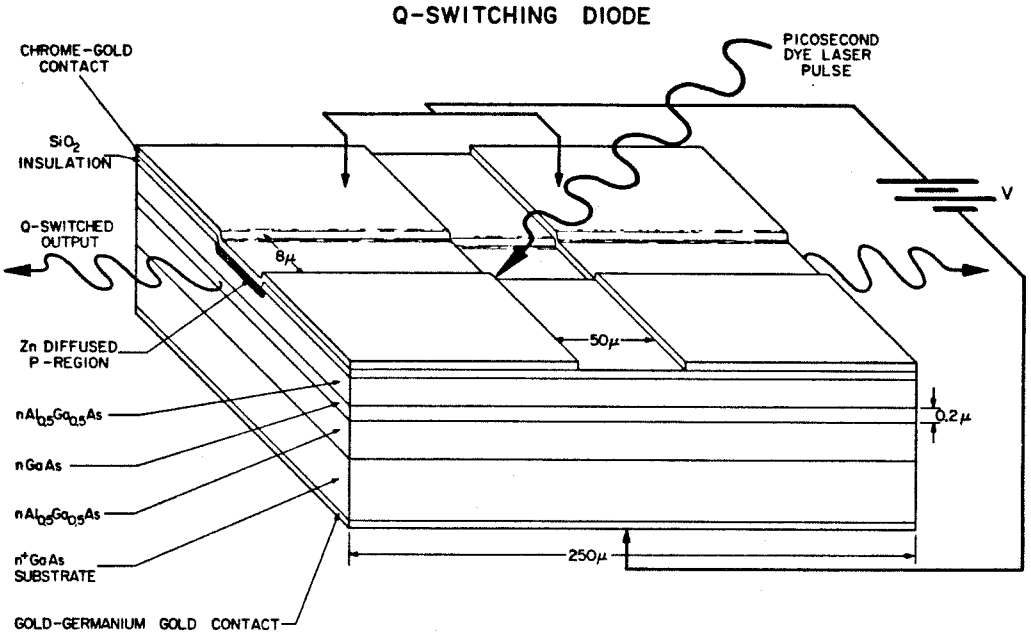

Figure 6.4 Geometry of picosecond optically Q-switched semiconductor laser used in experiments.

collimate the IR output for detection. The dye laser pulses were focussed onto the diode lasers from above at an angle of ~ 35° from the surface normal. The entire apparatus was under a stereoscopic microscope to aid in the pump pulse focussing and the probe placement on the diode surface. The semiconductor lasers were operated with a 50 nsec pulsed current source synchronized to the cavity dumped output of the picosecond dye laser oscillator at a repitition rate of 45 kHz. Typical threshold currents for the semiconductor lasers were ~ 100 mA, even with the unpumped central region losses.

To evaluate the expected behavior of this system, the spatially averaged model is used and the same gain and material constants are employed as in the earlier discussions. The effective mirror distributed loss is from Eq. 6.7

$$\alpha_{mirrors} = -\frac{\ln R}{L} = 45.6 \text{ cm}^{-1} \tag{6.32}$$

while the *averaged* effective distributed loss from the unpumped central section and the passive distributed loss is

$$\alpha_{effective} = \frac{\Delta L}{L}\alpha_{central} + \alpha = 46.8 \text{ cm}^{-1} + 15 \text{ cm}^{-1} = 61.8 \text{ cm}^{-1} \tag{6.33}$$

If the device is electrically pumped just to threshold, then the initial average gain would be $\Gamma\gamma_0 = 107.4 \text{ cm}^{-1}$, corresponding to an *average* inversion level $N = n - n_0$ of $4.59\text{x}10^{17} \text{ cm}^{-3}$, which requires an inversion level in the end regions 25% higher than this or a carrier density of $1.40\text{x}10^{18} \text{ cm}^{-3}$ in the ends. If the incident picosecond pump source is assumed sufficient to bleach the central region to transparency, i.e., creating a density of ~ $0.83\text{x}10^{18} \text{ cm}^{-3}$ from the data of the earlier discussion, then the device suddenly has a total effective distributed loss of only 60.6 cm^{-1}, and the threshold gain is now reduced to $\Gamma\gamma_T = 60.6 \text{ cm}^{-1}$ while the value of $\Gamma\gamma_0$ has remained unchanged, corresponding to a δ value of 0.77. It is thus apparant that the crude expectations of the small δ equations are roughly applicable, with $\delta \lesssim 1$.

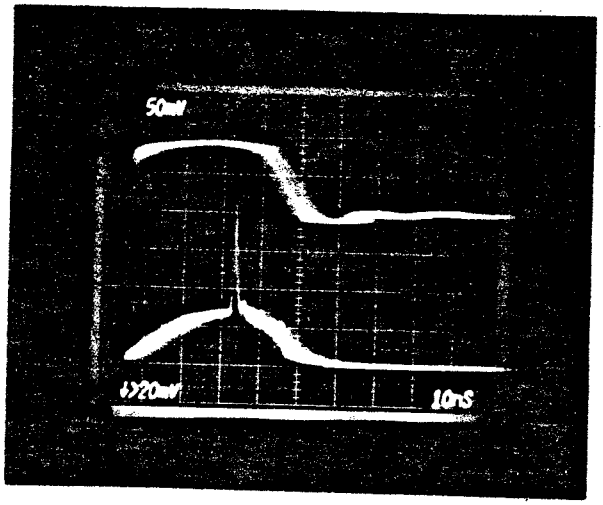

Figure 6.5 Upper trace: Current to diode with scale of 1mV = 1 mA. Lower trace: Unresolved Q-switched lasing output of diode. Spike is ~ coincident with dye laser pulse illumination.

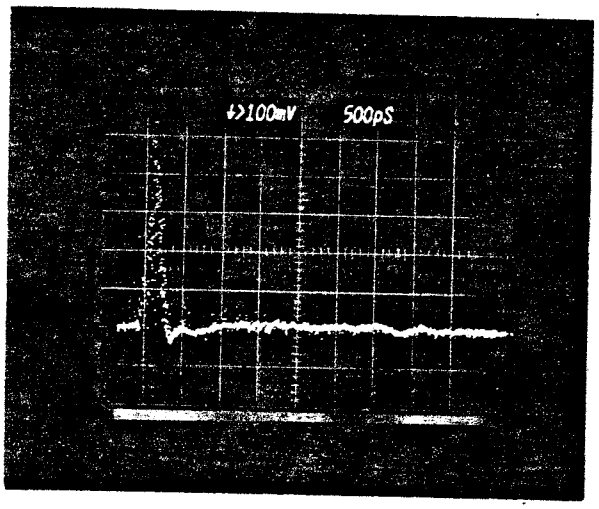

Figure 6.6 Q-switched lasing pulse output (detector limited) with diode biased below threshold; single spike results.

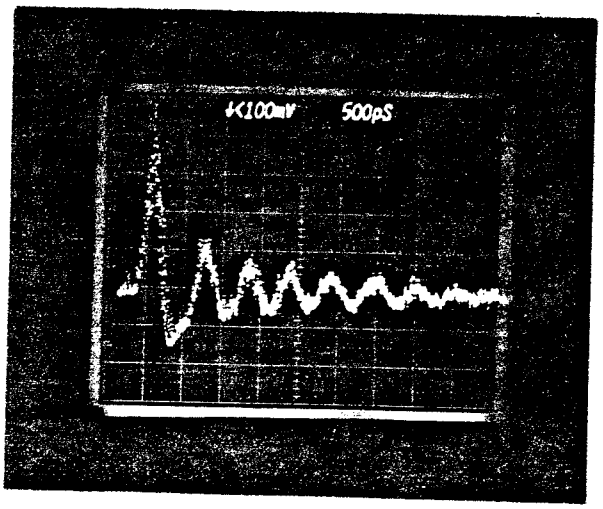

Figure 6.7 Q-switched lasing pulse output (detector limited) with diode biased at $I \approx 1.1\ I_{th}$. Relaxation oscillations following the Q-switched spike are clearly visible.

Powers of ~ 1 Watt, pulse widths T_{pulse} of ~ ten picosecond and delays of tens of picoseconds should be attainable.

Fig. 6.5 shows the current pulse applied to the diode laser in the upper trace, with a calibration of 1mV = 1mA. The jitter in the current pulse is due to the current generator being triggered 22 μsec earlier by the preceding dumped dye laser pulse. The bottom trace shows the IR output of the diode laser when it is pumped slightly below threshold. The broad base is mostly spontaneous emission while the spike, which is coincident with the arrival time of the dye laser pulse at the diode, is the unresolved Q-switched lasing output pulse. The monitor here was a PIN photodiode, but the trace is limited by the 350 MHz bandwidth of the oscilloscope. Fig. 6.6 shows the pulse when monitored with the same 100 psec risetime APD/sampling oscilloscope combination described in Chapter 5 for monitoring the argon ion laser mode-locked pulses. The pulse is still unresolved, but it indicates a FWHM T_{pulse} of less than 200 psec as expected. Fig. 6.7 shows the same diode with the current raised to I ~ 1.1 I_{th} , where I_{th} is the threshold current in the *absence* of optical excitation in the central region. Here the ringing observed experimentally is a good illustration of the well known relaxation oscillation phenomenon. For a linear gain dependence, the relaxation oscillation can easily be shown to have a period[9]

$$T_{osc} = 2\pi \left[\frac{\tau_p \tau_s I_{th}}{I - I_{th}} \right]^{\frac{1}{2}} \qquad (6.34)$$

The oscillations do not occur when the diode is electrically pumped below threshold since there is no mechanism for pumping the diode back to an above threshold state following the evolution of the giant pulse; i.e., the central region returns to its lossy state. Here we ignore the possibility of any bistability effects[10]. If the low Q state has a photon lifetime of 1.1 psec, which is the passive value with the central region losses, the nanosecond timescale τ_s and $I/I_{th} \approx 1.1$ yield a relaxation

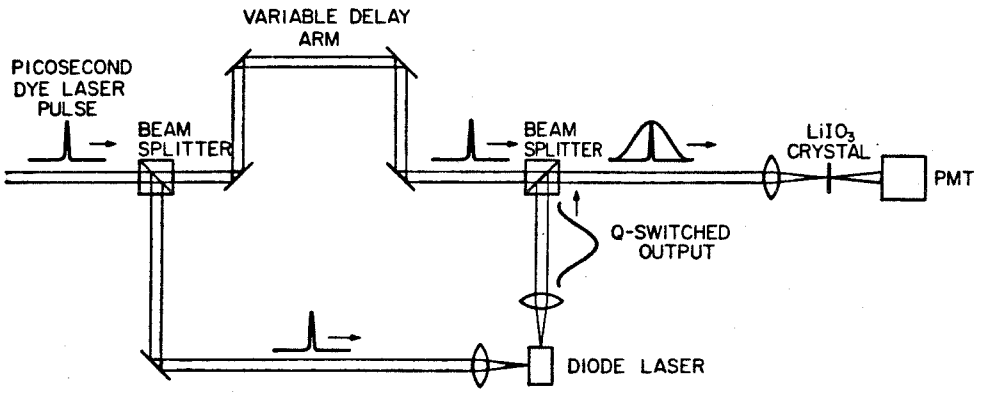

CROSS-CORRELATION MEASUREMENT

Fig. 6.8 Geometry of parametric sum frequency cross correlation apparatus.

oscillation period T_{osc} on the order of a nanosecond, in rough agreement with Fig. 6.7.

To actually revolve the short pulse IR output of the Q-switched diodes, the cross-correlation technique employing phase matched parametric sum frequency generation was employed as discussed in Chapter 5. Fig. 6.8 shows the physical layout. A picosecond dye laser pulse is split into two paths, one of which is used to optically Q-switch the semiconductor laser. The other pulse, after passing through a stepping motor controlled variable delay arm, is combined with the IR diode laser pulse using a dichroic mirror. The two are then focussed into a 1 mm thick $LiIO_3$ crystal obtained from Cleveland Crystals[11]. The crystal is cut with its optic axis at an angle of 46.5° from the surface normal, which from Eq. 5.7 is the phase matching angle for sum frequency generation using a 6100 Å dye laser pulse and a 8900 Å IR diode pulse. Angle tuning is possible to accommodate other wavelengths. The signals pass through a pair of Schott UG-11 filters which block the fundamentals as well as the room light, and an additional Schott WG-345 filter is used to block any second harmonic of the dye laser pulse which may be generated even in the absence of phase matching. Due to the low repitition rate, the signal to noise ratio is greatly improved when the peak PMT voltage is monitored with a sampling oscilloscope. A voltage proportional to the vertical trace on the sampling oscilloscope is then fed into the vertical amplifier of the Nicolet signal averaging system described in Chapter 5, which generates a recording of the sum frequency power at each stepping motor position. This can be displayed on the CRT of the signal averager, and if desired, multiple scans and signal averaging can be performed. In the limit that the picosecond mixing signal at ω_2 is very short (effectively a δ-function in time) compared to any features of interest on the diode laser pulse, the cross-correlation becomes an actual reproduction of the diode laser output pulse shape, i.e., from Eq. 5.11, $E_{2\omega}(\tau) \propto I_{\omega_1}(\tau)$. This technique then effectively synthesizes a picosecond

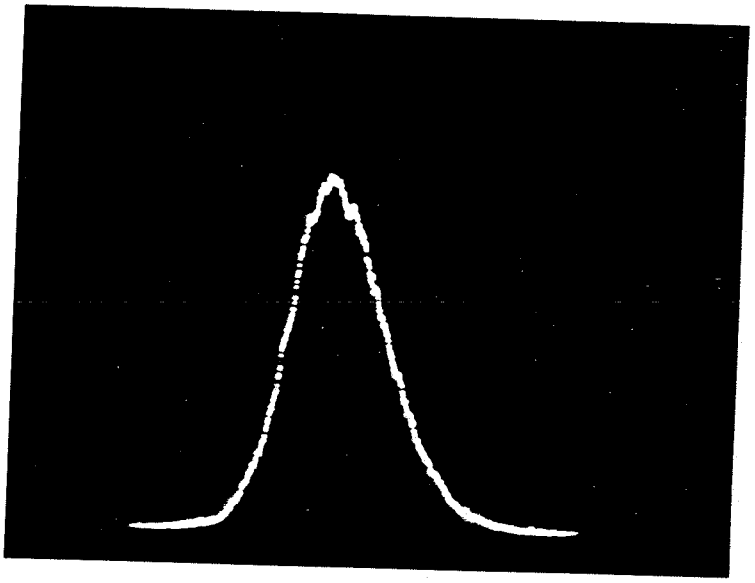

Figure 6.9 Typical output pulse from a 50 μm gap Q-switched laser. Full width of screen is 86.8 psec, pulse FWHM is $T_{pulse} \approx$ 20.8 psec.

resolution sampling oscilloscope for monitoring the diode laser optical waveform.

The actual system employed varied from the above description only slightly. The picosecond pump source for the *resolved* Q-switching experiments was derived from the gigawatt picosecond oscillator-amplifier system described in Chapter 5. The amplified dye laser pulse is split into two paths, one of which is small in amplitude and is used for the variable delay cross-correlation arm in Fig. 6.8. The other pumping beam is first focussed through a 10 cm cell containing fully deuterated acetone (D6 acetone) which serves as an efficient Raman shifting medium for picosecond pulses. The acetone value for the C-H stretching bond vibrational frequency is 2921 cm^{-1} , and this is the first mode to cross threshold for stimulated Raman scattering[12]. The good efficiency (on the order of up to a few tens of percents) for picosecond stimulated Raman scattering is due to the large integrated cross section for the C-H stretching bond and the low group velocity dispersion of acetone. For D6 acetone, the C-D frequency is reduced by the square root of the reduced mass ratio, $[\mu_{C-H}/\mu_{C-D}]^{1/2}$ where, for example, $\mu_{C-H}^{-1} = m_C^{-1} + m_H^{-1}$. This yields a value of ~ 2145 cm^{-1} for the expected Stokes shift for picosecond pulses in D6 acetone. Colored glass filters follow the Raman cell to filter out the fundamental, Anti-Stokes and higher order Stokes components, and in addition attenuating the first Stokes line to an energy more suitable for optical pumping and Q-switching of semiconductor lasers. The gigawatt dye laser system was typically operated in the range of 595 nm to 600 nm, leading to a first Stokes pulse of ~ 686 nm, with an attenuated energy entering the diode focussing optics of ~ 2×10^{-7} Joules.

Fig. 6.9 shows the resolved measurement of a typical IR Q-switched pulse from the diode structure of Fig. 6.1 using the cross-correlation apparatus described above. The diode was biased below threshold and the pulse FWHM T_{pulse} is ~ 20.8 psec, the same order of magnitude as expected from the simple considerations of Section 6.1. Since $T_{pulse} >> T_{RT} > \tau_p$, RT modulations are neither expected nor

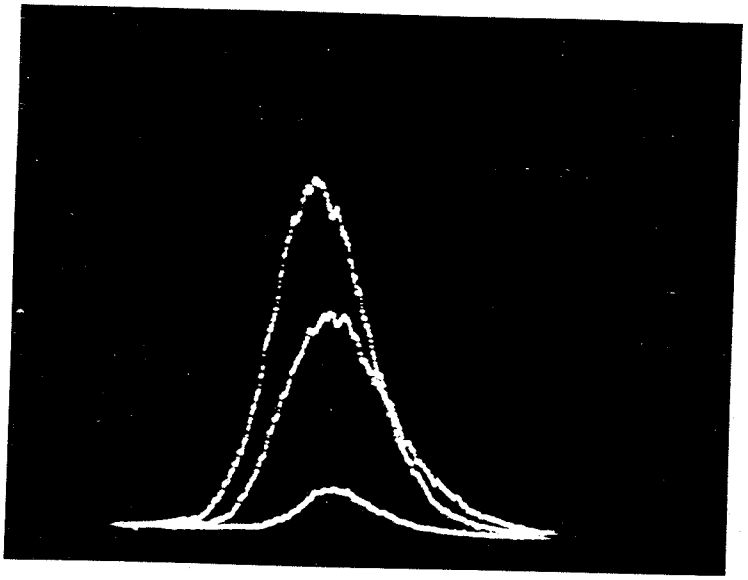

Figure 6.10 50 μm gap Q-switched laser output pulses with a bias current of $I \sim 0.6\ I_{th}$. The three traces are for relative Q-switching pulse illumination levels in the ratio 1:2.4:4 . Full screen width is 86.8 psec.

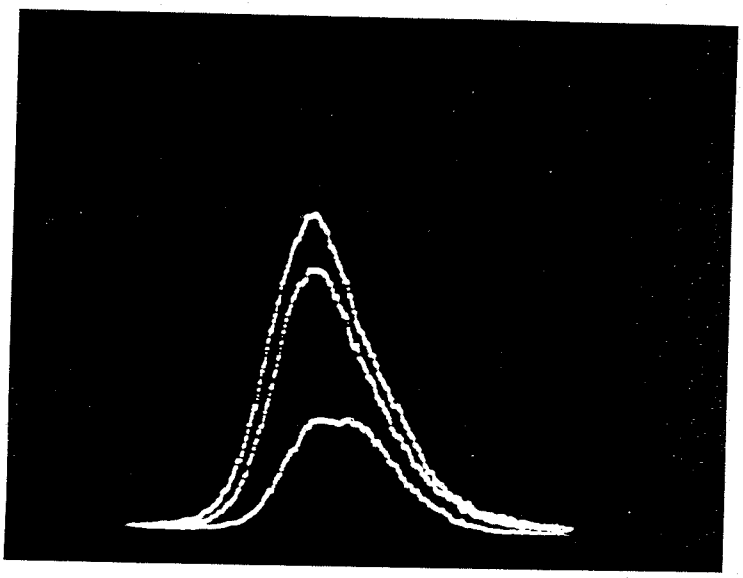

Figure 6.11 50 μm gap Q-switched laser output pulses with a fixed illumination level at the maximum value shown in Fig. 6.10. Here the three traces are with different bias currents of $I \sim 0.3\ I_{th}$, $\sim 0.6\ I_{th}$, and $\sim 0.94\ I_{th}$. Full screen width is 86.8 psec.

observed. Fig. 6.10 shows the cross-correlation traces for different Q-switching illumination levels. The current pumping level for all three traces is $I/I_{th} \sim 0.6$, and the relative 686 nm incident pulses are in the ratio of 1:2.4:4. As can be seen, the effect of the increasing δ value is the expected forward shifting of the pulse maximum, increasing amplitude, and decreasing pulse widths. The full screen time window here is 86.8 psec. The effects are perhaps not as marked as might be expected, but the uncertainties in the injection levels obviate any quantitive predictions of pulse widths, etc. The carrier density is estimated by assuming ~ 0.15 μJ actually incident on the diode surface, of which 40% is reflected and then only $\sim$ 30% of the remaining energy is absorbed in the 0.2 μm thick active region. The illumination was not cylindrically focussed, but was instead usually put in a ~ 300 μm spot which covered the entire diode surface to insure a fairly repeatable alignment process. This produces an expected carrier density of $\sim 4 \times 10^{18}$ cm^{-3} in the *central region* for a δ of ~ 7, but this number is very approximate. Fig. 6.11 shows the effects of different electrical pumping with a fixed level of Q-switching illumination. The current is varied from $\sim 0.3\ I_{th}$ to $\sim 0.6\ I_{th}$ to $\sim 0.94\ I_{th}$ and the full screen here corresponds to 86.8 psec again. As before, the effective increasing δ value leads to a forward shift in time, a marked increase in amplitude, and a slight pulse width reduction.

The Q-switching phenomenon was also investigated with different device dimensions and contact geometries than those depicted in Fig. 6.1. In particular, a 254 μm long diode was tested with a 106 μm section at one end with no contact (the Q-switching section) and a 141 μm contact region on the other end, followed by an unintentional but negligible 7 μm long unpumped region at the facet. The results from this diode were very similar. Due to the poor electrical diode structure, however, threshold currents were quite high and not well defined with low differential quantum efficiencies. Fig. 6.12 shows the small effect of current variations, with

currents for the four different traces being 75, 150, 225, and 300 mA; the full screen is 86.8 psec. There is only a slight forward shift in time, indicating that the performance is dominated by the optical injection level. Fig. 6.13 shows the effect of varying the Q-switching illumination intensity in the ratios of 1:2:4:8 for the four traces, with a fixed current of 150 mA. In this picture, the full screen has been set to 129.2 psec. As before the increasing pump levels lead to a forward shift in time by tens of picoseconds, along with an amplitude increase and a pulse width reduction. Again, there is no observable modulation at T_{RT}.

The basic conclusion of this chapter is that picosecond timescale optical pulses can indeed be generated with fairly standard semiconductor laser geometries using picosecond gain/loss switching techniques. The picosecond resolution parametric upconversion sampling technique also showed that the more basic features of the simple spatially averaged rate equations are born out experimentally.

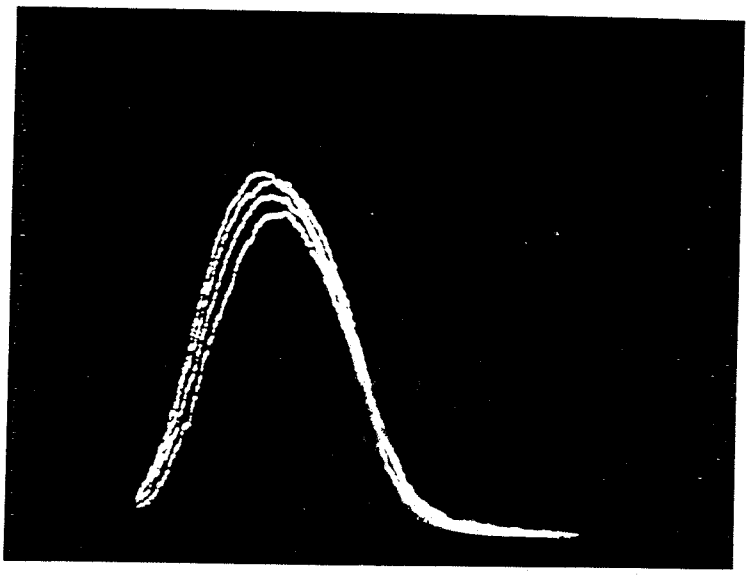

Figure 6.12 Output pulses from a 254 μm long laser with a 106 μm unpumped end section for optical "Q-switching". The four traces are for fixed (large) illumination level with bias currents of 75, 150, 225, and 300 mA. Full screen width is 86.8 psec.

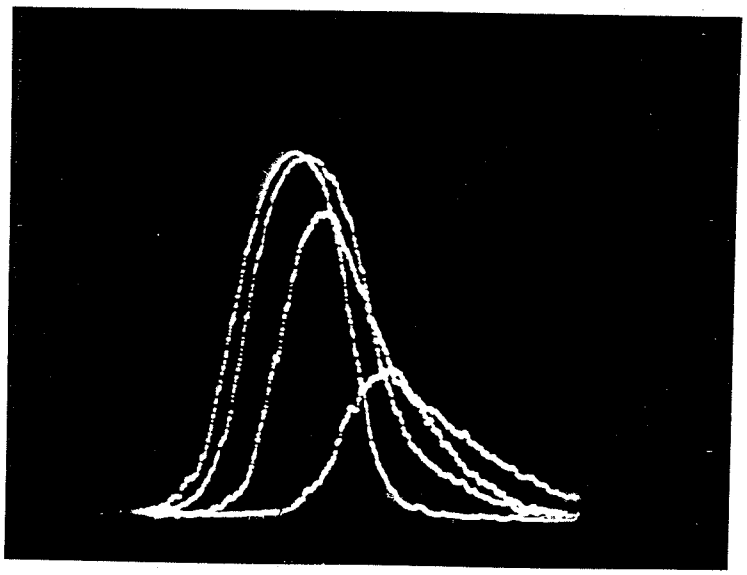

Figure 6.13 Output pulses from a 254 μm long laser with a 106 μm unpumped end section for optical "Q-switching". The four traces are for a fixed bias current of 150 mA, with relative "Q-switching" pulse illumination levels in the ratio 1:2:4:8 . Full screen width here is 129.2 psec.

CHAPTER 6 REFERENCES

1. H. C. Casey, Jr., and M. B. Panish, *Heterostructure Lasers*, Pt. A, Academic Press, New York, 1978.

2. Y. Suematsu and K. Furuya, Trans. of the IECE of Japan **E 60**, 467 (1977).

3. J. B. Moreno, J. Appl. Phys. **48**, 4152 (1977).

4. W. G. Wagner, B. A. Lengyel, J. Appl. Phys. **34**, 2042 (1963).

5. C. H. Henry, R. A. Logan, and K. A. Bertness, J. Appl. Phys. 2, 4457 (1981).

6. T. L. Koch, D. P. Wilt, and A. Yariv, " Q-Switching of Semiconductor Lasers with Picosecond Light Pulses " in *Picosecond Phenomena II*, Springer Series in Chemical Physics, Vol. 14, Ed. by R. M. Hochstrasser, W. Kaiser and C. V. Shank, Springer-Verlag, Berlin, Heidelberg, New York, p.34, 1980.

7. B. Monemar, K. K. Shih, and G. D. Petit, J. Appl. Phys. **47**, 2604 (1976).

8. P. Agmon, Ph.D. Thesis, California Institute of Technology, 1980.

9. A. Yariv, *Quantum Electronics*, John Wiley & Sons, Inc., New York, 1975.

10. Ch. Harder, K. Y. Lau and A. Yariv, Appl. Phys. Lett. **40**, 124 (1982).

11. Cleveland Crystals, Inc., Cleveland, Ohio.

12. M. Geller, D. P. Bortfeld, and W. R.. Sooy, Appl. Phys. Lett. **3**, 36 (1963).

CHAPTER 7

PICOSECOND CARRIER DYNAMICS AND LASER ACTION IN OPTICALLY PUMPED BURIED HETEROSTRUCTURE LASERS

Over the past several years there has been a continued interest in the generation of picosecond pulses from semiconductor diode lasers. The techniques for achieving this end range from active and passive mode-locking (which both require an external cavity) to direct pumping with short current pulses, to Q-switching as discussed in Chapter 6, to direct optical pumping with picosecond optical pump pulses. The latter technique is the topic of this chapter, and in Section 7.1 experimental results are presented from picosecond optically pumped buried heterostructure semiconductor lasers[1].

Before embarking on a discussion of the experimental aspects of optically pumped semiconductor lasers, it should be noted that a number of the schemes mentioned above have the common feature of large carrier densities and all involve sharp temporal transients in the laser parameters. In the simplistic analysis of Chapter 6, the dynamic characteristics of the semiconductor were all encompassed in the carrier density n, with the assumed linear dependence of gain on n. Clearly this breaks down when high density excited carrier distributions exist. In this case lasing can occur over a broad range of wavelengths, and during a picosecond time scale, the characteristics of the electron distribution in the sample may not be

those of the usually assumed room temperature equilibrium distribution. For these reasons, Section 7.2 presents a discussion of the relevant picosecond carrier dynamics to allow more realistic modeling of ultrafast processes in semiconductor lasers. Finally, Section 7.3 presents the application of these concepts to the picosecond optically pumped semiconductor laser to facilitate a deeper understanding of the observed experimental results.

7.1 Experimental Observation of Unusual Picosecond Lasing Action in Picosecond Optically Pumped Buried Heterostructure Lasers.

In a manner very similar to the "Q-switched" laser investigations of Chapter 6, an experimental study was conducted to observe the picosecond dynamics of optically pumped buried heterostructure (BH) semiconductor lasers. The cross-sectional geometries of the devices are shown in Fig. 7.1. The GaAs-AlGaAs lasers were grown in our laboratory by liquid phase epitaxy with aluminum contents and doping as shown. The gold contact was etched off over the active waveguiding region, leaving only a thin semi-transparent chromium contact. This permits optical pumping in place of, or in addition to, conventional electrical current pumped operation. When operated electrically, typical devices with lengths in the 100-300 μm range had threshold currents of $\sim$ 20-30 mA. In the experiments which follow, however, electrical operation was used only for alignment purposes. The buried heterostructure laser geometry was chosen to provide a more carefully controlled experiment than the Q-switching study of Chapter 6. There is no gain guiding to consider, with both the transverse spatial carrier profile and the optical waveguide being well defined independent of the excitation method or level. In addition the transparent contact scheme allowed uniform optical pumping over the whole cavity for a much "cleaner" experiment with more straightforward interpretation.

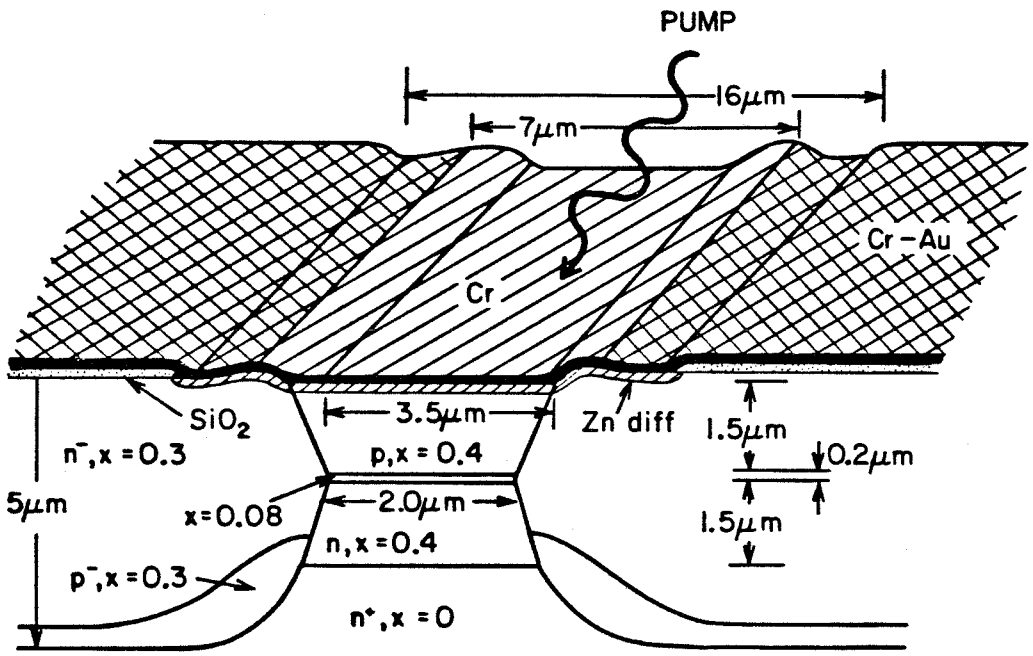

Figure 7.1 Geometry of picosecond optically pumped transparent contact buried heterostructure (BH) semiconductor laser.

The BH diodes were optically pumped at 10 Hz using the gigawatt picosecond dye laser oscillator-amplifier. In the same general experimental arrangement described at the end of Chapter 6, the amplified pulse train, with pulse durations of $\lesssim$ 1 psec, was split (unequally) for the cross-correlation measurement technique of Fig. 6.8. The smaller portion ($\sim$ 1%) was used for the stepping motor controlled variable delay arm of the cross-correlator. The majority of the energy was focussed into a 10 cm cell of D6 acetone to down shift the amplified pulse wavelength to $\sim$ 686 nm via stimulated Raman scattering. Again, colored glass filters pass only the first Stokes line, as well as attenuating it to $\sim$ 2×10^{-7} Joules/pulse. The 1.8 eV energy of the Raman shifted photons easily passes through the $Al_{0.4}Ga_{0.6}As$ upper cladding layer of the diode for optical pumping of the active region of the device only. As mentioned above, high duty cycle electrical operation provided an easily detectable signal using infrared viewers, etc., for setting up the preliminary collimation with a 60X microscope objective and alignment into the detection apparatus. For monitoring the 10 Hz optically pumped pulsed operation, the optical pulses from the diode were first fed into a PIN photodiode on a flip mirror mount. This PIN diode was monitored in real time on a 350 MHz bandwidth oscilloscope at a 10 Hz repitition with a time scale of $\sim$ 10 nsec/div, with the scope triggered from the auxiliary output of the gigawatt laser synchronizing circuitry described in Chapter 5. The effect of the optical pumping is then readily observable and the signal strength is easily optimized with simultaneous viewing of the pump beam placement under a stereoscopic microscope. The flip mirror is then retracted to pass the IR signal into the cross-correlator. Again a preliminary alignment is performed visually with IR viewing devices, at which point the electrical current pumping is shut off, leaving only the picosecond optically pumped output. As in Chapter 6, the pulse from the PMT detecting the sum frequency is monitored with a sampling oscilloscope and its peak height is fed into the Nicolet 1174 signal averager. The address is controlled

by the digital stepping motor drive circuitry for the variable delay arm, and the CRT of the signal averager then displays the cross-correlation of the picosecond amplified pulse and the IR output of the BH laser.

Fig. 7.2 shows the experimental results from a 200 μm long BH laser under picosecond optical pumping only. The three curves here represent the semiconductor laser *simultaneous* ouput at three *different wavelengths* with no change in the pumping conditions or the alignment process. The spectrally resolved temporal pulse profiles were obtained by angle tuning the $LiIO_3$ sum frequency generating crystal. Using Eq. 5.4, Eq. 5.6 and Eq. 5.7, it is then possible to determine the wavelength which is *phase-matched* for sum frequency generation at each angle ϑ of the crystal. Fig. 7.2a, b, and c show, respectively, the simultaneous output of the BH laser at λ_o, $\lambda_o - 12$, and $\lambda_o - 23$ nm with pulse widths of 15.6, 9.5, and 4.5 psec where $\lambda_o \approx$ 766nm $\pm$ 20 nm. The large uncertainty in the reference level is due only to the rough calculated *absolute* calibration of the angle tuning of the crystal. The important point is the large spread in wavelengths and the different temporal behavior at different wavelengths. This behavior contains information on the picosecond carrier dynamics during the lasing process. The estimated carrier density here is $\lesssim 5\text{x}10^{18}\ \text{cm}^{-3}$, although this is only an approximate figure due to the uncertainties of the transparent contact optical pumping scheme. In passing, we note that a "spectrally resolved" measurement of the temporal pulse profile necessarily contains a trade-off due to the uncertainty principle. This can be dealt with in a manner similar to the treatment of resolution in Chapter 5, with both the pulse width of the cross-correlating probe and the thickness of the crystal determining the experimentally observed bandwidth. For a 1 mm thick $LiIO_3$ crystal, the bandwidth for a CW probe would be $\sim$ 27Å, and the probe pulse begins to make a comparable contribution only when the probe pulse width reaches times as short as $\sim 10^{-13}$ sec. This bandwidth is definitely wide enough to insure that the temporal

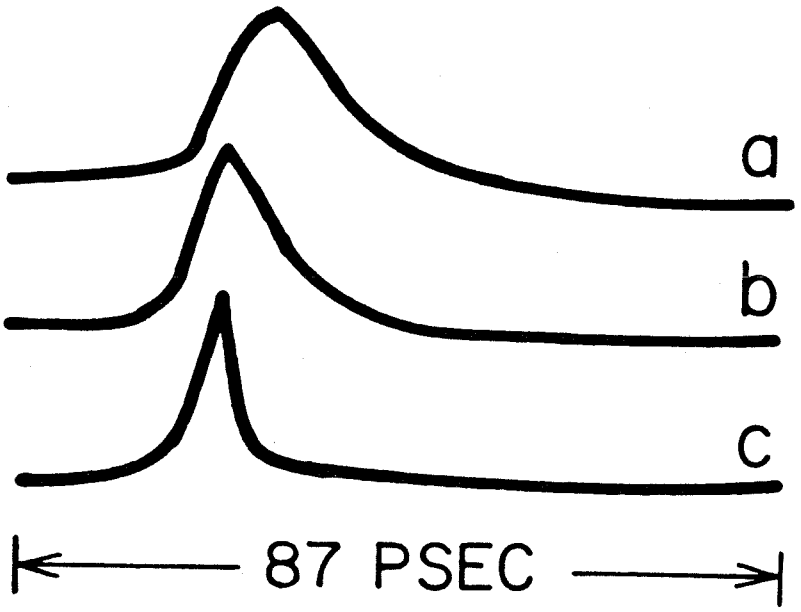

Figure 7.2 200 μm long BH diode laser output; **a**, **b**, and **c** are the long, medium, and short wavelength normalized outputs with pulsewidths of 15.6, 9.0, and 4.5 psec respectively.

resolution, which is the quantity of principle interest here, is maintained to a level controlled by the probe pulse. It should also be pointed out here that care must be exercised in interpreting angle tuning data, since changes in the relative angle of crystal rotation to the incident beams are *not* the same as changes in the relative angle of the crystalline *optical axis* due to the refraction which takes place upon entering the crystal.

A number of investigators in the past several years have obtained ultrashort optical pulses by optically pumping thin platelet ($\lesssim 1\mu$m thick) GaAs and InGaAsP lasers[2,3]. The traces shown in Fig. 7.2 confirms the general trend towards shorter pulses at higher energies under short-pulse high excitation conditions as observed by these investigators. However, the implication has been made that the picosecond timescale pulses are due to the ultrashort cavities ($\sim 2\ \mu$m long), while the pulses shown in Fig. 7.2 have comparable or even shorter pulse widths and are generated from a 200 μm long BH laser.

The discussions of Chapter 6 emphasized that the important quantity for short time scale "giant pulse" evolution is the photon lifetime τ_p which is already in the picosecond regime for normal semiconductor laser geometries. Since the analysis in Chapter 6 suggests that the simplistic spatially averaged rate equations remain valid for very short pulses, in the first approximation, the temporal dynamics of a given device are governed entirely by the initial local gain $\Gamma\gamma$ and the photon lifetime $\tau_p = [v_g(\alpha - \frac{\ln R}{L})]^{-1}$. Decreasing the cavity length will speed up the response of a given device somewhat if R is fixed, but to maintain the same relative initial gain over threshold, the excitation density must be simultaneously increased. More importantly, the introduction of highly reflecting mirrors[2,3] raises τ_p almost to ~ 1 psec again. Since the available longitudinally integrated gain in a $\lesssim 1\mu$m long device is small, the high reflecting mirrors are necessary to achieve lasing

action. However, for the same excitation *density*, the temporal pulse profiles of the ultrashort cavity laser with dielectric mirrors should be comparable to the much longer, low reflecting mirror BH laser which also has a sizable distributed loss α. Since the BH laser cavity is potentially much larger in *volume*, the optical "giant pulse" energies can be significantly larger than the ultrashort cavity device.

The pumping level was increased above the value shown in Fig. 7.2 to investigate the effect on pulse dynamics. The general trend was again similar to the Q-switched laser behavior described in Chapter 6, with a forward shift in time and a pulse width reduction. Using a computer model to be described in Section 7.3, the highest carrier densities attained were still estimated to be below $\lesssim 10^{19}\,cm^{-3}$ due to a dynamic Burstein-Moss[4,5] bleaching effect at the pump wavelength in the $Al_{0.08}Ga_{0.92}As$ active region of the laser. As the lasers are pumped up to this limit, several interesting features begin to appear. As expected from band filling, shorter wavelength pulses are generated, but the pulses also develop unusual temporal profiles. Fig. 7.3 shows the ~ 700 nm pulse output of an 80 μm long BH laser on an expanded scale with a FWHM T_{pulse} of 1.2 psec. Since this approaches the pump pulse width ($\lesssim$ 1 psec), the deconvolved BH laser pulse is also probably subpicosecond. Note that the rise time is more gradual than the fall time, in sharp contrast to the usual rate equation predictions of gain/loss switched laser action of Chapter 6. At longer wavelengths, the pulses are longer to start with, but they begin to acquire a distinct tail as the excitation density increases, even to the point of developing a secondary peak at the longest wavelengths of emission. This is shown in Fig. 7.4, and note the change in scale. Optical pumping was also attempted with a different Raman shifting medium following the gigawatt dye laser amplifier chain. Ethanol has a Raman shift of 2921 cm^{-1} [6], which shifts the 598 nm pump pulse out to 725 nm. When the BH diodes were optically pumped with this wavelength, the carriers were injected at a lower energy in the semiconductor. Experimentally,

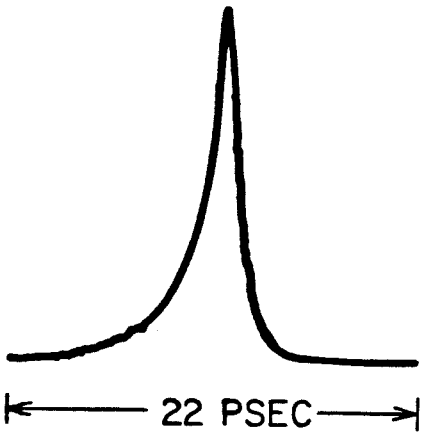

Figure 7.3 Short wavelength BH laser output under high pumping conditions. Pulse FWHM is 1.2 psec, and note unusual shape.

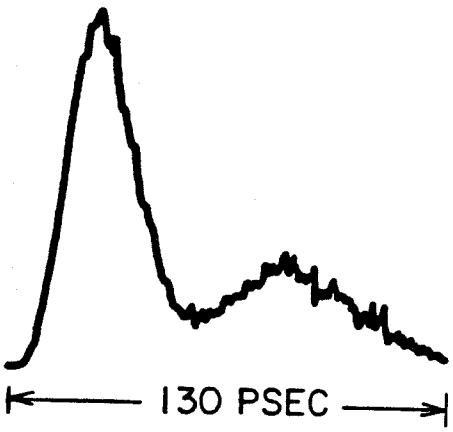

Figure 7.4 Long wavelength BH laser output under high pumping conditions. Primary peak of pulse has a 21.6 psec FWHM, but note the secondary peak.

results very similar to those shown in Fig. 7.2 were obtained. However, even at pumping levels high enough to ultimately damage the devices, no evidence of the double pulsing effect was observed with the strongest effect being a possible weak low-level shoulder developing on the trailing edge of the pulse.

Clearly the model of Chapter 6 is incapable of describing these features. There is no mechanism to generate any "double pulsing" and even more basically, there is no accomodation for the possible broadband laser emission of the optically pumped BH lasers when driven well over threshold. The fault does not lie in the description of the cavity dynamics; indeed it was shown that the spatially averaged equations can be expected to yield valid results even when $T_{pulse} < T_{RT}$. The problem lies in the gross simplification of the gain term in Eqs. 6.8-9 which does not incorporate any information about the excited state carrier dynamics during the short pulse lasing process. This is the subject of the next section.

7.2 Picosecond Carrier Dynamics in AlGaAs

The gain term used in Chapter 6 is given simply by $\Gamma\gamma(n) = \kappa(n - n_0)$. This was a semi-empirical result and holds well in many conditions of interest for normal semiconductor laser operation. To make some allowance for the frequency dependence of the gain, and to incorporate the dynamic behavior of the excited carrier distribution, many of the standard results of parabolic band semiconductor theory can be used.

The band structure of $Al_xGa_{1-x}As$ is shown in Fig. 7.5. The data on energy gaps and effective masses which follow are taken from Ref. 7, and refer to values at room temperature(300° K). The direct energy gap, hereafter referred to as E_g, is given experimentally by

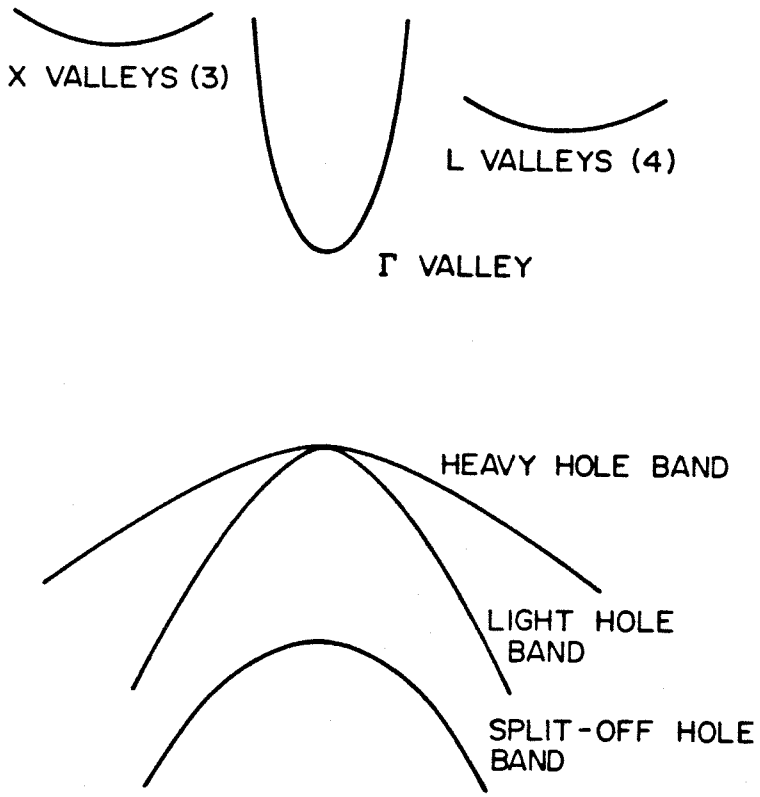

Figure 7.5 Simplified band structure of AlGaAs

$$E_g = 1.424 + 1.247x \quad eV \tag{7.1}$$

for $x \lesssim 0.45$. The spin orbit split-off valence band is located 0.34 eV below the light and heavy hole valence bands; since it is energetically unavailable under the situations considered here, it will be ignored. In pure GaAs, the light and heavy hole effective masses are

$$m_h^{heavy} = 0.45m_0 \qquad m_h^{light} = 0.082m_0 \tag{7.2}$$

In the material which follows, these bands will be treated as one with the density of states effective mass since for most considerations this is the relevant quantity. For $Al_xGa_{1-x}As$ this is given by

$$m_h = [\ (m_h^{heavy})^{\frac{3}{2}} + (m_h^{light})^{\frac{3}{2}}\ ]^{\frac{2}{3}} = 0.48 + 0.31x \tag{7.3}$$

The central Γ valley conduction band effective mass is

$$m_\Gamma = 0.067 + 0.083x \tag{7.4}$$

There are effectively four L valleys in the [111] symmetry directions at the Brillouin zone edge, and effectively three X valleys in the [100] symmetry directions. These valleys each have effective masses

$$m_L = 0.218 + 0.047x \qquad \text{and} \qquad m_x = 0.409 - 0.34x \tag{7.5}$$

where the L and X valley masses have been recomputed to refer to a *single* valley. The separation between the L and Γ valley minima is

$$\Delta E^{L\Gamma} \equiv \Delta = 0.284 - 0.605x \tag{7.6}$$

while the separation between the X and Γ valley minima is

$$\Delta E^{X\Gamma} = 0.476 - 1.122x + 0.143x^2 \tag{7.7}$$

As with the split-off valence band, the X valley system is energetically unavailable in the situations considered here and will be ignored in what follows.

In a general situation, the state of the semiconductor can be described by giving the occupation numbers of the $\vec{k}$ states in the various bands in the form of distribution functions $f_j(\vec{k})$ for each band j , where $2\int \frac{d^3k}{(2\pi)^3} f_j(\vec{k}) = n_j$, the number of electrons in the band j . In thermal equilibrium, all bands are described by the same Fermi-Dirac distribution $f_j(\vec{k}) \rightarrow f_\eta(\mathcal{E}_j(\vec{k}))$ where

$$f_\eta(x) = \frac{1}{e^{x-\eta}+1} \tag{7.8}$$

and $\mathcal{E}_j(\vec{k})$ is the energy in the band j , $\eta = \frac{\mu}{kT}$ where μ is the electron Fermi level or chemical potential, and T is the temperature of the sample.

The situations under study are far from equilibrium situations. However, at high concentrations, electron-electron scattering is extremely fast and tends to make the electrons reach an equilibrium *among themselves* in the form of a Fermi-Dirac distribution with a temperature T_e , which is, however, in general different from the lattice temperature T_L [8]. A simple estimate of the time scale necessary to achieve this equilibration for the electrons is given by considering the energy loss rate of an electron with energy $\mathcal{E}$ and effective mass m_e in a material of dielectric constant ϵ and free electron concentration n [9].

$$\frac{d\mathcal{E}}{dt} \approx -\frac{4\pi n e^4}{\epsilon^2\sqrt{2m_e\mathcal{E}}} \tag{7.9}$$

For an electron in the central Γ valley with mass 0.07 m_0 injected 0.25 eV over the band edge in a sample with free carrier density of 3×10^{18} cm^{-3} , this yields an energy loss rate of ~ 1.1 eV/psec. This rate *increases* as the electron cools, and thus in a very small fraction of a picosecond, the electron has given its injection energy to the other electrons in the "bath", reaching equilibrium with them. It is then possible to characterize the state of the electrons in the Γ valley with an electron number density n_Γ and a temperature T_e . We assume that electron-electron

collisions are equally effective in insuring that the electrons in the L valley system have the same temperature T_e. However, since momentum must be conserved, the electron-electron scattering is ineffective in transferring the electrons themselves into and out of the L valley system. Transfer of electrons from one valley system to the next is accomplished via phonon emission and absorption, and this occurs on a picosecond time scale. In practice, this means the Γ and L valleys will be characterized by the same T_e but the Fermi levels for each valley will be independent and the relative populations of the two valleys must be computed dynamically as part of the problem under consideration.

The energy loss rate of a hole to the other holes is also given by Eq. 7.9 with m_h substituted for m_e. The rate is then slower by the square root of the mass ratio, but since the holes will be injected at lower energy, the equilibration rate is still subpicosecond and the holes are then characterized by a number density p and a temperature T_h. It is implicitly assumed here that hole-hole scattering is effective in maintaining a distribution among the light and heavy hole bands. In any event, since most (~ 93%) of the electrons reside in the heavy hole band due to its larger effective mass, the dynamics will still be well approximated by using a single band approximation with the density of states effective mass.

Electron-hole energy transfer is hindered by their disparate masses. In general, the rate equivalent to Eq. 7.9 must be multiplied by the mass ratio $\frac{m_\Gamma}{m_h}$ for energy loss of electrons to holes, which brings the electron-hole equilibration rate up to a picosecond time scale comparable to other events of interest (lasing, etc.). The electron loss rate to the *light* holes would be faster, but their low number density negates any strong effect on the equilibration rate. For purposes of quantitative calculations, we employ as a good approximation standard Fokker-Plank results from two temperature plasma theory with Maxwellian distrubutions. The *average*

energy loss of an electron to the hole bath is given by[10]

$$\frac{d\bar{\varepsilon}_e}{dt} = -\frac{8\pi e^4 n(T_e - T_h)}{\sqrt{2\pi k}\, m_e m_h \epsilon^2 [\frac{T_e}{m_e} + \frac{T_e}{m_e}]^{\frac{3}{2}}} \tag{7.10}$$

where k is the Boltzman constant, and ϵ is the dielectric constant, and T_e and T_h are the electron and hole temperatures. The average hole energy loss rate is of course given by

$$\frac{d\bar{\varepsilon}_h}{dt} = -\frac{d\bar{\varepsilon}_e}{dt} \tag{7.11}$$

Here a logarithmic factor has been left out which is of the order of unity for the conditions under consideration. Also ignored is the fact that some of the electrons are in the upper valley with a different effective mass, but this is not a major effect since their number density will be fairly small.

The considerations above then permit a vast simplification in the description of the picosecond dynamics of the semiconductor. In the level of approximation we consider, the conduction bands are characterized by a single temperature T_e and the Γ and L valley system populations, n_Γ and n_L. The holes are characterized by a temperature T_h, and since we consider intrinsic material, or a high enough excitation density, the holes are characterized by a number density $p = n_\Gamma + n_L$. These become the dynamical variables in calculations for the time evolution of the semiconductor. The Fermi level is defined implicitly in terms of these dynamical quantities in each case by the relations

$$n_\Gamma = N_e^\Gamma \frac{2}{\sqrt{\pi}} F_{\frac{1}{2}}(\eta_e^\Gamma) \tag{7.12}$$

$$n_L = N_e^L \frac{2}{\sqrt{\pi}} F_{\frac{1}{2}}(\eta_e^L) \tag{7.13}$$

$$p = N_h \frac{2}{\sqrt{\pi}} F_{\frac{1}{2}}(\eta_h) \tag{7.14}$$

where $\eta = \frac{\mu}{kT}$ in each case and

$$N_e^\Gamma = 2\left(\frac{m_\Gamma kT_e}{2\pi\hbar^2}\right)^{\frac{3}{2}} \tag{7.15}$$

$$N_e^L = 4{\cdot}2\left(\frac{m_L kT_e}{2\pi\hbar^2}\right)^{\frac{3}{2}} \tag{7.16}$$

$$N_h = 2\left(\frac{m_h kT_e}{2\pi\hbar^2}\right)^{\frac{3}{2}} \tag{7.17}$$

and

$$F_j(\eta) = \int_0^\infty \frac{x^j\,dx}{e^{x-\eta}+1} \tag{7.18}$$

In practice, computational time is saved by using the analytic approximations for the Fermi levels, or η, given by[11]

$$\eta_e^\Gamma = \ln\left(\frac{n^\Gamma}{N_e^\Gamma}\right) + \frac{\sqrt{2}}{4}\left(\frac{n^\Gamma}{N_e^\Gamma}\right) - \left(\frac{\sqrt{3}}{9} - \frac{3}{16}\right)\left(\frac{n^\Gamma}{N_e^\Gamma}\right)^2 \tag{7.19}$$

$$+ \left(\frac{1}{8} + \frac{5\sqrt{2}}{48} - \frac{\sqrt{6}}{9}\right)\left(\frac{n^\Gamma}{N_e^\Gamma}\right)^3 - \left(\frac{\sqrt{5}}{25} + \frac{5\sqrt{3}}{24} - \frac{5\sqrt{2}}{32} - \frac{1585}{6912}\right)\left(\frac{n^\Gamma}{N_e^\Gamma}\right)^4 + \ldots$$

which is *very* accurate at lower densities $\left(\frac{n^\Gamma}{N_e^\Gamma}\right) \lesssim 1$ but even in the very degenerate case for $n^\Gamma = 10^{19}\ cm^{-3}$, or $\left(\frac{n^\Gamma}{N_e^\Gamma}\right) \sim 20$, the expression Eq. 7.19 is still accurate to within $\lesssim 4\%$. The same expression holds or course for the L valley electrons and the holes out to even higher densities due to the larger effective mass density of states.

The quantities which remain to be determined are then the physical processes which change the number densities and temperatures. One of the more important dynamical processes which occurs on a picosecond time scale and effects the temperatures is carrier *cooling* via phonon emission. Since $T_e > T_L$ in most of the

situations considered, the electrons give energy to the lattice. In quantum terminology, this is accomplished by emitting optical or acoustic phonons, and the rates for these processes have been calculated for Maxwell-Boltzman carrier distributions[9]. However, in the situations studied here, the larger carrier density makes modifications due to the Fermi-Dirac statistics important. In addition, Debeye screening can modify the phonon emission rates. We then discuss in some detail the carrier cooling process since it plays a large role in determining the nature of the picosecond time scale carrier dynamics.

The general Hamiltonian for the electron-phonon interaction is given by[9]

$$H' = \int \frac{d^3k}{(2\pi)^3} \left[M_{\vec{q}} a_{\vec{q}} e^{i\vec{q}\cdot\vec{r}} + M_{\vec{q}}^* a_{\vec{q}}^\dagger e^{-i\vec{q}\cdot\vec{r}} \right] \tag{7.20}$$

Here $a_{\vec{q}}$ and $a_{\vec{q}}^\dagger$ are the annihilation and creation operators for phonons of wavevector $\vec{q}$, and the H' above is the interaction for electrons at $\vec{r}$. For the conventional polar longitudinal optical phonon (PLO) interaction the matrix element is $M_{\vec{q}} = \frac{C}{q}$ where

$$C = i\left(\frac{2\pi\hbar\omega_{LO}e^2}{\bar{\epsilon}}\right)^{\frac{1}{2}} \tag{7.21}$$

and $\hbar\omega_{LO}$ is optical phonon energy, which is assumed dispersionless. For computational purposes, we use the GaAs value of 36.8 eV [12]. Here $\bar{\epsilon}$ is a dielectric constant given by

$$\frac{1}{\bar{\epsilon}} = \frac{1}{\epsilon_\infty} - \frac{1}{\epsilon_0} \tag{7.22}$$

where ϵ_∞ and ϵ_0 are the high frequency (optical, above the IR polar crystal resonance, but below the UV electronic absorption resonance) dielectric constant and the static dielectric constants, repsectively. Again we employ the GaAs values[8] of $\epsilon_\infty = 10.62$ and $\epsilon_0 = 12.53$.

For the interaction with longitudinal acoustic phonons, the matrix element is given by[9]

$$M_{\vec{q}} = i\, q^{\frac{1}{2}} D\left[\frac{\hbar}{2\rho s}\right]^{\frac{1}{2}} \tag{7.23}$$

where ρ is the density of the material, s is the sound velocity for longitudinal vibrations, and D is a deformation potential constant which in GaAs has the value 6 eV[9].

In $Al_xGa_{1-x}As$ it is well known that the PLO interaction is by far the dominant phonon cooling process except at very low electron temperatures[8], and we tentatively restrict our attention to this interaction. The Hamiltonian in this case is derived by considering the interaction of an electron with the charge density $\rho_{eff} = -\vec{\nabla}\cdot\vec{P}$ which results from a polarization wave $\vec{P}$. The polarization waves are then treated as quantized fields[13]. In the presence of a large free carrier density, this effective charge is screened by the carriers via the Thomas-Fermi or Debye dielectric constant[14]

$$\epsilon(q) = \left[\, 1 + \frac{Q^2}{q^2}\,\right]^{-1} \tag{7.24}$$

where Q is the Debeye screening wavevector. In the presence of the electrons in both valleys and the holes, this would be given by

$$Q = \left[\, \frac{4\pi e^2}{\epsilon}\left(\left.\frac{\partial n_\Gamma}{\partial \mu_e^\Gamma}\right|_{T_e} + \left.\frac{\partial n_L}{\partial \mu_e^L}\right|_{T_e} + \left.\frac{\partial p}{\partial \mu_h}\right|_{T_h} \right)\right]^{\frac{1}{2}} \tag{7.25}$$

Here ϵ is the usual dielectric constant of the semiconductor. The generalized interaction Hamiltonian then becomes

$$H' = \int \frac{d^3k}{(2\pi)^3} \frac{q}{q^2 + Q^2}\left[\, C a_{\vec{q}} e^{i\vec{q}\cdot\vec{r}} + C^* a_{\vec{q}}^\dagger e^{-i\vec{q}\cdot\vec{r}} \,\right] \tag{7.26}$$

and we consider transitions between electron and hole Bloch states which we approximate as plane waves.

For simplicity consider scattering within a single valley for electrons. The rate of change of electron energy density U_e is then given by

$$\left.\frac{dU_e}{dt}\right|_{\text{phonon cool}} = \sum_{\vec{k},\sigma} \varepsilon_{\vec{k}}^{\sigma} \frac{\partial f^{\sigma}(\vec{k})}{\partial t} \tag{7.27}$$

$$= -\sum_{\vec{k},\sigma}\sum_{\vec{k}',\sigma'} W_{\substack{\vec{k}\to\vec{k}' \\ \sigma\to\sigma'}} \varepsilon_{\vec{k}}^{\sigma} f^{\sigma}(\vec{k})[\,1 - f^{\sigma'}(\vec{k}')\,] + \sum_{\vec{k},\sigma}\sum_{\vec{k}',\sigma'} W_{\substack{\vec{k}'\to\vec{k} \\ \sigma'\to\sigma}} \varepsilon_{\vec{k}}^{\sigma} f^{\sigma'}(\vec{k}')[\,1 - f^{\sigma}(\vec{k})\,]$$

where σ is the spin index, and $f^{\sigma}(\vec{k})$ is the occupation number of the electron state σ, $\vec{k}$, and $W_{\substack{\vec{k}\to\vec{k}' \\ \sigma\to\sigma'}}$ is the transition rate given by Fermi's Golden Rule as

$$W_{\substack{\vec{k}\to\vec{k}' \\ \sigma\to\sigma'}} = \frac{2\pi}{\hbar}\sum_{\{n'\}} \left| < \vec{k}', \sigma', \{n'\}|\ H'\ |\vec{k}, \sigma, \{n\}> \right|^2 \tag{7.28}$$

$$\times\ \delta(\,\varepsilon_{\vec{k}}^{\sigma} - \varepsilon_{\vec{k}'}^{\sigma'} + E\{n\} - E\{n'\}\,)$$

where $\{n\}$ denotes the set of all phonon occupation numbers and $E\{n\}$ is the energy of the whole phonon state associated with those numbers. The PLO interaction is spin conserving, and to first order $\{n\}$ can only change by ± 1 since H' contains only the first power of $a_{\vec{q}}$ and $a_{\vec{q}}^{\dagger}$. The matrix element insures momentum conservation, and the result becomes

$$W_{\substack{\vec{k}\to\vec{k}' \\ \sigma\to\sigma'}} = \frac{2\pi}{\hbar}|C|^2 \frac{|\vec{k}' - \vec{k}|^2}{[\ |\vec{k}' - \vec{k}|^2 + Q^2\ ]^2} \tag{7.29}$$

$$\times\ \left\{\ n_{\vec{k}'-\vec{k}}\,\delta(\,\varepsilon_{\vec{k}}^{\sigma} - \varepsilon_{\vec{k}'}^{\sigma'} + \hbar\omega_{LO}\,)\,\delta_{\sigma,\sigma'} + (\,n_{\vec{k}-\vec{k}'} + 1\,)\,\delta(\,\varepsilon_{\vec{k}}^{\sigma} - \varepsilon_{\vec{k}'}^{\sigma'} - \hbar\omega_{LO}\,)\,\delta_{\sigma,\sigma'}\ \right\}$$

The energy delta functions are converted to delta functions in k, summations are converted to integrals and after much tedious algebra and a few integrations the result is

$$\left.\frac{dU_e}{dt}\right|_{\text{phonon cool}} = -\frac{2m_e|C|^2\hbar\omega_{LO}}{\hbar^3(2\pi)^3}[n(T_e) - n(T_L)] \tag{7.30}$$

$$\times \int_0^\infty kdk[f_{\eta_e}(\frac{\mathcal{E}_{\vec{k}}}{kT_e}) - f_{\eta_e}(\frac{\mathcal{E}_{\vec{k}} + \hbar\omega_{LO}}{kT_e})] \left\{ \ln[\frac{(k + \sqrt{k^2 + \frac{2m_e\omega_{LO}}{\hbar}})^2 + Q^2}{(k - \sqrt{k^2 + \frac{2m_e\omega_{LO}}{\hbar}})^2 + Q^2}] \right.$$

$$\left. - \frac{Q^2}{(k - \sqrt{k^2 + \frac{2m_e\omega_{LO}}{\hbar}})^2 + Q^2} + \frac{Q^2}{(k + \sqrt{k^2 + \frac{2m_e\omega_{LO}}{\hbar}})^2 + Q^2} \right\}$$

where equilibrium Boson phonon distributions have been assumed and Fermi-Dirac distributions at T_e have been assumed for the electrons, so

$$n(T_e) - n(T_L) = \frac{1}{e^{\frac{\hbar\omega_{LO}}{kT_e}} - 1} - \frac{1}{e^{\frac{\hbar\omega_{LO}}{kT_L}} - 1} \tag{7.31}$$

is the difference in phonon occupations at the electron temperature and the lattice temperature. This enters the calculations by noting during the simplification of the algebra in computing Eq. 7.30 that

$$f_{\eta_e}(\frac{\mathcal{E}_{\vec{k}} + \hbar\omega_{LO}}{kT_e})[\,1 - f_{\eta_e}(\frac{\mathcal{E}_{\vec{k}}}{kT_e})\,] = n(T_e)[\,f_{\eta_e}(\frac{\mathcal{E}_{\vec{k}}}{kT_e}) - f_{\eta_e}(\frac{\mathcal{E}_{\vec{k}} + \hbar\omega_{LO}}{kT_e})\,] \tag{7.32}$$

where $n(T_e)$ is the Boson phonon occupation number and the f_{η_e} are the Fermi-Dirac electron distributions.

When screening can be neglected, $Q \to 0$. If in addition the carrier density is low enough for Maxwell-Boltzman statistics to apply, then the electron distribution becomes

$$f_{\eta_e}(\frac{\mathcal{E}_{\vec{k}}}{kT_e}) \approx e^{\eta_e - \frac{\mathcal{E}_{\vec{k}}}{kT_e}} = \frac{n_e}{2}(\frac{\hbar^2}{2\pi kT_e})^{\frac{3}{2}}(2\pi)^3 e^{-\frac{\hbar^2k^2}{2m_ekT_e}} \tag{7.33}$$

where n_e is the election number density. Under these conditions, the integrals can be performed analytically to yield the result[9]

$$\left.\frac{dU_e}{dt}\right|_{\text{phonon cool}} = -n_e\left(\frac{2m_e\omega_{LO}^3}{\hbar}\right)^{\frac{1}{2}}\frac{e^2}{\bar{\epsilon}} \tag{7.34}$$

$$\times \frac{\left[\, e^{\left(\frac{\hbar\omega_{LO}}{kT_L} - \frac{\hbar\omega_{LO}}{kT_e}\right)} - 1 \,\right]}{\left[\, e^{\frac{\hbar\omega_{LO}}{kT_L}} - 1 \,\right]} F\left(\frac{\hbar\omega_{LO}}{2kT_e}\right)$$

where

$$F(x) = \sqrt{\frac{2}{\pi}}\, x^{\frac{1}{2}}\, e^x\, K_0(x) \tag{7.35}$$

and K_0 is the modified Bessel function and $F(x)$ has been separated out because it goes to unity in the limit $T_e \to 0$. The analogous result for acoustic phonons using Maxwell-Boltzman statistics is

$$\frac{dU_e}{dt} = -\frac{n_e 8\sqrt{2} m_e^{\frac{5}{2}} D^2}{\pi^{\frac{3}{2}}\hbar^4\rho}(kT_e)^{\frac{1}{2}}(kT_e - kT_L)\, f(\alpha,\beta) \tag{7.36}$$

where

$$f(\alpha,\beta) = \frac{2\alpha\, e^{-\beta}}{\alpha - 1}\int_0^\infty y^3 e^{-y^2}\frac{\sinh[(\alpha-1)\sqrt{\beta y}]}{\sinh[\alpha\sqrt{\beta y}]}\, dy \tag{7.37}$$

and $\alpha = \dfrac{T_e}{T_L}$ and $\beta = \dfrac{2m_e s^2}{kT_e}$. For reasonable temperatures, $f(\alpha,\beta)$ is nearly unity, given asymptotically as

$$f(\alpha,\beta) = 1 - \frac{2}{3}(\alpha - 1)\beta + \mathcal{O}(\beta^2) \tag{7.38}$$

At higher temperatures the acoustic phonon loss is a more rapidly increasing function of T_e than the PLO loss, but even for temperatures of many thousands of degrees the acoustic phonon cooling is still smaller than the PLO phonon cooling by at least two orders of magnitude, and for the purposes here is thus ignored.

Fig. 7.6 shows the *average* energy loss rate $\left.\frac{1}{n_e}\frac{dU_e}{dt}\right|_{PLO}$ for the Γ valley electrons

in meV/psec as a function of electron temperature T_e with no screening included ($Q = 0$). The dotted curve is the Maxwellian result Eq. 7.34 which is independent of density. The solid curves are the results of the full Fermi-Dirac expression Eq. 7.30 for electron densities of $1x10^{17}$, $1x10^{18}$, $3x10^{18}$ and $6x10^{18}$ cm^{-3} with the lowest density being the one closest to the Mawellian result. The effect of the density increase is quite apparent. The reduced energy loss rate here is due to the unavailability of free electron states following phonon emission from the Pauli exclusion principle. Fig. 7.7 displays this effect more clearly. The dotted lines again show the Maxwellian results while the solid lines are the Fermi-Dirac results, this time as a function of density for three values of temperatures, $T_e = 400°K$, $900°K$, and $1900°K$. Note that the vertical energy loss rate scale is *logarithmic* in these curves. The cooling rate has decreased by approximately a factor of 2 even for electron densities of $5x10^{18}$ cm^{-3} at a temperature of 400°K just from the electron statistics. Since the PLO interaction is derived from elementary electrostatic arguments, the formulas Eq. 7.30 and Eq. 7.34 hold equally well for holes, and the Maxwellian result is thus obtained from the electron Maxwellian result by multiplication with square root of the effective mass ratio, $(\frac{m_h}{m_e})^{\frac{1}{2}}$. Calculations for the holes using Eq. 7.30 were also performed, and the reduction of the cooling rate due to the exclusion principle is much less drastic than for the electrons due to the higher density of states effective mass for holes.

When screening is included, an equal density of electrons and holes were assumed to calculate Q in Eq. 7.25, and all the electrons were assumed to be in the Γ valley for simplicity. Fig. 7.8 and Fig. 7.9 show the *screened* results completely analagous to the data shown in Fig. 7.6 and Fig. 7.7 without screening. As can be seen, both the Maxwellian results and the Fermi-Dirac results are both affected a great deal, and the distinction between the two is quite small. A similar calculation

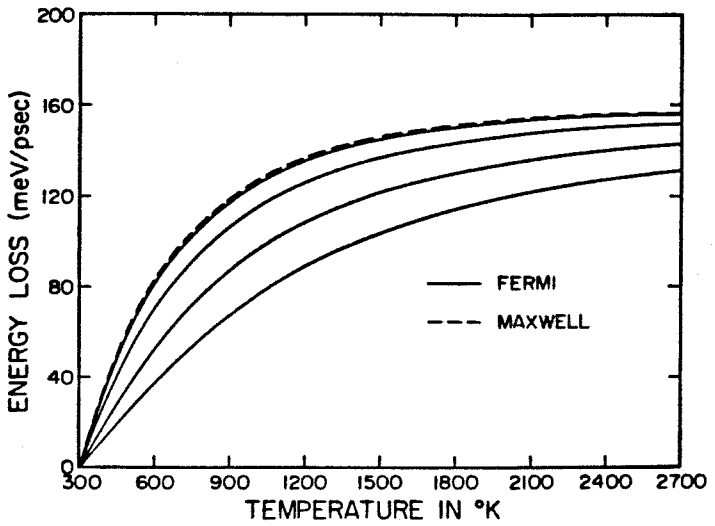

Figure 7.6 Electron energy loss rate to lattice via optical phonon emission as a function of electron gas temperature with no screening effects included. The Maxwellian result is independent of density while the Fermi-Dirac result is for carrier densities of 10^{17}, 10^{18}, $3x10^{18}$, and $6x10^{18}$ cm^{-3}.

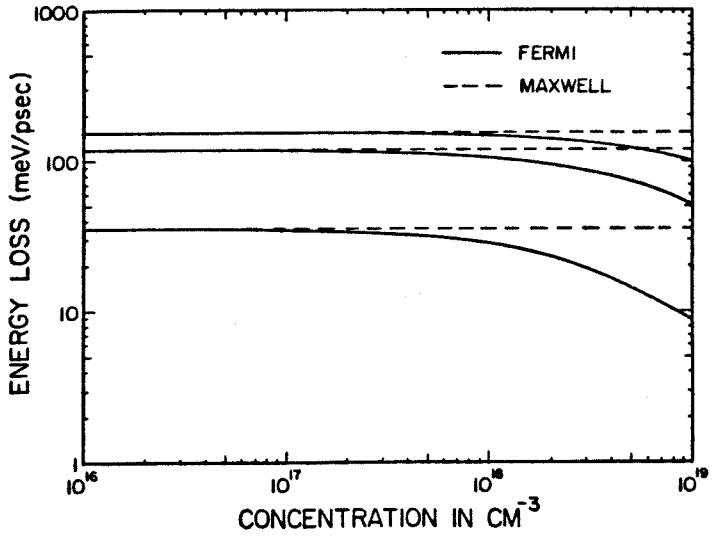

Figure 7.7 Electron energy loss rate vs. density on a logarithmic scale, again with no screening included. The reduction effect due to Fermi-Dirac statistics is shown more clearly here at three values of temperature: 400°K, 900°K, and 1900°K.

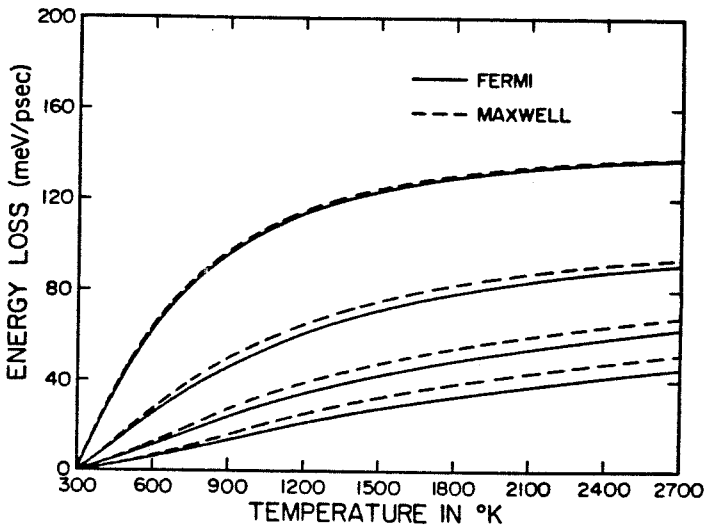

Figure 7.8 Electron energy loss rate to lattice via optical phonon emission as a function of electron gas temperature *with screening effects included*. The Maxwellian result is now very density dependent as well, with the screening overshadowing the effect of statistics. Carrier densities are again 10^{17}, 10^{18}, $3x10^{18}$, and $6x10^{18}$ cm^{-3}.

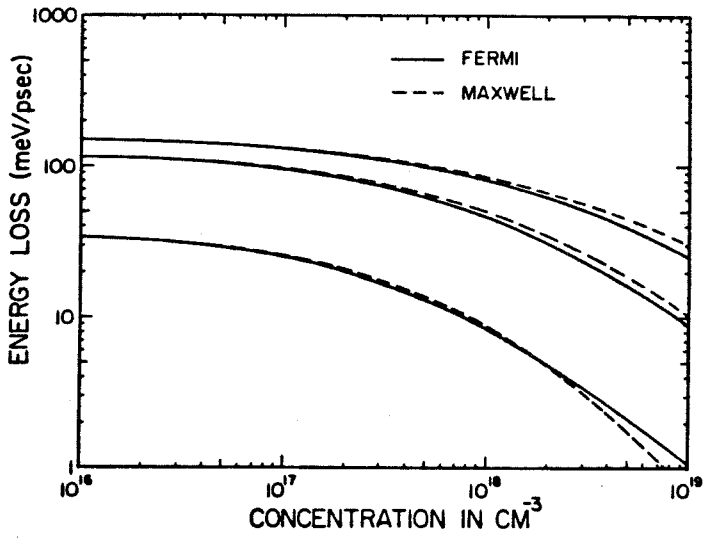

Figure 7.9 Electron energy loss rate vs. density on a logarithmic scale, *with screening included*. The reduction effect due to Fermi-Dirac statistics is again overshadowed by the effects of screening. The three curves are again for temperatures of 400°K, 900°K, and 1900°K.

for the holes revealed that, while the cooling was not reduced significantly by the exclusion principle, it *was* affected significantly by the screening. For the *dynamical* calculations performed for lasing dynamics, it was found that the screened Fermi-Dirac results derived from Eq. 7.30 could be represented within ~ 10% over the range of interest by multiplying the unscreened Maxwellian analytic results in Eq. 7.34 (and the equivalent version for holes) by the *reduction factors*

$$R^{\text{electrons}}_{\text{FD+SCREEN}}(p\ ,\ T_e) \approx \left(\ 1 + 1.15\text{x}10^{-15}\frac{p}{T_e}\ \right)^{-1} \tag{7.39}$$

$$R^{\text{holes}}_{\text{FD+SCREEN}}(p\ ,\ T_e) \approx \left(\ 1 + 1.30\text{x}10^{-16}\frac{p}{T_e}\ \right)^{-1} \tag{7.40}$$

where $p = n_\Gamma + n_L$ is the total carrier population. For the case of 400°K electrons at a carrier density of $5\text{x}10^{18}\ \text{cm}^{-3}$, the reduction is by a factor of ~ 15, which is quite substantial.

The final energy density loss rate used in the dynamical calculations for the electrons is then

$$\left.\frac{d(U_e^\Gamma + U_e^L)}{dt}\right|_{\text{phonon cool}} = \left(\ n_\Gamma + \left(\frac{m_L}{m_\Gamma}\right)^{\frac{1}{2}} n_L\ \right)\left[1 + 1.15\text{x}10^{-15}\frac{p}{T_e}\right]^{-1} \tag{7.41}$$

$$\times\ \left(\frac{2m_\Gamma\omega_{LO}^3}{\hbar}\right)^{\frac{1}{2}}\frac{e^2}{\bar{\epsilon}}\ \frac{\left[\ e^{\left(\frac{\hbar\omega_{LO}}{kT_L} - \frac{\hbar\omega_{LO}}{kT_e}\right)} - 1\ \right]}{\left[\ e^{\frac{\hbar\omega_{LO}}{kT_L}} - 1\ \right]}\ F\left(\frac{\hbar\omega_{LO}}{2kT_e}\right)$$

while for the holes the energy density loss rate is

$$\left.\frac{dU_h}{dt}\right|_{\text{phonon cool}} = p\left[1 + 1.30\text{x}10^{-16}\frac{p}{T_h}\right]^{-1} \tag{7.42}$$

$$\times\ \left(\frac{2m_h\omega_{LO}^3}{\hbar}\right)^{\frac{1}{2}}\frac{e^2}{\bar{\epsilon}}\ \frac{\left[\ e^{\left(\frac{\hbar\omega_{LO}}{kT_L} - \frac{\hbar\omega_{LO}}{kT_h}\right)} - 1\ \right]}{\left[\ e^{\frac{\hbar\omega_{LO}}{kT_L}} - 1\ \right]}\ F\left(\frac{\hbar\omega_{LO}}{2kT_h}\right)$$

In general, the cooling rate for holes is faster by at least the factor ~ $\left(\frac{m_h}{m_\Gamma}\right)^{\frac{1}{2}}$ as

noted earlier. One of the principal energy loss routes for electrons is then to give their energy to the *holes* via the Coulomb equilibration given by Eq. 7.10, and for the holes to lose this energy via optical phonon emission. The electrons of course also lose a significant amount of their energy through the phonon emission, especially if the electron distribution is initially very hot, since this *decreases* the Coulomb equilibration but *increases* the phonon cooling rate.

Intervalley scattering is computed in a similar manner to that above. The electron in this case is scattered from the central Γ valley to near the L valley minima at the Brillouin zone edge, and hence the wavevector of the phonon must have a large nearly constant value $\vec{q}_0$. Whatever the type of phonon interaction which accomplishes this, the matrix element $M_{\vec{q}_0}$ in the interaction Hamiltonian will then be approximately a constant. Using the phenomenology of the acoustic phonon matrix element, the interaction can then be characterized by a matrix element

$$M_{\vec{q}_0} = i\tilde{D}\left(\frac{\hbar}{2\rho\omega}\right)^{\frac{1}{2}} \tag{7.42}$$

where $\tilde{D} \equiv q_0 D$. With typical phonon dispersion characterstics, the phonon involved in the interaction will have an energy nearly the same as the optical phonon energy at $\vec{q} = 0$, and ω is thus taken to be a constant, $\omega \approx 0.8\omega_{LO}$ [9]. The scattering rate of an electron of energy $\mathcal{E}$ in the Γ valley to the L valleys whose minima lie an energy Δ above the Γ valley minimum is computed in a manner similar to that outlined above with the result[9]

$$W_{\Gamma \to L} = \frac{4m_L^{\frac{3}{2}}\tilde{D}^2}{\sqrt{2}\pi\rho\hbar\omega\hbar^2} \tag{7.43}$$

$$\times \left[(\mathcal{E} - \Delta - \hbar\omega)^{\frac{1}{2}} (n+1) + (\mathcal{E} - \Delta + \hbar\omega)^{\frac{1}{2}} n \right]$$

while the *return* scattering rate from the L valley system back into the Γ valley system is given by

$$W_{L\to\Gamma} = \frac{m_\Gamma^{\frac{3}{2}}\tilde{D}^2}{\sqrt{2}\pi\rho\hbar\omega\hbar^2} \tag{7.44}$$

$$\times \left[(\tilde{\mathcal{E}} + \Delta - \hbar\omega)^{\frac{1}{2}} (n+1) + (\tilde{\mathcal{E}} + \Delta + \hbar\omega)^{\frac{1}{2}} n \right]$$

where $\tilde{\mathcal{E}}$ is the energy in the L valley system measured with respect to the L valley minimum. This rate is considerably smaller due to the low mass of the Γ valley and the fact that the scattering rate *out* is enhanced by the large density of states generated by the *four* L valleys.

The Fermi-Dirac carrier distribution for electrons in the Γ valley with energies comparable to Δ is well approximated by a simple exponential but the Fermi level must be determined carefully since the chemical potential determined from Maxwell-Boltzman statistics does not apply in general. The high density of states in the L valley system allows the same approximation to be made for the L valley distribution. The rates Eqs. 7.43-4 are then integrated to get the *net* scattering rate of electrons from the Γ valley into the L valley system as

$$\left.\frac{dn_\Gamma}{dt}\right|_{\Gamma\to L} = -\frac{\tilde{D}^2 4(m_L m_\Gamma)^{\frac{3}{2}} kT_e\, e^{-\frac{\Delta}{2kT_e} - \frac{\hbar\omega}{2kT_e}}}{2\pi^3\rho\hbar^5 \left(e^{\frac{\hbar\omega}{kT_e}} - 1\right)} \tag{7.45}$$

$$\times \left[\left(e^{\frac{\mu_e^\Gamma}{kT_e}} - e^{\frac{\mu_e^L + \Delta}{kT_e}} e^{\left(\frac{\hbar\omega}{kT_L} - \frac{\hbar\omega}{kT_e}\right)} \right) \left(\frac{\Delta - \hbar\omega}{\hbar\omega}\right) K_1\left(\frac{\Delta - \hbar\omega}{2kT_e}\right) \right.$$

$$\left. + \left(e^{\frac{\mu_e^\Gamma}{kT_e}} e^{\left(\frac{\hbar\omega}{kT_L} - \frac{\hbar\omega}{kT_e}\right)} - e^{\frac{\mu_e^L + \Delta}{kT_e}} \right) \left(\frac{\Delta + \hbar\omega}{\hbar\omega}\right) K_1\left(\frac{\Delta + \hbar\omega}{2kT_e}\right) \right]$$

where $K_1(x)$ is the modified Bessel function. Here it should be recalled that the chemical potentials are measured with respect to their own band edges.

This summarizes the relevant results for the carrier dynamics in AlGaAs which will be needed in the next section to characterize the carrier and lasing dynamics in

the picosecond optically pumped BH laser.

7.3 Ultrafast Carrier and Lasing Dynamics in Picosecond Optically Pumped BH lasers

In this section a model is developed to replace the simple linear gain rate equation analysis with a more comprehensive treatment incorporating broadband stimulated emission and the picosecond carrier dynamics described in Section 7.2. It has been shown in Section 7.2 that the carriers will be well described by Fermi-Dirac distributions with temperature T_e and T_h for the electrons and holes respectively. This fact is then incorporated to describe optical interactions by modifying the standard parabolic band semiconductor gain/loss coefficient[15] to have different carrier temperatures, yielding

$$\gamma(\nu,n_\Gamma,p,T_e,T_h) = A(h\nu - E_g)^{\frac{1}{2}} \left(f_{\eta_e^\Gamma}(Z_e) + f_{\eta_h}(Z_h) - 1\right) \tag{7.46}$$

where $f_\eta(x)$ is the Fermi-Dirac distribution as in Eq. 7.8, and as before $\eta = \frac{\mu}{kT}$ in each case. Here

$$Z_e \equiv \frac{m_r}{m_\Gamma}\frac{(h\nu - E_g)}{kT_e} \tag{7.47}$$

and

$$Z_h \equiv \frac{m_r}{m_h}\frac{(h\nu - E_g)}{kT_h} \tag{7.48}$$

where m_r is the *reduced* mass for the optical transition which is assumed $\vec{k}$ conserving, $m_r^{-1} = m_\Gamma^{-1} + m_h^{-1}$. The constant A is given by

$$A = \left(\frac{2m_r}{\hbar^2}\right)^{\frac{3}{2}} 2\,\frac{e^2}{m_0^2 cn\omega}\left|< c, \vec{k} = 0\ |\vec{\varepsilon}\cdot\vec{p}|\ v, \vec{k} = 0 >\right|^2 \tag{7.49}$$

where $\vec{p}$ is the electron momentum and $\vec{\epsilon}$ is the optical polarization vector. In practice, A is fit to experimentally measured absorption coefficients at fairly high energies, and the value we employed was $2.8\text{x}10^4\ \text{cm}^{-1}\text{eV}^{-\frac{1}{2}}$. The convention throughout will be that hole energies are measured with their zero reference level at the valence band edge with energy increasing *down* into the band, i.e.,

$$E_h = \frac{\hbar^2 k^2}{2m_h} \tag{7.50}$$

Electron energies are similarly measured from a reference level at their respective band edges. The Fermi levels are then determined implicitly by the results Eqs. 7.12-14 in terms of the dynamic variables n_Γ, p, T_e, T_h where we have omitted n_L since it is always determined by the relation $n_L = p - n_\Gamma$.

The usual result[15] for the total spontaneous emission rate $r(\nu)$ into the frequency interval $d\nu$ about ν is extended to be

$$r(\nu_p,n_\Gamma,p,T_e,T_h)\ d\nu = \gamma(\nu,n_\Gamma,p,T_e,T_h)\ \frac{8\pi n^2\nu^2 d\nu}{c^2}\ \frac{f_{\eta_e^\Gamma}(Z_e) f_{\eta_h}(Z_h)}{\left(f_{\eta_e^\Gamma}(Z_e) + f_{\eta_h}(Z_h) - 1\right)} \tag{7.51}$$

The above describes the optical interactions, and we now derive the temperature dynamics by considering an energy balance equation. In general, for plasma type j, the rate of change of energy density U_j is given by

$$\left.\frac{dU_j}{dt}\right|_{\text{total}} = \left.\frac{\partial U_j}{\partial n_j}\right|_{T_j} \cdot \frac{dn_j}{dt} + \left.\frac{\partial U_j}{\partial T_j}\right|_{n_j} \cdot \frac{dT_j}{dt} \tag{7.52}$$

Here the LHS consists of the calculated sum of all the energy loss rates and energy gain rates from all processes in the optically pumped BH laser which will be addressed shortly. Since $\frac{dn_j}{dt}$ is also a dynamical calculated quantity, Eq. 7.52 is inverted to give a differential equation for the temperature evolution of the plasma

type j

$$\frac{dT_j}{dt} = \frac{1}{\left.\frac{\partial U_j}{\partial T_j}\right|_{n_j}}\left[\frac{dU_j}{dt} - \left.\frac{\partial U_j}{\partial n_j}\right|_{T_j}\cdot\frac{dn_j}{dt}\right] \tag{7.53}$$

The energy densities U_j of the plasma type j are given by standard results

$$U_j = N_j k T_j \frac{2}{\sqrt{\pi}} F_{\frac{3}{2}}(\eta_j) \tag{7.54}$$

where the N_j are defined by Eqs. 7.15-17 and $F_{\frac{3}{2}}$ is defined by Eq. 7.18. For dynamical calculations, an analytic approximation for $F_{\frac{3}{2}}$ was used[16]

$$F_{\frac{3}{2}}(\eta) = \left[\frac{10\sqrt{2}}{[2.64 + \eta + (|\eta - 2.64|^{\frac{9}{4}} + 14.9)^{\frac{4}{9}}]^{\frac{5}{2}}} + \frac{4\, e^{-\eta}}{3\sqrt{\pi}}\right]^{-1} \tag{7.55}$$

which is accurate to < 0.63% for all η .

It is straightforward to show that

$$\left.\frac{\partial U_e^\Gamma}{\partial T_e}\right|_{n_\Gamma} = \frac{5}{2} k N_e^\Gamma \frac{2}{\sqrt{\pi}} F_{\frac{3}{2}}(\eta_e^\Gamma) + \frac{3}{2} n_\Gamma k T_e \left.\frac{\partial \eta_e^\Gamma}{\partial T_e}\right|_{n_\Gamma} \tag{7.56}$$

and

$$\left.\frac{\partial U_e^\Gamma}{\partial n_\Gamma}\right|_{T_e} = \frac{3}{2} n_\Gamma k T_e \left.\frac{\partial \eta_e^\Gamma}{\partial n_\Gamma}\right|_{T_e} \tag{7.57}$$

with similar results holding for the L valley electrons and the holes.

The total energy loss rate of the LHS of Eq. 7.52 is given by a number of separate terms. These are the energy gain from injection (pumping)

$$\left.\frac{dU_j}{dt}\right|_{inj} = [\Delta\mathcal{E}_{inj}]_j \left.\frac{dn_j}{dt}\right|_{inj} \tag{7.58}$$

where $[\Delta\mathcal{E}_{inj}]_j$ is the fraction of the injected energy $\mathcal{E}_{inj}$ which goes to carrier type j. Recombination, including both stimulated and spontaneous, is handled similarly

$$\left.\frac{dU_j}{dt}\right|_{\text{recomb}} = \int [\Delta\mathcal{E}_{\text{recomb}}]_j \left.\frac{dn_j}{dt}\right|_{\text{recomb at }\mathcal{E}} d\mathcal{E} \tag{7.59}$$

where $\left.\frac{dn_j}{dt}\right|_{\text{recomb at }\mathcal{E}}$ is the rate of radiative recombination which removes carriers of type j with energies within $d\mathcal{E}$ of $[\Delta\mathcal{E}_{\text{recomb}}]_j$. The phonon cooling has been detailed in Section 7.2 and gives a contribution referred to as

$$\left.\frac{dU_j}{dt}\right|_{\text{phonon cool}} \tag{7.60}$$

The energy loss due to the Coulomb interactions with carriers of the other type is given in Section 7.2 by Eqs. 7.10-11, and is referred to as

$$\left.\frac{dU_j}{dt}\right|_{\text{e-h collisions}} \tag{7.61}$$

For the electron energy density loss rates, the Γ valley and L valley contributions are summed. In doing so, we note that each time an electron is transferred from the Γ to the L valley system, and amount of kinetic energy Δ is lost where Δ is given by Eq. 7.6. A term must then be added to the total electron energy density loss rate of

$$\left.\frac{dU_e^{\text{total}}}{dt}\right|_{\text{intervalley}} = -\Delta \left.\frac{dn_\Gamma}{dt}\right|_{\Gamma \to L} \tag{7.62}$$

where the derivative on the RHS is given by Eq. 7.45.

This provides the complete conceptual approach for solving the picosecond dynamics of the optically pumped semiconductor laser. To complete the scheme, we employ the uniform cavity rate equation for the photon density $\varphi(\nu)$ which is now a broadband photon density. Also, the pumping term in Eq. 6.9 is now dependent upon carrier densities and temperatures since the optical gain given by Eq. 7.46 also governs the absorption coefficient in the active region at the pump frequency ν_p.

The final set of integro-differential rate equations to be solved can then be written schematically as

$$\frac{dn_\Gamma}{dt} = -\frac{I_p(t)}{h\nu_p}\gamma(\nu_p,n_\Gamma,p,T_e,T_h) + \left.\frac{dn_\Gamma}{dt}\right|_{\Gamma\to L}$$

$$-\int_0^\infty \left[\frac{c}{n}\gamma(\nu,n_\Gamma,p,T_e,T_h)\,\varphi(\nu) + r(\nu,n_\Gamma,p,T_e,T_h)\right] d\nu \qquad (7.63)$$

$$\frac{dn_L}{dt} = -\left.\frac{dn_\Gamma}{dt}\right|_{\Gamma\to L} \qquad (7.64)$$

$$\frac{d\varphi(\nu)}{dt} = \left[\Gamma\,\frac{c}{n}\gamma(\nu,n_\Gamma,p,T_e,T_h)\,\varphi(\nu) + \beta r(\nu,n_\Gamma,p,T_e,T_h)\right] - \frac{\varphi(\nu)}{\tau_{ph}} \qquad (7.65)$$

$$\frac{dT_e}{dt} = \frac{1}{\left[\frac{\partial U_e^\Gamma}{\partial T_e} + \frac{\partial U_e^L}{\partial T_e}\right]}\left[\frac{m_r}{m_e}\left(1-\frac{E_g}{h\nu_p}\right)I_p(t)\gamma(\nu,n_\Gamma,p,T_e,T_h)\right.$$

$$-\frac{m_r}{m_e}\int_0^\infty\left[\frac{c}{n}\gamma(\nu,n_\Gamma,p,T_e,T_h)\,\varphi(\nu) + r(\nu,n_\Gamma,p,T_e,T_h)\right] h\nu\, d\nu \qquad (7.66)$$

$$-\Delta\left.\frac{dn_\Gamma}{dt}\right|_{\Gamma\to L} + \left.\frac{dU_e^\Gamma}{dt}\right|_{\text{phonon cool}} + \left.\frac{dU_e^L}{dt}\right|_{\text{phonon cool}}$$

$$\left.+\left.\frac{d\,(U_e^\Gamma + U_e^L)}{dt}\right|_{\text{e-h collisions}} - \frac{\partial U_e^\Gamma}{\partial n_\Gamma}\frac{dn_\Gamma}{dt} - \frac{\partial U_e^L}{\partial n_L}\frac{dn_L}{dt}\right]$$

$$\frac{dT_h}{dt} = \frac{1}{\frac{\partial U_h}{\partial T_h}}\left[\frac{m_r}{m_h}\left(1-\frac{E_g}{h\nu_p}\right)I_p(t)\gamma(\nu,n_\Gamma,p,T_e,T_h)\right.$$

$$-\frac{m_r}{m_h}\int_0^\infty\left[\frac{c}{n}\gamma(\nu,n_\Gamma,p,T_e,T_h)\,\varphi(\nu) + r(\nu,n_\Gamma,p,T_e,T_h)\right] h\nu\, d\nu \qquad (7.67)$$

$$\left.+\left.\frac{dU_h}{dt}\right|_{\text{phonon cool}} - \left.\frac{d\,(U_e^\Gamma + dU_e^L)}{dt}\right|_{\text{e-h collisions}} - \frac{\partial U_h}{\partial p}\frac{dp}{dt}\right]$$

Here $I_p(t)$ is the pump intensity, and we have assumed that the active layer is thin enough such that $e^{\gamma d} - 1 \approx \gamma d$ although this approximation is not essential. τ_{ph} is the photon lifetime, β is the fraction of spontaneous emission into the lasing modes, and all the other quantities have been defined earlier in Chapter 7.

This relatively simple model predicts almost all of the observed features of the short pulse laser performance. In particular, the strong λ dependence of the pulse width is correctly predicted, even in detail down to the unusual shapes as shown in Fig. 7.3 The important physical effects seem to arise just from the cooling of the plasma and the downward motion of the Fermi levels. After a preliminary cooling period of a few picoseconds the gain is sufficient over a broad range of wavelengths for stimulated emission to begin. An unusual and perhaps non-intuitive computed result is that the lasing actually re-heats the plasma due to the preferential elimination of lower energy carriers. This reduces the gain and lasing action slows or subsides and the plasma then cools again. This mechanism in itself could lead to shoulders on the long wavelength pulses and actually produce double peaks on a picosecond time scale if the cooling were slower than the theoretically predicted value. It was concluded that a more likely mechanism responsible for the these secondary peaks is the many-valley effect included in Eqs. 7.63-7 and shown schematically in Fig. 7.10. Because of the high density of states in the L valleys, electrons are rapidly scattered there during the initial excitation when the plasma is still hot and the Γ valley Fermi level is high. After lasing has virtually emptied the central Γ valley, the L valley electrons return slowly because of the low density of states in the Γ valley. Here they cool to the band edge to allow the long wavelength emission to continue.

Fig. 7.11 shows the evolution of the Γ valley electron density n_Γ , the L valley electron density n_L , and the electron and hole temperatures T_e and T_h computed from the set of equations outlined in Eqs. 7.63-67. The integrals in freqency were

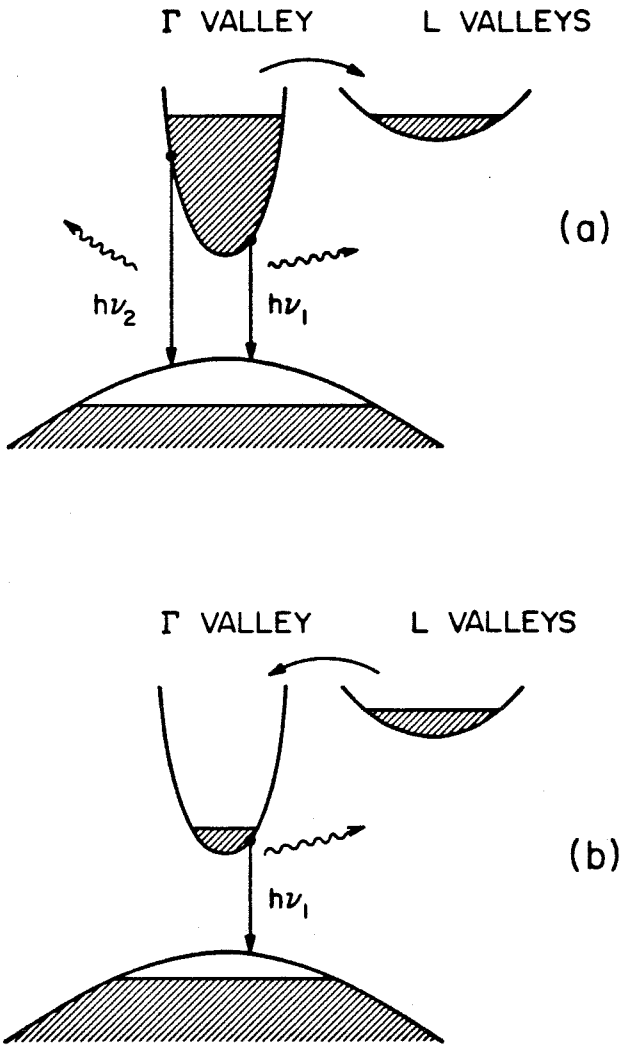

Figure 7.10 Many valley effect for the double pulsing phenomenon. **(a)** Immediately following excitation the high density hot carrier distribution spills over into the L valley system and lasing begins at both short and long λ. **(b)** After lasing has virtually depleted the central Γ valley population the L valley slowly empties to allow the long λ emission to continue for a second, delayed peak.

handled discretely in the same manner as the treatment of the spatial variable in the full TW cavity rate equations in Chapter 6. The carrier reheating effect is seen, and the rapid equilibration of the electrons and holes is also evident. The carrier density reaches a maximum of $\sim 5 \times 10^{18}$ cm^{-3} here, although the injected intensity is sufficient to produce a carrier density ~ 50% higher than this in a 0.2 μm thick region if there were no Burstein-Moss bleaching at the pump wavelength. The small build-up of electrons in the L valley system returns "slowly" into the Γ valley as expected. The sum of the powers at all frequencies is shown in Fig. 7.12 along with the pump power incident onto the active region (only ~ 25% of this power is initially absorbed with even less integrated absorption due to the dynamic Burstein-Moss bleaching effect). The *average* pulse width is thus seen to be several picoseconds with a peak power of ~ 6 Watts, quite similar to the power levels seen in Chapter 6. The total pumping energy here was ~ 0.15 mJ/cm^2 incident onto the active region at a wavelength of 686 nm, and was a $sech^2$ intensity profile pulse with a FWHM of 1 psec centered at time t = 0 .

Fig. 7.13 and 7.14 show the computed normalized pulse shapes from the system of equations outlined above at short and long wavelength (~ 67 nm and ~ 8 nm shorter than the band edge wavelength, respectively) under the pumping conditions given above. The overall agreement with the observed behavior of Fig. 7.3 and Fig. 7.4 is seen to be quite good. Calculations were performed at many pumping levels, etc., and at lower pumping levels the long wavelength secondary peaks are not present, again in agreement with experiment. Also, when an ethanol Raman shifted pulse was used in the computation, thereby lowering the injected energy of the carriers, the L valley population was significantly lower, thereby reducing the double pulsing as observed experimentally. Another fact which is perhaps more important than the lower injected energy effect on the carrier temperature is that in this case the Burstein-Moss bleaching is a stronger effect, and lowers the total number of

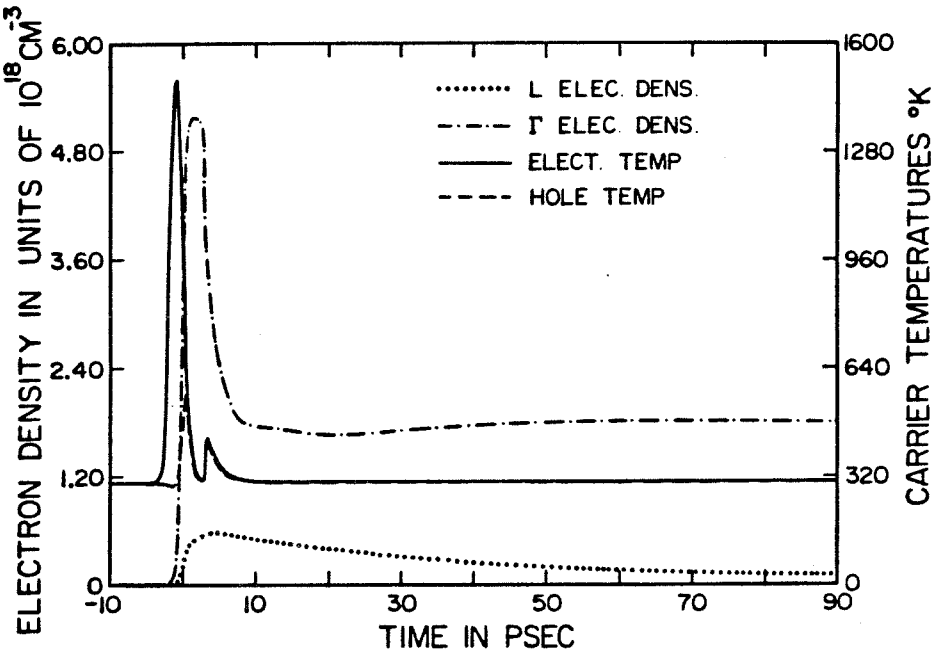

Figure 7.11 Electron number density in the Γ and L valleys and electron and hole temperatures from the numerical calculation. For parameters used see text.

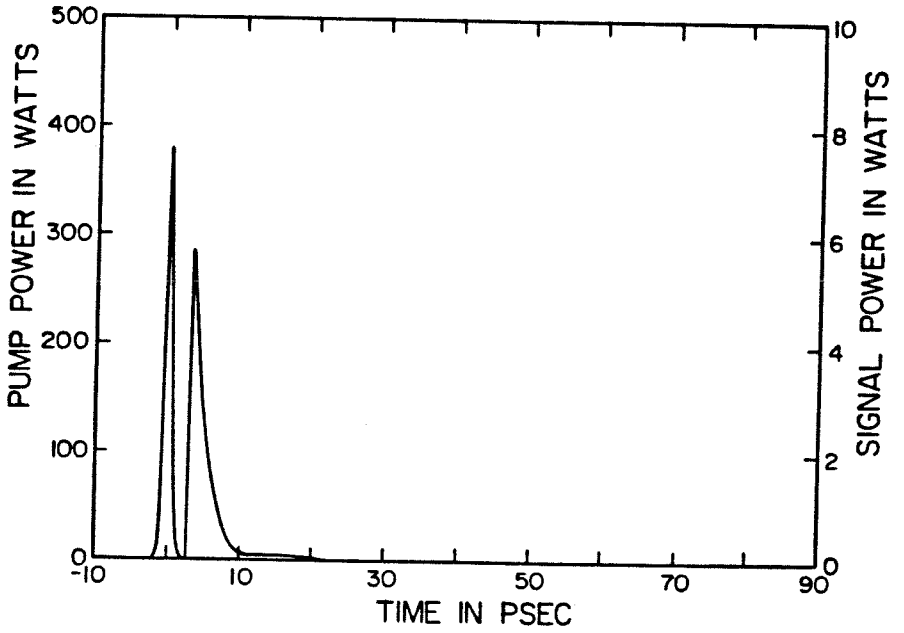

Figure 7.12 Total optical power from the "gaint pulse" BH laser output. The calculation is the same one shown in Fig. 7.11.

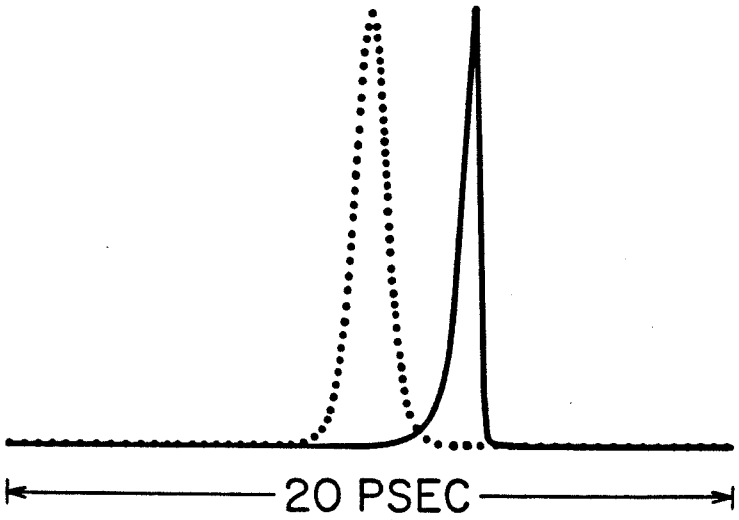

Figure 7.13 Computed response of semiconductor laser at short wavelength under high pumping conditions; dotted line is normalized pump pulse shown for time reference. Shape is similar to observed behavior show in Fig. 7.3. Calculation is the same one shown in Fig. 7.11.

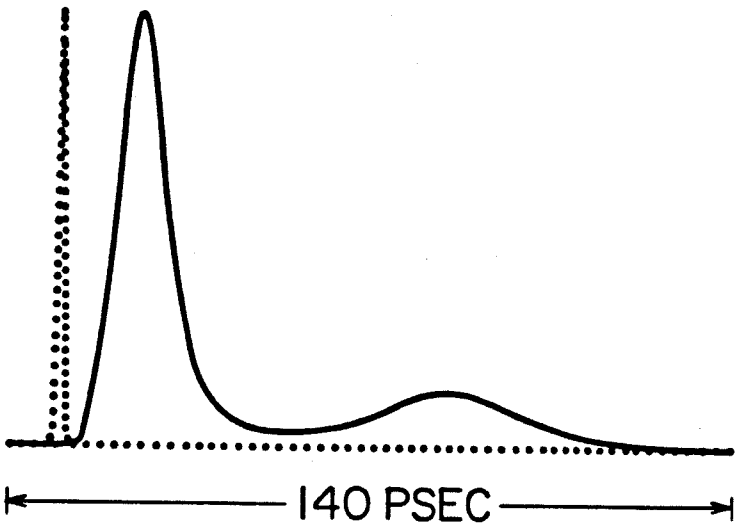

Figure 7.14 Computed response of semiconductor laser at long wavelength under high pumping conditions; dotted line is normalized pump pulse shown for time reference. Shape is similar to observed behavior show in Fig. 7.4. Calculation is the same one shown in Fig. 7.11.

injected carriers considerably.

The constant in the calculation which is least well known is the "deformation potential" for intervalley scattering. The value used was 1.5×10^8 eV/cm which is in the same range as values successfully employed in Gunn effect calculations[9]. Since the scattering rate varies as the square of this parameter its value has a sizable effect on the relative number of carriers which reach the L valley system as well as their return rate. However, over a fairly wide range of values, at *some* wavelengths the double pulsing occurs with the time scale observed experimentally. This occurs because the magnitude of the gain is wavelength sensitive, and this also plays a role in the time scale of the secondary peak evolution. In this sense, the model is not overly sensitive to this parameter.

To a large extent the lasing dynamics is governed by the Fermi level positions since these determine via Eq. 7.46 which wavelengths experience optical gain and which experience loss. Fig. 7.15 shows the Γ valley Fermi level and the hole Fermi level as functions of time with the pump pulse also shown as a reference point. From this it can be seen that the holes never become very degenerate at the density considered in this calculation. Also shown is the rapid drop of the Fermi levels at the onset of lasing action. This is the mechanism responsible for the extremely short pulse behavior shown experimentally in Fig. 7.3 and theoretically in Fig. 7.13. Normally the photon density in "giant pulse" evolution decays away on a time scale of the photon lifetime τ_p, and the shapes are always similar to those shown in Chapter 6. However, at the higher lasing energies in the semiconductor, the gain term involves some subtleties which modify the usual dynamics. It was already noted that when lasing begins, there is a temperature reheating effect due to the preferential elimination of lower energy carriers. In addition to this, the number density is dropping due to the recombination by stimulated emission. *Both* of these effects lead to a drop in the Fermi levels for the electrons and holes. The Fermi

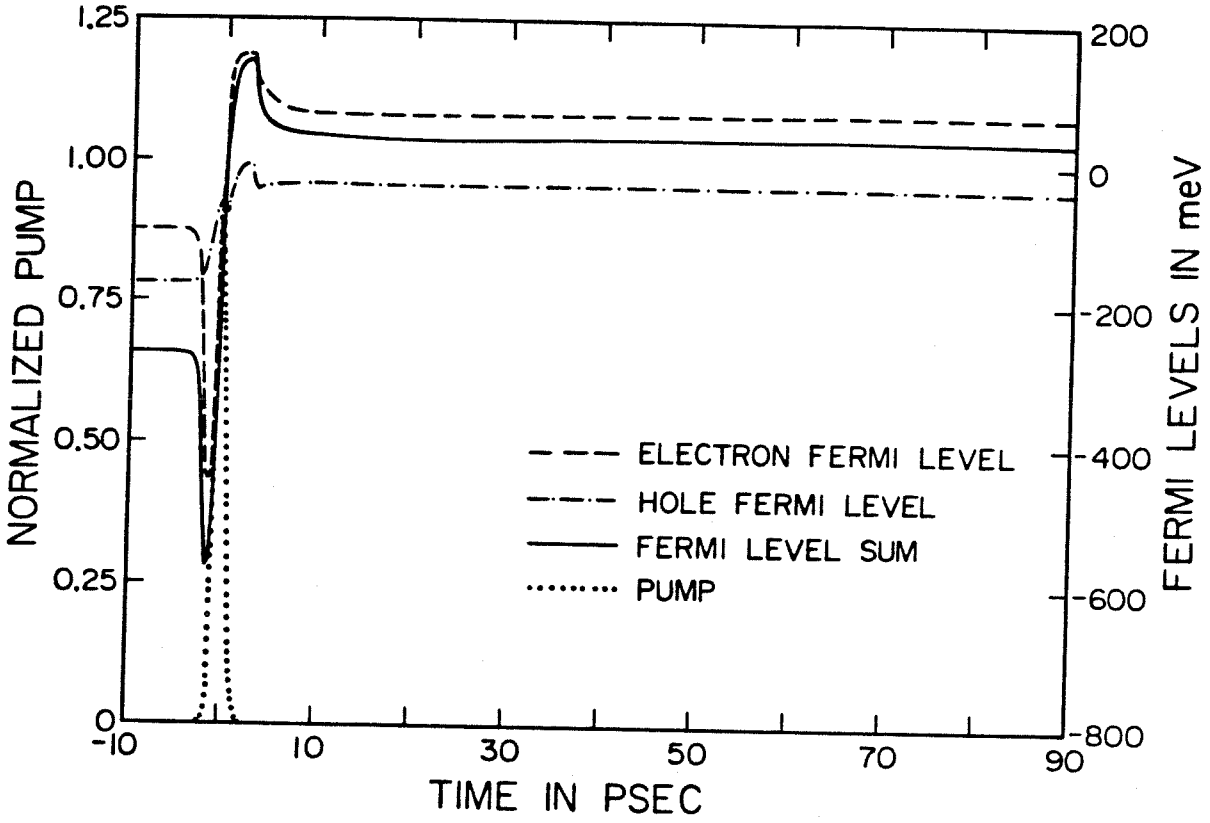

Figure 7.15 Electron and hole Fermi levels as a function of time, and the sum of Fermi levels which determines which wavelengths have gain and which have loss.

levels are thus "whipped" down very rapidly during the lasing which, by Eq. 7.46, converts the high photon energy gain to a very large loss. This happens halfway through the pulse evolution, leading effectively to a sudden enormous decrease in the photon lifetime. The computed dynamic gains at the long wavelength pulse and short wavelength pulse shown in Fig. 7.13 and Fig. 7.14 are shown in Fig. 7.16a and Fig. 7.16b. The principle of the short wavelength pulse cut-off thus results from the fact that at high photon energies, while there is a potential for a very high gain which is difficult to achieve, there is also a potential for a very high loss (many thousands of inverse centimeters) which obtains very quickly once the lasing begins.

Since any ultrashort pulse driving scheme for semiconductor diode lasers without optical feedback involves large gain and carrier population transients, the phenomena observed here, especially the carrier re-heating effects, could play a role under other injection schemes as well and could affect the ultimate short pulse performance of semiconductor lasers.

In conclusion we have used picosecond spectroscopic techniques to observe some novel picosecond laser dynamics in high quality BH laser structures. We also have shown that a relatively simple hot carrier model which allows for broadband stimulated emission and intervalley scattering accounts for most of the observed features of our experiment.

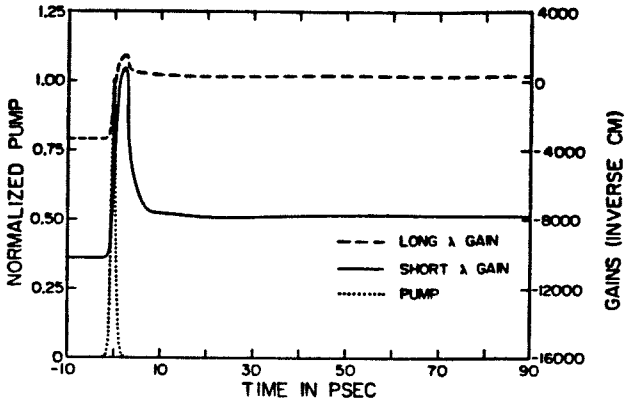

Figure 7.16 Gain at the short and long wavelengths shown in Fig. 7.13 and Fig. 7.14 as a function of time.

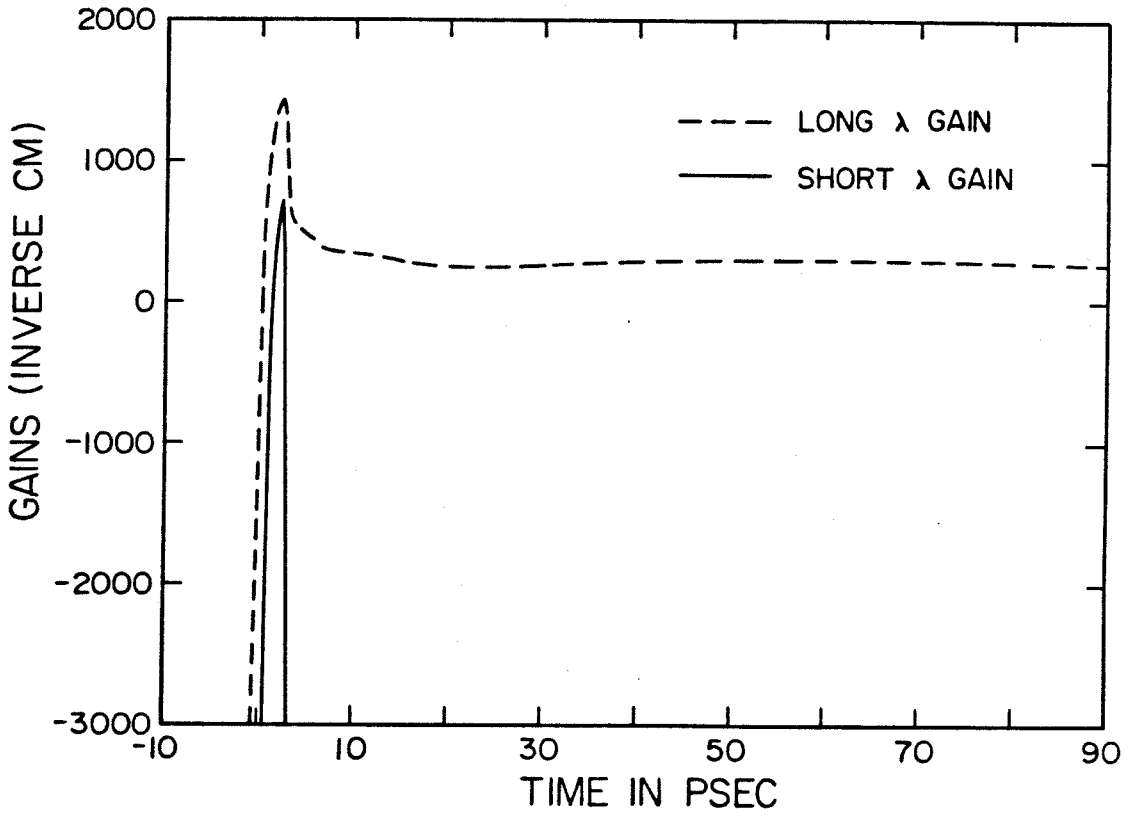

Figure 7.17 Same as above on a slightly expanded scale. Sharp conversion of gain to extreme loss at the short λ lasing wavelengths is responsible for sharp cutoff behavior on pulse shape.

CHAPTER 7 REFERENCES

1. T. L. Koch, L. C. Chiu, Ch. Harder, and A. Yariv, " Picosecond Carrier Dynamics and Laser Action in Optically Pumped Buried Heterostructure Lasers," to appear in Appl. Phys. Lett. (1982).

2. T. C. Damen, M. A. Duguay, J. Shah, J. Stone, J. M. Wiesenfeld, and R. A. Logan, App. Phys. Lett. **39**, 142 (1981).

3. J. Stone, J. M. Wiesenfeld, A. G. Dentai, T. C. Damen, M. A. Duguay, T. Y. Chang and E. A. Caridi, Opt. Lett. **6**, 534 (1981).

4. E. Burstein, Phys. Rev. **93**, 632 (1954).

5. T. S. Moss, Proc. Phys. Soc. **B67**, 775 (1954).

6. F. M. Johnson, " Stimulated Brillioun Scattering," in *CRC Handbook of Lasers with Selected Data on Optical Technology*, Ed. by R. J. Pressley, The Chemical Rubber Co., Cleveland, Ohio, 1971.

7. H. C. Casey, Jr., and M. B. Panish, *Heterostructure Lasers*, Pt. A, Academic Press, New York, 1978.

8. J. Shah and R. C. C. Leite, Phys. Rev. Lett. **22**, 1304 (1964).

9. E. M. Conwell, *High Field Transport in Semiconductors*, Supp. 9 in Solid State Physics Series, Ed. by F. Seitz, D. Turnbull, and H. Ehrenreich, Academic Press, New York, 1967.

10. G. Schmidt, *Physics of High Temperature Plasmas*, Second Ed., Academic Press, New York, 1979.

11. W. B. Joyce and R. W. Dixon, Appl. Phys. Lett. **31**, 354 (1977).

12. A. Mooradian and G. B. Wright, Solid State Commun. **4**, 431 (1966).

13. H. Frohlich, Proc. Roy. Soc. **A160**, 280 (1937).

14. See for example: N. W. Ashcroft and N. D. Mermin, *Solid State Physics*, Holt, Rinehart and Winston, New York, 1976.

15. See for example: T. S. Moss, G. J. Burrell, and B. Ellis, *Semiconductor Opto-Electronics*, John Wiley and Sons, New York, 1973.

16. X. Aymerich-Humet, F. Serra-Mestres, and J. Millan, S. S. Electron. **24**, 981 (1981).